A HYBRID CONSTITUTIVE MODEL FOR CREEP, FATIGUE, AND CREEP-FATIGUE DAMAGE

by

CALVIN M STEWART
B.S. University of Central Florida, 2008
M.S. University of Central Florida, 2009

A dissertation submitted in partial fulfillment of the requirements
for the degree of Doctor of Philosophy
in the Department of Mechanical and Aerospace Engineering
in the College of Engineering and Computer Science
at the University of Central Florida
Orlando, Florida

Fall Term
2013

Major Professor: Ali P. Gordon

ABSTRACT

In the combustion zone of industrial- and aero- gas turbines, thermomechanical fatigue (TMF) is the dominant damage mechanism. Thermomechanical fatigue is a coupling of independent creep, fatigue, and oxidation damage mechanisms that interact and accelerate microstructural degradation. A mixture of intergranular cracking due to creep, transgranular cracking due to fatigue, and surface embrittlement due to oxidation is often observed in gas turbine components removed from service. The current maintenance scheme for gas turbines is to remove components from service when any criteria (elongation, stress-rupture, crack length, etc.) exceed the designed maximum allowable. Experimental, theoretical, and numerical analyses are performed to determine the state of the component as it relates to each criterion (a time consuming process). While calculating these metrics individually has been successful in the past, a better approach would be to develop a unified mechanical modeling that incorporates the constitutive response, microstructural degradation, and rupture of the subject material via a damage variable used to predict the cumulative "damage state" within a component. This would allow for a priori predictions of microstructural degradation, crack propagation/arrest, and component-level lifing. In this study, a unified mechanical model for creep-fatigue (deformation, cracking, and rupture) is proposed. It is hypothesized that damage quantification techniques can be used to develop accurate creep, fatigue, and plastic/ductile cumulative- nonlinear- damage laws within the continuum damage mechanics principle. These damage laws when coupled with appropriate constitutive equations and a degrading stiffness tensor can be used to predict the mechanical state of a component. A series of monotonic, creep, fatigue, and tensile-hold creep-fatigue tests are obtained from literature for 304 stainless steel at 600°C (1112°F) in an air.

Cumulative- nonlinear- creep, fatigue, and a coupled creep-fatigue damage laws are developed. The individual damage variables are incorporated as an internal state variable within a novel unified viscoplasticity constitutive model (zero yield surface) and degrading stiffness tensor. These equations are implemented as a custom material model within a custom FORTRAN one-dimensional finite element code. The radial return mapping technique is used with the updated stress vector solved by Newton-Raphson iteration. A consistent tangent stiffness matrix is derived based on the inelastic strain increment. All available experimental data is compared to finite element results to determine the ability of the unified mechanical model to predict deformation, damage evolution, crack growth, and rupture under a creep-fatigue environment.

Dedicated to the Stewart family.
“God keep us strong”

ACKNOWLEDGMENT

I would like to thank my advisor Dr. Ali P. Gordon for his guidance, thoughtful suggestions, and support throughout my graduate education. My thanks go to the member of my thesis committee, who are: Dr. Jayanta Kapat, Dr. Kevin Mackie, Dr. Faissal Moslehy, and Dr. Seetha Raghavan.

I would like to thank all the people who have provided technical, emotional, or spiritual support during my studies including: God, family, fiancé, and the McKnight doctoral fellows' network.

Most importantly, I would like to thank the McKnight Doctoral Fellowship for provide financial support through the Florida Education Fund. Without their support reaching this point would have been considerably harder.

TABLE OF CONTENTS

LIST OF FIGURES

LIST OF TABLES

CHAPTER ONE: INTRODUCTION

1.1 **Motivation**

Modern industrial gas turbines (IGTs) experience a combination of high pressure ratios in excess of 18 and rotor inlet temperatures above 1425°C (Figure 1.1). This creates a situation where material behavior and component design play a critical role in long term reliability [1]. Drives to further increase efficiency through higher boundary conditions have led to the advent and applications of austenitic, participate-hardened superalloys [2]. Within the combustion zone high operating temperatures, mechanical stresses, thermal stresses, sharp geometric discontinuities, and foreign objects lead to a number of damage mechanisms. These damage mechanisms are creep, fatigue (mechanical, fretting, and/or thermal), corrosion, oxidation, and erosion [3]. The interaction of these mechanisms leads to creep-fatigue (CF) or thermomechanical-fatigue (TMF) distinguished by constant and dynamic thermal loading respectively. Creep-fatigue and thermomechanical-fatigue are the principal cause of microstructural damage leading to eventual failure of hot section components [4].

The combustion zone consists of a ring of combustor baskets and transition pieces as depicted in Figure 1.2 (a)-(c). The purpose of the combustor basket is to mix the compressed air coming from the compressor with the fuel and ignite the mixture to a temperature of 3500°F (1900°C) [1]. An example of a combustor is provided Figure 1.2(a). Compressed air is passed across the outer hull, the secondary hull (air casing), and through secondary/dilution air holes which create a protective boundary layer to reduce internal hull and combustion gas temperature.

The temperature gradient in the hull leads to thermal stresses. External pressure is higher than internal pressure causing mechanical stress in the hull which induces creep buckling. The combustion process generates high-frequency vibrations which induce high-cycle fatigue. The thin walls of the hull make failure due to oxidation a concern. Gas exits the combustor and enters the transition piece. An example of a transition piece is provided Figure 1.2(b).The purpose of the transition piece is to improve the uniformity of the combustion gas and direct the gas against the first row of nozzle guide vanes. Less active cooling is possible on this component due to the need to normalize the combustion gas flow thus transition pieces are more susceptible to creep buckling and cracking particular in the upper panel [5]. It has been found that the principle causes of combustor and transition piece failure are transgranular body and craze cracks due to creep, corrosion, and high-cycle fatigue [6]. Common materials used for combustion zone components are isotropic nickel-based superalloys such as: Hastelloy X, RA333, Nimonic 263, HS-188, GTD-222, and IN617 [5]. Plasma-sprayed thermal barrier coatings (TBCs) are widely used to reduce the temperature of the base metal and reduce creep buckling.

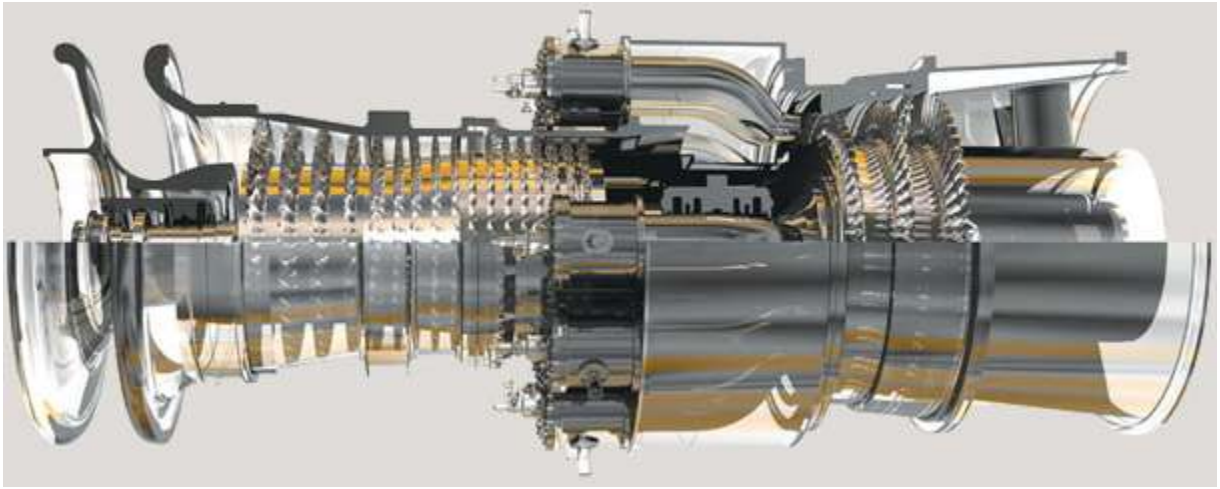

Figure 1.1 – GE 7EA Heavy Duty Gas Turbine [7]

(a) **(b)**

(c)

Figure 1.2 – W501F gas turbine components (a) combustor (b) transition piece (c) fixture [8]

The turbine zone consists primarily of nozzle guide vanes and buckets/blades as depicted in Figure 1.3(a) and (b). The purpose of the stationary nozzle guide vanes is to accelerate the combustion gases while channeling them to intersect the rotating turbine blades at the optimum angle. These components almost always have a thermal barrier coating, internal tubular steam or air cooling holes, and are made of a base metal with high creep strength and oxidation resistance

[9,10]. While these components are susceptible to creep deformation, of greater concern is the failure of the TBC which can lead to enhanced creep deformation, and excessive oxidation of the vane. Common materials used are cobalt-base alloys, X-40, X-45, FSX-414, ECY768, as well as nickel-base superalloys IN939 and GTD-222 [11]. Once the gas has been directed by the stationary vane, it strikes the rotating blades. The purpose of the rotating turbine blades are to capture the combustion pressure and cause the rotor to spin. Turbine blades experience high stress due to combustion pressure, centrifugal and thermal loads. Blades are susceptible to creep, oxidation, and corrosion, as well as thermal and low-cycle fatigue. High-cycle fatigue can also arise due to blade flutter, rotor-speed induced excitation, and fretting at the blade root. Turbine blade materials have evolved from isotropic (IN738, IN939, and IN792) to directionally-solidified (DS GTD-111) and finally single crystalline alloys (CMSX 4, PWA1483, Rene N5) due to steady increasing combustion pressure and temperatures over the years [1].

(a)

(b)

Figure 1.3 – Turbine zone components (a) row one nozzle guide vane (b) row one bucket/blade

The original equipment manufacturer (OEM) of industrial gases turbines typical divide engineering efforts into: research and development, customer order engineering, and field service. The research and development team focus on product optimization and integration of new IGT products. Fundamental issues of structural integrity, crack initiation, and lifing are investigated. Once a demonstrator plant has been constructed and refinements to the operation and design of the product made, the product is then made available to customers. The customer order engineering team works on taking established IGT designs and customizing them base on specifications negotiated with the customer. Special attention is given to ensure components will not failure between service intervals. Guarantees are made to the owner in terms of plant performance with harsh non-conformance costs associated with missed performance metrics. Finite element simulations of thermal, mechanical, vibration, creep, and fatigue responses are conducted often independent of each other. Crack initiation, oxidation, and corrosion calculation are analytical calculated from experimental data using in house codes and design manuals. The field service engineering team focuses on providing standby, running, and disassembly inspections of IGTs based on a negotiated service contract in addition to forced outage support. Combustor inspections occur every 12,000 hours. Major inspections occur at 100,000 hours. During a hot-gas-path inspection all transition pieces and first row nozzle guide vanes are removed and inspected. The remaining vanes and blade are inspected in place. A non-destructive evaluation (NDE) technique such as fluorescent penetrant inspect (FPI) is used to detect the precise of cracks [12]. Where cracks are detected the blade must be removed from service. In addition, blades are checked for displacement, clearances, rubbing, oxidation, and erosion with set criteria for remove from service.

There is a lack of accuracy in the determination of the state of components within industrial gas turbines. As described above OEM's prefer to design and provide fixed service intervals at which components should be replaced or repaired based on independent fixed criteria. The actual damage state of the component and remaining life is not generally of interest. OEM's are more concerned with safety and reducing the likelihood of incurring non-conformance costs due to a forced outage caused by unpredicted failure of components. On the other hand plant owners are more concerned with service costs associated with repairing or replacing components. For example, an undisclosed Frame 6B plant underwent a hot-gas-path inspection by an OEM [13]. The OEM recommended the replace of blades due to potential cracking on the airfoils. The plant owner to avoid service costs decided instead to repurpose blades from second unit that exhibited slight shroud-lifting. No thought was give to the current damage state of the component and remaining life which led to a forced outage as depicted in Figure 1.4. Cracks formed in the airfoils due to thermo-mechanical fatigue. The critical crack length was reached in a single airfoil and the blade fractured. The failed airfoil passed through the turbine causes substantial collateral damage. This could have been avoided had the damage state and the remaining life of the repurposed blades been known before installation. The interaction of creep, fatigue, and oxidation damage mechanism contributed to the damage state. The dominance and balance of active damage mechanisms are controlled by stress state, temperature, frequency, hold time, wave shape, aging, material processing, environment and other miscellaneous variables. Plant owners would like to extend the service intervals between inspections. Owners would like to extract more of the remaining life from components. OEM's would like to reduce non-conformance costs [5-7].

(a)

(b)

Figure 1.4 - Forced outage of frame 6B IGT due to customer error (a) hot-gas inspection (b) forced outage [13]

1.2 **Research Objectives**

The objective of this research is to develop a unified mechanical model for creep-fatigue which incorporates the physical degradation, constitutive response, and cracking of superalloys. The resulting unified model can be used to more accurately determine the damage state and remaining life in components which have undergone history.

The goals of thesis research are as follows:

1) **Unified Mechanical Model for Creep**

   Creep data is obtained from literature. A coupled creep-damage zero yield surface viscoplastic constitutive model is developed based on continuum damage mechanics. The phenomenological creep damage evolution is correlated to mechanical property degradation. An analytical technique to determine material constants from experimental data is created. An implemented of the constitutive model in multiaxial form is derived.

2) **Unified Mechanical Model for Creep-Fatigue**

   Fatigue data is obtained. A coupled creep-fatigue-damage yielding viscoplastic constitutive model is developed based on continuum damage mechanics. The phenomenological fatigue and plastic damage evolution is correlated to mechanical property degradation. A functional relationship between creep, fatigue, and plastic damage is obtained for total damage and the viscous behavior. Analytical and numerical optimization is used to determine material constants. An implemented of the constitutive model in multiaxial form is derived.

3) **Finite Element Simulations**

A series of service-like and atypical loading conditions are simulated to evaluate the capabilities of the unified mechanical model to predict mechanical behavior.

1.3 Organization

This work is organized as follows. Chapter 2 introduces the fundamental concepts of creep, fatigue, and creep-fatigue. It covers constitutive and damage modeling as well as a review of the issues facing continuum damage mechanics-based numerical crack growth. Chapter 3 is a literature review of the subject material 304SS. In Chapter 4, a novel unified mechanical model for creep is proposed, based on extensive evaluation of experimental data and existing constitutive modeling techniques. In Chapter 5, a novel unified mechanical model for creep-fatigue is proposed, based on extensive evaluation of experimental data and existing constitutive modeling techniques. Afterwards, in Chapter 6, a series of parametric one-dimensional simulations are performed to evaluate the capabilities of the unified mechanical model for creep-fatigue. Finally, Chapter 7 contains concluding remarks and recommendations for future work. Appendix A contains the custom one-dimensional FEA code written in the FORTRAN programming language.

CHAPTER TWO: BACKGROUND

2.1 **Introduction**

Towards the development of a new mechanical model for creep-fatigue, a review of existing modeling techniques must be conducted. The fundamental concepts, constitutive equations, and damage laws for creep, fatigue, and coupled fatigue are discussed in sections 2.2-2.4 respectively. A pivotal goal in the current study is the development of a numerical technique to model crack nucleation, initiation, and propagation. A review of numerical crack propagation techniques is provided in section 2.5 with an emphasis on the continuum damage mechanics approach. Finally, a summary of the limitation of existing efforts is provided with a description of the proposed alternative. It should be noted, that while a serious effort has been expended to include as much detail as possible; it is not possible to include an exhaust review of all methodologies used to model creep, fatigue, and coupled creep-fatigue. Additional background information pertaining to the development of the creep and creep-fatigue mechanical models is discussed in the respective chapters.

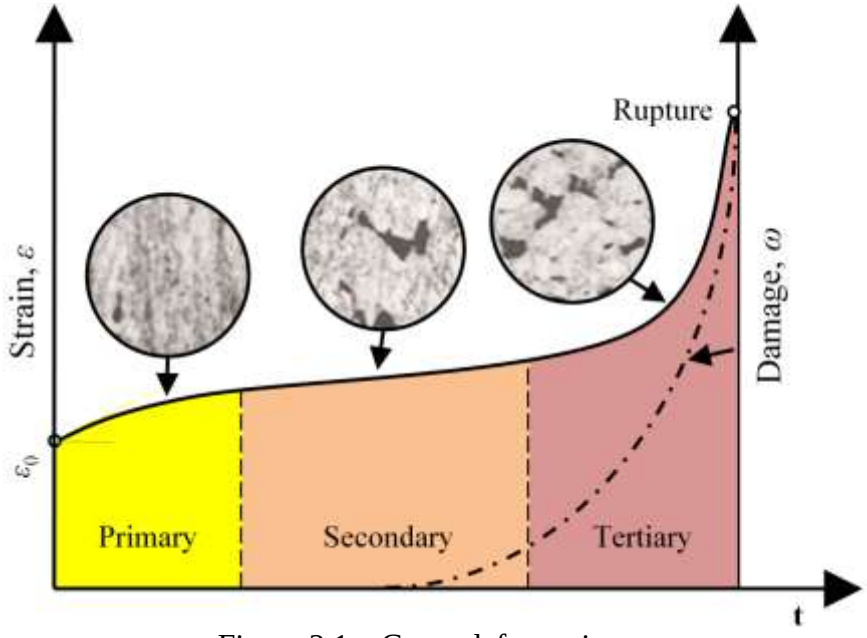

Figure 2.1 – Creep deformation

2.2 **Creep**

Under relatively high temperatures (above $0.4T_m$ for most metals) and low cyclic loading, creep dominant deformation and damage occurs. Creep is a viscoplastic deformation that has a zero yield surface (plastic flow occurs when $\sigma > 0$). Depending on the subject material, creep is dependent on temperature, time (aging effects), loading rate, and the state of stress. Classically, creep deformation is separated into three distinct stages, primary, secondary, and tertiary creep as depicted in Figure 2.1. Descriptively, these stages are associated with transient, steady-state, and accelerating creep, respectively [14]. In the case of superalloys, primary creep, is due to strain-hardening where pre-existing dislocations encounter obstacles (solid solution atoms, dispersoids, precipitates, grain boundaries, etc.) and becoming immobilized [15]. It initially occurs at a high rate, but the eventual saturation of dislocation density inhibits further primary creep deformation. After this stage, secondary creep is observed

and is characterized by an almost constant strain rate (typically called the minimal strain rate) due to a balance between strain-hardening and recovery mechanics. Increased mobility enhanced by thermal activity (temperature induced diffusion) can cause cross slip where dislocations can diffuse away from obstacles [16]. In this region, the nucleation of grain boundaries and grain boundary sliding occur. Finally, tertiary creep becomes dominant and is characterized by a rapid non-linear increase of strain rate until creep rupture. This stage is driven by the net area reduction due to elongation (substantial in ductile material) and the evolution of microcracks and voids into macro-cracks leading to rupture.

In the vicinity of the crack tip, the three creep regimes persist. The distribution of creep deformation strongly mirrors the stress field. As damage accumulates the primary, secondary, and tertiary creep stages grow in size along the crack propagation path as observed in Figure 2.2 [17]. The tertiary creep zone is nearest to the crack tip as it is the region where the stress concentration is highest. The size of each zone is transient due to inelastic strain driven stress relaxation and crack propagation driven stress redistribution. It is encircled by secondary creep followed by primary creep. Elasticity is remote.

Deformation mechanism maps offer a convenient way to identify the dominant creep mechanism under various boundary conditions. For 304SS, the maps clearly indicate two mechanisms, diffusion creep and (dislocation-core-diffusion controlled) power-law creep as shown in Figure 2.3. Within diffusion creep the bulk-self (lattice) and grain boundary (boundary) zones are also depicted.

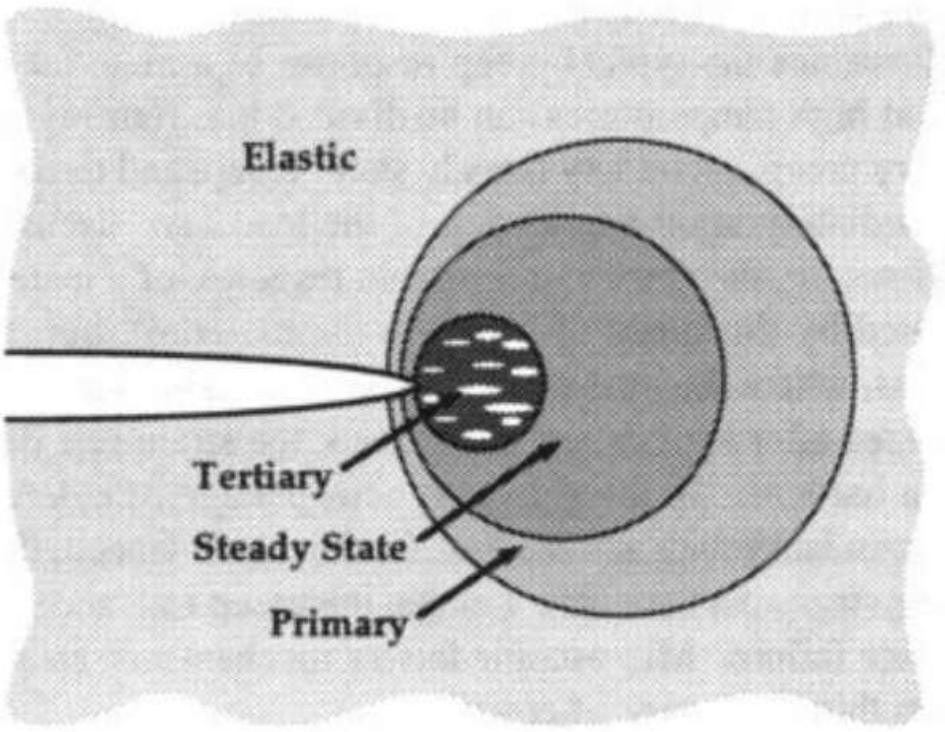

Figure 2.2 - Creep zones at the crack tip [17]

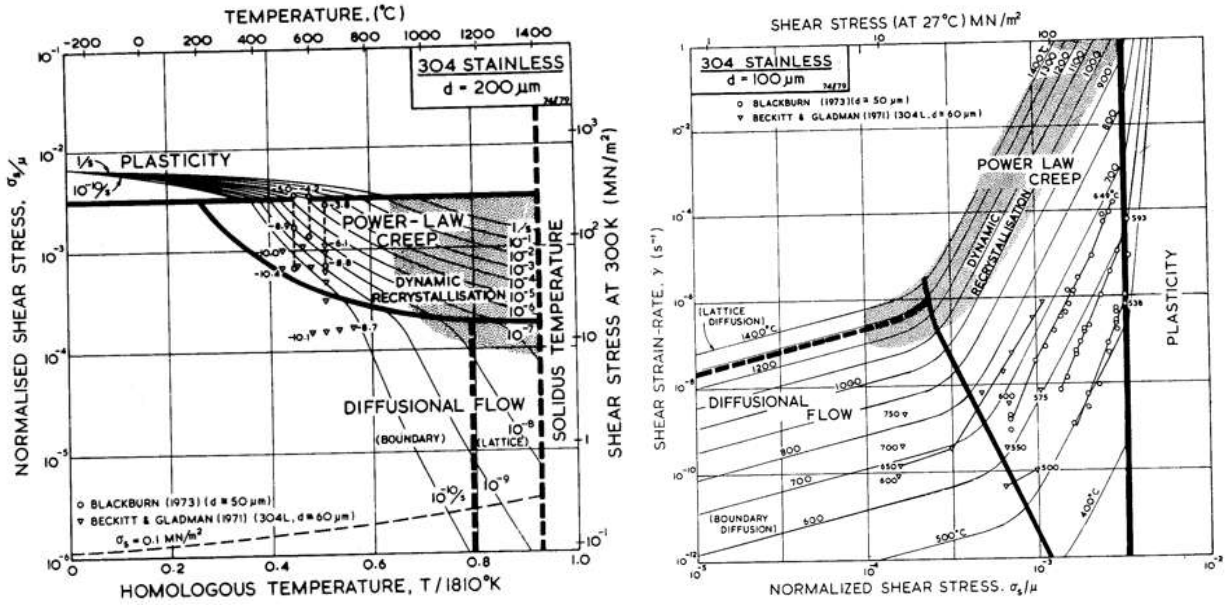

Figure 2.3 - Deformation mechanism maps of 304SS (a) stress/temperature, grain size 200μm (b) strain-rate/stress, grain size 100μm [18]

The basic approach to modeling time-to-failure is by way of stress-rupture. Two popular equations are the Larson-Miller (*LMP*) and Monkman-Grant (*MG*) parameters. Larson-Miller is one of the earliest creep rupture prediction approaches [19]. This approach is based on a time-temperature relationship as follows

$$LMP = T\left(\log t_r + C\right)/1000 \tag{2.1}$$

where T is temperature in Kelvin, t_r is rupture time, C is a constant, and *LMP* is the Larson-Miller parameter. For metals, C is typically set to 20 [19]. The Larson-Miller parameter can be determined for stress or strain-controlled experiments through either applied stress or strain rate [20]. The Larson-Miller method requires a suitable set of creep deformation tests to be performed to rupture. In the case of stress-controlled experiments, a plot of stress versus *LMP* is created and the C constant is adjusted until the *LMP* parameter is described as a logarithm of stress. Once the C constant has been determined, rupture time predictions can be produced by using the known T and *LMP* from the applied boundary conditions. Plotting $\log(\sigma)$ versus LMP gives a master plot which represents the strength for all combinations of stress, temperature, and rupture time [21]. A linear equation for *LMP* as a function of $\log(\sigma)$ can be found. Rupture predictions can then be produced by rearranged the Larson-Miller relation into the following form

$$t_r = 10^{\frac{LMP(\sigma) - T \cdot C}{T}} \tag{2.2}$$

This method has been used consistently with Ni-based superalloys [22]. Ibanez and colleagues produced LMP predictions for DS GTD-111 in both L and T-orientations [23].

Monkman and Grant [24] observed that creep rupture can be predicted for many alloy systems using the following expression

$$\log\left(t_r\right)+m\log\left(\dot{\varepsilon}_{\min}\right)=k_{MG} \tag{2.3}$$

where $\dot{\varepsilon}_{\min}$ is the minimum creep strain rate, t_r is the creep rupture time, m is a constant, and k_{MG} is the referred to as the Monkman-Grant constant. For some materials m is assumed equal to unity furnishes a simplified form of Eq. (2.3) expressed as

$$\dot{\varepsilon}_{\min}t_r=k_{MG} \tag{2.4}$$

Previous studies show that the Monkman-Grant relationship produces accurate rupture time predictions for various DS Ni-based superalloys [23,25]. The Monkman-Grant method requires a set of creep deformation tests to be performed to rupture. Using the minimum creep strain rate, $\dot{\varepsilon}_{\min}$ and rupture time, t_r the m and K_{MG} constants can be determined. The minimum creep strain rate can be expressed as a function of stress, $\dot{\varepsilon}_{\min}\left(\sigma\right)$. By rearranged the Monkman-Grant relation into the following form

$$t_r=\frac{10^{k_{MG}}}{\dot{\varepsilon}_{\min}\left(\sigma\right)^m} \tag{2.5}$$

a rupture prediction can be made.

2.2.1 Constitutive Modeling

A creep constitutive model can be considered a viscoplasticity model where the yield surface is zero. Generally, two types of constitutive models for creep have been developed, mechanistic and phenomenological. Mechanistic constitutive models focus on determining the stress-creep strain relationship as it relates to fundamental microstructural mechanisms. These constitutive models are used when looking at micro/nano-scale creep. Phenomenological constitutive models focus on determined the bulk stress-creep strain relationship through functional relations that may have no bearing on the microstructural mechanisms. Theses constitutive models are used when looking at macro-scale creep. This section focuses on phenomenological constitutive models; however, a brief review of popular mechanistic constitutive models is provided.

Creep can be divided into two mechanisms: diffusion (bulk-self and grain boundary diffusion) and dislocation-core-diffusion controlled power-law creep. The active mechanism is dependent on grain size, stress, and temperature [26,27].

Diffusion creep is divided into bulk-self and grain boundary diffusion. In bulk-self diffusion atoms diffuse through the lattice within grains. To model this behavior the Nabarro-Herring constitutive model has been developed

$$\dot{\varepsilon}_{NH} = A\frac{D}{d^2}\frac{\sigma\Omega}{kT} \tag{2.6}$$

where A is a dimensionless constants, D is the lattice diffusion coefficient, d is the grain size, σ is the applied stress, Ω is activation enthalpy, k is the Boltzmann's constants, and T is the absolute temperature [26,27]. The activation enthalpy, Ω is equal to the activation enthalpy of bulk-self

diffusion, Ω_{SD}. In grain boundary diffusion, atoms diffuse along grain boundaries. To model this behavior the Coble constitutive model has been developed

$$\dot{\varepsilon}_{Co} = A\frac{D}{d^3}\frac{\sigma\Omega}{kT} \tag{2.7}$$

where the activation enthalpy, Ω is equal to the activation enthalpy of grain boundary diffusion, Ω_{GB}.

In dislocation-core-diffusion, atoms diffuse into and out of dislocation cores, causing climb and glide. To model this behavior the Weertman constitutive model has been developed as follows

$$\dot{\varepsilon}_{Co} = A\frac{DGb}{kT}\left(\frac{\sigma}{G}\right)^n \tag{2.8}$$

where A and n are dimensionless constants, D is the lattice diffusion coefficient, b is the magnitude of the Burgers vector, and G is the shear modulus [27]. Multiple mechanisms can contribute to the inelastic strain-rate either in parallel or in series demonstrated below

$$\dot{\varepsilon} = \sum_i \dot{\varepsilon}_i \tag{2.9}$$

$$\dot{\varepsilon} = \sum_i \left(1/\dot{\varepsilon}_i\right)^{-1} \tag{2.10}$$

Historically, more phenomenological models have been generated and used to model the creep of materials. An examination of phenomenological models for primary, secondary, or tertiary regimes is now provided.

The transient nature of the primary creep regime detonates a dependence on time. Numerous phenomenological primary constitutive equations have been developed. A list of the earliest and most popular is provided in Table 2.1.

One of the most popular and well received models is Andrade's law for primary creep

$$\varepsilon_{cr} = At^{1/q} \tag{2.11}$$

where ε_0 is instantaneous creep, A ($t^{-1/q}$) is a coefficient, and q is a unitless exponent. The constant q has been experimentally observed to be 3 for most materials [28,29]. A number of authors have attempted to disprove the uniformity of this constant with limited success [30]. A more advantageous equation for primary creep adds stress dependence in a power law form

$$\varepsilon_{cr} = A\sigma^n t^m \tag{2.12}$$

where σ (MPa) is the applied load and A ($MPa^{-n} hr^{-m}$), n, and m are temperature-dependent primary creep constants [31]. When stress is assumed to be constant, a time-hardening primary creep strain rate equation can be developed of the form

$$\dot{\varepsilon}_{cr} = \frac{d\varepsilon_{cr}}{dt} = Am\sigma^n t^{m-1} \tag{2.13}$$

where the units of A change to $MPa^{-n} hr^{-(m-1)}$. By taking time, t from Eq. (2.12) and inserting it into Eq. (2.13), a strain harden-hardening primary creep strain rate equation is of the form

$$\dot{\varepsilon}_{cr} = \frac{d\varepsilon_{cr}}{dt} = mA^{1/m}\sigma^{n/m}\varepsilon_c^{(m-1)/m} \tag{2.14}$$

Generally, the time-hardening solution predicts a slightly higher creep strain rates than strain-hardening. Combined theories have been developed to produce intermediate results between time and strain-hardening theories of the form

$$\dot{\varepsilon}_{cr} = \frac{d\varepsilon_{cr}}{dt} = C\sigma^{\gamma}\varepsilon_{cr}^{\delta} t^{\eta} \tag{2.15}$$

where $C(1/MPa)^{-\gamma}(1/hr)^{-\eta}$, γ, δ, and η are constants.

Table 2.1 – Primary creep consituive equations [16]

Source	Creep Law
Andrade, 1910	$\varepsilon_{cr} = \left(1 + At^{1/q}\right)\exp\left(kt\right) - 1$ $\varepsilon_{cr} = At^{1/q} \quad \left(t \to 0, k \to 0\right)$
Bailey, 1935	$\varepsilon_{cr} = Ft^{n} \quad \left(\frac{1}{3} \le n \le \frac{1}{2}\right)$
McVetty, 1943	$\varepsilon_{cr} = G\left(1 - e^{-qt}\right) + Ht$
Graham and Walles, 1955	$\varepsilon_{cr} = \sum_{i} a_i t^{n_i}$
Garofalo, 1965	$\varepsilon_{cr} = \theta_1\left(1 - e^{-\theta_2 t}\right) + \dot{\varepsilon}_s t$

The secondary creep regime is denoted by the minimum creep strain rate, $\dot{\varepsilon}_{\min}$ observed in constant load tests. Numerous studies have demonstrated a strong relationship between stress and the minimum creep strain rate. Numerous stress-dependent constitutive equations have been developed. A list of the earliest and most popular is provided in Table 2.2.

One of the most popular models is the classical Norton power law for secondary creep [32]

$$\dot{\varepsilon}_{cr} = \frac{d\varepsilon_{cr}}{dt} = A\bar{\sigma}^{n} \tag{2.16}$$

where *A* and *n* are the secondary creep constants, and $\bar{\sigma}$ is an equivalent stress. This popularity is derived from the simplicity of implementation and the retention of functional shape regardless of stress magnitude. A proportional load increase will not change the stress distribution. In contrast, most other models undergo a functional change that causes a redistribution of stress as

load increases. Typical the von Mises equivalent stress which is both isotropic and pressure insensitive is used

$$\sigma_{vm} = \sqrt{\frac{3}{2}\mathbf{S}_{ij}\mathbf{S}_{ij}}, \quad \mathbf{S}_{ij} = \boldsymbol{\sigma}_{ij} - \sigma_H, \quad \sigma_H = \sigma_{kk}/3; \tag{2.17}$$

where σ_H is the hydrostatic (mean) stress and **S** is the deviatoric stress tensor. The Norton power law is sometimes referred to as the Norton-Bailey law. The secondary creep constants *A* and *n* exhibit temperature-dependence. Stress provides a substantial contribution to the creep strain rate as the *n* secondary creep constant is an exponent of stress.

Dorn [33] suggested that temperature contributions can be accounted for by replacing the *A* constant with an Arrhenius equation

$$A(T) = B\exp\left(\frac{-Q_{cr}}{RT}\right) \tag{2.18}$$

where *B* is the pre-exponential factor in units $MPa^{-1}\ hr^{-1}$, Q_{cr} is the apparent activation energy for creep deformation in units $J\ mol^{-1}$, *R* is the universal gas constant 8.314 $J\ mol^{-1}\ K$, and *T* is temperature in units Kelvin. Introducing Eq. (2.16) into Eq. (2.18) leads to

$$\dot{\varepsilon}_{cr} = \frac{d\varepsilon_{cr}}{dt} = B\bar{\sigma}^n \exp\left(\frac{-Q_{cr}}{RT}\right) \tag{2.19}$$

Historic application of this model has shown that the *B*, Q_{cr}, and *n* secondary creep constants exhibit stress dependence when comparing constants obtain from high stress (high creep strain rate) experiments with those at lower stress (low strain rate). A high stress modification was proposed as

$$\dot{\varepsilon}_{cr} = \frac{d\varepsilon_{cr}}{dt} = B\exp(\beta\sigma)\exp\left(\frac{-Q_{cr}}{RT}\right) \tag{2.20}$$

where β is an additional secondary creep constant. An interface of Eq. (2.19) and Eq. (2.20) was proposed by Garofalo [34] as follows

$$\dot{\varepsilon}_{cr} = \frac{d\varepsilon_{cr}}{dt} = B\left(\sinh \alpha\sigma\right)^{n} \exp\left(\frac{-Q_{cr}}{RT}\right) \tag{2.21}$$

where the model reverts to Eq. (2.19) when $\alpha\sigma < 0.8$ and reverts to Eq. (2.20) when $\alpha\sigma > 1.2$ provided that $\beta = \alpha n$ [35]. Typically due to equipment and time constraints creep tests at both high and low stress levels are not available; therefore, the commonly implemented method is the simple Norton power law with the Arrhenius relation, Eq. (2.19).

The tertiary creep regime is denoted by a rapid increase in creep deformation consistent with the microstructural degradation that leads to rupture. Most tertiary creep constitutive models are mixed regime requiring that both secondary and tertiary regimes be modeled together. A list most popular is provided in Table 2.3.

Table 2.2 – Steady-state creep constitutive equations [16]

Source	Creep Law
Norton, 1929	$\dot{\varepsilon}_{cr} = A\left(\sigma/\sigma_0\right)^{n}$
Soderberg, 1936	$\dot{\varepsilon}_{cr} = A\left\{\exp\left(\sigma/\sigma_0\right)-1\right\}$
McVetty, 1943	$\dot{\varepsilon}_{cr} = A\sinh\left(\sigma/\sigma_0\right)$
Dorn, 1955	$\dot{\varepsilon}_{cr} = A\exp\left(\sigma/\sigma_0\right)$
Johnson, Henderson, and Kahn, 1963	$\dot{\varepsilon}_{cr} = A_1\left(\sigma/\sigma_0\right)^{n_1} + A_2\left(\sigma/\sigma_0\right)^{n_2}$
Garofalo, 1965	$\dot{\varepsilon}_{cr} = A\left\{\sinh\left(\sigma/\sigma_0\right)\right\}^{n}$

Table 2.3 – Mixed regime creep constitutive equations [36-39]

Source	Creep Law	Creep Regimes
Kachanov-Rabotnov, 1967-69	$\dot{\varepsilon}_{cr} = A\left(\frac{\bar{\sigma}}{1-\omega}\right)^{n}, \ \dot{D} = \frac{M\bar{\sigma}^{\chi}}{(1-D)^{\phi}}$	Secondary Tertiary
Evans-Wilshire (Theta Projection), 1984	$\varepsilon = \theta_1\left(1-e^{-\theta_2 t}\right)+\theta_3\left(e^{\theta_4 t}-1\right)$	Primary Secondary Tertiary
Prager, M. (Omega Method), 1995	$\dot{\varepsilon}_{cr} = \dot{\varepsilon}_0 \exp\left(\Omega_p \varepsilon\right)$	Secondary Tertiary

2.2.2 Damage

Over 25 creep damage models have been developed since 1938 [36-37,40,41-48]. A list of the earliest and most popular is provided in Table 2.4. Creep damage if often modeled using continuum mechanics; where heterogeneous micro-scale damage is modeled as a homogenous macro-scale effective constitutive response within a finite volume [49,50]. Creep damage can be considered equal to the reduction-in-area from microcrack, cavities, voids, and etc. as a structure undergoes creep deformation. This reduction-in area can be represented mathematically as the net/effective stress

$$\tilde{\sigma} = \bar{\sigma}\frac{A_0}{A_{net}} = \frac{\bar{\sigma}}{\left(1-\frac{A_0 - A_{net}}{A_0}\right)} = \frac{\bar{\sigma}}{(1-\omega)} \tag{2.22}$$

where A_{net} is the current area, A_0 is the initial area, $\bar{\sigma}$ is equivalent stress, $\tilde{\sigma}$ is the net/effective stress, and ω is damage. The effective stress increase leads to an accelerated rate of creep deformation.

D_1 - Damage due to mobile dislocation density

D_2 - Damage due to creep-constrained cavitation

t_{ri} - Rupture time under conditions σ_i, T_i

ε_{ri} -Ductility under conditions σ_i, T_i

$M, \chi, \phi, \alpha, \beta, n, h, C, R, N, B, d, k$ - Material constants

Table 2.4 - Creep damage laws [40, 36-37,41-48].

Source	Damage Law
Robinson Life-fraction, 1938	$D = \sum \frac{t_i}{t_{ri}}$
Lieberman Strain-fraction, 1962	$D = \sum \frac{\varepsilon_i}{\varepsilon_{ri}}$
Mixed rule, 1959	$D = \sum \left(\frac{t_i}{t_{ri}}\right)^{1/2} \left(\frac{\varepsilon_i}{\varepsilon_{ri}}\right)^{1/2}$
Extended Mixed rule, 1972	$D = k\sum \frac{t_i}{t_{ri}} + (1-k)\sum \frac{\varepsilon_i}{\varepsilon_{ri}}$
Kachanov, 1958 & Rabotnov, 1969	$dD = M\sigma^{\chi}(1-D)^{-\phi}\,dt$
Hayhurst 1972	$dD = M\sigma_{eqv}{}^{\chi}(1-D)^{-\phi}\,dt,$ $\sigma_{eqv} = \alpha\sigma_1 + \beta\sigma_m + (1-\alpha-\beta)\sigma_e$
Greenwood 1973	$d(n/n_0) = (\sigma/\sigma_0)^2\, d(\varepsilon/\varepsilon_0), \quad d(v/v_0) = \left[(\sigma/\sigma_0)/t_0\right]dt,$ $d(\varepsilon/\varepsilon_0) = \left[(\sigma/\sigma_0)^5/t_0\right]dt, \quad D = nv^{\frac{2}{3}}/n_0 v_0^{\frac{2}{3}} = A/A_0$
Hayhurst 1983	$dD = M\sigma_{eqv}{}^{\chi}(1-D)^{-\phi}\,dt,$ $\sigma_{eqv} = \sigma_1^{\alpha} + \sigma_e^{1-\alpha}$
Constesti, 1986	$dD = A\sigma_1^{\alpha}\varepsilon_{eq}{}^{\beta}d\varepsilon_{eq}$
Othman, Hayhurst, Dyson, 1993	$dH = \frac{h}{\sigma_e}\frac{A\sinh\{B\sigma_e(1-H)\}}{(1-\omega_1)(1-\omega_2)^n}\left(1-\frac{H}{H^*}\right)^2 dt,$ $dD_1 = \frac{CA\sinh\{B\sigma_e(1-H)\}(1-\omega_1)}{(1-\omega_2)^n}dt, 0 < D_1 < 1$ $dD_2 = \frac{RAN\sinh\{B\sigma_e(1-H)\}}{(1-\omega_1)(1-\omega_2)^n}\left(\frac{\sigma_1}{\sigma_e}\right)^d dt, 0 < D_2 < 0.3$

2.3 **Fatigue**

Fatigue refers to the behavior of a material under cyclic loading, where over time localized fatigue damage builds (nucleates) leading to crack initiation and propagation. Depending on the subject material, fatigue is a function of load, mean stress, stress ratio, surface condition, size, temperature, frequency and occurs above the endurance limit of a material. Fatigue damage occurs in both elastic and plastic regimes. Fatigue cracks have the possibility of arresting. Fatigue damage is progressive and irreversible [51].

Typical fatigue failures exhibit three observable features; a crack initiation site, beach marks or a rubbed surface (due to growth per-cycle), and a final granular fracture surface. The fatigue damage process during initiation is primarily driven by slip. Slip is where individual grains by dislocation move along crystallographic planes. Dependent on material history, the existing dislocations may increase leading to hardening or rearrange with enhanced dislocation mobility leading to softening. In brittle materials, dislocations are not mobile and slip is minimal. In ductile materials, dislocations are mobile and slip is free to occur. Materials with mixed behaviors exhibit both limited mobility and slip planes. Initiation typical occurs at the surface of a material. Intrusion and extrusion under cycling leads to slip bands. Crack initiation occurs at slip band intrusions near stress concentrations. Slip bands increase over time and are also referred to as slip lines. Slip bands are 3D dimensional with varying thickness, depth, and orientation at the surface.

Once nucleation of an initial microcrack has occurred, under continuous cycling two distinct stages of growth are observed. The two distinct stages are (Stage 1) shear mode and (Stage 2) tensile mode as observed in Figure 2.4 [51]. In stage 1, also known as the short crack

propagation stage, growth occurs primarily due to a shear stresses and strains across a finite number of grain boundaries (dependent on subject material). Cracks will growth along the maximum shear planes. The end of this stage is signified by a deceleration of the crack growth rate due to microstructural barriers including grain boundaries and inclusions. In Stage 2, as known as the long crack propagation stage, striations/beach marks are observable under magnification. Cracks grow perpendicular to the maximum tensile stress direction and under magnification follow a "zigzag" pattern [52]. Fatigue cracks are typically transgranular; however have been observed to be intergranular dependent on grain size, stress, and temperature. This is typically attributed to the activation of the creep damage mechanism. Once a cyclically loaded material has reached its fatigue life, fracture will occur. Fracture occurs at the dominant crack.

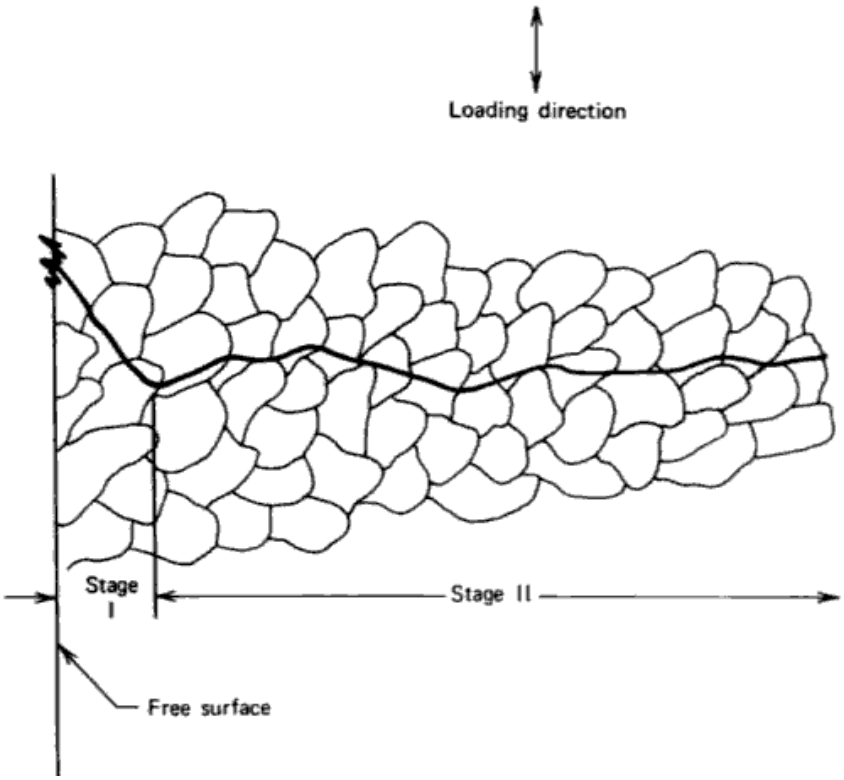

Figure 2.4 - Schematic of stages I and II transcrystalline microscopic fatigue crack growth [51]

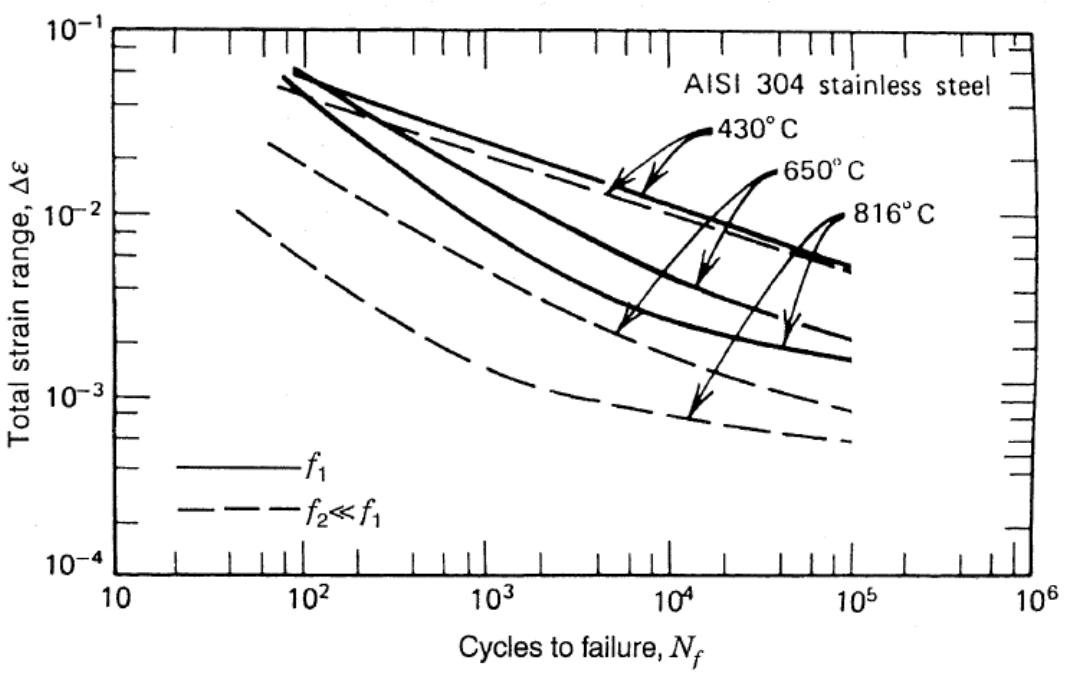

Figure 2.5 - The effect of temperature and frequency on strain-life fatigue of 304SS [53]

At high temperature fatigue is influenced by and interacts with the creep damage mechanism. Additional factors influence damage evolution such as: oxidation, creep/relaxation, frequency, wave shape, and metallurgical aspects such as aging and phase change [51]. Intergranular creep cracking is observed with increased temperature corresponding with a decrease in fatigue resistance. In many metals, the weak fatigue resistance of the oxide scale reduces crack initiation time and accelerates crack propagation rates. The frequency and wave-shape of the applied boundary conditions can lead to either fatigue or creep damage dominance indicating time- and rate-dependence [54-56]. At long hours, the formation of laves phase particles can have a dramatic effect on remaining life. At high temperature a continuous decrease in fatigue strength is observed for most metals. Notches can either weaken or strength the material based on the net section stress and whether fatigue or creep damage is dominant. The

strain-life curve for 304SS is provided in Figure 2.5 [53]. The frequencies f_1 and f_2 are 10 and 0.001 *cpm* respectively [57]. Examining the graph it is found as frequency decreases the fatigue resistance also decreases. This is due to the increased period which allows more creep damage to be imparted on the material. As temperature increases strength decreases.

The simple approach to modeling fatigue is the use of fatigue-life equations. The three traditional methods are stress-life (s-N), strain-life (ε-N) and linear elastic fracture mechanics (LEFM) [51]. Each approach is employed based on the expected life or the presence/absences of prior damage to the structure. The stress-life (s-N) approach involves the relationship between cycles to failure and applied alternating stress. The Basquin equation suggests a power law relationship as follows

$$S_a \ or \ S_{Nf} = A\left(N_f\right)^B \tag{2.23}$$

where S_a is the applied alternating stress, S_{Nf} is the fully-reversed fatigue strength at N_f cycles, and *A* and *B* are material constants. To incorporate mean stress and the influence of creep the following equation is used

$$\left(\frac{S_a}{S_f}\right)^2 + \left(\frac{S_m}{S_R}\right)^2 = 1 \tag{2.24}$$

where S_f is the fully-reversed fatigue limit (at 10^8 cycles), S_m is the mean stress, and S_R is the creep rupture strength replacing S_u in the modified Goodman equation [51]. Finally, a uniaxial yield criterion is incorporated as

$$\frac{S_a}{S_{y'}} + \frac{S_m}{S_y} = 1 \tag{2.25}$$

where S_y is the yield strength and $S_{y'}$ is the cyclic yield strength.

The strain-life (ε-N) approach involves the relationship between cycles to failure and applied strain amplitude, ε_a (or strain range, $\Delta\varepsilon$). The Coffin-Manson relationship is the classic approach

$$\varepsilon_{a,ij} = \Delta\varepsilon_{ij} = A'\left(N_{ij}\right)^c \tag{2.26}$$

where $\Delta\varepsilon_{ij}$ is an applied strain range, A' and *c* are material constants and *ij* denotes the type of strain.

The LEFM approach involves the relationship between cycle/time to failure and crack length. The classic approach developed by Paris, follows

$$\frac{da}{dN} = C(\Delta K)^m \tag{2.27}$$

where *C* and *m* are the coefficient and exponential constants respectively and ΔK the range of the stress intensity factor.

2.3.1 Constitutive Modeling

Viscoplastic constitutive models are ideal for modeling the cyclic deformation observed during low-cycle fatigue at high temperature. Viscoplastic materials exhibit rate-dependent strain hardening/softening where strain rate influences the apparent yield strength. Osgerby and Dyson demonstrated that the peak stress in a constant strain-rate test is equal to the load of constant-load creep test where the minimum creep strain rate is equal to the applied constant strain-rate [58].

The isochronous relationship allows the viscous properties of materials to be determined rapidly from creep tests compared with traditional constant strain-rate tests.

Viscoplastic constitutive models require the following: a yield criterion, flow rule, and hardening rule. The yield criterion specifies the onset of plastic deformation based on the stress tensor via an equivalent stress term. A yield surface is a surface in stress space where inside the region elastic deformation occurs and on the surface inelastic deformation occurs. During unloading the state of stress is within the yield surface resulting in elastic behavior. During neutral loading, the state of stress moves on the yield surface but causes no plasticity. During loading, the state of stress moves outwards from the yield surface expanding it in two ways isotropic and/or kinematic hardening [59].

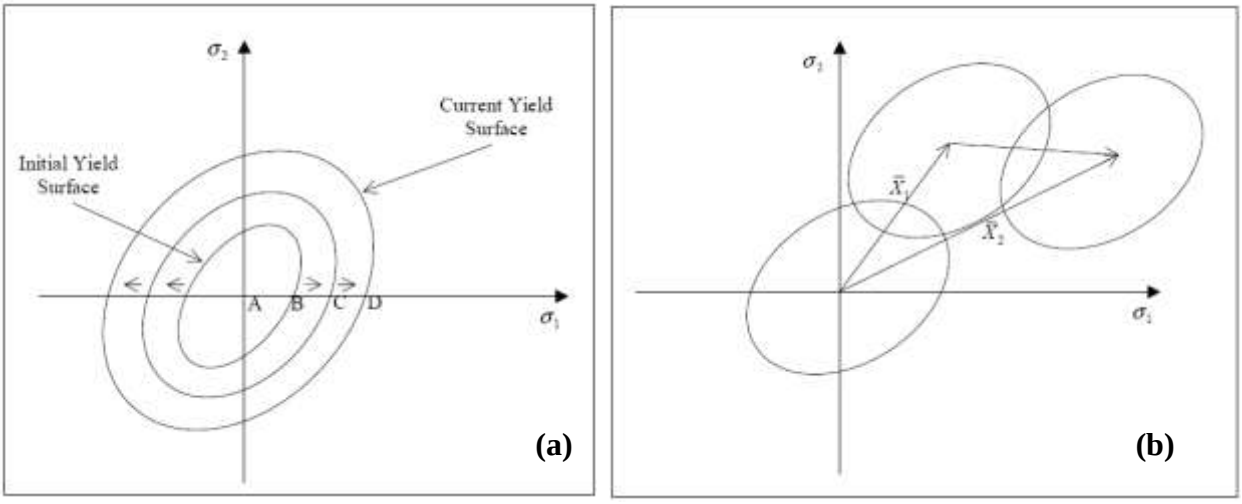

Figure 2.6 – Schematic of hardening: (a) isotropic and (b) kinematic [60]

The flow rule relates the rate of plastic deformation to the stress components (e.g. Levy-Mises [61-63] or Prandtl-Reuss [64-65]), generally described as

$$d\varepsilon_{ij} = \dot{p}\frac{df}{d\sigma_{ij}}\Delta t \tag{2.28}$$

where $\dot{p}$ is the equivalent strain rate known as a viscous function, and the term f is a scalar-valued plastic potential function of σ_{ij} [92]. The viscous function is the inelastic strain-rate equation. It includes the hardening variables. The hardening rule describes the work hardening of the material (isotropic or kinematic).

Isotropic hardening is a type of hardening where the apparent yield strength increases uniformly in all directions. Solute atoms, precipitate particles, dislocation tangles, sub-grains, and grain boundaries contribute to this form of hardening. It allows for the change in size of the yield surface but with no change in shape (Figure 2.6a) [60]. Isotropic hardening is not suitable for modeling cyclic loading as it does not account for the Bauschinger effect.

The Bauschinger effect is where progressive tensile/compressive asymmetry develops over a number of cycles. An increase in tensile strength causes a decrease in subsequent compressive strength.

Kinematic hardening is a type of hardening where the apparent yield strength increases directionally based on the existence of mean stress. This can lead to increased strengthen in tension or compression to the detriment of the other, which is the Bauschinger effect. This mechanism is physically represented by dislocation pileups and bowing of pinned dislocations. Kinematic hardening allows the translation of the yield surface, without change in shape, size, or

orientation during yielding (Figure 2.6b) [60]. The yield surface will shift in the stress space along the applied loading direction.

Gilman proposed that isotropic hardening could be represented by drag stress, the D variable [66]. In the viscous function D is a ratio with the applied stress, σ / D. Rice proposed that kinematic hardening could be represented by rest stress, the R variable [67]. In the viscous function R is subtracted from applied stress, $\sigma - R$. Rest stress is often referred to as "back stress" due to it being positioned behind the applied stress. The relationship $\sigma - R$ is described as "overstress" due to it being positioned over the drag stress. Many viscoplasticity laws have been created and continue to be developed in literature [68].

A number of authors have proposed mixed hardening rules, where a combination of isotropic and kinematic hardening leads to a more generalized formulation [69]. Generally these formulations allow for different degrees of the Bauschinger effect allowing for both translation and expansion of a yield surface. Cyclic hardening, softening, and saturation effects can be incorporated into viscoplasticity constitutive models through the incorporation of mixed hardening rules [68].

A special type of viscoplasticity model eliminates the concept of a yield surface. Instead, an equilibrium surface is considered where some rate-dependent equilibrium stress must be overcome to allow plastic flow. An advantage of these types of viscoplasticity models is the ability to model cyclic plastic and creep deformation simultaneously. Models by Miller, Bodner, and Krempl follow this approach [70,71,72].

A list of the viscous functions for a number of viscoplasticity constitutive models is provided in Table 2.5. In these models the hardening variables are introduced in the viscous

function to simulate microstructural mechanisms. Hardening equations have been developed to represent various mechanisms such as: creep, strain hardening, dynamic recovery, static recovery, Bauschinger's effect, induced/ pre-existing anisotropy, strain range memorization, out-of-phase effects, metallurgical instabilities (phase change), and aging [68].

Table 2.5 – Viscoplasticity constitutive models [68]

Source	Viscous Function	Hardening Variable
Bodner, 1975	$\dot{p} = \dot{p}_0 \exp\left[-\left(\frac{Z}{\sigma_{eq}}\right)^{2n}\right]$	$Z = K + D'$
Miller, 1976	$\dot{p} = \theta(T)\left[\sinh\left(\frac{\sigma/E - R}{D}\right)^{\frac{3}{2}}\right]^n$	D, R
Chaboche, 1977	$\dot{p} = \left\langle \frac{\lVert \underset{\sim}{\sigma} - \underset{\sim}{\mathbf{X}} \rVert - R}{D} \right\rangle^n$	$R, D, \underset{\sim}{\mathbf{X}}$
Krempl, 1980	$\dot{p} = \frac{\sigma_v}{E\phi(\sigma_v)}, \quad \varepsilon_p = \frac{3}{2}\dot{p}\frac{\sigma' - \mathbf{g}'}{\sigma_v}, \quad \sigma_v = \lVert \sigma - \underset{\sim}{\mathbf{g}} \rVert$	$\mathbf{g}$
Walker, 1981	$\dot{p} = \dot{p}_0 \left\langle \frac{\lVert \underset{\sim}{\sigma} - \underset{\sim}{X} \rVert}{D(p)} \right\rangle^n$	$D(p), X$
Delobelle, 1988	$\dot{p} = \dot{p}_0 \sinh\left(\frac{\sigma_v}{D(p,T)}\right)^n, \quad \sigma_v = \lVert \sigma - X \rVert$	$D(p,T), \underset{\sim}{\mathbf{X}}$

K – isotropic hardening variable
D'– Kinematic hardening variable
D – Drag stress (isotropic)
R – Rest Stress (kinematic)
X – Back Stress (kinematic)
$\mathbf{g}$ – over stress (kinematic)

2.3.2 Damage

Over 50 fatigue damage models have been developed since 1924 [46,73]. A list of the earliest and most popular is provided in Table 2.6. The concept of fatigue was initially developed to explain the tiring of metals. An investigation by Albert determined that fatigue failure in iron mine-hoist chain is dependent on load and the number of cycles [74]. One of the earliest fatigue damage models is that proposed separately by Palmgren [75] and Miner [76] where damage is considered a linear relationship between the number of cycles n and the number of cycles to failure N_f. When under VAL conditions summation provides a simple method to predict damage. Failure is reached once the total value of damage reaches unity.

$$D = \sum \frac{n_i}{N_{fi}} = 1 \tag{2.29}$$

A limitation of the Palmgren-Miner rule is that damage accumulation is dependent on the order of loading. A number of modified versions of this equations where proposed by authors up to the 1960s [77]. When comparing specimen that are loaded from low to high and high to low amplitudes, the high to low specimen was found to exhibit more microstructural damage; therefore, non-linear rules are necessary to accurately predict damage. A depiction of linear and non-linear damage evolution is shown in Figure 2.7. A number of authors have investigated this issue and developed non-linear rules [58, 78-81]. A recent advancement has been the use of continuum damage mechanics (CDM) to predict fatigue damage.

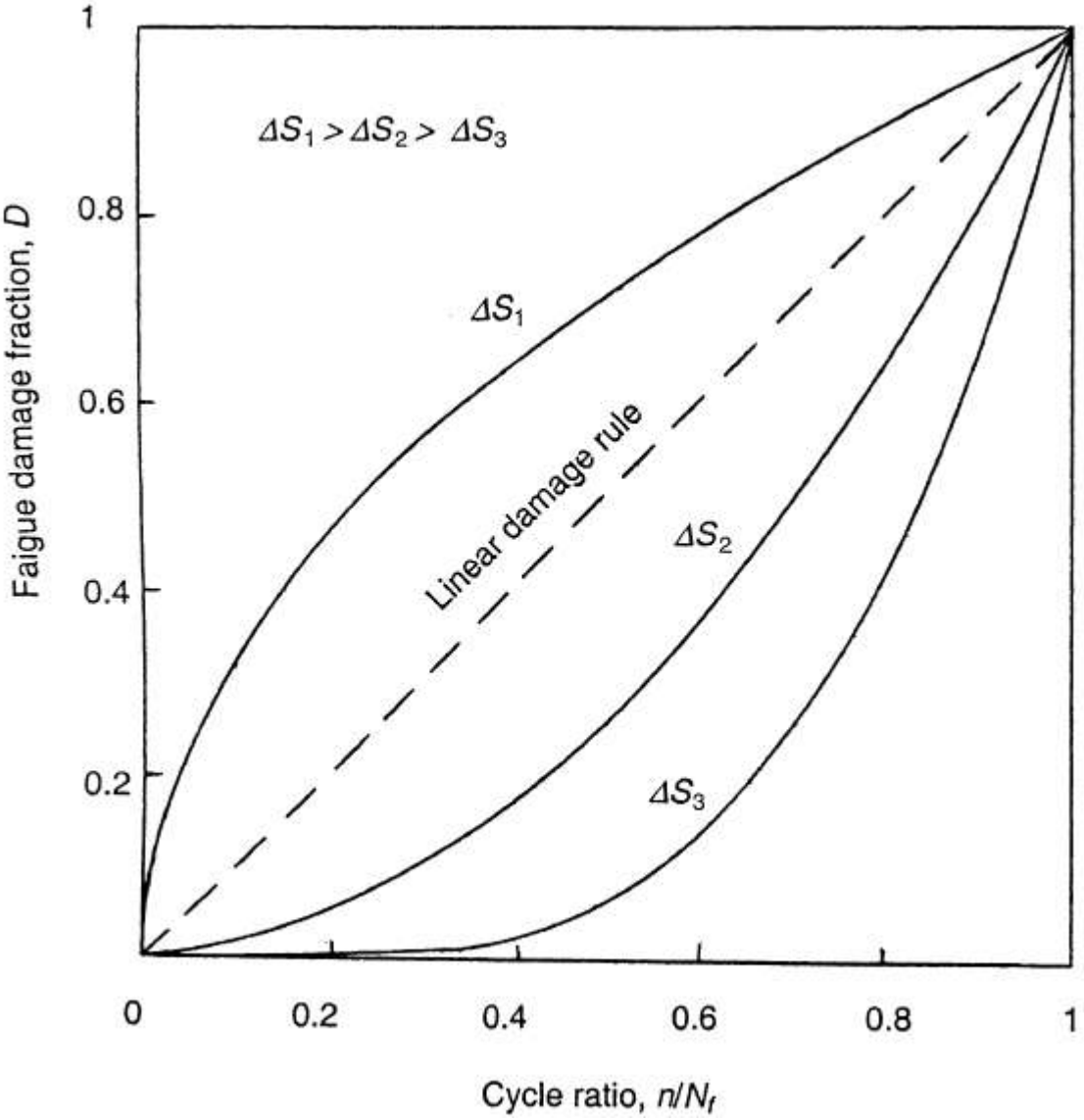

Figure 2.7 - Fatigue damage fraction versus cycle ratio [51]

Table 2.6 – Fatigue damage laws [51,40,46,73]

Source	Damage Law
Palmgren-Miner, 1924,1945	$D = \sum_i n_i / N_i$
Robinson Life-fraction, 1938	$D = \sum \frac{t_i}{t_{ri}}$
Lieberman Strain-fraction, 1962	$D = \sum \frac{\varepsilon_i}{\varepsilon_{ri}}$
Mixed rule, 1959	$D = \sum \left(\frac{t_i}{t_{ri}}\right)^{1/2} \left(\frac{\varepsilon_i}{\varepsilon_{ri}}\right)^{1/2}$
Extended Mixed rule, 1972	$D = k\sum \frac{t_i}{t_{ri}} + (1-k)\sum \frac{\varepsilon_i}{\varepsilon_{ri}}$
Coffin, 1956	$D = \sum_i \frac{n_i \left(\Delta\varepsilon_p\right)_i^{1/\alpha}}{C^{1/\alpha}}$
Frudenthal-Heller, 1959	$D = \sum_i n_i \omega_i / N$
Kliman Theory, 1984	$D_b = \frac{W_b}{W_{fR}} = \frac{1}{W_{fR}} \sum \Delta W_i n_{bi}$
Manson and Halford,1986	$D = \sum \left[(pr)^k + (1-p^k) r^{fq} \right]^{1/k}, r = \frac{n}{N},$ $p = A\left(N_{ref}/N\right)^{\alpha} \Big/ \left[1 - B\left(N_{ref}/N\right)^{\alpha}\right]$
Chaboche, 1988	$dD = D^{\alpha(\sigma_M, \bar{\sigma})} \left[\frac{\sigma_M - \bar{\sigma}}{M(\tilde{\sigma})}\right]^{\beta} dN$

2.4 **Creep-Fatigue**

Creep-fatigue is the condition where both creep and fatigue damage mechanisms actively contribute to the microstructural degradation of a material. It involves the application of cyclic load above the creep activation temperature such that both creep and fatigue contribute to the constitutive response, material degradation, and crack propagation [82]. The dominant damage mechanism depends on load, mean stress, stress ratio, surface condition, size, temperature, frequency, stress ratio, dwell time and geometry [83-89].

Failure in alloys can be observed as transgranular, intergranular, or mixed sequential draw in Figure 2.8 [90]. Transgranular cracking occurs when slip bands of plasticity form in favorably oriented grains under high stress and low temperature [40]. Few cavities form and typical develop near the fracture surface. Cyclic application of load produces ductile striations, each striation representing a single cycle. In some cases there is not a one to one relationship between striations and cycles indicating secondary damage mechanisms are active. Intergranular cracking is a micro-cavitation and sliding process on grain boundaries under low stress and high temperature [51]. A large number of micro-voids nucleate on grain boundaries. The coalescence of voids contributes to the micro and macro-cracking processes.

Fatigue damage dominated failure is associated with transgranular fracture, while creep damage dominated failure is primarily intergranular; however, the creep isotherms of most metals show that mixed trans-intergranular cracking can occur during experiments conducted at high stress and/or low temperature [82,91]. In Figure 2.9 and Figure 2.10, triangular and trapezium load cyclic shapes are shown with lines indicating that active damage mechanism. Assuming an isothermal test under stress cycling, under a triangular load history (Figure 2.9a)

both creep and fatigue damage mechanisms are active throughout the application of load. The dominant damage mechanism is dependent on the interplay between loading and the microstructural aspects of the material and can be determined through fractography. Under a trapezium load history (Figure 2.9b) the fatigue damage mechanism is only active during cycles of loading and unloading. Increasing the hold period will increase the amount of creep damage; however, again dominance is dependent on boundary conditions. Assuming zero applied mechanical stress, and thermal cycling, under a triangular load history (Figure 2.10a) the fatigue mechanism is always active, while the creep mechanism becomes active only when temperature is above the creep activation temperature ($0.4T_m$). As the temperature increases, the creep damage mechanism becomes more dominant. Under a trapezium load history (Figure 2.10b), the activation and deactivation of creep and fatigue becomes highly complex. Under these conditions, mixed sequential cracking is expected to occur.

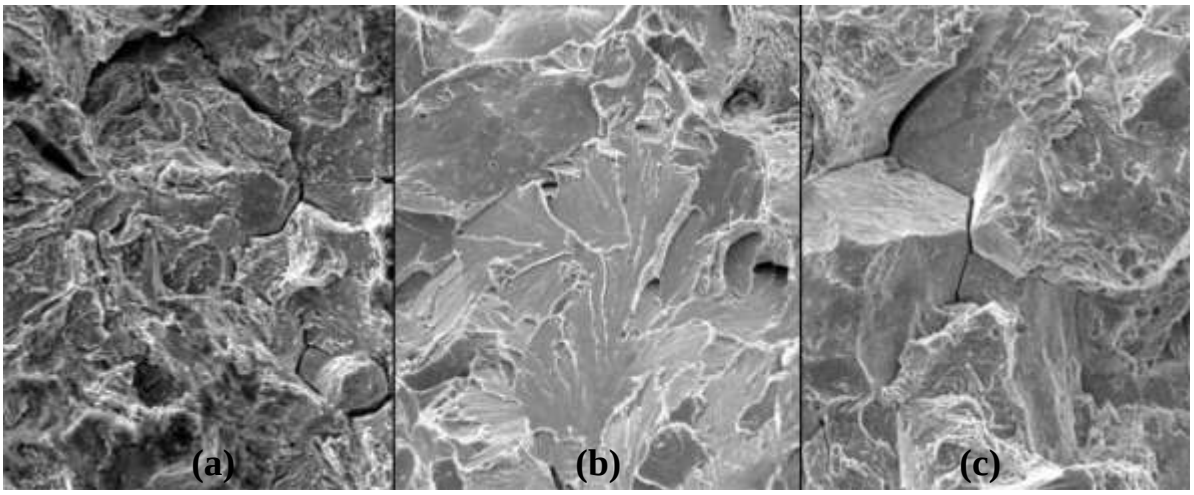

Figure 2.8 – SEM of low carbon steel (a) transgranular and (b) intergranular cracking (c) mixed-mode [90]

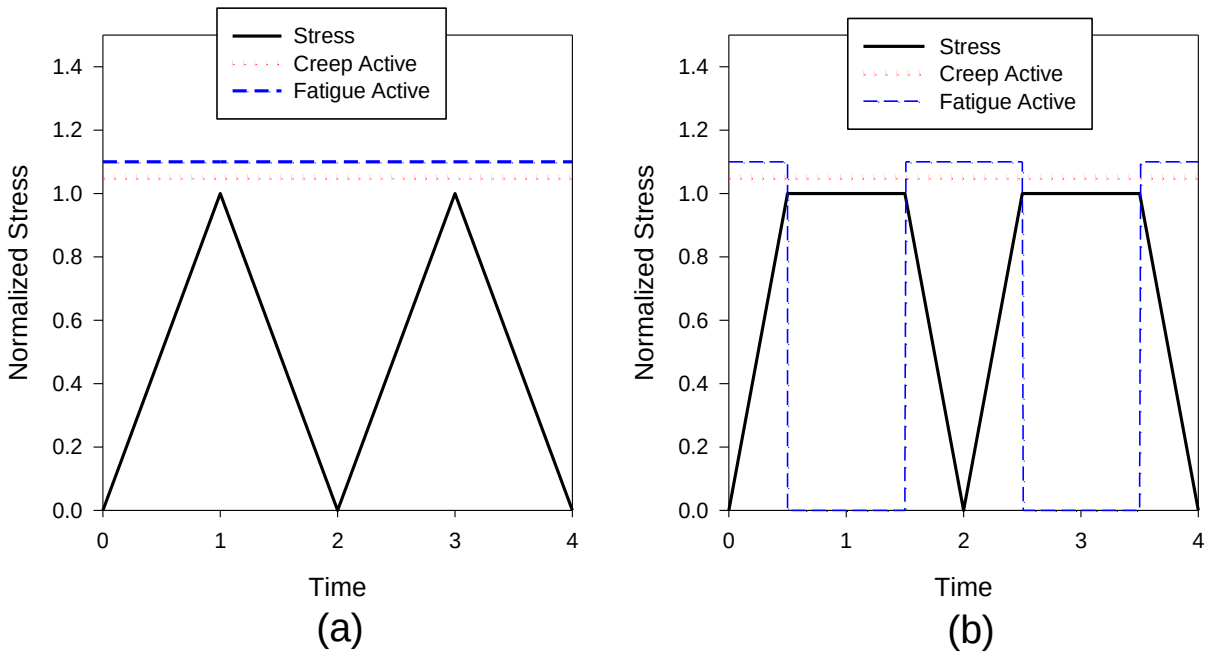

Figure 2.9 – Stress-time plot demonstrating active damage mechanisms during a cycle

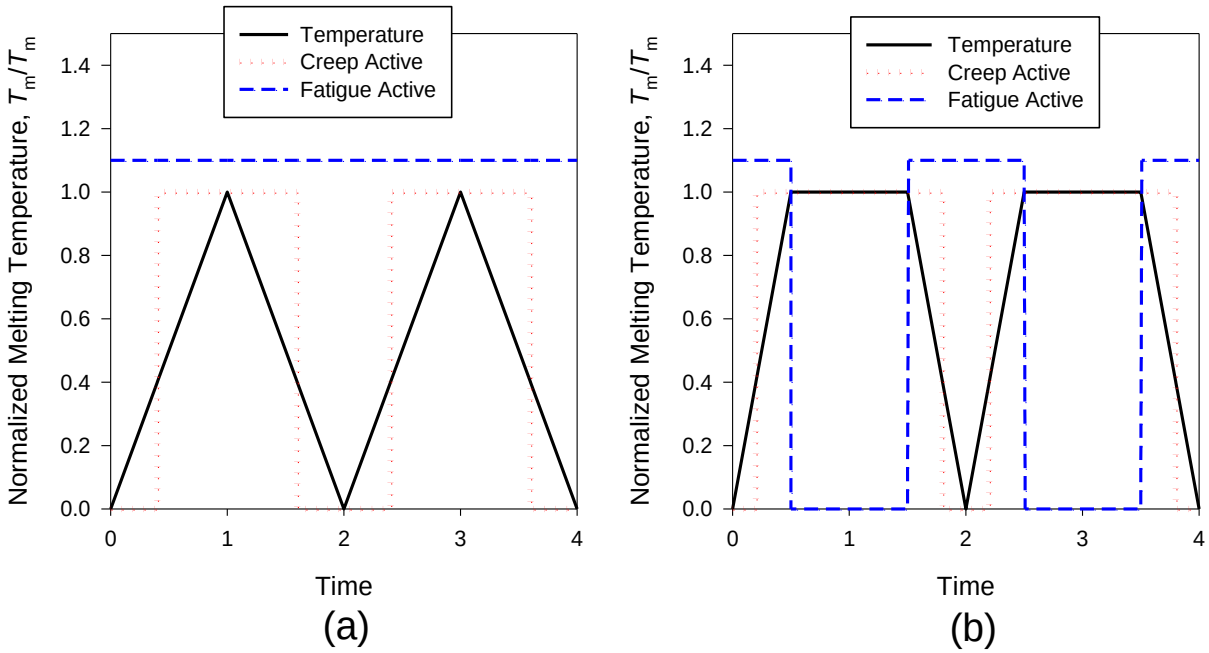

Figure 2.10 – Temperature-time plot demonstrating active damage mechanisms during a cycle

Using the strain life approach and strain partitioning the total inelastic strain range as follows

$$\Delta\varepsilon_{in} = \Delta\varepsilon_{vp} + \Delta\varepsilon_{cc} + \Delta\varepsilon_{pc}\left(or\ \Delta\varepsilon_{cp}\right) \tag{2.30}$$

where $\Delta\varepsilon_{vp}$ is fatigue (yielding viscoplasticity), $\Delta\varepsilon_{cc}$ is creep (zero yield viscoplasticity), and $\Delta\varepsilon_{pc}$ and $\Delta\varepsilon_{cp}$ are mutually exclusive representations of combined fatigue and creep. A specialized test program is needed to determine the independent Coffin-Manson material constants for each of these strains.

A linear summation similar to strain range partition is used to incorporate the fatigue and crack mechanisms leading to

$$\frac{da}{dN} = \left(\frac{da}{dN}\right)_{fatigue} + \left(\frac{da}{dt}\right)_{creep} \tag{2.31}$$

where the cycle-dependent fatigue and time-dependent creep mechanisms work together to produces crack initiation and growth.

2.4.1 Constitutive Modeling

A classical approach to dealing with modeling the constitutive response of a material under creep-fatigue is to use strain partitioning [88]. This approach assumes that elastic, creep, and yielding viscoplastic strains can be linearly summed to equal total strain. The strain-life approach to fatigue life is similarly based on "strain range partitioning" with $\Delta\varepsilon_t$, total strain range [51]. The linear summation of strain suggests that there are independent damage mechanisms for each strain contribution. Total strain takes the following form

$$\varepsilon_t = \varepsilon_e + \varepsilon_{cr} + \varepsilon_{vp} \tag{2.32}$$

where ε_e is the elastic, ε_{cr} is creep (zero yield viscoplastic), and ε_{vp} is fatigue (yielding viscoplastic) strain. It should be noted that creep is a form of viscoplasticity with a zero yield surface; therefore, creep will occur at all non-zero stress values. The tensorial form of strain can be obtained using a general flow rule and strain potential function. The flow rule determines the direction of straining and is given as

$$d\varepsilon_{ij} = d\varepsilon \frac{df\left(\sigma_{ij}\right)}{d\sigma_{ij}} \tag{2.33}$$

where $d\varepsilon$ is the equivalent strain increment, and the term f is a scalar -valued plastic potential function of σ_{ij} [92].

2.4.2 Damage

Generally, the microstructural damage of a material in the creep regime, under cyclic loading above material yield strength can be said to consist of

$$D = D_p + D_f + D_c \tag{2.34}$$

where D_p, D_f, and D_c are the rate-independent plastic, and rate-dependent fatigue and creep damage respectively [93]. Often these damage terms are described as having one-to-one mapping (i.e. a linear summation equal to unity results in failure). The physical mechanisms that contribute to these damage terms are dislocation motion and cavitation. Damage is an irreversible heterogeneous process with the damage rate and distribution influenced by boundary conditions, material evolution, time, and environment.

Continuous development since the 1970's has led to various approaches: cycle counting, continuum damage, crack length, strain, strain-energy, and hybrids [35,46,73,94]. In a review, Fatemi and Yang provides found over 50 different models [73]. A list of the earliest and most popular is provided in Table 2.7. The earliest approaches focused on extending the Palmgren-Miner by separating the fatigue (cycling) and creep (hold time) into individual components where rupture is reached when the sum equations unity.

Continuum damage mechanics (CDM) based creep-fatigue damage models have the advantage of being inherently non-linear while allowing a linear summation of the contribution of creep and fatigue to damage evolution. Generally, creep-fatigue continuum damage models would take one of three forms

$$\begin{aligned} dD &= f_c\left(\sigma, D\right)dt + f_f\left(\sigma_1, \sigma_H, D\right)dN \\ dD &= f_c\left(\sigma, D_c\right)dt + f_f\left(\sigma_1, \sigma_H, D_f\right)dN \\ dD &= f_c\left(\sigma, D_c\right)dt + f_f\left(\sigma_1, \sigma_H, D_f\right)dN + f_{cf}\left(\sigma_1, \sigma_H, D_c, D_f\right)dN \end{aligned} \tag{2.35}$$

where is σ equivalent stress, σ_1 is first principal stress, σ_H is hydrostatic mean stress, and is D_c creep damage, D_f is fatigue damage, and D is total damage. The first form assumes one-to-one mapping of creep and fatigue contributions to total damage (Chaboche, 1988). The second form assumes creep and fatigue damage independently contribute to total damage. The third form is a bridge which connects the independent creep and fatigue damage through a mixing damage.

Table 2.7 – Coupled creep-fatigue damage laws [35,46,73]

Source	Damage Law
Manson, 1971	$D = \frac{1}{N_f} = \sum \frac{f_{ij}}{N_{ij}} = \frac{f_{cc}}{N_{cc}} + \frac{f_{pp}}{N_{pp}}, + \frac{f_{cp}}{N_{cp}},$ $\Delta\varepsilon_{ij} = A'\left(N_{ij}\right)^{c}, f_{ij} = \frac{\Delta\varepsilon_{ij}}{\Delta\varepsilon_{in}},$ $\Delta\varepsilon_{in} = \Delta\varepsilon_{cc} + \Delta\varepsilon_{pp} + \Delta\varepsilon_{cp}$
Chaboche, 1980	$dD = f_c\left(\sigma, D\right)dt + f_f\left(\sigma_M, \tilde{\sigma}, D\right)dN$
Levaillant-Pineau, 1982	$\frac{da}{dN} = \left(\frac{da}{dN}\right)_{pp}\left(1 - ND_c\right)^{-2}$
Dasgupt, Oyan, Barker, Pecht; 1992	$E = U_e + W_p + W_c$
Webster, 1994	$\frac{da}{dN} = C\Delta K^m + \frac{D_0 C^{*\phi}}{f}$

2.5 **Numerical Crack Propagation**

A number of linear elastic fracture mechanics (LFEM) based computer codes exist to model crack growth (FRANC2D, FRANC3D, FEACrack, CurvedCrack, ADAPCrack3D, ZenCrack, BEASY, XFEM) [95]. A majority of these codes are third-party extensions to established FEM software; requiring that the crack propagation information be calculated externally after each iteration. The mesh and/or geometry are modified and an updated FE model provided to the solver (ANSYS, ABAQUS, and Nastran). This process is repeated iteratively until some fracture criterion is reached. The crack increment Δa is determined after directions of crack extension is defined and typically calculated using fatigue crack growth models such as the Paris law. The crack direction is calculated using well established criteria: Griffith's

maximum energy release rate (the direction where the energy release rate is maximum) [96], maximum circumferential stress criterion (normal to the direction of the maximum hoop stress) [97], minimum strain energy density criterion (normal to the direction of minimum strain energy) [98], or minimum mode II stress intensity factor (along the direction where mode II SIF vanishes) [99].

Linear Elastic Fracture Mechanics (LEFM) has a number of limitations when compared to CDM when simulating crack propagation [100]. It requires a new geometry and mesh after each iteration (during propagation) or local enrichment of approximation space through the partition of unity concept (PUFEM) or the extended finite element method (XFEM) [95]. Plasticity at the crack tip requires a plastic zone correction that is only valid at moderate plastic strain [51]. The stress intensity factor is dependent on specimen geometry and loading conditions. Short and long crack growths are typically modeled using different parameters. The nucleation of numerous microcracks observed during intergranular cracking leads to convergence issues in FEM. Alternatively, CDM approaches incorporate the constitutive response, multiple crack initiation sites, micro-void coalesce, crack propagation, and rupture. It can be quickly implemented into FEM, and readily applied to contour geometry.

Since the 1980's, continuum damage mechanics (CDM) has been used as a technique to describe crack initiation and propagation. Discrete representative volume elements (RVE) are used to model the discontinuous and heterogeneous solid. It is assumed that within the RVE micro-defects are homogenously distributed. The RVEs contain the constitutive response and damage state of the solid [101]. In each RVE the stiffness is a function of damage such that degradation is localized [102]. The elements, when brought together in the finite element method

(FEM), produce a balanced solution to the mechanical state of a solid. When applied to fracture mechanics, a crack can be measured by the critical damage zone. This zone is where the damage variable in an element has exceeded the critical value. The distance between node points which have reached the critical damage value is equal to the measured flaw size. These flaws phenomenological represent any micro-defect which degrades structural integrity. It is assumed that the crack propagation rate and direct are driven by the damage evolution equation as it relates to the dynamic stress at the crack tip. Another method is to introduce relaxation nodes (coincident nodes) along the proposed crack path [103]. Once damage reaches a critical value relaxation of the connection between these nodes occurs through the use of weak springs until a point where they are completely released from DOF constraints [104]. Authors have developed CDM-based models using contact elements, node release, element removal, dynamic remeshing, and/or meshless techniques to achieve crack extension [105]. Many local CDM-based crack growth models have been developed [46,94,106,107]. JianPing and colleagues developed a CDM-based creep-fatigue crack growth model to predict the rupture of a steam turbine rotor [108]. Yatomi used CDM-based creep crack growth with nodal-release to evaluate the C* and Q* integrals [109]. Recently, Götting developed a CDM-based creep crack growth model with nodal release for a Ni-base superalloy [110]. The accuracy of CDM-based crack propagation is limited by flaws in FEM. Two major problems are mesh discretization and stress sensitivity.

2.5.1 Mesh Discretization

A contributing factor to the inconsistency in local CDM approaches is mesh discretization. Damage evolution is based on the localized state of stress in each element. This leads to crack propagation being highly dependent on the state of stress near the crack tip. Thus the mesh size and shape can negatively influence crack propagation rate and direction. Murakami and colleagues, using the elastic and creep material properties for copper, conducted a parametric study examining the effect of mesh discretization using different configurations of triangular elements [102]. The results are shown in Figure 2.11. As observed, due to localization, crack growth is restricted to elements adjacent to the highly damage elements. In Mesh I, the direction of crack growth is constrained due to the triangular elements providing only three possible directions for growth. Mesh II and III provide more flexibility with a block configuration of two triangular element. They show that the crack propagation path is highly dependent on the aspect ratio of the two elements. It is observed that crack propagation is highly dependent on mesh configuration.

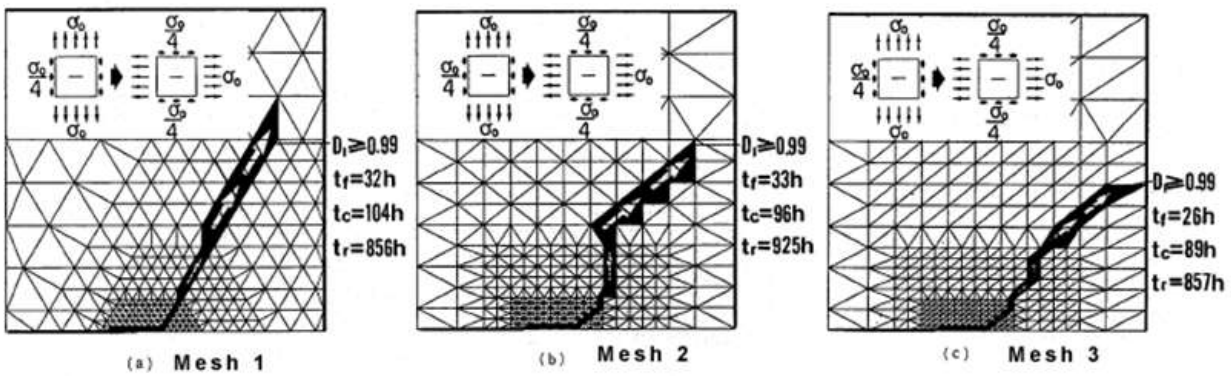

Figure 2.11 - Effect of finite element discretization on creep crack growth [102]

To overcome this issue, a number of authors have developed dynamic remeshing algorithms [111-113]. These algorithms dynamic remesh zones of high damage into smaller and smaller elements until a minimum element size is reached at which point, when critical damage is reached, the minimized element is removed. This provides a method by which the stress gradient observed across the rupturing element is minimized. The crack propagation path is therefore trapped along a boundary of finely meshed elements minimizing the influence of mesh size and shape has on crack path. The primary limitation of dynamic meshing is computational cost.

2.5.2 Stress Sensitivity

A major factor leading to the inaccuracy of the local CDM approach is the way in which damage is implementation in the damage evolution equation. In the classic damage models the damage evolution equation contains $1/(1-\omega)^q$ (where $0 < \omega < 1.0$). This relation encapsulates both creep damage and the instantaneous elastic-plastic damage (fast fracture) which facilitates rupture of a creep specimen [114]. Examining, Figure 2.12 it is observed that the classic model does not produce a metallographically valid damage evolution [115]. Calculated A-Parameter and Voronoi simulations of grain boundary cavity area density result in a vastly different damage evolution when compared with the classic damage model [116]. The ill-formed damage evolution equation is the source of stress sensitivity. To avoid this issue some authors suggest implementing variable critical damage criterion, $\omega_{cr} = f(\sigma, T)$ [117]; however, this leads to additional prediction error. Extensive work has been done in analytically determining this critical

damage criterion [101,102,118]. The better alternative is to develop a damage evolution equation which better represents the physical damage evolution rate of metals. Liu and Murakami demonstrated that by introducing an exponential form of previous damage in the damage evolution equation leads to better correlation with physical damage processes and relative insensitivity to mesh size [115].

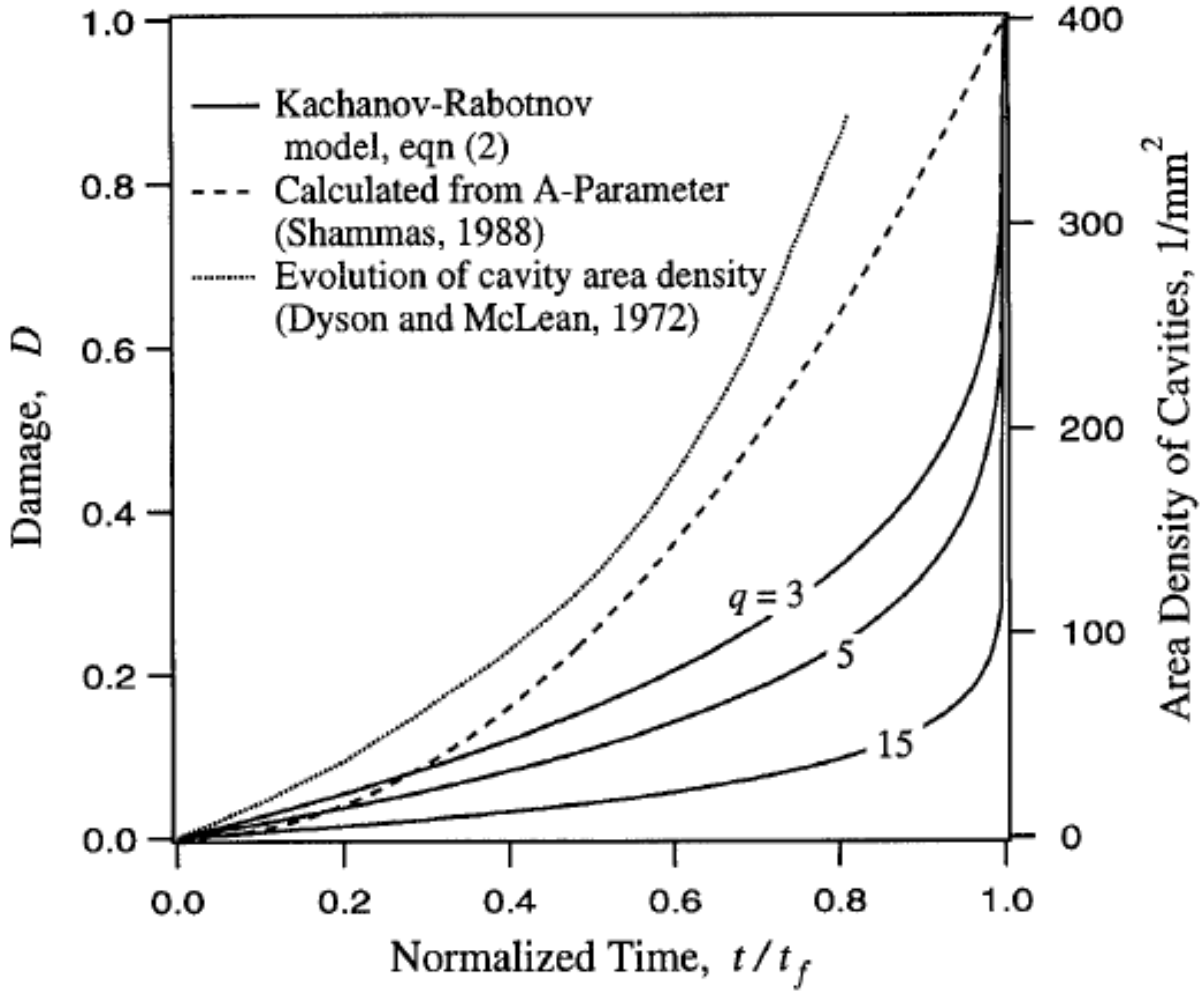

Figure 2.12 - Damage evolution under uniaxial tension [115]

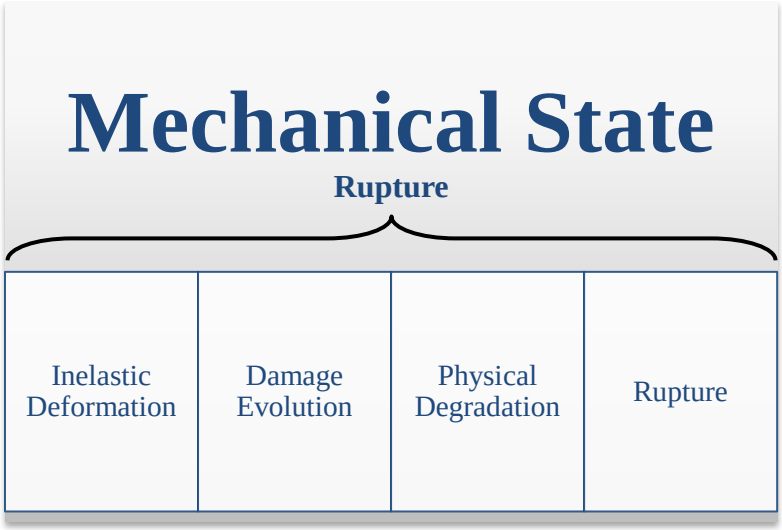

Figure 2.13 - Schematic of mechanical state

2.6 **Summary**

As discussed in this chapter, significant effort has gone towards modeling the constitutive response, damage, and rupture of materials subject to creep, fatigue, and coupled creep-fatigue. It is found that most efforts focus on modeling only a portion of the mechanical response of materials. The global state of a material should be considered. Boundary conditions induce inelastic deformation a symptom of damage evolution caused by microstructural degradation. As microstructural degradation occurs; the nucleation of defects contributes to the initiation of cracks and subsequent crack propagation. The constitutive response, damage evolution, microstructural degradation, and rupture of materials are inherently linked. It is therefore, necessary to develop a new "unified" methodology to accurately model this phenomenon and their interaction to fully realize the mechanical state of a material in FEM.

CHAPTER THREE: MATERIAL

3.1 **304 Stainless Steel**

The subject material of this study is rod-stock dual certified 304/304L Stainless Steel (SS), an austenitic Fe-Ni-Cr stainless steel that has been used extensively in the power generation and pressure vessel and piping industry. It has been prepared to meet ASTM A276 and A479 [119,120] with the chemical composition provided in Table 3.1. The rod has been annealed and cold finished improving strength and straightness. It should be noted that rod 304SS was chosen over plate/sheet due to the reduced machining cost of cylindrical specimen.

The material 304SS was selected for a two reasons:

1. Well documented mechanical behavior: Using data from literature it is possible to reduce the number of mechanical tests needed to characterize the material properties. It is possible to verify the accuracy of the proposed model via comparison to deformation and fatigue crack growth data from literature.
2. Acquisition: 304SS is a standardized material used in numerous structural applications. The cost of the material is low compared to the more advanced Ni-base superalloys used in rotating gas turbine components while it retains a similar mechanical behavior and creep resistance.

Table 3.1 – Chemical composition of dual certified 304/304L stainless steel (wt%) [119,120]

	Fe	Cr	Ni	C	Mn	Cu	Mo	Si	S	P	Co	N
Min	74	18	8	0	0	0	0	0	0	0	0	0
Max	64	20	10.5	0.08	2	1	1	1	0.03	0.045	0.2	0.1
Avg.	69	19	9.25	0.04	1	0.5	0.5	0.5	0.015	0.023	0.1	0.05

In this chapter an extensive review of the mechanical behavior of rod, bar, plate, and sheet 304SS subject to high temperature is presented. In section 3.2, the tensile behavior is evaluated. In section 3.3, the creep behavior subject to tensile, multiaxial, and material processing effects are investigated. In section 3.4, the fatigue behavior subject to load amplitude, mean stress, frequency, hold time, wave shape and form, multiaxiality, and material processing is investigated.

3.2 **Tensile Response**

The tensile behavior of 304SS was evaluated using a number of sources and include bar, plate and sheet specimen [121-125]. The mechanical properties according to ASTM are provided in Table 3.2. Antoun and colleagues investigated the influence of temperature on the tensile and compressive properties of 304SS [121]. The tests were conducted under extension-control to produce a strain rate of 0.001/s at temperature ranging from 25 to 800°C. The stress-strain response is provided in Figure 3.1 [121]. It is observed that as temperature increases there is a marked increase in elongation and decreases in yield strength and ultimate tensile strength a typical behavior for most materials.

Table 3.2 – Mechanical properties of a304/304L at room temperature [119,120]

Modulus of Elasticity	Ultimate Tensile Strength	Yield Strength	Elongation	Brinell Hardness
KSI x 10^3	*KSI [MPa]*	*KSI [MPa]*	*%*	*B*
28	75-90	30-40	30-70	80-99

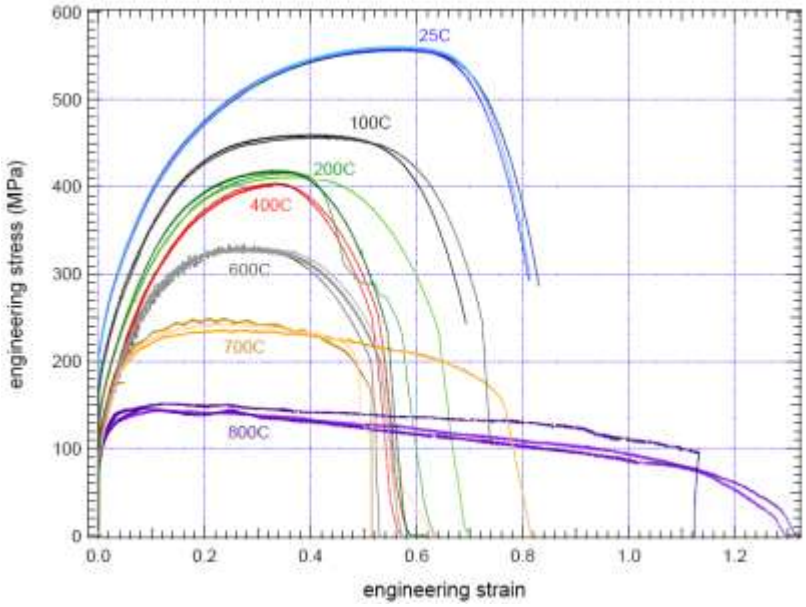

Figure 3.1 - Stress-strain curve of 304L stainless steel in tension [121]

The yield and ultimate tensile strength with respect to temperature are plotted in Figure 3.2 [122-125]. It is observed that 304SS exhibits an anomalous yield strength between 300 and 500°C. Sikka conducted a study on the elevated temperature ductility of 304 stainless steel with ductility versus temperature plotted in Figure 3.3 [126]. It is observed that as temperature increases the total elongation (*EL*%) and reduction-in-area (*RA*%) decrease. Examining the effect of strain rate, it is observed that if the applied strain rate is decreased the resulting *EL*% and *RA*% decrease. The effect is greatly influenced by temperature. This strain rate, temperature, *EL*%, and *RA*% relationship suggests the activation of both creep and oxidation mechanisms.

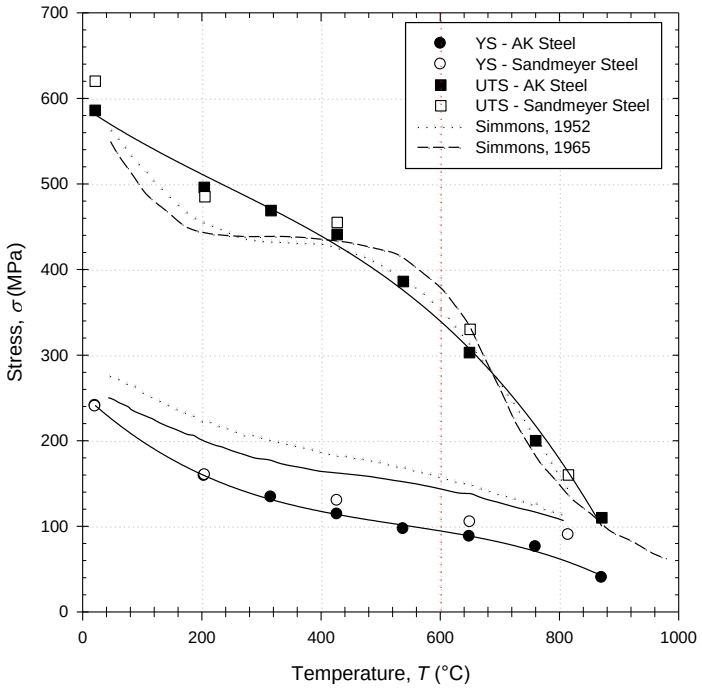

Figure 3.2 –Yield strength and ultimate tensile strength vs temperature of 304SS [122-125]

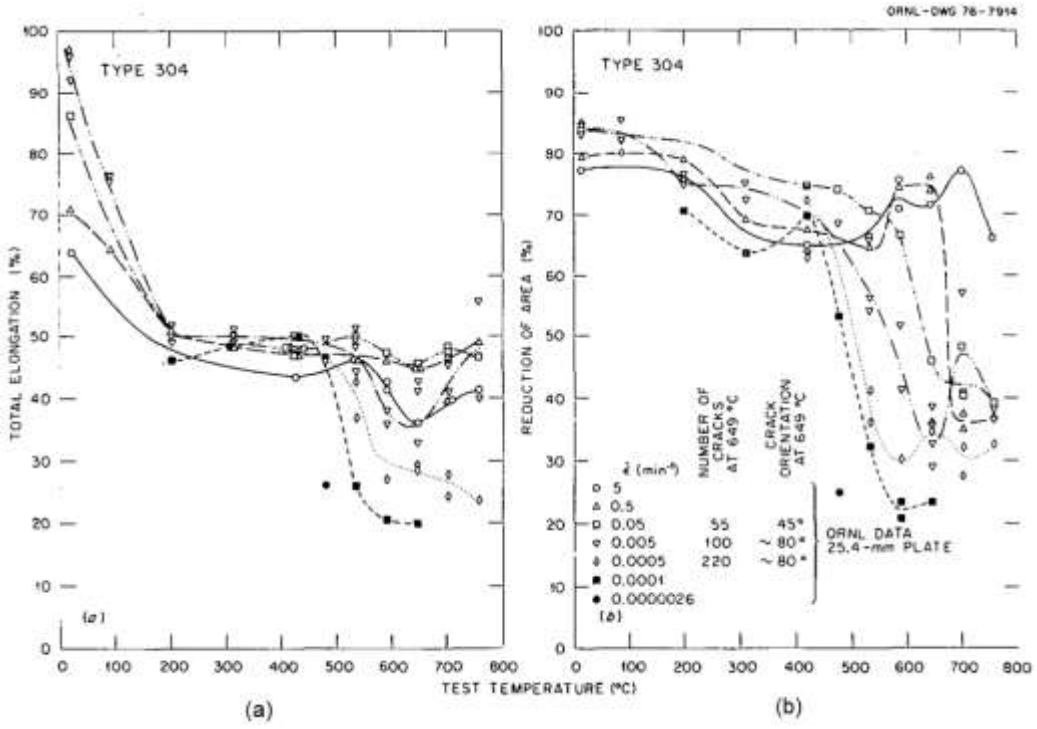

Figure 3.3 - Ductility versus temperature for 25mm plate of 304SS (a) elongation (b) reduction-of-area [126]

The stress-strain curve of 304SS subject to monotonic and cyclic loading (R=0) is provided in Figure 3.4 [127]. Comparing monotonic and cyclic loading, it is clearly observed that under cyclic loading the material exhibits isotropic cyclic hardening. For both loading conditions when the applied strain rate is reduced the material exhibits less hardening. This suggests that the material exhibits viscoplasticity, where the applied strain rate influences hardening and softening behavior.

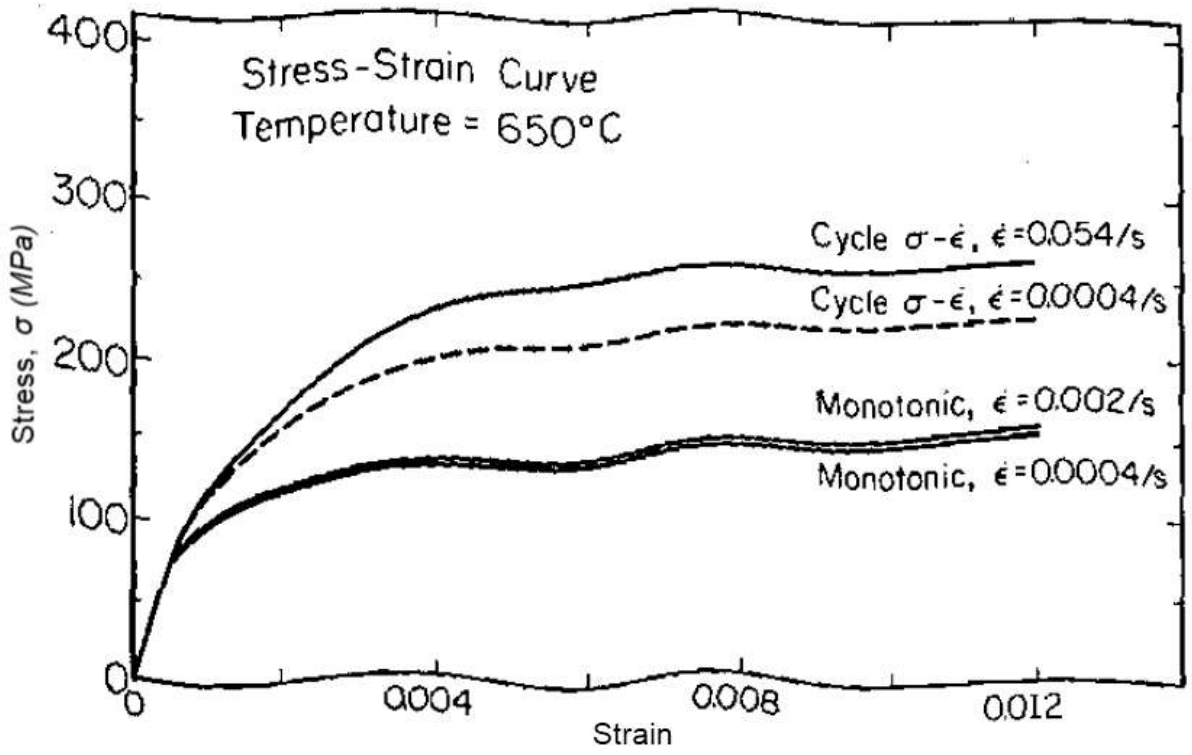

Figure 3.4 - The effect of constant strain rate on Stress-Strain Curve of 304SS [127]

3.3 **Creep**

Considerable efforts have been conducted by various researchers to characterize the creep properties of 304SS. Simmons conducted two studies compiling the elevated-temperature mechanical properties of commercial available stainless steels for ASTM and ASME [122,123]. ASM International produced a handbook with a compilation of creep and stress-rupture curves for various alloys [128]. Kim and colleagues investigated at the statistical properties of creep-rupture as pertaining to STS304 [129]. Creep curves are provided within a stress range of 160-320 MPa and temperature range of 600-700°C in Figure 3.5. It is observed that depending on the stress and temperature conditions all three creep regimes are present. Clearly, a multistage creep constitutive model is needed to characterize the deformation under creep conditions. There is substantial scatter observed in the creep curves, represented in the key factors of: total creep strain, primary creep strain, steady state creep rate, total creep rate, and rupture time. This scatter seems to decreases when test temperature is increased. Scatter also decreases when tests are conducted at elevated stress under constant temperature. Kim and colleagues found that the probability density function of creep-rupture data follows a Weibull distribution. It is suggested that statistical modeling should be used when conducting long-term creep rupture predictions to improve reliability. Minimum creep strain rate versus strain data from multiple sources was digitized and plotted in Figure 3.6 [129-136]. Significant scatter is observed in the minimum creep strain rate where data from different temperature sets overlay; however, it should be noted that the data is compiled from multiple source with different testing equipment and subject material manufacturers.

Kim and college investigated the high temperature creep-rupture of 304 subject to triaxial stress in comparison to uniaxial [131]. Optical micrographs of ruptured 304 specimen subject to uniaxial tension of 60 and 180MPa at 760°C are provided in Figure 3.7(a) and (b) where the 180MPa ruptured much sooner than the 60 MPa test. In both figures, intergranular microcracks due to cavitation are observed perpendicular to the applied load direction. Notice, the smaller cavities observed under the high load test. Cavitation is a homogenous time-dependent process. Rupture of the 180MPa specimen occurred due a more localized phenomena that did not require homogenous cavitation.

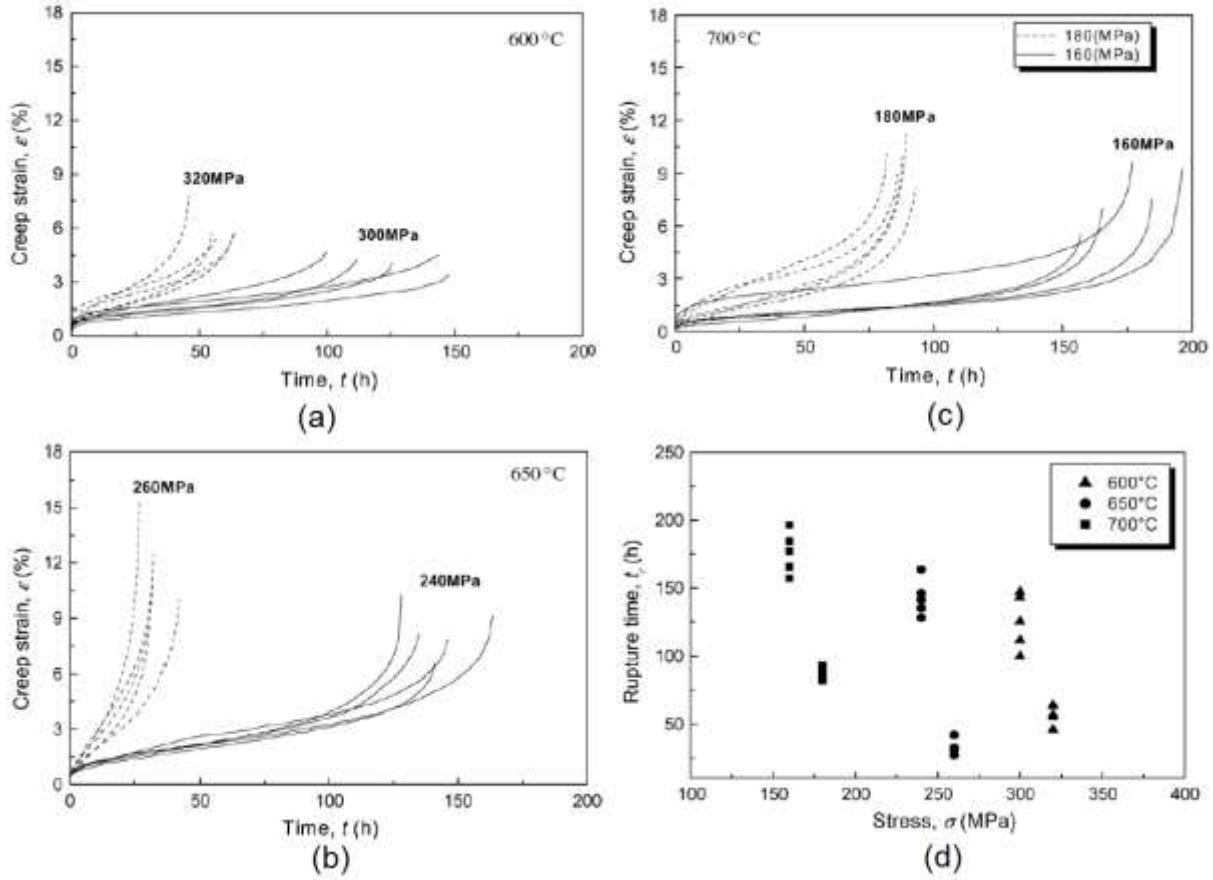

Figure 3.5 - Creep curves for STS304 (a) 600°C (b) 650°C and (c) 700°C with (d) rupture [129]

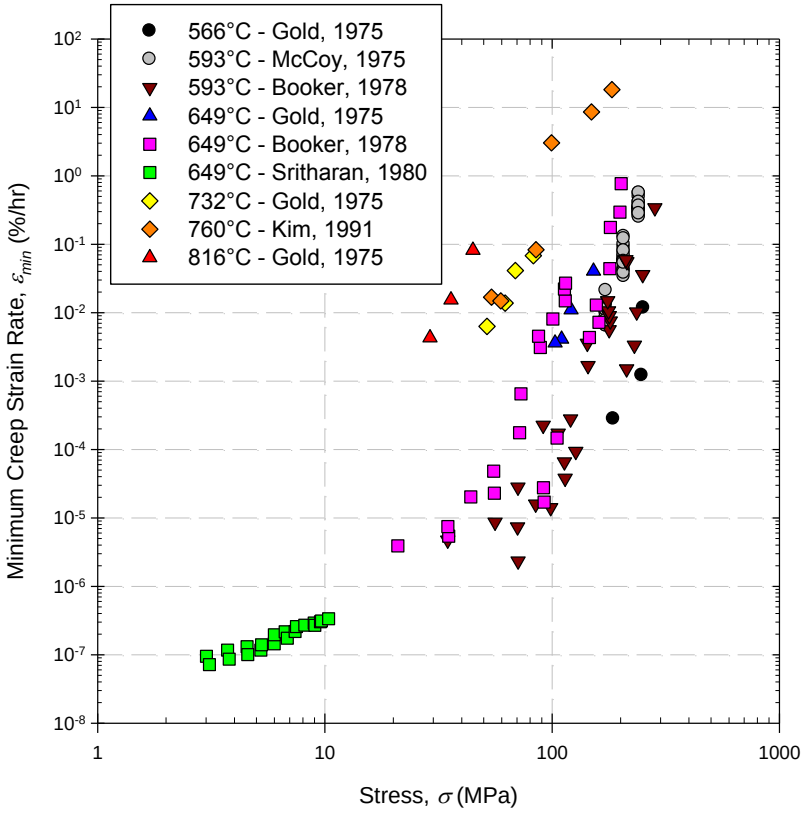

Figure 3.6 - Minimum creep rate versus stress of 304 stainless steel [129-136]

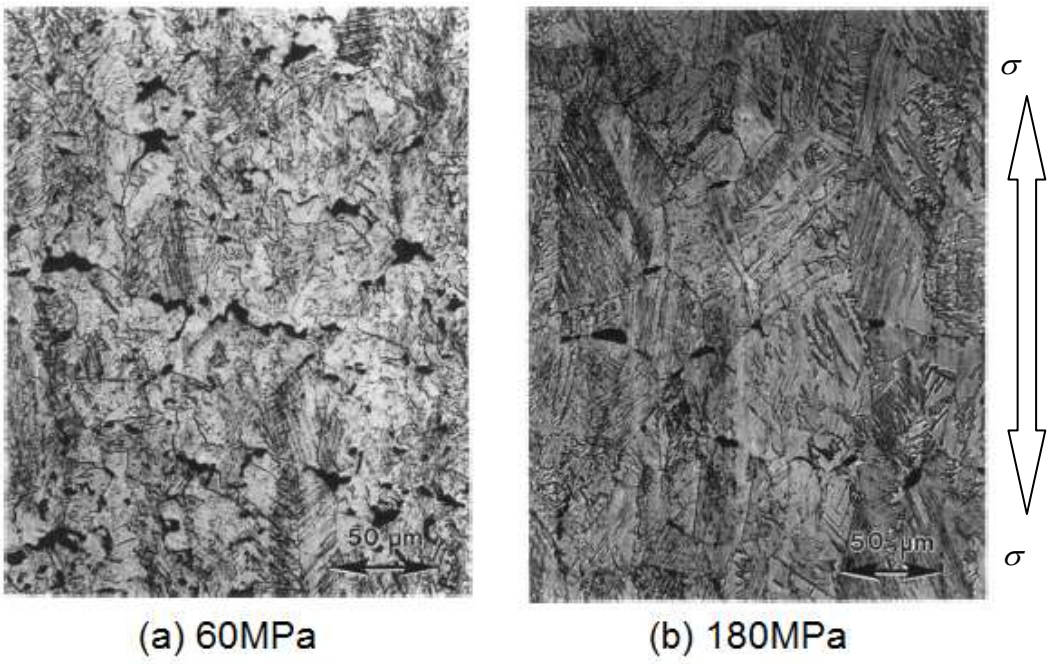

Figure 3.7 - Optical micrograph of 304SS creep test at 760°C and (a) 60MPa (b) 180MPa [131]

Examining the closeness of microcracks in the micrographs, it is observed that creep cavitation is localized and does not require homogenous cavitation damage before rupture. More creep cavitation was observed at (a) 60MPa than at (b) 180MPa suggesting that the material is more damage tolerant at low stress. The distribution of cavities at low stress is wider providing multiple sites from which microcrack can initiate and grow. At low stress, the unexpected coalescence of multiple microcracks causes the scatter observed in rupture data. At high stress, cavitation is more localized such that the coalescence of microcracks is less like to produce unexpected rupture of the specimen. Grain boundary cavitation coupled with localized deformation processes control the life of 304SS under creep [131].

Creep-rupture data from multiple sources was digitized and plotted in Figure 3.8 [129-134]. The causes of scatter in Figure 3.8 can be attributed to variations of each of the following

- Chemical compositions which met the ASME and ASTM standards
- Product types (rod, bar, sheet, plate, orientation)
- Specimen size (gage diameter)
- Material processing (cold working, annealing, surface roughness etc.)

Scatter appears to decreases as temperature is increased which also correlates with a reduced applied stress to produce comparable rupture time across temperature sets. Perhaps, this scatter is associated with the energy provided by the applied stress. At high stress a localized damage mechanism is activated where the pre-existing flaws unique to each specimen results in rupture. This provides significant more scatter, then the homogenous cavitation mechanism which is active at high temperature and low stress.

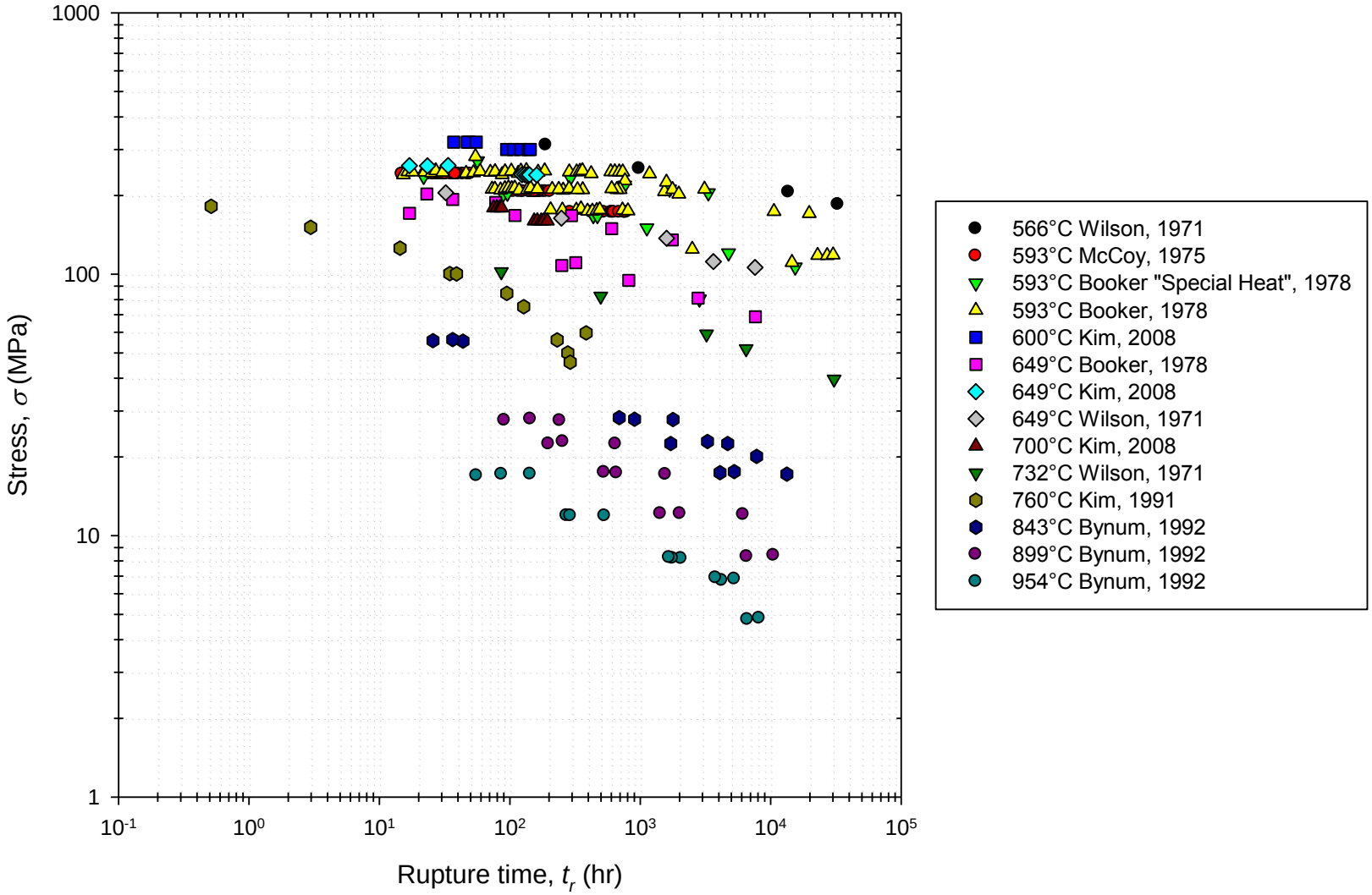

Figure 3.8 – Compiled creep-rupture data [129-134]

3.3.1 Multiaxiality

A multiaxial state of stress greatly influences the creep-rupture properties of most metals including 304SS. Kuang conducted a study evaluating the effect of notches on the creep-rupture of 304SS at 650°C; the results depicted in Figure 3.9 [127]. In the figure, stress is defined as the mean stress in the minimum cross section. Comparing the smooth and notched specimen, it is observed that notch strengthening occurs. The strengthening ratio (mean stress in minimum cross section over the uniaxial stress) is given for circular-notched specimen as 1.30 and sharp-notched specimen as 1.38. In the circular-notched specimen (K_t=1.61), considerable cavitation was observed throughout the specimen with voids concentrated at the center away from the notch. In the sharp-notched specimen (K_t=4.4), minimum cavitation is observed. Metallography suggesting fatigue damage due to the true stresses at the notch tip exceeding the yield strength. Microcracks are localized at the crack tip.

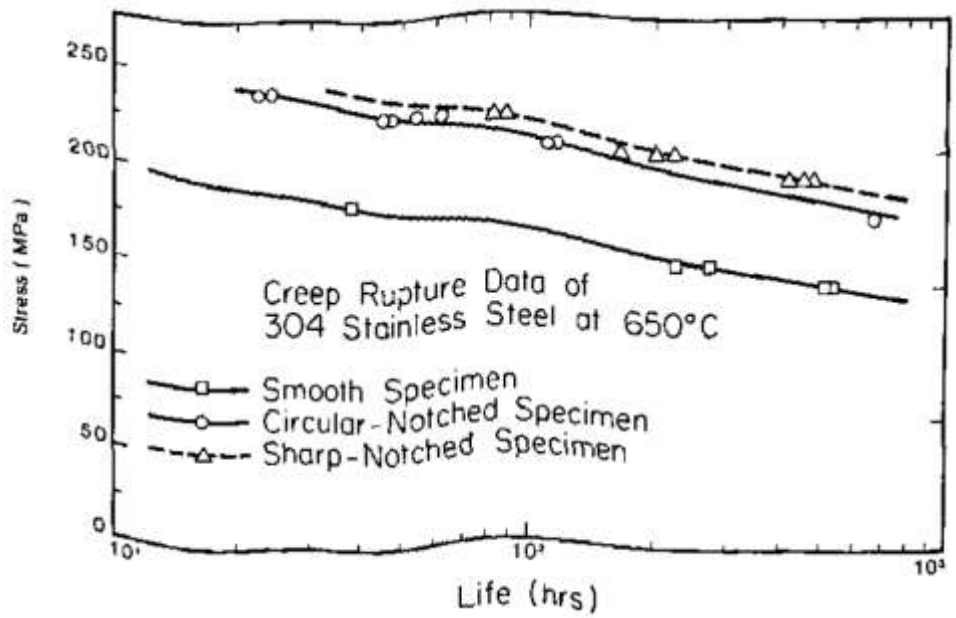

Figure 3.9 - Creep-rupture results for smooth and notched specimen [127]

The behavior of circular and sharp-notched specimens can be attributed to the effect low and high stress has on cavitation damage [131]. The high stress concentration in the sharp-notched specimen leads to considerable localized plastic deformation at the notch. Degradation is concentrated at this zone of weakness and cavitation appears in a limited fashion. In the circular-notched specimen, the lower stress concentration allows homogenous initiation of microcracks throughout the specimen geometry.

3.3.2 Material Processing

The industrial process used to chemically and mechanically convert raw chemicals into a desirable alloy greatly influences the mechanical properties of the resulting "product". McCoy and colleagues investigate the effect material processing has on mechanical properties of 304 [132]. The primary objects where to study the effect re-annealing and product type (plate, bar, pipe, tube) have on the stress-rupture curve. A graph compare the creep deformation of various products of 304SS was produced for 304SS annealed 0.5 hours at 2000°F and tested at 593°C and 172.3MPa, as shown in Figure 3.10. Comparing the creep curves of various products, it is observed that the scatter observed is no different than that which would be observed during repeated testing of a single product. This becomes obvious when comparing Figure 3.10 with Figure 3.5. Gold studied the effects of varying degrees of cold work on the creep-rupture properties of 304SS the resulting plotted provided in Figure 3.11. Cold working was found to improve the strength of 304SS at low temperature, however; increasing the degree of cold working lowers the recrystallization temperature. In cold worked 304SS once it reaches the recrystallization temperature, over time, the strength level can reduce to below that of annealed

304SS as observed in Figure 3.11(d). Materials that are heavily cold-worked are more susceptible to creep rupture at high temperature.

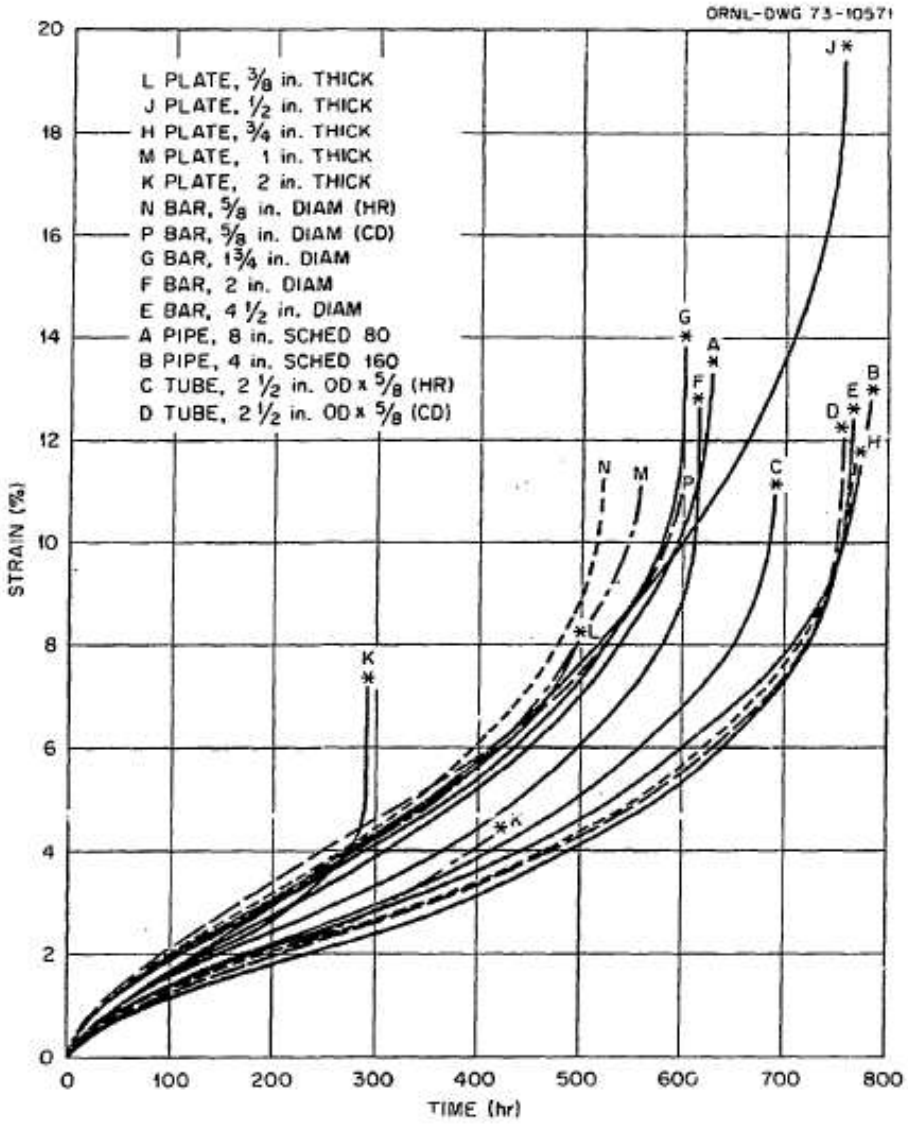

Figure 3.10 - Creep curves of 304SS annealed 0.5 hours at 2000°F and tested at 593°C and 172.3MPa [132]

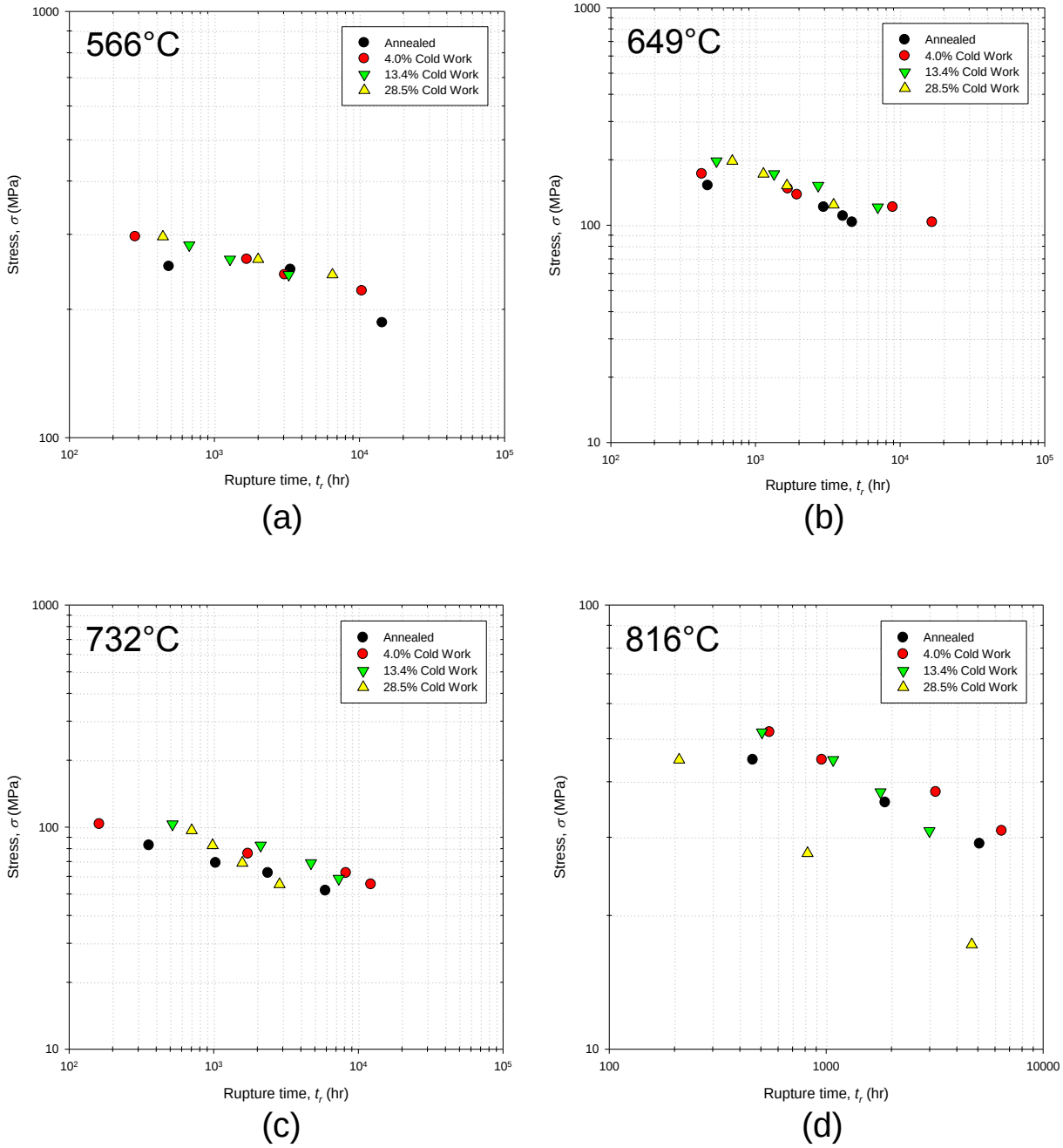

Figure 3.11 - The effect of percent (%) cold work on the creep-rupture of 304SS at (a) 566°C (b) 649°C (c) 732°C and (d) 816°C [136]

3.4 **Creep-Fatigue**

High temperature fatigue is an important engineering challenge and has been the subject of numerous investigations. The classic fatigue process occurs in three stages; the nucleation of microstructural small defects into initiated cracks, the stabilized propagation of the dominant crack, and the unstable acceleration of the crack leading to sudden fracture [137]. Load amplitude and applied mean stress influence the cycles to failure. When subject to high temperature 304SS exhibits time-dependence. Over time, creep and/or relaxation cause stress redistribution to occur at the crack tip changing the constitutive response. Factors such as frequency, hold time, wave shape, and wave form that incorporate time as a variable will effect fatigue life. When subject to a multiaxial state of stress (either via application or due to a notch), the multiaxial behavior of the material and the presence of a stress concentration factor will influence fatigue life. Additionally, the manufacturing process and environment a material is subject to will influence life.

At high temperature and under cyclic loading conditions, both the fatigue and creep mechanisms are active suggesting the term creep-fatigue. Creep is primarily an intergranular process and fatigue primarily transgranular. Fatigue test above the creep activation temperature (creep-fatigue) can undergo intergranular, transgranular, and mixed-mode cracking depending on load history and temperature. Merah and colleagues investigated the creep-fatigue crack growth of 304SS plate at 600°C [139]. Micrographs from the study are provided in Figure 3.12 [138,139]. Figure 3.12(a) was conducted at 276 *MPa* with a frequency of 1 *Hz*. Regular transgranular ductile striations are observed suggesting fatigue dominated damage. In Figure 3.12(b) the frequency is reduced to 0.0033 Hz and a hold time of 5 min introduced, intergranular

dimples are observed with few fatigue striations visible suggesting creep damage dominance. The variables of load amplitude, mean stress, temperature, frequency, hold time, wave shape/form, multiaxiality, and material processing all influence the dominant cracking mechanism.

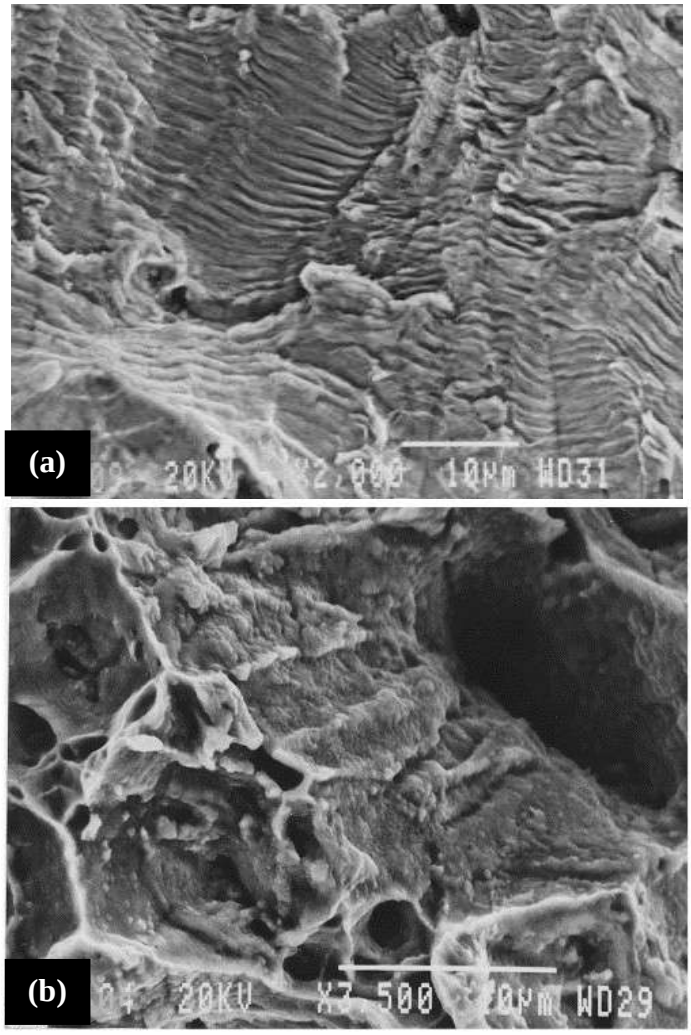

Figure 3.12 - Microstructure of notched 304SS specimen at 600°C (a) Transgranular ductile striations at (276MPa, 1Hz) (b) Intergranular dimples observed (300MPa, t_h=5min, 0.0033 Hz) [138,139]

3.4.1 Load Amplitude

Load amplitude is a key factor relating to the number of cycles to failure. In the cases of creep-fatigue load can be stress (force), strain (displacement), and/or temperature. In Figure 3.13 the relationship between maximum stress and the number of cycles to failure is given [140]. It is observed that as the maximum stress is increased, the number of cycles to failure decreases. It is also worth noting that the fatigue strength at room temperature 446 MPa drops to 353 MPa at 538°C lowering by 20%. Suh and colleagues studied the initiation, growth, and coalescence of fatigue microcrack in smooth 304SS using quantitative analysis [140]. It was found that microcracks begin to initiate at 10-20% of fatigue life, and grow until fracture. New microcracks continuously initiate at grain-boundaries due to creep. Microcrack density undergoes a parabolic increase with cycle. At room temperature microcrack density is low and localized around the primary flaw. At elevated temperature microcrack density is high and increases with load cycle ratio.

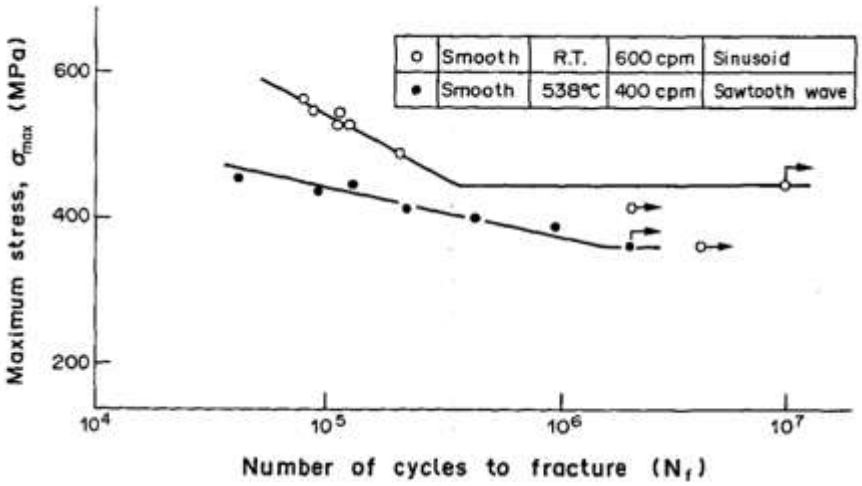

Figure 3.13 - Stress-Life curve for 304SS at room temperature and 538°C where *R*=0.1 [140]

An examination of total strain range data provides insight into how displacement control loading influences rupture. In Figure 3.14 the relationship between total strain range and the number of cycles to failure is given [141]. It is observed that as the applied total strain range increases, the number of cycles to failure decreases. Nishino, S. and colleagues conducted a quantitative damage analysis of 304SS under creep-fatigue. The researchers attempted to use a combination creep and fatigue of linear damage rules to predict failure and had limited success. While linear damage rules can provide accurate estimates of cycles to failure they do not represent the true state of degradation within a material. Both creep and fatigue damage are non-linear degradation processes which require more detailed representative equations.

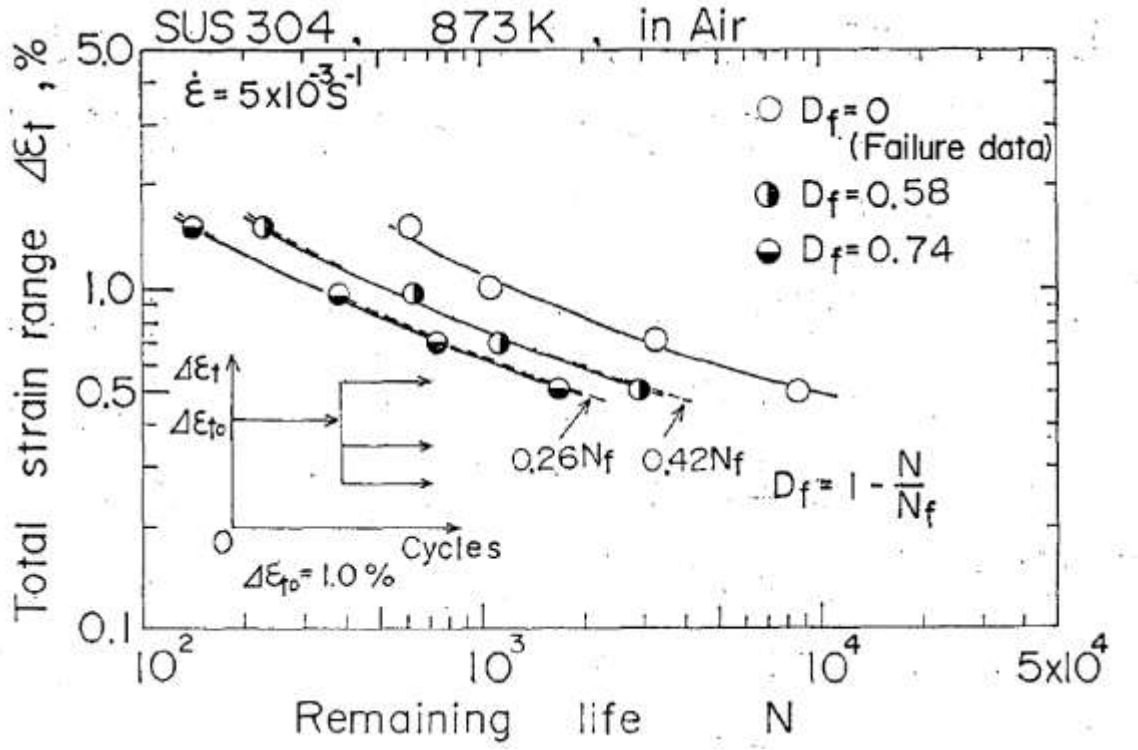

Figure 3.14 - Total strain range-life curve of 304SS at 600°C [141]

3.4.2 Mean Stress

Mean stress has a dramatic influence on fatigue behavior. The effect of tensile and compressive mean stress on fatigue strength is provided in Figure 3.15(a) and (b) respectively [142,143]. It is observed that tensile mean stress is detrimental to fatigue strength while compressive mean stress improves fatigue strength.

When 304SS is subject to asymmetric cyclic loading, ratcheting will occur. Ratcheting is the plastic strain accumulated under cyclic loading with nonzero mean stress [144]. Ratcheting can lead to the severe deformation and greatly decreases the cycles to failure. After a suitable number of cycles, at low temperature, shakedown is expected to occur. Shakedown is where plastic deformation ceases to occur due to translation and expansion of the yield surface. Shakedown is greatly delayed and often not observed at elevated temperature due to the accumulation of creep strain. The stress-life curve of most materials translates downwards as mean stress is increased. Ratcheting experiments have been conducted by Basaruddin [144], Gao [145], and Kang [146]. It should be noted that hold times are not necessary to induce ratcheting only a non-zero mean stress is needed. In Figure 3.16 the ratcheting of 304SS with various hold times are reported. It is observed that ratcheting strain accumulates and appears to harden with respect to cycles. It is also apparent that ratcheting strain significantly increases with increases in hold time. The ratcheting strain continuously increases with not shakedown observed. This is attributed to the accumulation of creep strain which is active above and below the yield strength.

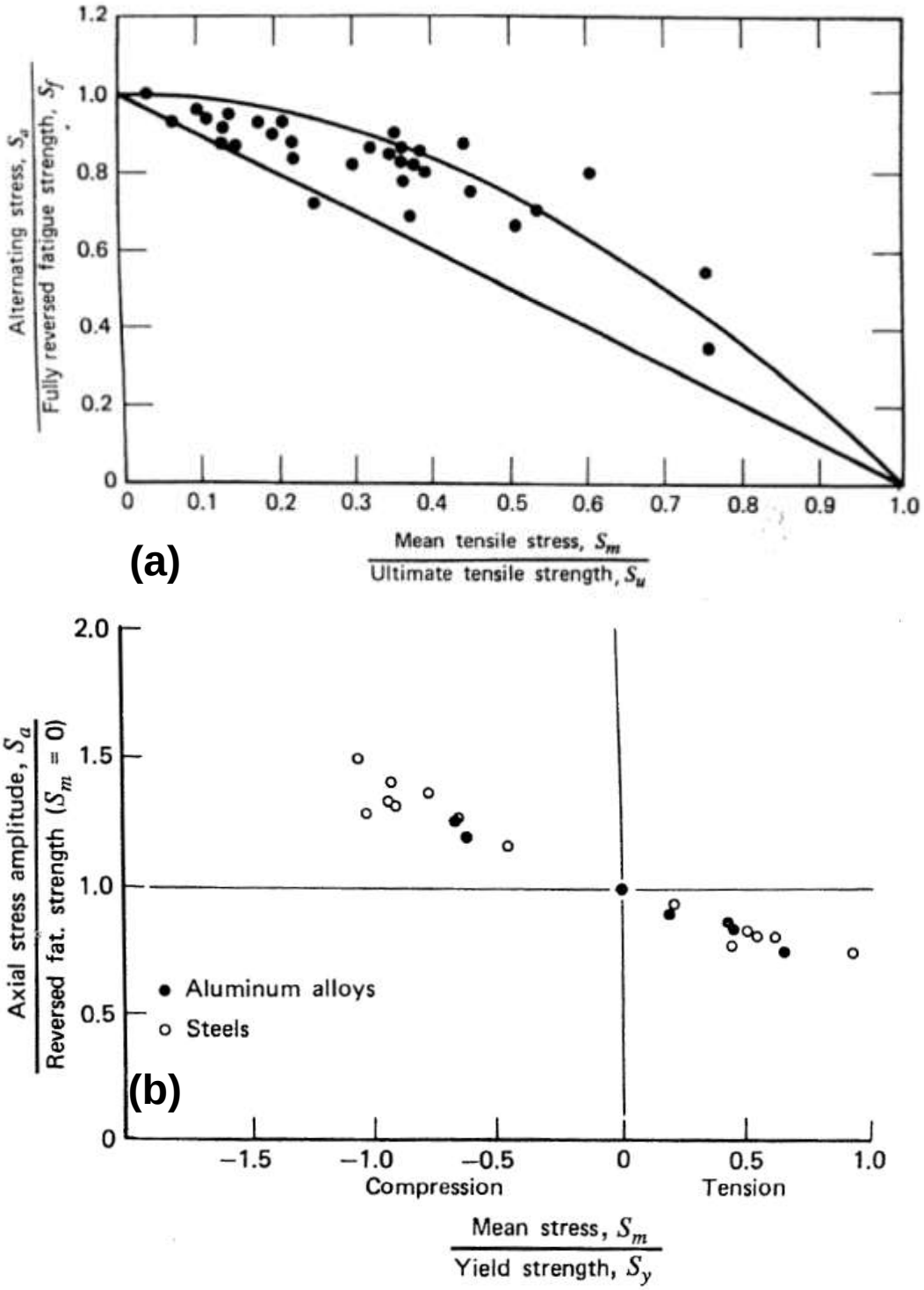

Figure 3.15 - Effect of mean stress on fatigue strength under (a) tension [142] (b) compession [143]

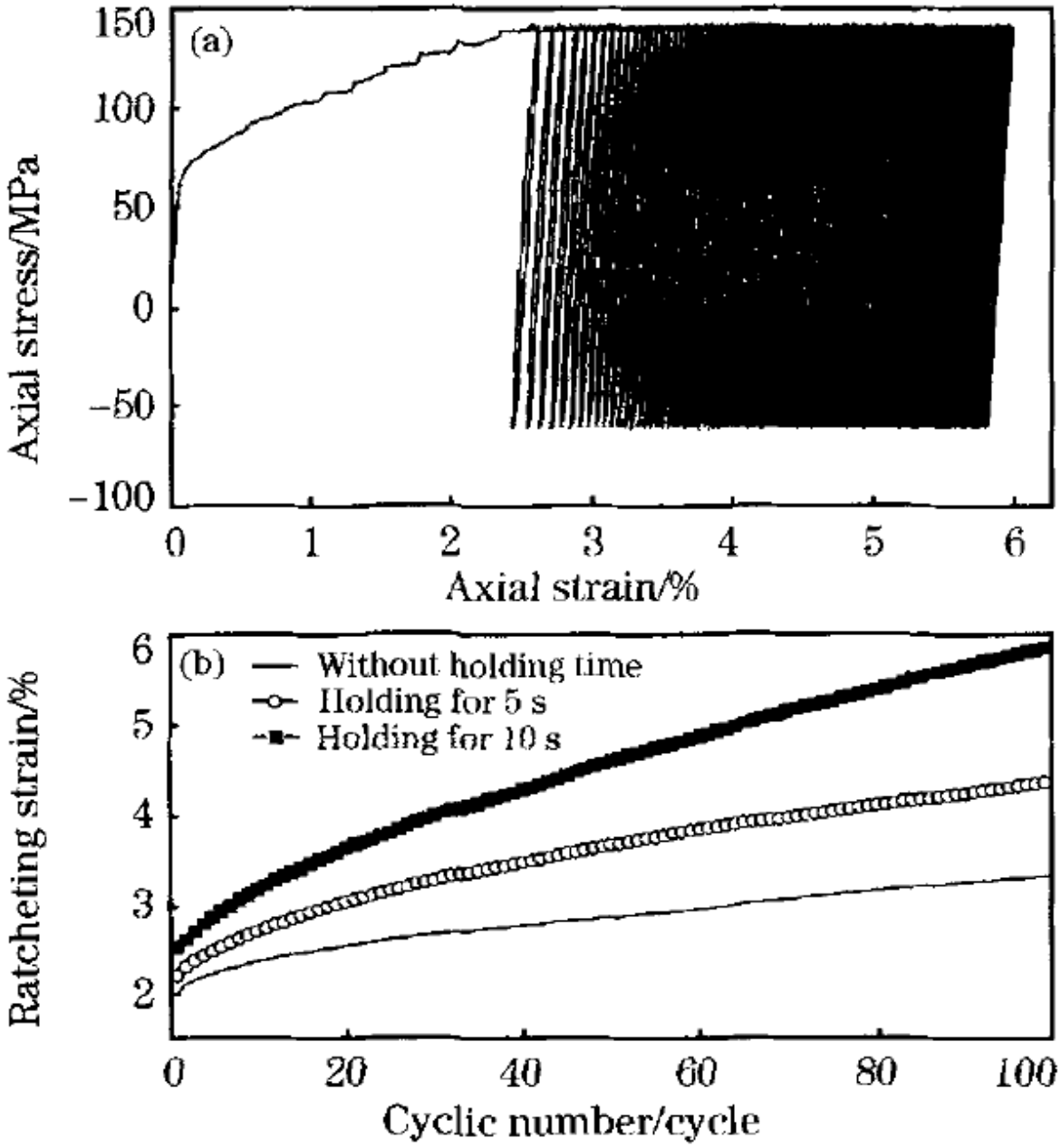

Figure 3.16 - Ratcheting of 304SS at 700°C with various hold times (a) stress-strain curve (b) ratcheting strain vs. cyclic number [146]

3.4.3 Temperature

Temperature greatly influences the creep-fatigue behavior of 304SS. In Figure 3.17 the elevated temperature strain-life of 304SS is provided [51,147]. It is observed that as temperature increases, the strain-life curve develops a knee and fatigue resistance decreases. The knee that develops represents the transition between elastic-dominated high-cycle fatigue, and plastic-dominated low-cycle fatigue. With increasing temperature the transition fatigue life shifts to lower values of life. Coffin found the elevated temperature behavior can be attributed to the environment, more specifically oxygen [148]. Evidence shows that at low frequency and elevated temperature, most fatigue cracks are filled with oxide products. When subject to a vacuum at elevated temperature the strain-life behavior of a metal will be equivalent to a room temperature experiment. This is demonstrated in Figure 3.18 for A286 alloy [148]. Increasing temperature greatly increases the crack growth rates of 304 exposed to air as depicted in Figure 3.19 [149].

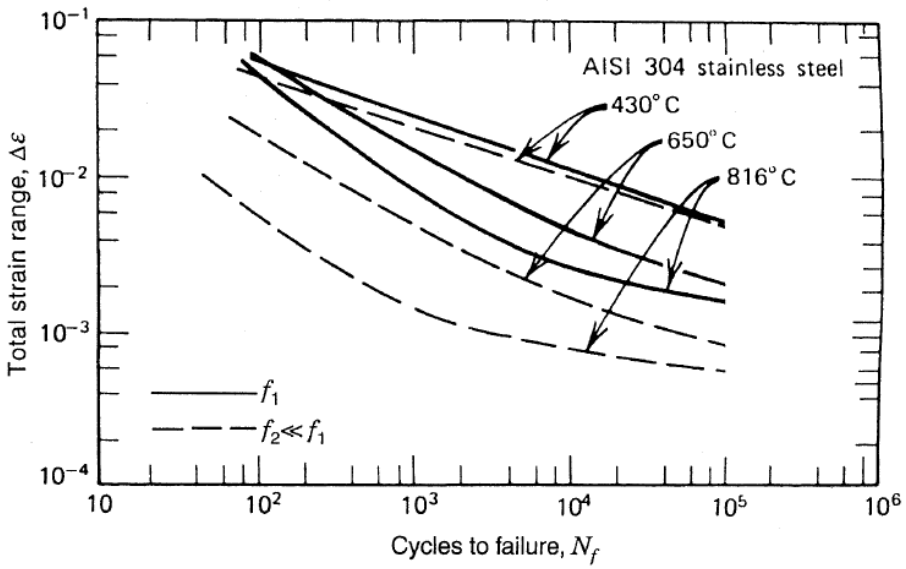

Figure 3.17 - The effect of temperature and frequency on strain-life fatigue of 304 stainless steel [51,147]

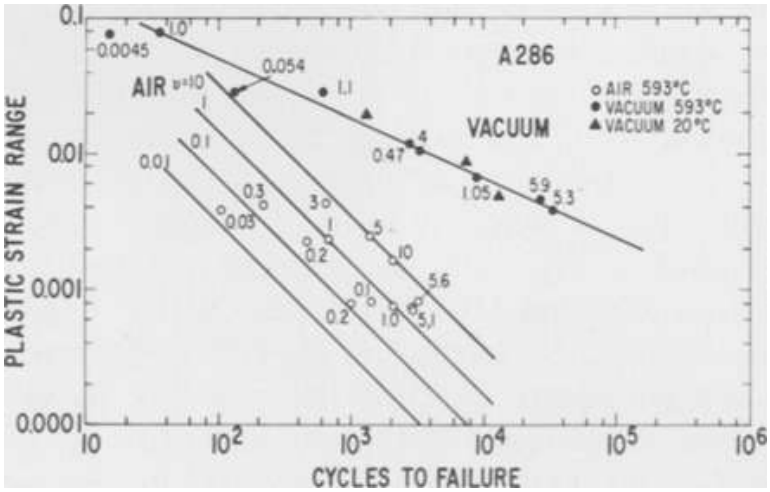

Figure 3.18 - Plastic strain-life curve for A286 alloy in air and vacuum at 593°C (numbers indicate frequency in cpm) [148]

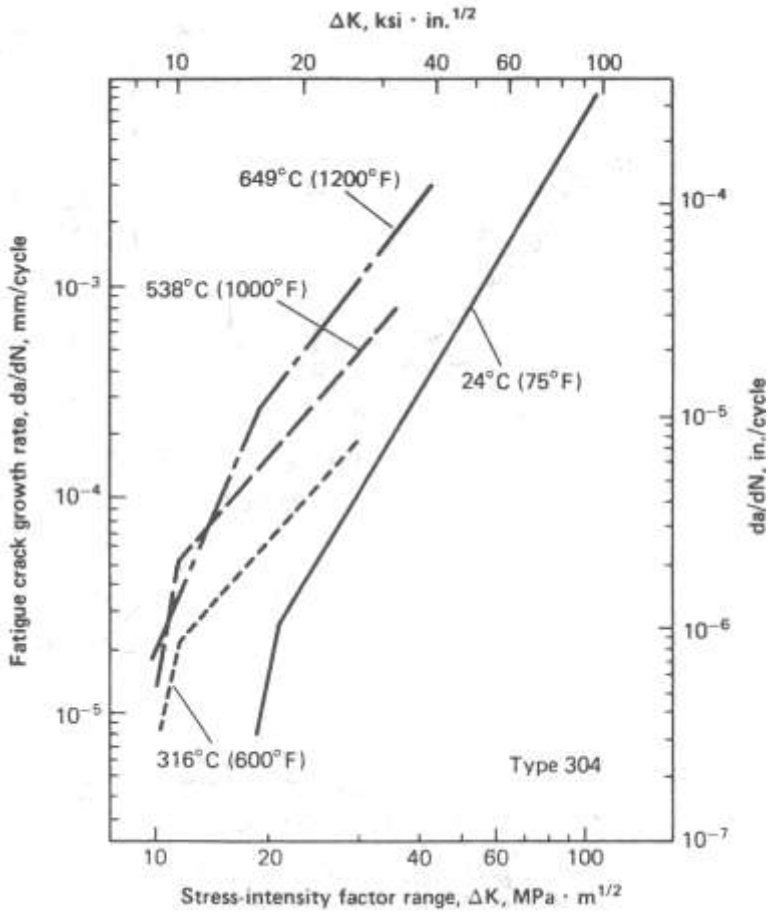

Figure 3.19 - The effect of temperature on the fatigue crack growth rates for annealed 304SS at 0.066 Hz, with an *R* ratio of 0 to 0.05 [149]

3.4.4 Frequency

As mentioned in the previous section there is an interaction between temperature and frequency. At higher temperature the frequency effect is enhanced as observed in Figure 3.17. For a given temperature, the lower frequency has less fatigue resistance. As depicted in Figure 3.18 the frequency effect disappears when experiments are conducted in a vacuum. This suggests that similar to temperature, the frequency effect is a result of the environment. At ultra low frequencies, the fatigue behavior is time-dependent and failure occurs due to time-dependent creep. At low to intermediate frequencies the failure process is due to interaction of time-dependent creep and cyclic damage. At ultra high frequencies cyclic-dependent failure dominates [148]. The crack growth rate versus stress intensity factor, ΔK, for annealed 304SS at 538°C and various frequencies is provided in Figure 3.20 [51,150]. It is observed that as frequency is decreased, the crack growth rate increases. Interestingly, frequency has little effect on the slope [139]. It is also observed that the scatter-band becomes larger. This can be attributed accumulative time-dependent creep.

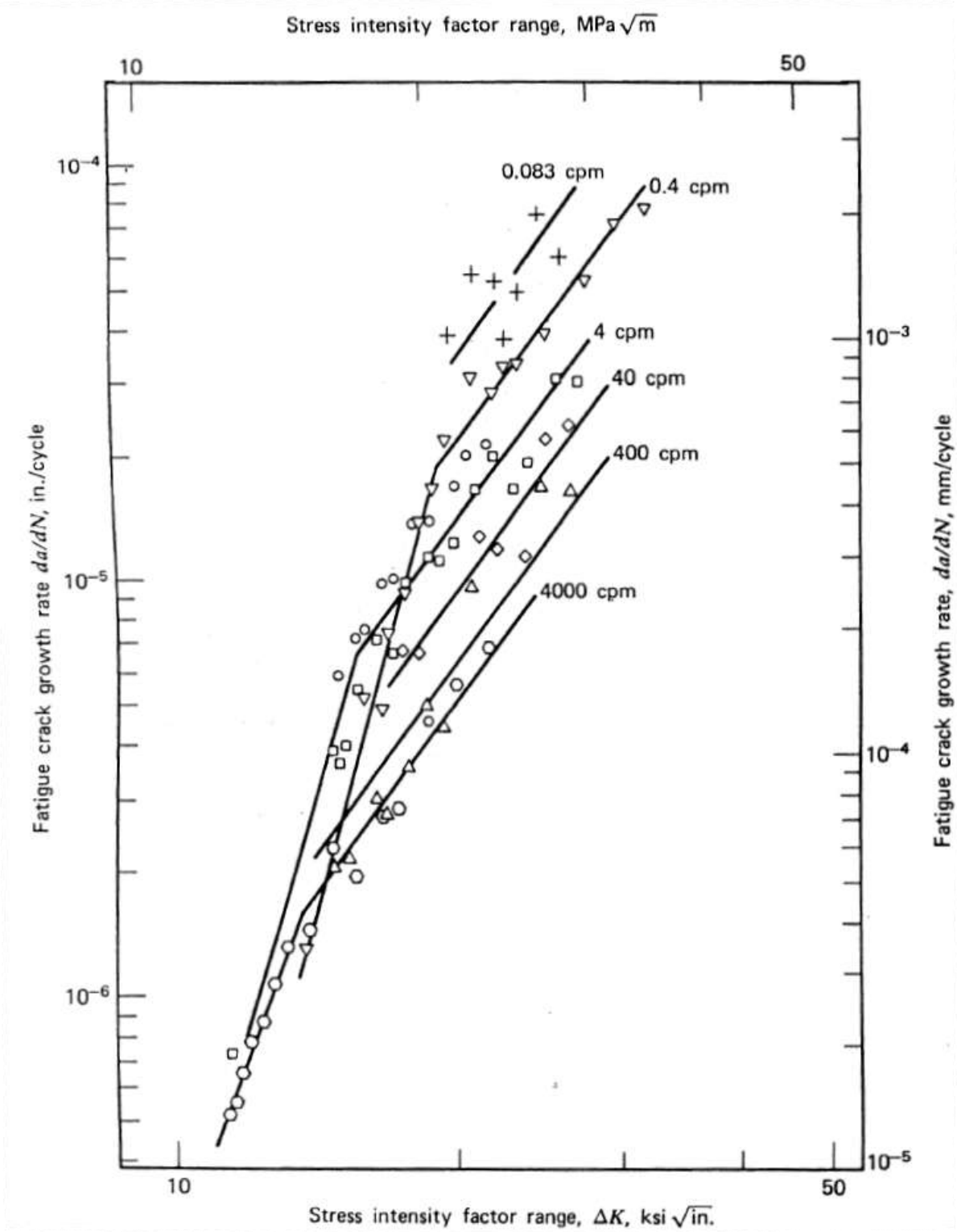

Figure 3.20 - The effect of frequency on fatigue crack growth behavior of 304SS at 538°C *R*=0.05 [51,150]

3.4.5 Hold time

Hold time can greatly influence the creep-fatigue behavior of 304SS. Hold time is representative of a component which undergoes a dwell period where loads are held constant before being discharged. In Figure 3.21, Berling and Conway studied the effect of hold time on 304SS at 593°C [151]. 304SS was found to be extremely sensitive to tensile holds. It is observed that as the applied tensile hold time is increased, life decreases drastically. This was not observed for symmetrical and compressive hold times suggesting that compressive holds do not contribute to degradation and may enhance oxide-induced crack closure [152]. While oxidation of the fracture surface is observed in both tensile and compressive hold tests, compressive holds produce a much thicker oxide scale [153].

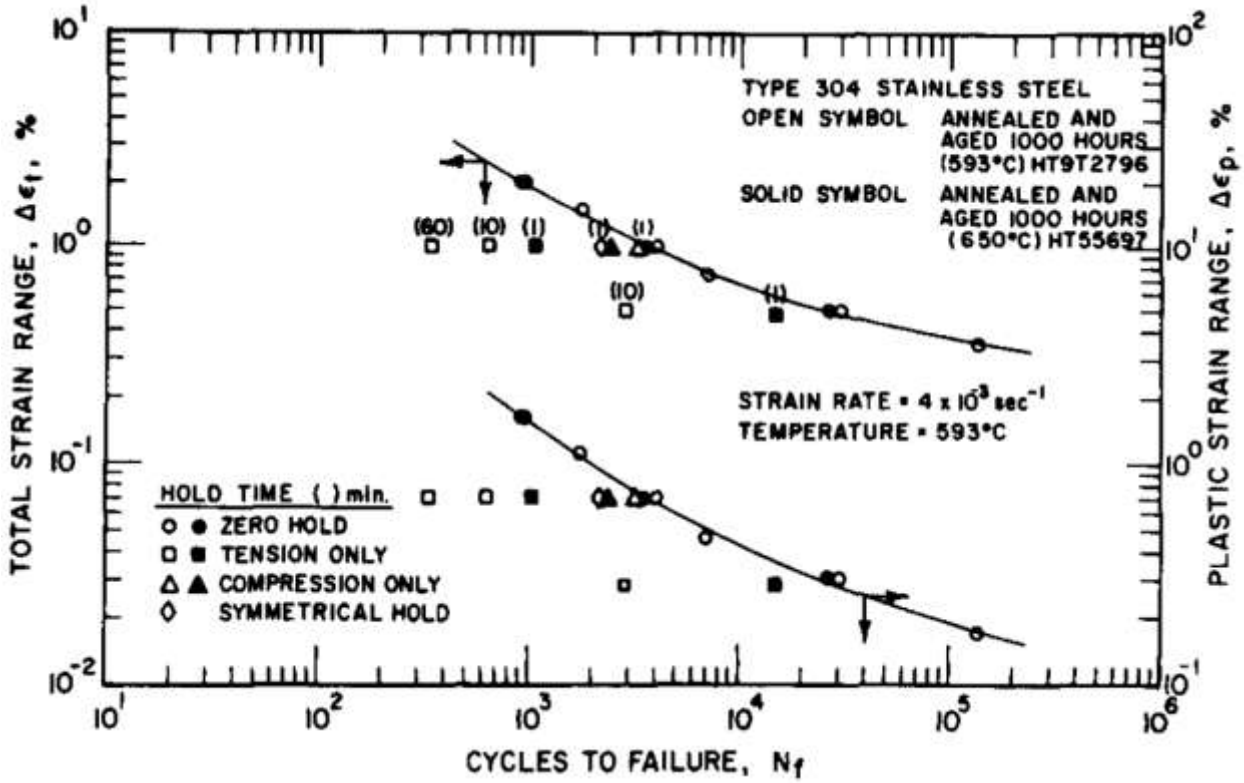

Figure 3.21 – The effect of hold time on 304SS at 593°C [51,151]

Cheng and Diercks studied the fractography of 304SS subject to various hold conditions with micrographs provided in Figure 3.22 [154]. For no hold time, and compressive and symmetric hold times the fracture surface displays ductile fatigue striations indicative of transgranular cracking. Under tensile hold, no fatigue striations are observed suggesting intergranular cracking. Examining the symmetric test it is clear that the compressive hold mitigates the negative effects of the tensile hold. Hold tests can be thought of as mixed creep-fatigue test where the hold portion corresponds to static load creep tests and the cyclic portion corresponds to fatigue.

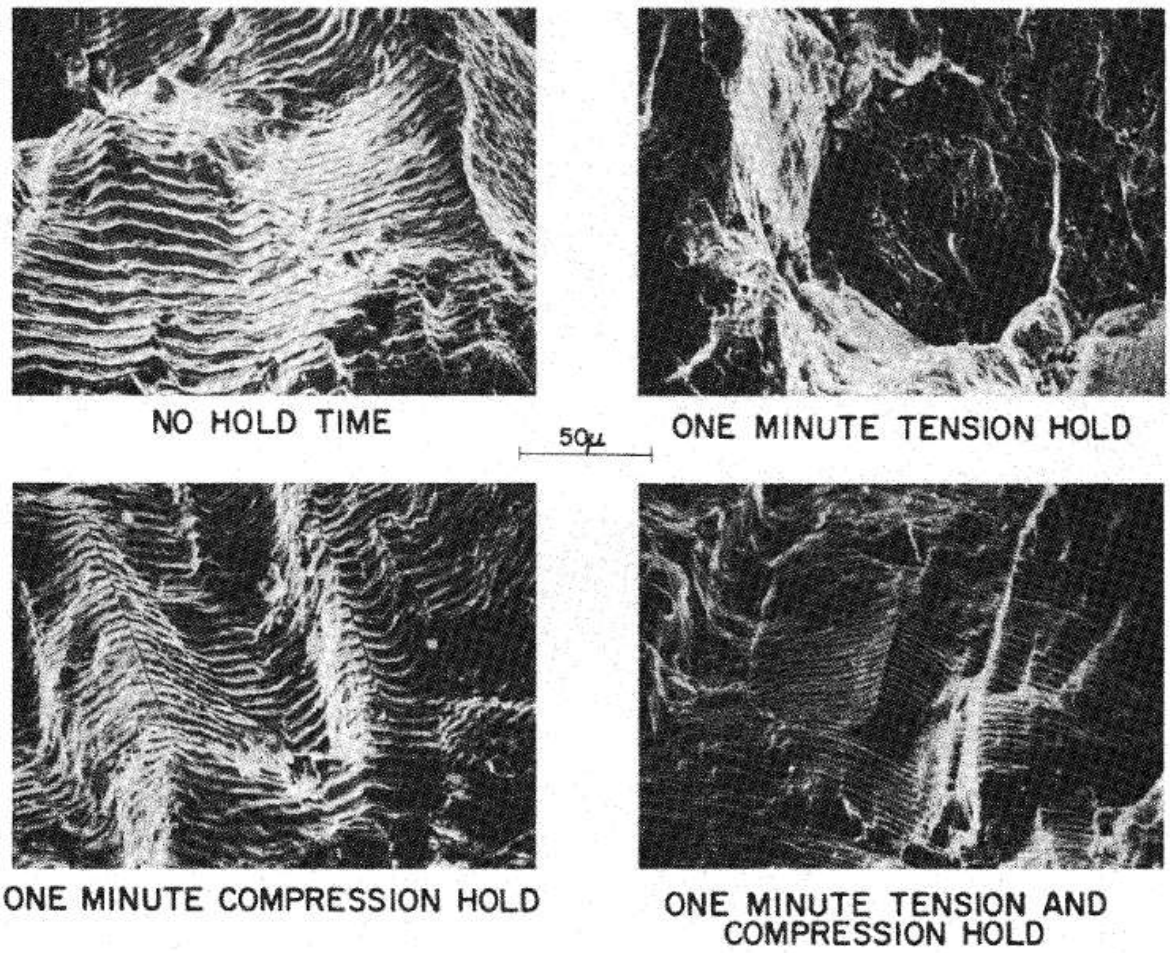

Figure 3.22 - Influence of hold time and loading condition on fracture surface at 593°C [154]

Plumtree and Tang found that when tensile hold times are suitably small (between, a mixed cracking mode is observed as depicted in Figure 3.23 [155]. Successive sections of transgranular and intergranular cracking correspond to fatigue and hold time (creep) periods. After hold periods, grain boundary cavities are observed ahead of the crack tip. During subsequent fatigue cycling a few beachmarks are missing. This suggests that the first few cycles after a hold contribute to intergranular crack of the nucleated grain boundary cavities ahead of the crack tip. Intergranular fracture will occur as temperature is increased, frequency is decreased, and/or plastic range is decreased. Intergranular facture is strongly tied to the environment as testing under a high vacuum will completely eliminate intergranular cracking.

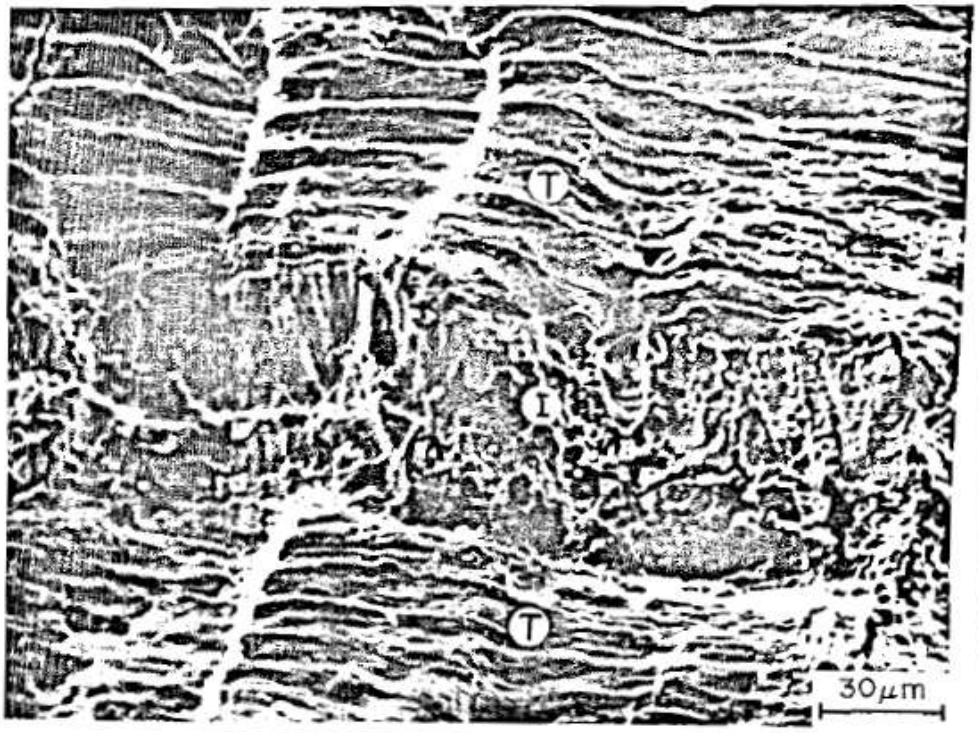

Figure 3.23 - Mixed intergranular (I) and transgranular (T) frature of 304SS under tensile hold [155]

The rate of crack propagation under hold time is a function of stress intensity factor ΔK, sequence, and the length of the hold period [155]. Different configuration of these three factors can dramatically change the crack propagation rate and the dominant failure mechanism. At low stress intensity oxide-induced crack closure retards crack propagation. At high stress intensity crack propagation is accelerated. Cheng conducted a study on 304SS at 593°C under continuous cycling with zero, symmetric and compressive holds of minute, depicted in Figure 3.24 [154]. It was found that crack propagation rate is sensitive to hold time. Crack initiation and propagation occurs the quickest under a symmetric hold time. A compressive hold time has the effect of retarding the crack initiation process; however, zero hold time produces the largest fatigue life. Plumtree studied 304SS at 570°C under 50, 500, and 1000 cycle blocks with 15 and 120 minute hold times as depicted in Figure 3.25 [155]. It is apparent that the influences of cycle block size and hold time on the crack propagation rate varies with sequence and stress intensity factor. The fastest propagation rates are observed in sequences where the smallest cyclic block (N=50) is used. This can be attributed to an increase in hold periods which allow significant activation of the creep damage mechanism to occur. The lowest rates are observed when the cyclic blocks are highest (N=1000) where minimal creep damage occurs. The influence of sequence and hold time on crack propagation rate is a function of temperature. At low temperature the disparity between various sequence and hold times will be greatly reduced.

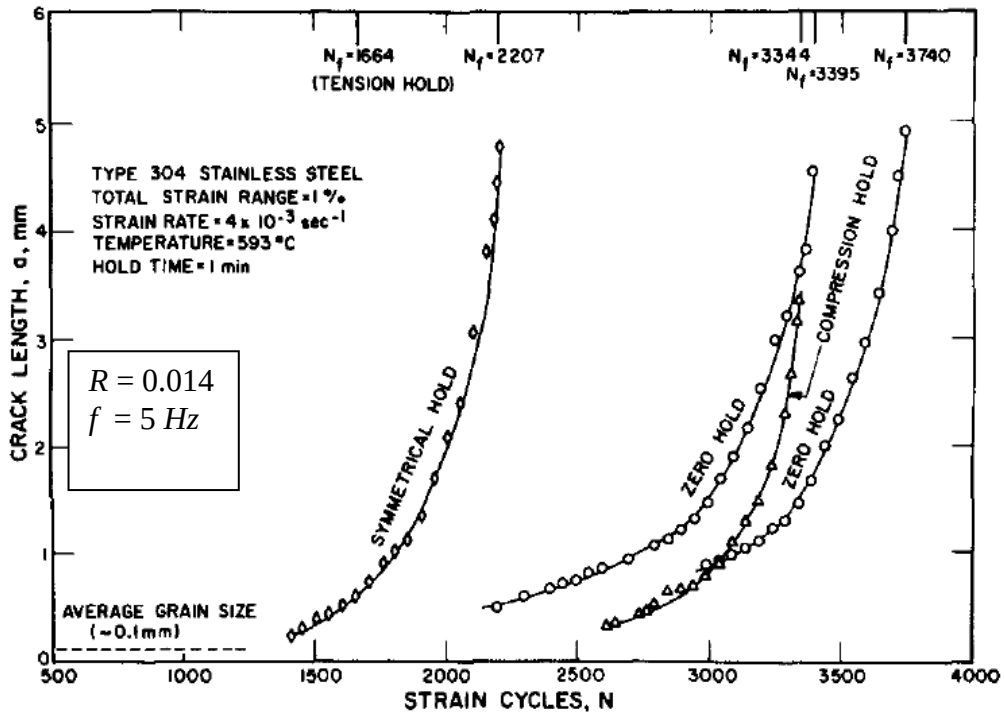

Figure 3.24 – Crack length vs strain cycles for specimens tested under various loading conditions [154]

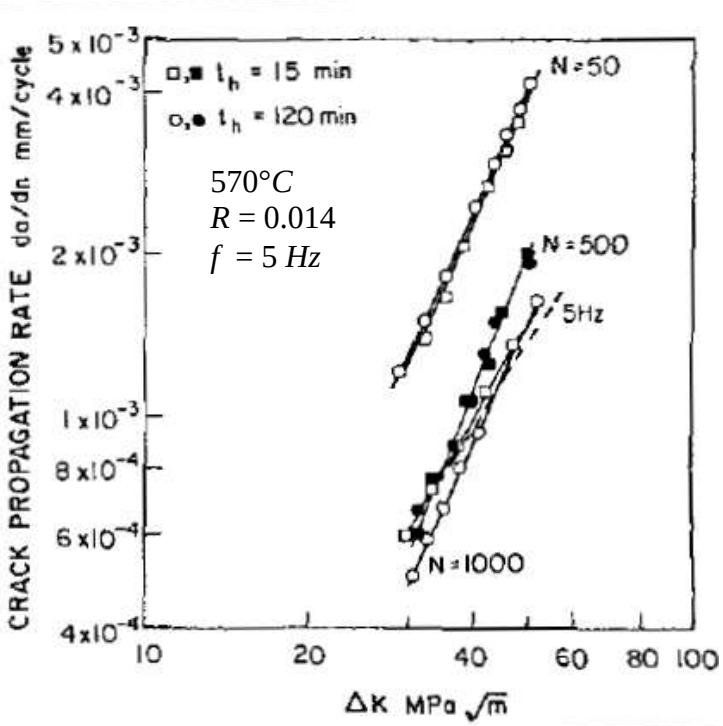

Figure 3.25 - The effect of hold time and sequence on 304SS at 570°C [155]

3.4.6 Waveform

The waveform of an applied loading condition can dramatically influence the fatigue life of materials. Lee and colleagues studied the effect of waveform on 304SS at 650°C results of which are plotted in Figure 3.26 [156]. Three waveforms were studied; fast-fast, slow(tension)-fast(compression), and fast(tension)-slow(compression). The fast and slow strain rates were $4 \cdot 10^{-3}/s$ and $4 \cdot 10^{-5}/s$ respectively. The fatigue life under slow-fast cycling was dramatically reduced. The slow tension left the material susceptible to creep cavitation with intergranular cracking observed on the fracture surface. The fatigue life under fast-slow cycling was reduced but by a smaller degree. Typical transgranular cracking was observed with regular ductile fatigue striations. James conducted a study examining the influence of wave shape on crack propagation [157]. Two wave shapes were used: saw tooth and trapezoid with tensile hold at 4, 0.333, and 0.083 cpm. Wave shape sensitive was not observed at 4 and 0.333 cpm. At 0.083 cpm the crack growth rate was lower through the trapezoid with tensile hold wave shape.

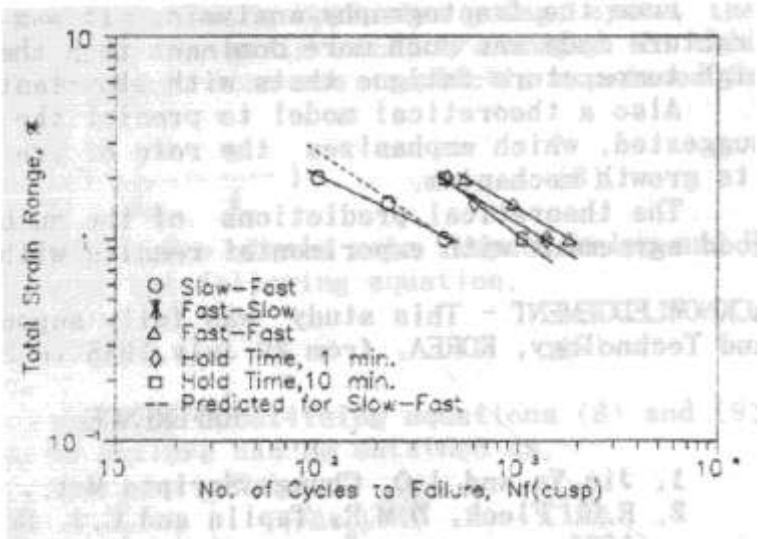

Figure 3.26 - Waveform effect on the low cycle fatigue behavior of AISI 304 Stainless Steel at 650°C [156]

3.4.7 Notch Sensitivity

The failure of 304SS is greatly influenced by the applied state of stress. Kuang conducted a study evaluating the effect of notches on the life of 304SS at 650°C; the results depicted in Figure 3.27 [127]. Notch strengthening is observed for both circular and sharp-notched specimen. This indicates that the multiaxial state of stress at the crack tip greatly influences life.

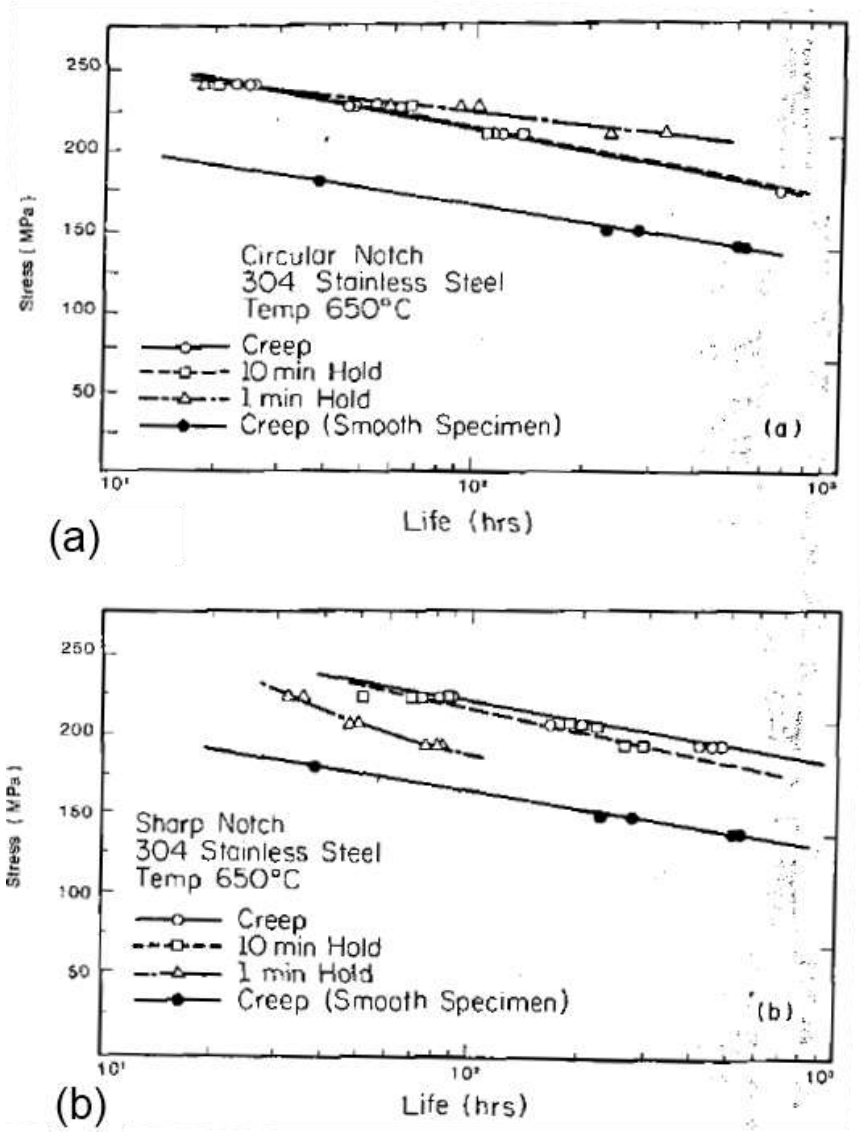

Figure 3.27 - Stress-Life Curve of 304SS at 650°C (a) circular-notched (b) sharp-notched [127]

3.4.8 Material Processing

Michel and Smith studied the fatigue crack growth of aged 304SS 5000 hours at 593°C as plotted in Figure 3.28 [158]. Examining the figure it is clear that aging has no negative effect on crack growth rates. Lee and Nam studied the effect surface roughness has on low cycle fatigue life [156]. At low to intermediate temperature the number of cycles to crack initiation decreased with surface roughness. Cracks were found to initiate at surface grooves. When temperature and grain size is increased 304 becomes less sensitive to grain size. Crack initiate at both the surface and grain boundaries. Mechanical surface treatment techniques such as deep rolling, laser shock peening, shot peening, and brushing have been found to greatly improve the cycles to failure; however, as temperature increases, the effect is lessened due to residual stress relaxation[159].

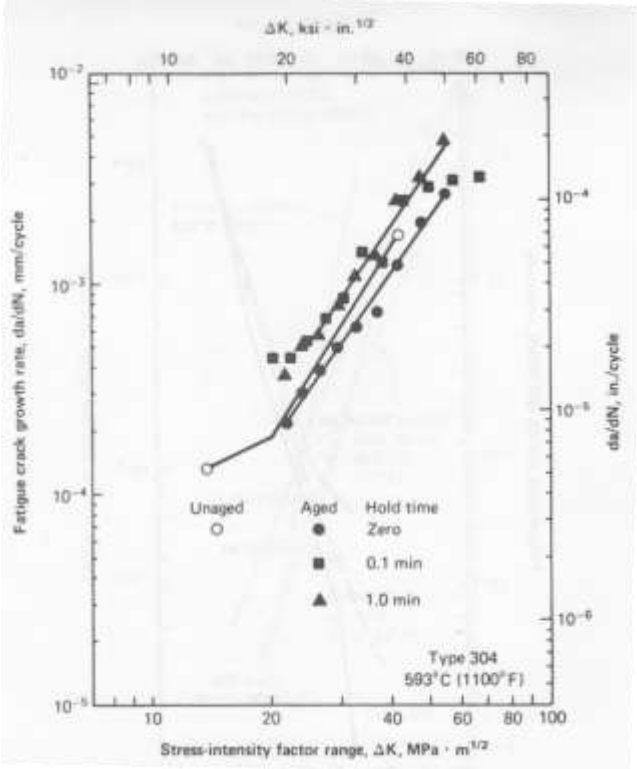

Figure 3.28 - Effect of Aging (593°C for 5000h) on fatigue crack growth rates of 304SS at 593°C, 0.17 Hz, and *R*=0 [158]

3.5 **Summary**

The exhaustive literature review on 304 stainless steel has provided substantial insight into the behavior of the material. The knowledge gain is key towards developing an accurate mechanical model for creep-fatigue. The question of how to validate the proposed mechanical model arises. It is necessary to conduct a set of "specialized" mechanical tests to verify the hypothesis that a unified mechanical model for creep-fatigue can be developed which incorporates the physical degradation, constitutive response, and rupture of superalloys. Monotonic tensile and fatigue tests were performed using the following equipment.

3.6 **Testing Equipment**

A single universal testing machines (UTMs) is used in this study. The UTM is a first generation MTS-810 which was donated to the University of Central Florida as depicted in Figure 3.29. It is a servo-hydraulic load frame produced by MTS. It has been designed for fatigue, environmental, monotonic, fracture, high temperature, and thermo-mechanical fatigue testing conditions. The system support dynamic tests up to 20 Hz. It has water-cooled grips with a force capacity of 100kN and a maximum operating pressure of 45 MPa. An Ameritherm HOTShot 3500Watt induction heater is used to heat the specimen with a specially wound copper induction coil as depicted in Figure 3.30. A K-type thermocouple is welded directly to the center of specimen. A MTS 632.53 high temperature extensometer is used to measure displacement in the specimen visible in Figure 3.29(b). This device is capable of operating at temperatures up to 1200°C and is not-cooled. The UTM is centrally controlled by desktop computer running the MTS TestStar II

acquisition and control system. Load, displacement, and temperature (through the induction heater and convective cooling valves) are controlled and data is stored. The device will be used to conduct fatigue tests on novel specimen designed to evaluate the capabilities of the proposed constitutive model.

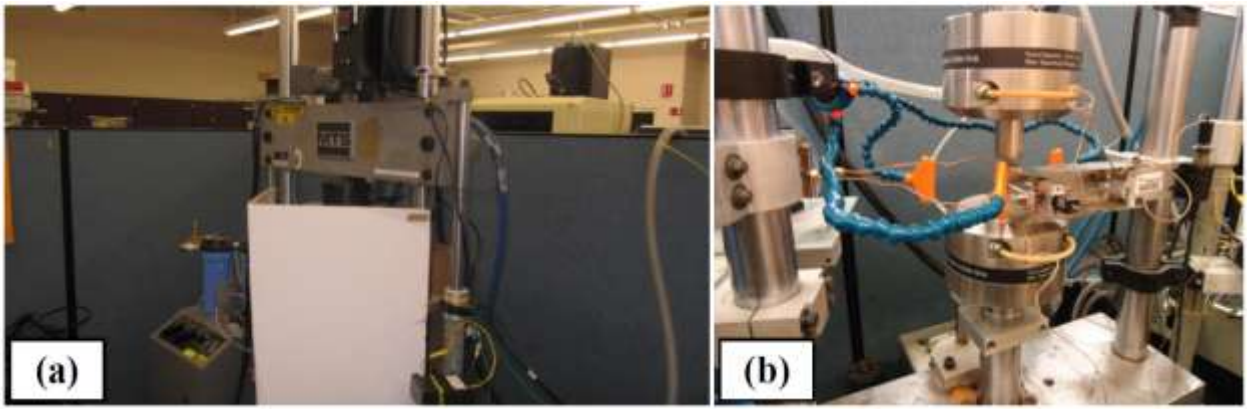

Figure 3.29 - MTS 810 Universal Test Machine (a) covered (b) close up

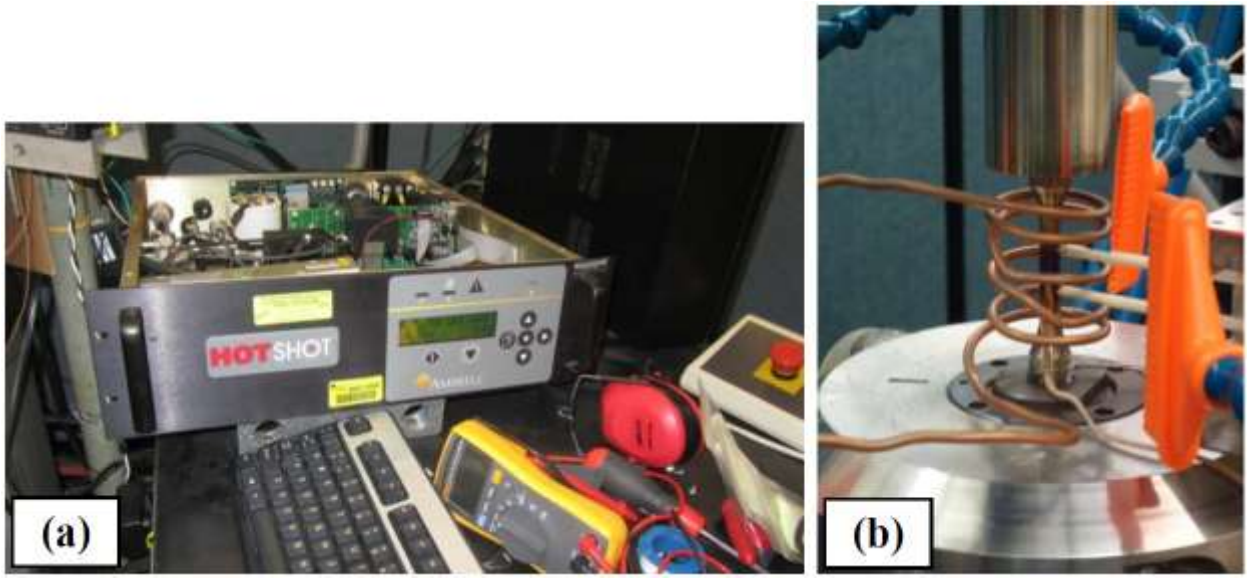

Figure 3.30 - Temperature Control (a) control box (b) induction coil

CHAPTER FOUR: UNIFIED MECHANICAL MODEL FOR CREEP

4.1 Introduction

The development of a unified mechanical model for creep involves many steps. First an appropriate viscous function which relates the minimum creep strain rate to stress must be determined for the subject material. This function must incorporate the ability to deal with temperature-dependence. Next, a damage evolution equation must be generated and coupled with the viscous function. This coupling must be done is such a way that the viscous function reverts back to its original form when damage is zero. The damage evolution equation must be formulated to mitigate stress-sensitivity and replicate the evolution of microstructural defects. Afterwards, a "special" equivalent stress must be found to incorporate the issue of multiaxiality. This "special" equivalent stress is incorporated into the viscous and damage evolution equations. Finally, an appropriate approach for the degradation of the stiffness material Jacobian is determined.

4.2 Proposed Constitutive Model

The proposed constitutive model is multistage where primary, secondary, and tertiary creep regimes are modeled. This is done by separation into primary and secondary viscous function as follows

$$\dot{\varepsilon}_{cr} = \dot{\varepsilon}_{pr} + \dot{\varepsilon}_{sc}(\omega) \tag{4.1}$$

where the tertiary regime arises from the damage variable, ω.

4.2.1 Secondary Viscous Function

The secondary viscous function must be found. The form of the secondary viscous function is given by the relationship between the minimum creep strain rate and stress as follows

$$\dot{\varepsilon}_{\min} = f(\sigma)\, g(T) \tag{4.2}$$

where σ is constant stress, and T is temperature. Literature has provided numerous types of viscous functions for secondary creep as listed in Table 2.2. For conveniences the viscous functions (given subscripts, a, b, c, d, f, and g) are relisted below as

a	Norton, 1929	$\dot{\varepsilon}_a = A\left(\sigma/\sigma_s\right)^n$	(4.3)
b	Soderberg, 1936	$\dot{\varepsilon}_b = A\left\{\exp\left(\sigma/\sigma_s\right)-1\right\}$	(4.4)
c	McVetty, 1943	$\dot{\varepsilon}_c = A\sinh\left(\sigma/\sigma_s\right)$	(4.5)
d	Dorn, 1955	$\dot{\varepsilon}_d = A\exp\left(\sigma/\sigma_s\right)$	(4.6)
f	Johnson, Henderson, and Kahn, 1963	$\dot{\varepsilon}_f = A_1\left(\sigma/\sigma_s\right)^{n_1} + A_2\left(\sigma/\sigma_s\right)^{n_2}$	(4.7)
g	Garofalo, 1965	$\dot{\varepsilon}_g = A\left[\sinh\left(\sigma/\sigma_s\right)\right]^n$	(4.8)

where A, A_1,A_2, n, n_1, n_2, and σ_s are material constants. An analytical exercise of the viscous functions as a function of stress produced Figure 4.1.

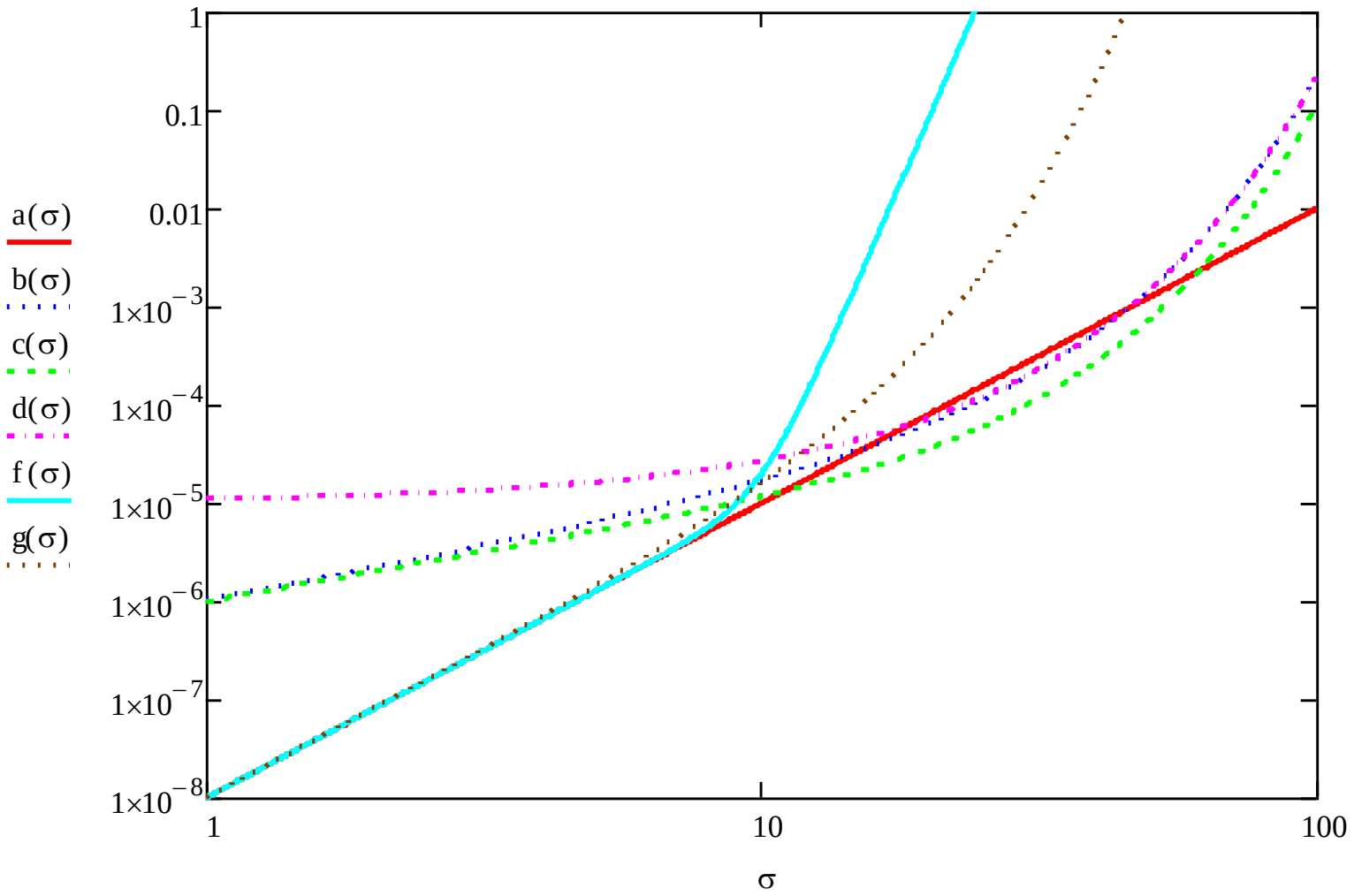

Figure 4.1 – Analytical evaluation of various viscous functions

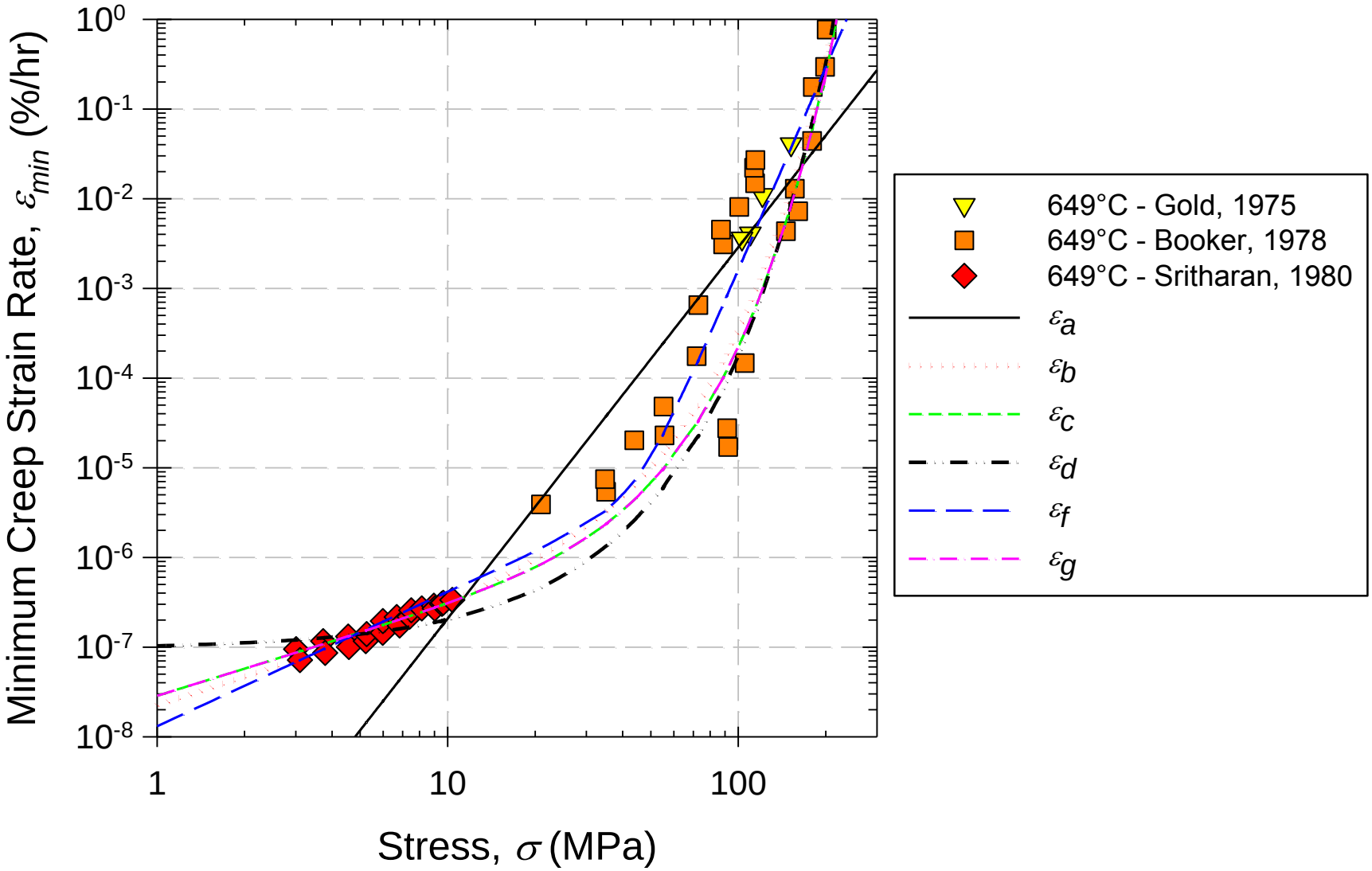

Figure 4.2 – Viscous function fit to experimental data at 649°C [130,135,136]

The viscous functions were fit to 649°C experimental data as depicted in Figure 4.2 [130,135,136]. The equations where fit using regression analysis by minimization of the residual sum of squares. This metric is sensitive to scale and would not fit the low stress data; therefore, constants found through regression where then adjusted by hand. Function A had the lowest quality fit to the data and is unacceptable for this study. Examining the deformation mechanism map in Figure 2.3, it is clear that function A does not take into account transition from diffusion-creep at low stress to power-law-creep at high stress. Examining function D, it is shown that it does not model the low stress behavior accurately. A more critical assessment shows that when stress is equal to zero the minimum strain rate calculated does not equal zero. This makes equation D unacceptable. Functions B, C, F, and G produce similar high quality fits of the experimental data yet it is still necessary to determine the optimal function. In function B, an extra term (negative one) is needed to zero out the function. In function F, there are excess constants that do not contribute equal weight to the solution. In function G, the constant, *n*, has no weight on the solution. The optimal function for 304 stainless steel is C, a hyperbolic-sine function developed by McVetty [160] as follows

$$\dot{\varepsilon}_{sc} = A(T)\sinh\left(\sigma/\sigma_s\right) \tag{4.9}$$

where *A* (1/s) and σ_s (MPa) are the creep coefficient and secondary creep mechanism-transition stress respectively. This viscous function has been used by a number of authors in literature [48,161,162].

The viscous function must be modified to incorporate temperature-dependence. This is done by making the material constants as function of stress either $A(T)$ or $\sigma_0(T)$.

In the case of the creep coefficient, $A(T)$, a common approach is to use an Arrhenius type relation as follows

$$A(T) = A_0 \exp\left(\frac{-Q_{cr}}{RT}\right) \tag{4.10}$$

where A_0 ($MPa^{-1}\ hr^{-1}$) is the pre-exponential factor, Q_{cr} ($J\ mol^{-1}$) is the apparent activation energy, R is the universal gas constant 8.314 $J\ mol^{-1}K^{-1}$, and T (K) is temperature [33]. Introducing Eq. (4.10) into Eq. (4.9) leads to

$$\dot{\varepsilon}_{sc} = A_0 \sinh\left(\sigma/\sigma_s\right)\exp\left(\frac{-Q_{cr}}{RT}\right) \tag{4.11}$$

The mechanism transition stress, $\sigma_0(T)$, is not often used to account for the temperature-dependence of creep; however, the ultimate tensile strength and yield strength of materials are temperature-dependent and can be used as follows

$$\begin{aligned}\sigma_0(T) &= f\left[\sigma_{UTS}(T)\right] \\ \sigma_0(T) &= f\left[\sigma_{UTS}(T)\right]\end{aligned} \tag{4.12}$$

The minimum creep strain rate versus stress data in Figure 3.6 is used to evaluate temperature-dependence. The A constants was fixed and optimization done to find the mechanism-transition stress σ_0 at each temperature. Temperature-dependence was not observed. The fit to experimental data was of very low quality. Next, the mechanism-transition stress σ_0 was fixed and optimization done to find the A constant for each temperature. The resulting constants are plotted in Figure 4.3. Using regression analysis, [Eq. (4.10)] was fit to the data. The

pre-exponential factor, A_0, is equal to 3.1754E+16 *% hr*$^{-1}$. The apparent activation energy was calculated to be 4.058E+5 *J*/*mol*. This compares well to the value reported by Williams with an apparent activation energy equaling 3.977e5 *J*/*mol* [163]. The viscous function becomes

$$\dot{\varepsilon}_{sc} = 3.1754 \cdot 10^{16} \sinh\left(\sigma/\sigma_s\right) \exp\left(\frac{-4.085 \cdot 10^5}{RT}\right) \tag{4.13}$$

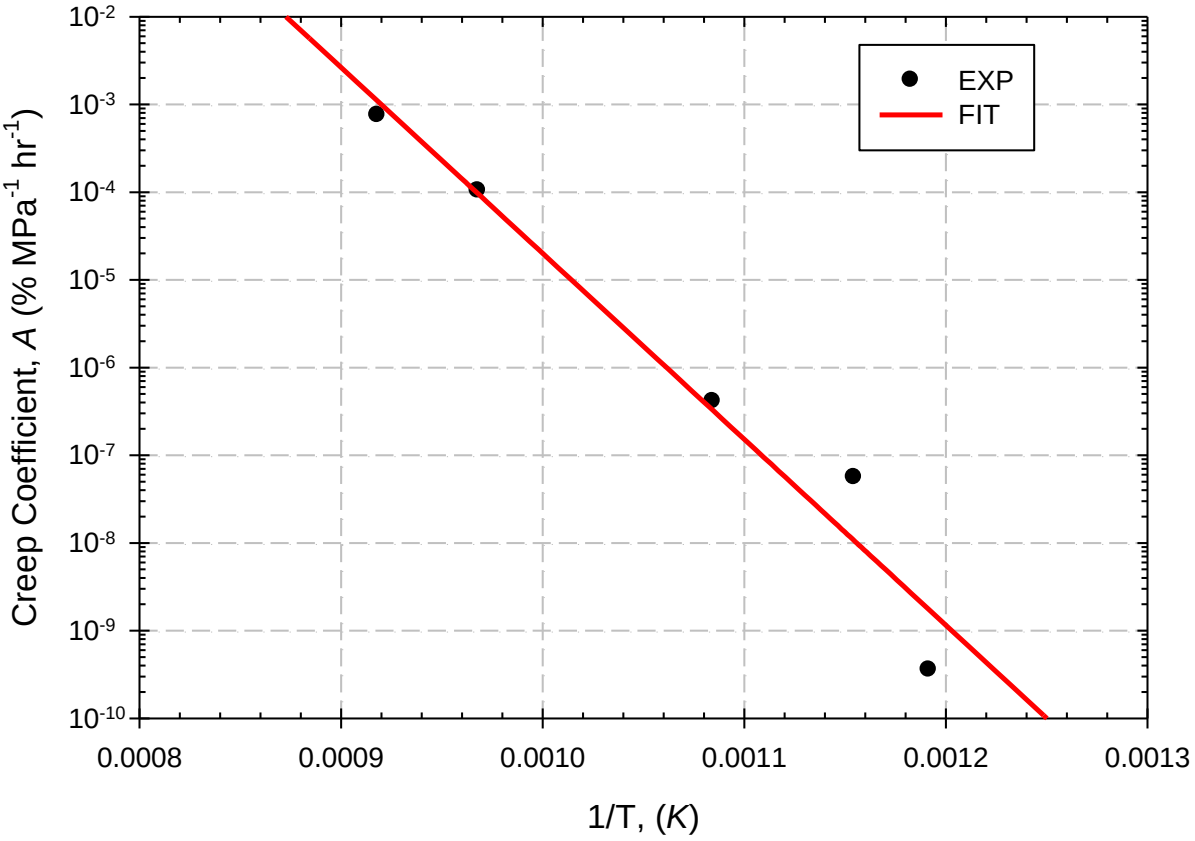

Figure 4.3 – Plot of *A* versus 1/*K*

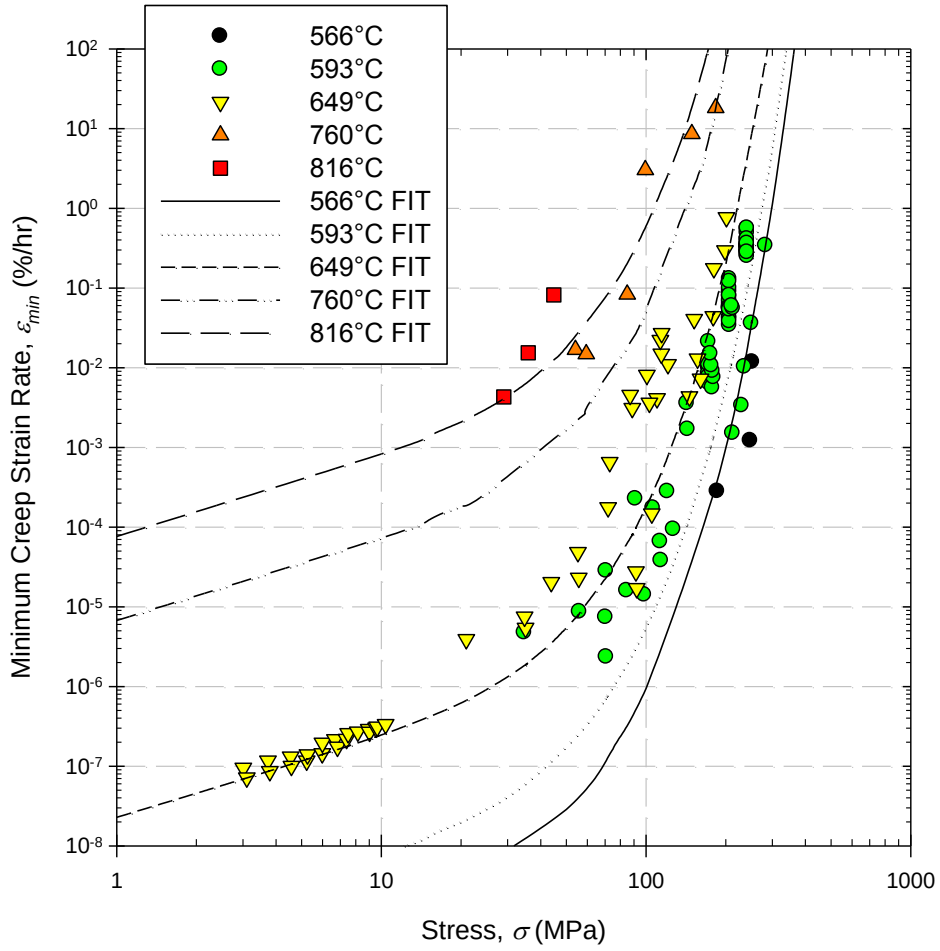

Figure 4.4 – The viscous function fitted to minimum creep strain rate data [129-136]

Using [Eq. (4.13)], the minimum creep strain rate versus stress data is plotted in Figure 4.4 . Examining the figure, it is observed that the modified viscous function successfully fits the experimental data. For non-isothermal conditions, this equation would successful model the creep behavior. In the current study, all tests are conducted under isothermal conditions and at a single set temperature. The modified viscous function will not be used in this study; however, it was important to demonstrate the ability to deal with temperature-dependence.

4.2.2 Primary Viscous Function

With knowledge of a suitable secondary viscous function, a suitable primary viscous function must now be determined. Time-, strain-, and mixed/work-hardening viscous functions have been developed to model the primary creep regime. Preference has been given to time-hardening based laws because the simplicity of numerical implementation [48,161,162,164,165]. These laws typically take the following form

$$\varepsilon_{pr} = \varepsilon_{pr,\max}(\sigma) H(t) \tag{4.14}$$

where the maximum primary creep strain, $\varepsilon_{pr,\max}$, is a function of stress, and the hardening variable, *H*, a function of time. Investigations by Phaniraj and colleagues have shown that for 304 stainless steel the primary creep strain can be correlated to the minimum creep strain rate as follows

$$\varepsilon_{pr} = K\dot{\varepsilon}_{\min} t_0 \tag{4.15}$$

where *K* is a constant and t_0 is the time at which the minimum creep strain rate, $\dot{\varepsilon}_{\min}$, is reached [166]. This suggests that the maximum primary creep strain, $\varepsilon_{pr,\max}$ will take a similar form to the secondary viscous function as

$$\varepsilon_{pr,\max} = K \cdot A\sinh\left(\sigma/\sigma_s\right) \tag{4.16}$$

where *K* is a enhancement coefficient that incorporates t_0.

The hardening variable $H(t)$ can take various forms as depicted in Table 2.1. The McVetty time-hardening variable, a decaying exponential, confirmed by various authors

[34,166-168], has been shown to successful model the high temperature primary creep behavior of steels

$$H(t) = 1 - \exp(-qt) \tag{4.17}$$

where q (t^{-1}) is the primary creep exhaustion rate. This time-hardening function is a simplification of dislocation immobilization based micromechanical models where q is the rate of dislocation immobilization [169]. Bring together [(4.16)] and [(4.17)] into [(4.14)] produces the following

$$\begin{aligned} \varepsilon_{pr} &= K \cdot A\sinh(\sigma/\sigma_s)\left[1 - \exp(-qt)\right] \\ \varepsilon_{pr} &= K \cdot A\sinh(\sigma/\sigma_s) - K \cdot A\sinh(\sigma/\sigma_s)\exp(-qt) \end{aligned} \tag{4.18}$$

where the expanded form shows two deformations of Voigt and Maxell elements respectively [16]. Differentiation furnishes the primary creep strain rate as

$$\dot{\varepsilon}_{pr} = qK \cdot A\sinh(\sigma/\sigma_s)\exp(-qt) \tag{4.19}$$

Work by Stewart and Gordon has shown that to obtain the optimal fit of primary creep data requires three unique material constants [170]. This can be attributed to the active deformation mechanism. When the deformation mechanism transitions from diffusion to power-law creep, the relationship between the maximum creep strain, $\varepsilon_{pr,\max}$, and minimum creep strain rate, $\dot{\varepsilon}_{\min}$ depict in [(4.15)] will change. To account for this changes coefficient, B and stress, σ_p must be introduced. The incorporate of this parameters and simplification produces the following primary viscous function

$$\varepsilon_{pr} = \frac{B}{q}\sinh(\sigma/\sigma_p)\left[1 - \exp(-qt)\right] \tag{4.20}$$

$$\dot{\varepsilon}_{pr} = B\sinh\left(\sigma/\sigma_p\right)\exp\left(-qt\right)$$

where B (t^{-1}) is the primary creep coefficient, σ_p (MPa) is the primary creep mechanism-transition stress, and q (t^{-1}) is the primary creep exhaustion rate.

Combining the primary and secondary viscous functions produces the following

$$\begin{aligned}\dot{\varepsilon}_{cr} &= \dot{\varepsilon}_{pr} + \dot{\varepsilon}_{sc} \\ \dot{\varepsilon}_{cr} &= B\sinh\left(\sigma/\sigma_p\right)\exp\left(-qt\right) + A\sinh\left(\sigma/\sigma_s\right)\end{aligned} \tag{4.21}$$

where $\dot{\varepsilon}_{cr}$ is the total creep strain. Implementation of this model is straightforward. Finite difference furnishes the creep strain rate. The minimum creep strain rate is regression fit to the secondary viscous function. Subtracting the secondary creep rate from the total creep rate produces the primary creep rate. This data is fit to the primary viscous function through regression. Averaged creep curves of 304 stainless steel at 600°C are used to evaluate the capabilities of the primary viscous function, original depicted in Figure 3.5 [129]. The results of fitting are provided in Figure 4.5. The material constants are provided in Table 4.1. The proposed model produces a high quality fit to the experiment data with minimal residual sum of squares. A similar temperature-dependence is observed in primary creep data to that observed in secondary creep data. The suggested Arrhenius function, [Eq. (4.10)] can also be used to model the temperature dependence of primary creep data where $A(T)$ and A_0 are replaced with $B(T)$ and B_0 respectively.

Table 4.1 – Primary and Secondary Creep Constants for 304 Stainless Steel at 600°C

Material Constant	Units	Value
A	$\%\ hr^{-1}$	5.270E-07
σ_s	MPa	27.823
B	$\%\ hr^{-1}$	2.835E-04
σ_p	MPa	37.447
q	hr^{-1}	0.415

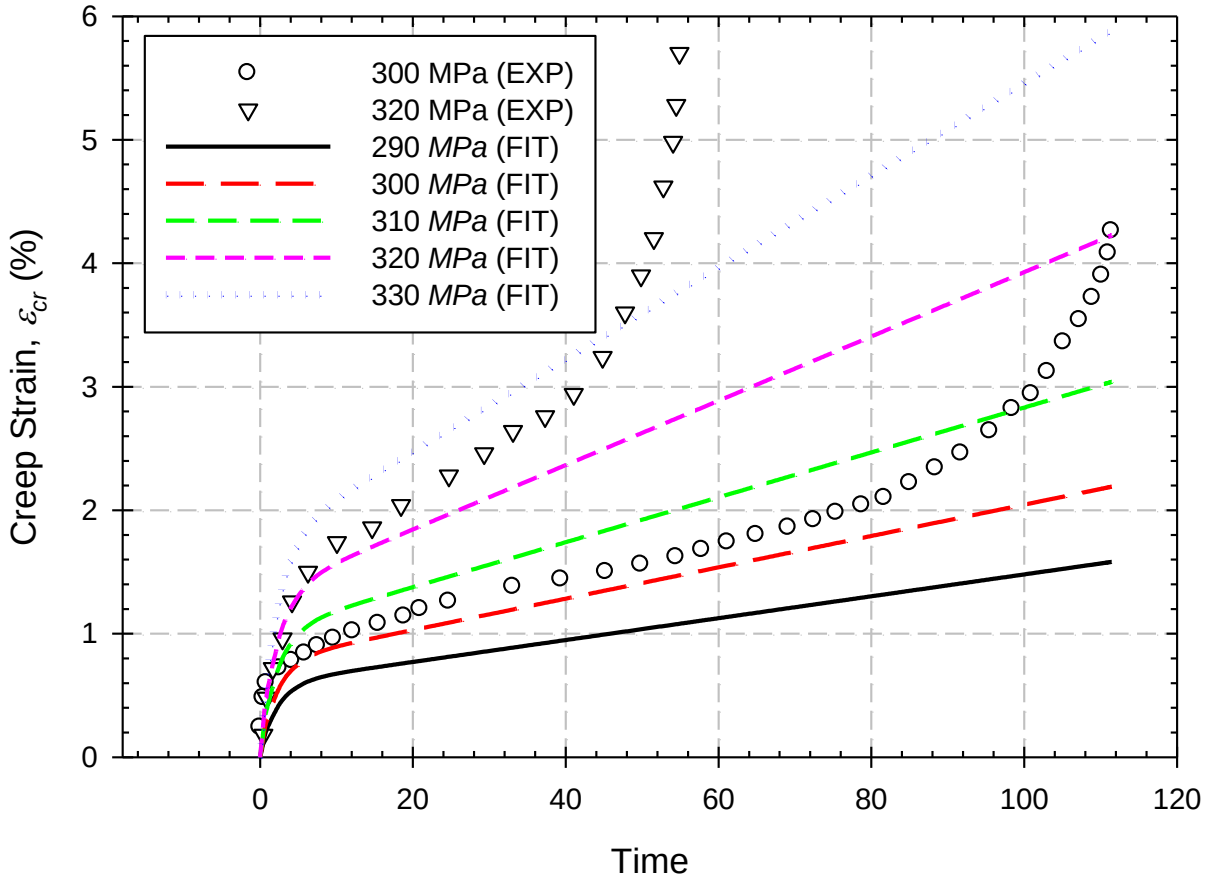

Figure 4.5 – Fit of Proposed Model to Creep Deformation [129]

4.2.3 Damage Evolution and Microstructural Degradation

The purpose of the damage evolution equation is three-fold:

- To model the tertiary creep regime
- To track the evolution of creep driven defects (cavities, microcracks, etc.)
- To predict rupture

To achieve these goals, the damage variable, ω, must be coupled to the secondary viscous function as follows

$$\dot{\varepsilon}_{sc} = f(\sigma)\cdot g(T)\cdot h(\omega) \tag{4.22}$$

where $f(\sigma)$ and $g(T)$ are [Eq. (4.9)] and [Eq. (4.10)] respectively. The $h(\omega)$ function describes how damage influences the strain rate. The classic continuum damage mechanics (CDM) approach was developed by Kachanov and Rabotnov [36-37]. It evolved from the assumption that damage is driven by a net-area-reduction from microcracks, cavities, voids, etc. This reduction in area furnishes a net/effective stress described as follows

$$\tilde{\sigma} = \sigma\frac{A_0}{A_{net}} = \frac{\sigma}{\left(1-\frac{A_0 - A_{net}}{A_0}\right)} = \frac{\sigma}{(1-\omega)} \tag{4.23}$$

where A_{net} is the current area, A_0 is the initial area, σ is equivalent stress, $\tilde{\sigma}$ is the net/effective stress, and ω is damage. From this net/effective stress, Kachanov and Rabotnov (K-R) proposed the following coupled creep-damage equations

$$\dot{\varepsilon}_{sc} = A\left(\frac{\sigma}{1-\omega}\right)^n \tag{4.24}$$

$$\dot{\omega} = \frac{M\sigma^{\chi}}{(1-\omega)^{\phi}}, \qquad 0 \le \omega < 1 \tag{4.25}$$

where A and n are the secondary creep constants of Norton's power law for secondary creep [32], σ is von Mises stress, and M, χ, and ϕ are tertiary creep damage constants. When damage is equal to unity the material has reached fracture. Variations of this formulation have been used to model the creep response of numerous materials [117, 170-174].

There are several limitations when using the classic K-R model for the prediction of creep cracking:

- Critical damage is a function of stress and temperature necessitating a cumulative damage law to account for variable amplitude loading and stress gradients. The details of this problem have been detailed elsewhere by the author [117].
- The structure of the formulation leads to a localization of the damage field and the mesh-dependence of damage evolution rate and cracking.

The describe the problem, integration of the K-R damage rate [Eq. (4.25)] produces

$$\begin{gathered} (1-\omega)^{\phi}\, d\omega = M\sigma^{\chi} dt \\ -\frac{(1-\omega)^{\phi+1}}{1+\phi}\Bigg|_{\omega_o}^{\omega} = M\sigma^{\chi}\Big|_{t_o}^{t} \end{gathered} \tag{4.26}$$

where stress and temperature are constant. Assuming initial time, t_o and initial damage, ω_o equals zero, and solving for damage, ω, produces

$$\omega(t) = 1 - \left[1 - (\phi+1) M\sigma^{\chi} t\right]^{\frac{1}{\phi+1}} \tag{4.27}$$

where $\omega(t)$ is damage as a function of time. Taking a variation of $\omega(t)$ with an infinitesimal variation of stress $\partial\sigma(t)$ produces

$$\partial\omega(t) = \chi \frac{M\sigma(t)^{\chi} t}{\left[1-(\phi+1)M\sigma(t)^{\chi} t\right]^{\frac{\phi}{\phi+1}}} \frac{\partial\sigma(t)}{\sigma(t)} \tag{4.28}$$

Replacing the portion, $M\sigma(t)^{\chi} t$, by rearranging [Eq. (2.20)] and introducing into the above gives

$$\partial\omega(t) = \chi \frac{1-(1-\omega)^{\phi+1}}{(1-\omega)^{\phi}} \frac{\partial\sigma(t)}{\sigma(t)} \tag{4.29}$$

When damage is critical (near unity), the damage variation $\partial\omega(t)$ is near infinite due to an infinitesimal variation of stress $\partial\sigma(t)$. Damage can never equal unity (due to divide by zero). This damage evolution equation is highly sensitive to the stress field. The stress sensitivity leads to a localization of the damage field. Changes in mesh size will lead to small changes in the stress field that produce enormous changes in the damage field. This is the primary contributing factor to the mesh-dependence of the classic CDM approach. The classic approach attempts to model the near instantaneous plasticity of fracture at the end of life resulting in astronomical damage rates. This process is better described as a step function loss of stiffness rather than a near infinite damage rate at rupture.

To overcome this issue, a damage evolution equation which exhibits a finite variation of damage $\partial\omega(t)$ under an infinitesimal variation of stress $\partial\sigma(t)$ must be developed. Liu and Murakami demonstrated that damage evolution is better represented as an exponential growth function [115]. In the current study, the following damage evolution equation is proposed

$$\dot{\omega} = \frac{M\left[1-\exp(-\phi)\right]}{\phi}\sinh\left(\frac{\sigma}{\sigma_t}\right)^{\chi}\exp(\phi\omega) \tag{4.30}$$

where M, ϕ, χ, and σ_t are material constants which must be greater than zero. The portion $(1-e^{-\phi})/\phi$ is necessary to avoid an undefined error when damage evolution is integrated. Integration of damage evolution produces

$$\begin{gathered}\frac{1}{\exp(\phi\omega)}d\omega = \frac{M\left[1-\exp(-\phi)\right]}{\phi}\sinh\left(\frac{\sigma}{\sigma_t}\right)^{\chi}dt \\ -\frac{\exp(-\phi\omega)}{\phi}\Bigg|_{\omega_o}^{\omega} = \frac{M\left[1-\exp(-\phi)\right]}{\phi}\sinh\left(\frac{\sigma}{\sigma_t}\right)^{\chi}t\Bigg|_{t_o}^{t}\end{gathered} \tag{4.31}$$

where stress and temperature are constant. Assuming initial time, t_o and initial damage, ω_o equals zero, and solving for damage, ω, gives

$$\begin{gathered}\omega(t) = -\frac{1}{\phi}\ln\left[1-\left[1-\exp(-\phi)\right]M\sinh\left(\frac{\sigma}{\sigma_t}\right)^{\chi}t\right]; \\ \omega(t) = -\frac{1}{\phi}\ln\left[1-\left[1-\exp(-\phi)\right]\frac{t}{t_r}\right]; \qquad t_r = \left[M\sinh\left(\frac{\sigma}{\sigma_t}\right)^{\chi}\right]^{-1}\end{gathered} \tag{4.32}$$

The M, ϕ, and χ material constants can be determined by from stress-rupture data. Taking a variation of $\omega(t)$ with an infinitesimal variation of stress $\partial\sigma(t)$ produces

$$\partial\omega(t) = -\frac{\left[\exp(\phi)-1\right]M\sinh\left(\frac{\sigma}{\sigma_t}\right)^{\chi}t}{\phi\left[-\exp(-\phi)+\left[\exp(\phi)-1\right]M\sinh\left(\frac{\sigma}{\sigma_t}\right)^{\chi}t\right]}\frac{\partial\sigma(t)}{\sigma_t}, \tag{4.33}$$

Replacing the portion, $M\sinh\left(\sigma/\sigma_t\right)^{\chi}$, by rearranging [Eq. (4.32)] and introducing into the above gives

$$\partial\omega(t)=\frac{\left(e^{-\phi\omega}-1\right)\left(e^{\phi}-1\right)}{\phi\left(e^{-\phi}-1\right)\left[e^{\phi}-\frac{\left(e^{-\phi\omega}-1\right)\left(e^{\phi}-1\right)}{\left(e^{-\phi}-1\right)}\right]}\frac{\partial\sigma(t)}{\sigma_t} \tag{4.34}$$

where after simplification becomes

$$\partial\omega(t)=\frac{\left[\exp(\phi\omega)-1\right]}{\phi}\frac{\partial\sigma(t)}{\sigma_t} \tag{4.35}$$

Examining the above equation, damage can equal unity. When damage is equal to unity, the damage variation $\partial\omega(t)$ is finite due to an infinitesimal variation of stress $\partial\sigma(t)$. The parameter ϕ controls stress sensitivity. Increasing the value of ϕ increases the damage variation and thus stress sensitivity. The constant ϕ is hereafter called the damage trajectory constant. A comparison of the K-R model [Eq. (4.27)] and the proposed [Eq. (4.32)] damage equations are presented in Figure 4.6. The subscripts 1, 2, and 3 indicate the value of damage trajectory constant ϕ. The K-R equation produces a steep damage evolution that is near infinite at rupture. The (new) proposed equation produces a less steep damage evolution (only slightly non-linear) that is finite at rupture.

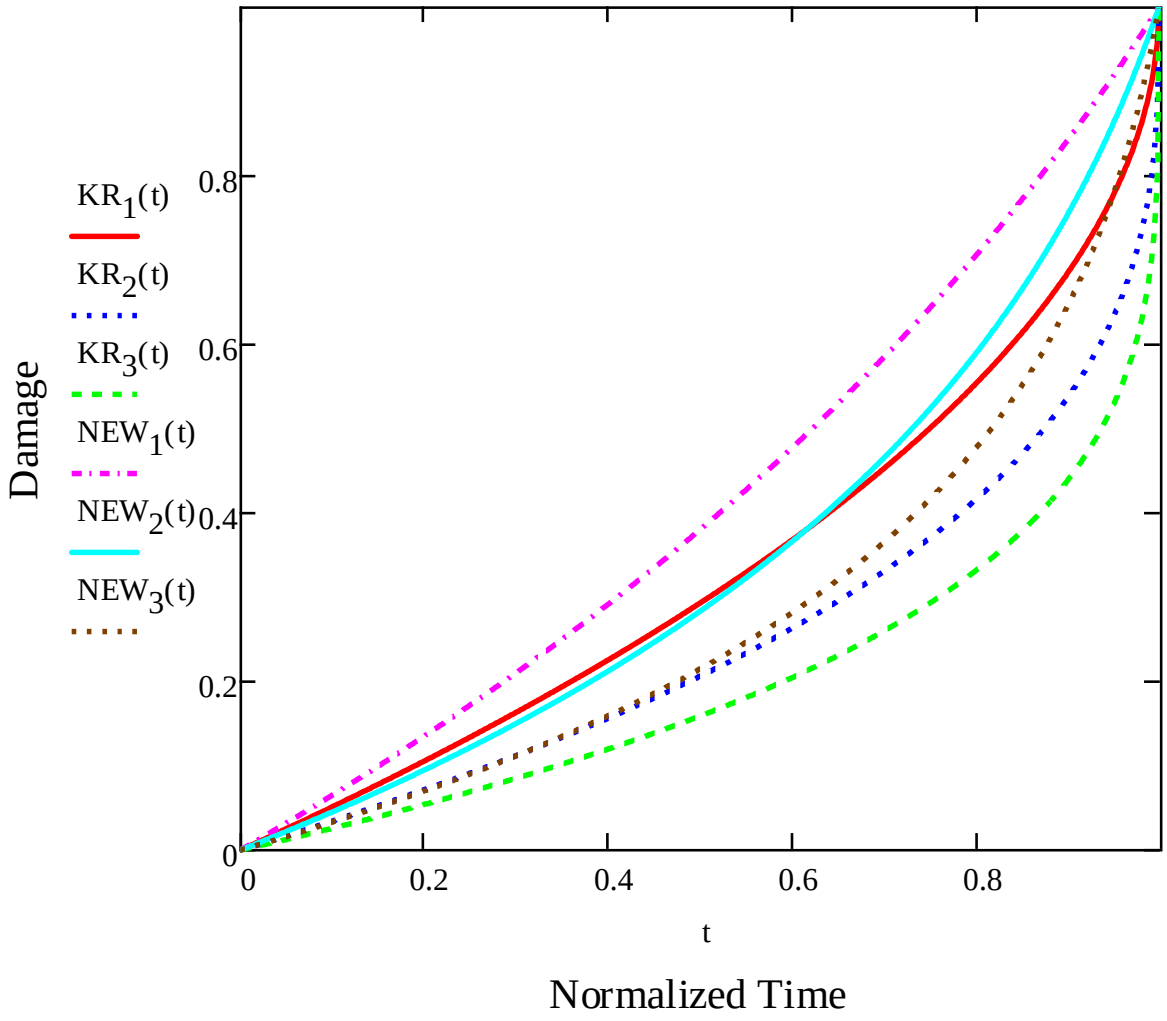

Figure 4.6 - Comparison of the K-R and proposed damage evolution equations

For the proposed damage evolution equation [Eq. (4.32)], the damage trajectory constant ϕ can be determined by fitting the damage equation to normalized mechanical, crack, physical, and/or microstructural damage quantities. Theory suggests that creep damage arises primarily due to internal-grain and grain-boundary cavitation. Liu and Murakami have shown that the use of cavity-based microstructural damage quantities can be advantageous [115]. Parameters such

as the cavity area density, ρ (number of cavities within a set area) and the A_p-Parameter (number of cavitated grain-boundaries) can be correlated to the CDM damage variable, ω, in a number of ways [175]. The simplest form follows

$$\omega = \frac{A_p}{A_{p,cr}} = \frac{\rho}{\rho_{cr}} \tag{4.36}$$

where $A_{p,cr}$ and ρ_{cr} are the critical A_p-Parameter and cavity area density respectively. For complex versions for the A_p-Parameter have been develop

$$\begin{aligned} \omega &= \left(\frac{A_p}{A_{p,cr}} \right)^2 \\ \omega\left[1-(1-\omega)^L\right] &= \left(\frac{A_p}{A_{p,cr}} \right)^2 \end{aligned} \tag{4.37}$$

where *L* is a material constant. The relationship between the CDM damage variable and the A_p-Parameter is dependent on the structure of the damage evolution equation such that the equation is better described as an unknown function

$$\omega = f\left(\frac{A_p}{A_{p,cr}} \right) \tag{4.38}$$

It should be noted that both $A_{p,cr}$ and ρ_{cr} are measured on the plane perpendicular to the applied load vector. The proper methods to measure the quantities have been established [175-177].

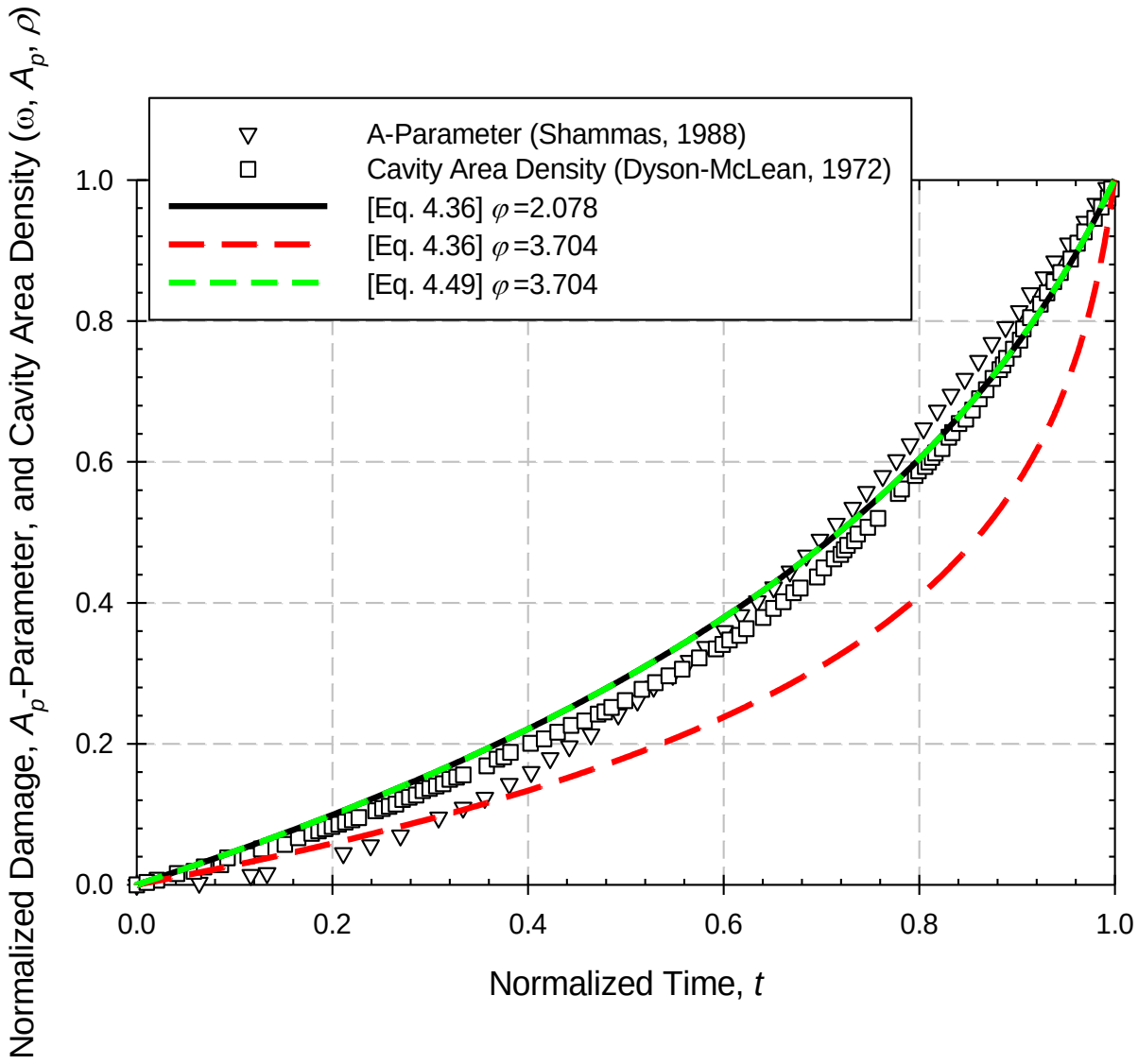

Figure 4.7 - Comparison of microstructural quantities to the CDM damage [178,179]

For the subject material 304 stainless steel, A_p and ρ data is not available; therefore, the microstructural quantities from Nimonic 80A and 1Cr-1/2Mo HAZ are used to give an estimate of the damage trajectory ϕ constant [178,179]. Assuming the simplest relationship $\omega = A_p / A_{p,cr} = \rho / \rho_{cr}$ [Eq. (4.36)], regression analysis is used to fit the damage variable, ω [Eq.

(4.32)] to the $A_{p,cr}$ and ρ_{cr} quantities (plotted in Figure 4.7). The best fit value of the damage trajectory constant ϕ is 2.078. To determine the true relationship between damage and the microstructural quantities [Eq. (4.38)] the damage trajectory constant ϕ must be determined from creep deformation data.

To that end, mathematical manipulation of the creep deformation data follows. As depicted in [Eq. (4.22)] some unknown function $h(\omega)$ describes how damage influences the strain rate. The total creep strain rate, [Eq. (4.21)] then becomes

$$\begin{aligned} \dot{\varepsilon}_{cr} &= \dot{\varepsilon}_{pr} + \dot{\varepsilon}_{sc} \\ \dot{\varepsilon}_{cr} &= B\sinh\left(\sigma/\sigma_p\right)\exp\left(-qt\right) + A\sinh\left(\sigma/\sigma_s\right)h(\omega) \end{aligned} \tag{4.39}$$

where solving for $h(\omega)$ produces

$$\begin{aligned} \dot{\varepsilon}_{cr} &= \dot{\varepsilon}_{pr} + \dot{\varepsilon}_{sc} \\ h\left[\omega(t)\right] &= \frac{\dot{\varepsilon}_{cr}(t) - B\sinh\left(\sigma/\sigma_p\right)\exp\left(-qt\right)}{A\sinh\left(\sigma/\sigma_s\right)} \end{aligned} \tag{4.40}$$

Using experimental data the A, σ_s, B, σ_p, and q material constants can be determined as discussed in sections 4.2.1and 4.2.2. In most constitutive models the relationship that damage has within the creep strain rate and damage evolution equations are similar. In the current study that would suggest the $h(\omega)$ function takes an exponential form.

A number of micromechanics-based constitutive models with an exponential-function of damage have been developed to model the tertiary creep regime [115,180,181]. Riedel [181] suggested that the creep strain rate relates to some microcrack damage parameter, ρ_c, as follows

$$h(\omega) = \exp(\rho_c) \tag{4.41}$$

work by Hutchinson [180] describes ρ_c as

$$\rho_c = \frac{n+1}{2\sqrt{1+3/n}} Nd^3 \tag{4.42}$$

where n is a material constant, d is average diameter of the microcracks and N is the number of microcracks per unit volume. Liu and Murakami [115] found that using the geometry of a cavitated cylindrical grain the relationship between the microcracking damage parameter, ρ_c and the CDM damage, ω is

$$\rho_c = \frac{2(n+1)}{\pi\sqrt{1+3/n}} \omega^{3/2} \tag{4.43}$$

The problem with most micromechanics-based creep models are the assumptions made about the shape, location, and nucleation rate of flaws (microcracks, cavities, voids, etc.). These assumptions limit the ability to accurately model the tertiary creep regime.

As an alternative, the function is assumed to have the following structure

$$h(\omega) = \exp(\lambda \omega^p) \tag{4.44}$$

where λ and p are unitless material constants. Introducing this into [Eq. (4.40)] and solving for damage produces the following

$$\omega^*(t) = \left\{ \frac{1}{\lambda} \ln \left[\frac{\dot{\varepsilon}_{cr}(t) - B\sinh\left(\sigma/\sigma_p\right)\exp\left(-qt\right)}{A\sinh\left(\sigma/\sigma_s\right)} \right] \right\}^{1/p} \tag{4.45}$$

where $\omega^*(t)$ is the analytical damage derived from the creep strain rate, $\dot{\varepsilon}_{cr}(t)$. Considering the time just before fracture $t \simeq t_r$, where $\dot{\varepsilon}_{pr} = 0$, the creep strain rate [Eq. (4.39)] becomes

$$\dot{\varepsilon}_{cr} = \dot{\varepsilon}_{final} \approx A\sinh\left(\sigma/\sigma_s\right)\exp(\lambda)$$
$$\lambda = \ln\left(\frac{\dot{\varepsilon}_{final}}{\dot{\varepsilon}_{\min}}\right); \qquad \dot{\varepsilon}_{\min} = A\sinh\left(\sigma/\sigma_s\right) \tag{4.46}$$

Clearly, the constant λ can be described as the natural logarithm of the creep strain rate ratio (final over minimum). The *p* and ϕ constants can be numerically found by equating damage [Eq. (4.32)] to the damage derived from creep strain rate data [Eq. (4.45)]

$$\omega(t) = \omega^*(t) \tag{4.47}$$

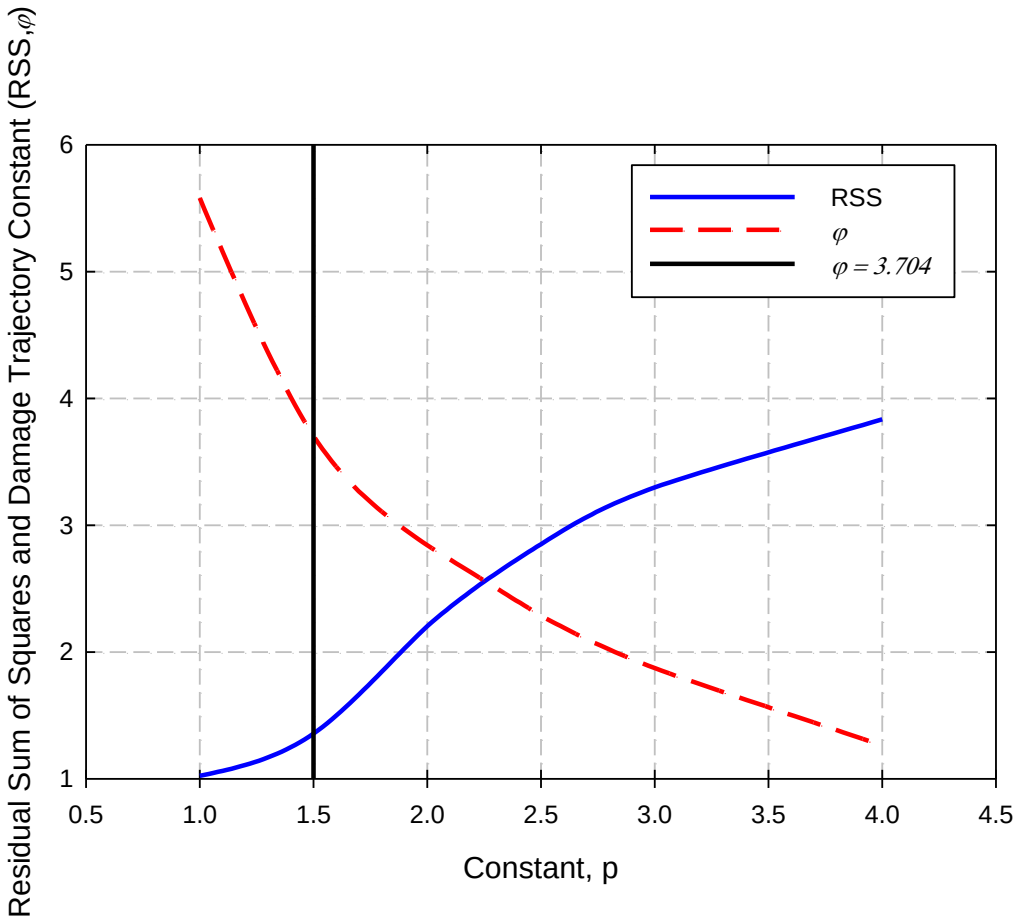

Figure 4.8 - Parametric study to determine *p* and ϕ constants.

A study was conducted where the constant p was increase at increments of 0.5 and regression analysis performed to find ϕ based on the creep deformation residual sum of squares (RSS) for averaged creep curves of 304 stainless steel at 600°C depicted in Figure 4.5 [129]. The results are provided in Figure 4.8. The optimal fit of both creep deformation and damage evolution was obtained when p equaled to 1.5, with ϕ found to be 3.704. This suggests that the $h(\omega)$ function should take a similar structure that obtained by Liu and Murakami [115]. (It should be noted that with p <1.5 the creep deformation produced less error but the fit to damage evolution become more conservative and stress sensitive). The $h(\omega)$ function becomes

$$h(\omega) = \exp(\lambda\omega^{3/2}) \tag{4.48}$$

Return to the relationship between the microstructural damage quantities and the CDM damage variable. It is found, assuming $\omega = A_p / A_{p,cr} = \rho/\rho_{cr}$, that ϕ equal to 3.704 does not accurately predict the microstructural damage quantities as depicted in Figure 4.7. Using evolutionary computation [182], the function relationship of microstructural damage to the CDM damage variable is found to be

$$\frac{A_p}{A_{p,cr}} = \frac{\rho}{\rho_{cr}} = \sin(\frac{3}{2}\omega) \tag{4.49}$$

This produces a perfect fit to the microstructural damage quantities as depicted in Figure 4.7.

Finally, the multistage coupled-creep damage constitutive model is complete as follows

$$\begin{aligned} \dot{\varepsilon}_{cr} &= \dot{\varepsilon}_{pr} + \dot{\varepsilon}_{sc} \\ \dot{\varepsilon}_{cr} &= B\sinh\left(\sigma/\sigma_p\right)\exp\left(-qt\right) + A\sinh\left(\sigma/\sigma_s\right)\exp\left(\lambda\omega^{3/2}\right) \end{aligned} \tag{4.50}$$

$$\dot{\omega} = \frac{M\left[1-\exp(-\phi)\right]}{\phi}\sinh\left(\frac{\sigma}{\sigma_t}\right)^{\chi}\exp(\phi\omega)$$

$$\frac{A_p}{A_{p,cr}} = \frac{\rho}{\rho_{cr}} = \sin(\frac{3}{2}\omega)$$

The averaged creep curves of 304 stainless steel at 600°C are used to evaluate the damage evolution law, Figure 4.5 [129]. The primary and secondary creep constants *A*, *B*, *q*, σ_s, and σ_p are listed in Table 4.1. Using regression analysis the damage constants, λ, ϕ, *M*, χ, and σ_t are found as listed in Table 4.2. The creep deformation and damage evolution are plotted in Figure 4.9. The proposed model produces an extremely accurate prediction of the creep deformation. The damage is fitted to the damage derived from creep strain rate data [Eq. (4.45)] and as a result is fuzzy. The anomalous damage at $t_n < 0.5$ can be attributed to the sensitivity of the derived damage to the primary creep strain rate. At times $t_n > 0.5$ the damage predicted is accurate.

Table 4.2 – Tertiary Creep Constants for 304 Stainless Steel at 600°C

Material Constant	Units	Value
λ	none	3.586
ϕ	none	3.704
M	hr^{-1}	1.898E-06
χ	none	3.09
σ_t	*MPa*	87.4

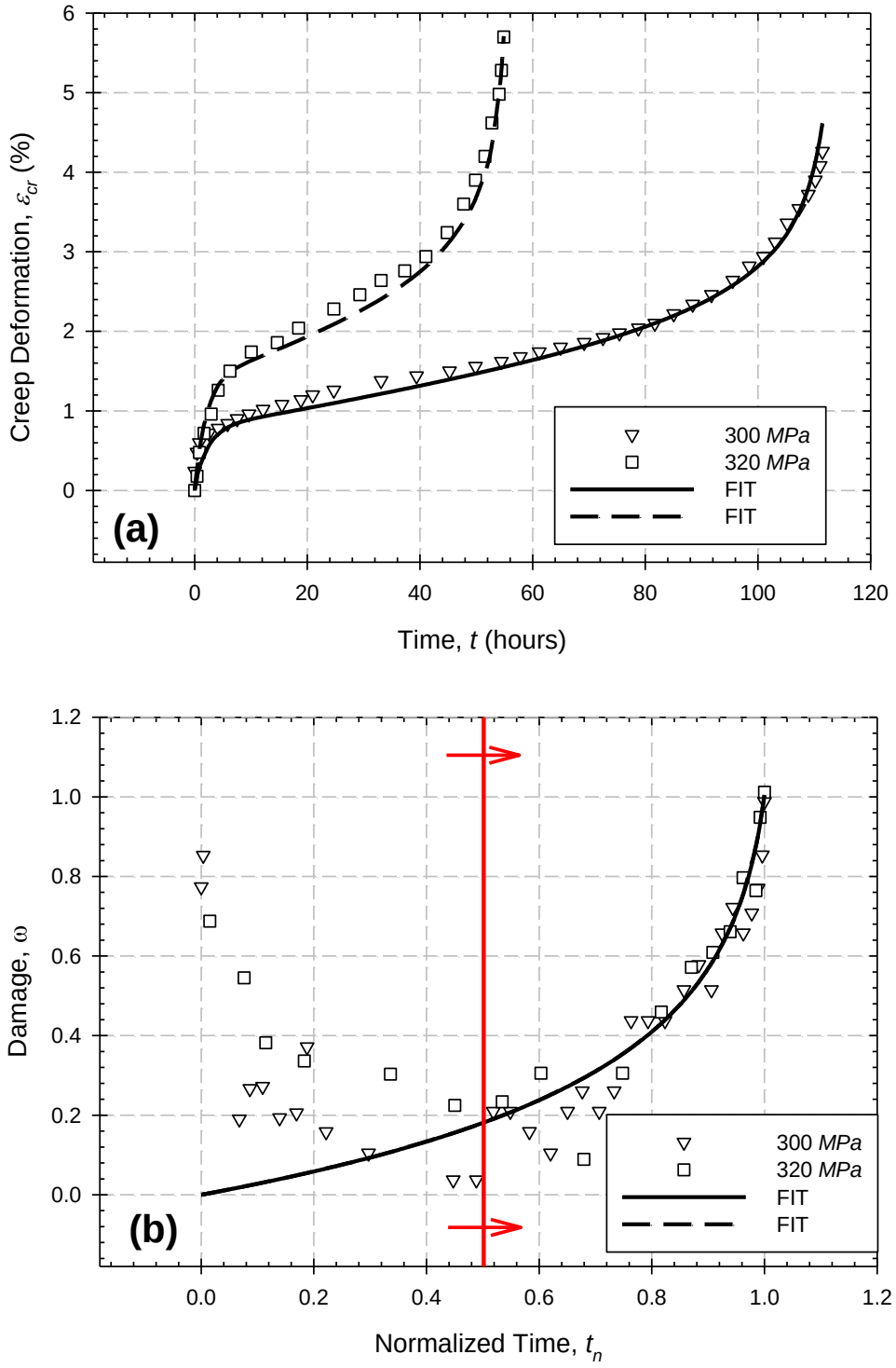

Figure 4.9 –Proposed Model Fit (a) Creep Deformation and (b) Damage Evolution at 600°C

4.2.4 Notch Strengthening

As discussed in section 3.3.1, a multiaxial state of stress (often called a triaxial stress field) greatly influences the creep-rupture of most metals. Alloys subject to creep often exhibit a notch strengthening effect. The underlying mechanism that causes this behavior is anisotropic cavity damage. For most metals, cavitation can be indentified in two material classes, aluminum-like and copper-like [40,183]. For aluminum-like materials, cavity damage is mostly distributed isotropically (Figure 4.10a). For copper-like materials, cavity damage is mostly observed on the plane perpendicular to the first principal stress direction (Figure 4.10b). Anisotropic cavity damage can be incorporated into most isotropic constitutive models by some stress- or strain-based modification of the equations.

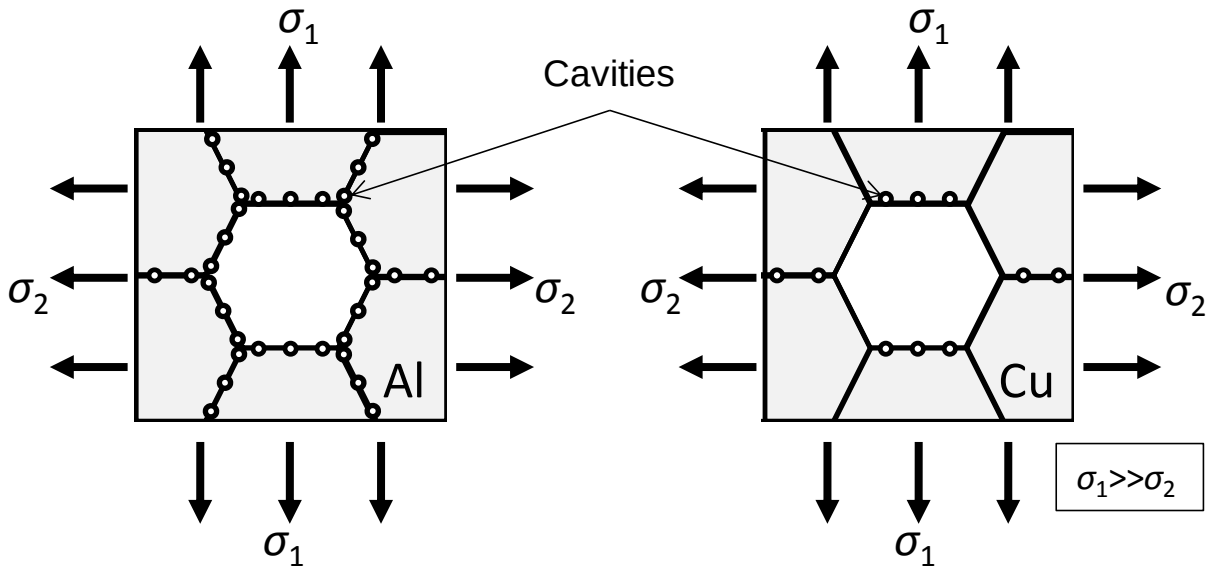

Figure 4.10 - Schematic of cavity growth on grain boundaries for (a) Aluminum and (b) Copper

Yao and colleagues have produced an exhaustive review of multiaxial equations [184]. Historically two approaches to dealing with anisotropic cavity growth have been proposed: multiaxial creep ductility, ε_f^* and representative stress, σ_{rep} approaches.

The multiaxial creep ductility approach involves predicting a multiaxial ductility based on some function of stress and uniaxial ductility. Ductility is the failure strain at rupture. A number of models have been proposed that correlate cavity growth and imposed stress and strain [185-190]. An early and popular model is the Rice and Tracey [186] void growth model based on an isolated spherical void in remote-uniformed stress and strain rate field. The model follows

$$\frac{\varepsilon_f^*}{\varepsilon_f} = \frac{0.521}{\sinh\left(\frac{3\sigma_m}{2\sigma_e}\right)} \tag{4.51}$$

where ε_f^* is the multiaxial ductility and ε_f is the uniaxial ductility. Cocks and Ashby [187] proposed a model based on the constrained cavity growth mechanism which has been used in various design codes (British R5, ASME III, French RCC-MR, etc.) as follows

$$\frac{\varepsilon_f^*}{\varepsilon_f} = \sinh\left[\frac{2}{3}\left(\frac{n-1/2}{n+1/2}\right)\right] \Big/ \sinh\left[2\left(\frac{n-1/2}{n+1/2}\right)\frac{\sigma_m}{\sigma_e}\right] \tag{4.52}$$

where *n* is a material constant. The limitation of the multiaxial creep ductility approach is that there is no direct modification of the constitutive equations; therefore, the deformation and damage fields produced will not represent the evolution of defects under multiaxial conditions. The multiaxial creep ductility approach will only predict the appropriate rupture strain and time.

An alternative is the representative stress, σ_{rep} approach. Sdobyrev [191] proposed the following representative stress

$$\sigma_{rep} = \alpha\sigma_1 + (1-\alpha)\sigma_{vm} \tag{4.53}$$

where σ_1 and σ_{vm} are the first principal and von Mises stress and α is a constant. The value of α for various metals have been established including: stainless steel $\alpha \approx 0.75$, aluminum alloys $\alpha \approx 0$, commercially pure copper $\alpha \approx 0.848$, extruded copper bar $\alpha \approx 0.70$, Ni-base alloy $\alpha \approx 0.15$, and titanium alloy $\alpha \approx 0$ [192,193,194]. The fastest way to determine α is to perform FEM simulations at various values of α, plot α vs. rupture time, and then select the value which matches rupture data [192]. Alternatively, α constant can be found using a skeletal stress approach [192,195]. The skeletal stress approach takes the following form

$$\frac{\sigma_{rep}}{\sigma_{net}} = \alpha\frac{\sigma_1^*}{\sigma_{net}} + (1-\alpha)\frac{\sigma_{vm}^*}{\sigma_{net}} \tag{4.54}$$

where $\sigma_{rep}/\sigma_{net}$ is the ratio of net stress in a uniaxial specimen to that in the necked area of a Bridgman specimen that gives equal rupture time [196,197]. The ratio $\sigma_{rep}/\sigma_{net}$ is found by plotting the rupture time versus net stress of the uniaxial specimen and Bridgman specimen. A curve fit of these lines will produce the ratio [192]. An excel solver can do this quickly. Kachanov produces an analytical theory to predict the stress which arises in a Bridgman specimen [197]. The ratios σ_1^*/σ_{net} and $\sigma_{vm}^*/\sigma_{net}$ represent the ratio of skeletal maximum principal and von Mises stress to the net stress within a Bridgman specimen. The skeletal stress is an invariant stress located some distance from the notch tip in the Bridgman specimen. It can be determined by running FEM simulations and plotting the stress ratio across the net section of the specimen (from notch tip to the center) [198]. At a point along this line a semi-stable value of stress will be observed. This is the location and quantity of the skeletal stress [199]. Hayhurst [200] proposed a more complex equation that includes the hydrostatic stress and two additional

constants; however, the additional complexity does not produce much improve over the original equation. Some authors have suggested the use of the principal facet stress (the average tensile stress on grain boundary facet perpendicular to the maximum principal stress); however, this term does not correlate well for materials where cavitation is not the dominant mechanism, such as aluminum [131].

The in the current study, the Sdobyrev representative stress [Eq. (4.53)] is selected. The stress is incorporated in the damage evolution equation as follows

$$\dot{\omega} = M \sinh\left(\frac{\sigma_{rep}}{\sigma_t}\right)^{\chi} \exp(\phi\omega)\frac{(1-e^{-\phi})}{\phi} \qquad (4.55)$$
$$\sigma_{rep} = \alpha\sigma_1 + (1-\alpha)\sigma_{vm}$$

where the value of α is assumed to be 0.75.

4.2.5 Mechanical Degradation

As damage occurs within a material it induces a measurable change in most physical quantities. In the case of the mechanical quantities Young's modulus and Poisson's ratio it is important to model this degradation such that the mechanical stresses are accurately predicted [40]. Two theories of mechanical degradation have been suggested: the hypotheses of strain and strain-energy equivalence. For clarity a schematic describing the virgin, damaged, and pseudo-undamaged state of a material is provided in Figure 4.11. The assumption of 1D and isotropic material is used.

As discussed earlier [Eq. (4.23)], the effective stress, $\tilde{\sigma}$ and effective strain, $\tilde{\varepsilon}$ can be derived from the net-area-reduction as follows

$$\tilde{\sigma} = \frac{\sigma}{1-\omega}, \quad \tilde{\varepsilon} = (1-\omega)\varepsilon \tag{4.56}$$

For the cases of the damaged state Hooke's law becomes

$$\sigma = \tilde{E}\varepsilon_e \tag{4.57}$$

where $\tilde{E}$ is the degraded Young's modulus. For the pseudo-undamaged state Hooke's law becomes

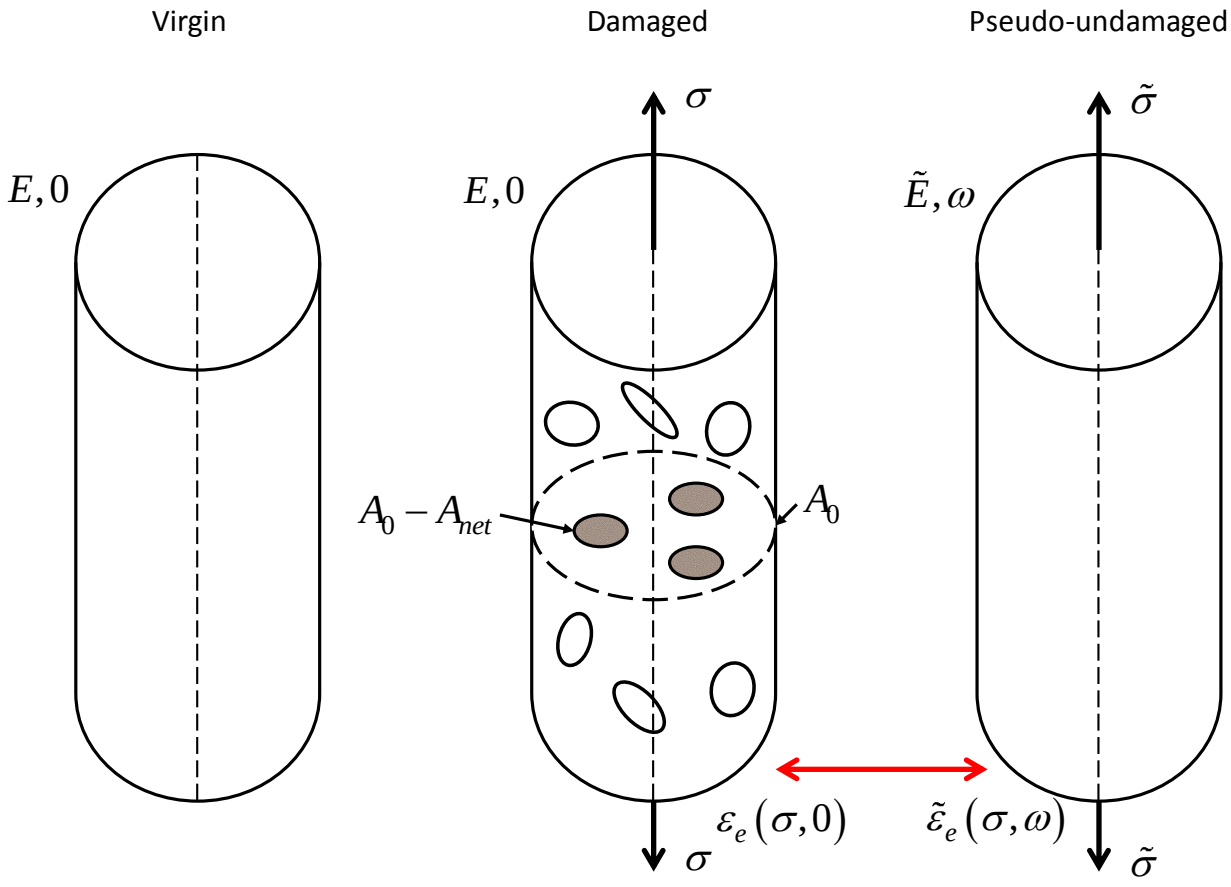

Figure 4.11 - 1D schematic of the effective stress concept

$$\tilde{\sigma} = E\tilde{\varepsilon}_e \tag{4.58}$$

where E is the initial Young's modulus.

In the hypothesis of strain equivalence it is assumed that the elastic strain observed in the damaged state is equated to that observed in the pseudo-undamaged state ($\varepsilon_e = \tilde{\varepsilon}_e$) [40]. Using the effective stress [Eq. (4.23)] we find the following

$$\frac{\sigma}{\tilde{E}} = \frac{\sigma}{(1-\omega)E} \tag{4.59}$$

where after rearranging for the damage variable and the degraded Young's modulus are

$$\omega = 1 - \left(\frac{\tilde{E}}{E}\right), \quad \tilde{E} = E(1-\omega) \tag{4.60}$$

It should be noted that this hypothesis assumes that the Poisson's ratio is not affected by damage. This is not true for most engineering materials, and thus limits the applicability of the strain equivalence approach.

As an alternatively, the hypothesis of strain-energy equivalence has been proposed, where the strain-energy of the damage state is equated to that of the pseudo-undamaged state [201]. Using both the effective stress and strain [Eq. (4.56)] the following is found

$$\frac{\sigma^2}{2\tilde{E}} = \frac{\sigma^2}{2E(1-\omega)^2} \tag{4.61}$$

where after rearranging for the damage variable and the degraded Young's modulus are

$$\omega = 1 - \left(\frac{\tilde{E}}{E}\right)^{1/2}, \quad \tilde{E} = E(1-\omega)^2 \tag{4.62}$$

With the 3D assumption the strain and strain-energy hypothesis become more complex. While the virgin material is initial isotropic, upon application of load microscopic defects (microcracks,

voids) form and are distributed anisotropically. Thus damage induces an anisotropic response in isotropic materials [14]. Murakami and Ohno [202] found that the scalar damage variable, ω, becomes a second-order symmetric damage tensor, $\mathbf{D}$,

$$\mathbf{D} = \begin{bmatrix} \omega_{11} & \omega_{12} & \omega_{13} \\ \omega_{21} & \omega_{22} & \omega_{23} \\ \omega_{31} & \omega_{32} & \omega_{33} \end{bmatrix} \quad \omega_{12} = \omega_{21}, \ \omega_{13} = \omega_{31}, \ \omega_{23} = \omega_{32} \tag{4.63}$$

Solve the Eigen problem to find D_i and n_i, the principal value and axes of damage

$$\mathbf{D} = \sum_{i=1}^{3} D_i n_i \otimes \tag{4.64}$$

The effective stress and strain vectors become

$$\tilde{\boldsymbol{\sigma}} = \mathbf{M}^{-1} : \boldsymbol{\sigma}, \quad \tilde{\boldsymbol{\varepsilon}}_e = \mathbf{M} : \boldsymbol{\varepsilon}_e \tag{4.65}$$

where $\boldsymbol{\sigma}$ is the Cauchy stress tensor, $\tilde{\boldsymbol{\sigma}}$ is the symmetric effective stress tensor, and $\mathbf{M}$ is a fourth-order integrity/damage effect tensor. This fourth-order integrity tensor $\mathbf{M}$ is a function of the second-order damage tensor $\mathbf{D}$ described various ways in literature [40,203]. Due to symmetry the fourth-order integrity tensor can be represented by a 6x6 matrix and thus through transformation the effectives stress is represented as follows

$$\begin{bmatrix} \tilde{\sigma}_{11} \\ \tilde{\sigma}_{22} \\ \tilde{\sigma}_{33} \\ \tilde{\sigma}_{12} \\ \tilde{\sigma}_{23} \\ \tilde{\sigma}_{13} \end{bmatrix} = \begin{bmatrix} M_{1111} & M_{1122} & M_{1133} & M_{1112} & M_{1123} & M_{1113} \\ M_{2211} & M_{2222} & M_{2233} & M_{2212} & M_{2223} & M_{2213} \\ M_{3311} & M_{3322} & M_{3333} & M_{3312} & M_{3323} & M_{3313} \\ M_{1211} & M_{1222} & M_{1233} & M_{1212} & M_{1223} & M_{1213} \\ M_{2311} & M_{2322} & M_{2333} & M_{2312} & M_{2323} & M_{2313} \\ M_{1311} & M_{1322} & M_{1333} & M_{1312} & M_{1323} & M_{1313} \end{bmatrix} \begin{bmatrix} \sigma_{11} \\ \sigma_{22} \\ \sigma_{33} \\ \sigma_{12} \\ \sigma_{23} \\ \sigma_{13} \end{bmatrix} \tag{4.66}$$

General linear elasticity can be described by the Hooke's law as

$$\begin{aligned} \sigma_{ij} &= C_{ijkl}\varepsilon_{kl} \\ \boldsymbol{\sigma} &= \mathbf{C}_{EL}\boldsymbol{\varepsilon}_e \end{aligned} \tag{4.67}$$

where σ_{ij} are the components of the Cauchy stress tensor $\boldsymbol{\sigma}$ (9 terms), ε_{kl} are the components of the Cauchy strain tensor $\boldsymbol{\varepsilon}$ (9 terms), and C_{ijkl} are components of the elastic stiffness tensor $\mathbf{C}_{EL}$ (81 terms) containing the mechanical properties of the material. An alternative approach has also been employed by rearranging Eq. (4.67) to

$$\begin{aligned} \varepsilon_{ij} &= S_{ijkl}\sigma_{kl} \\ \boldsymbol{\varepsilon}_e &= \mathbf{S}_{EL}\boldsymbol{\sigma} \\ \mathbf{C}_{EL} &= \left(\mathbf{S}_{EL}\right)^{-1} \end{aligned} \tag{4.68}$$

where S_{ijkl} are components of $\mathbf{S}_{EL}$ the elastic compliance tensor. The fourth order tensors $\mathbf{C}_{EL}$ and $\mathbf{S}_{EL}$, through symmetry of the Cauchy stress and strain shear terms (down to 6 independent terms) reduces from 81 (9x9) components to 36 (6x6). In the case of isotropic (PC) materials linear elasticity takes the following form

$$\boldsymbol{\varepsilon} = \frac{1+\nu}{E}\boldsymbol{\sigma} - \frac{\nu}{E}tr\left(\boldsymbol{\sigma}\right)\mathbf{I} \tag{4.69}$$

when taken into matrix form produces

$$\begin{bmatrix} \varepsilon_{11} \\ \varepsilon_{22} \\ \varepsilon_{33} \\ \varepsilon_{12} \\ \varepsilon_{23} \\ \varepsilon_{13} \end{bmatrix} = \begin{bmatrix} \frac{1}{E} & -\frac{\nu}{E} & -\frac{\nu}{E} & 0 & 0 & 0 \\ -\frac{\nu}{E} & \frac{1}{E} & -\frac{\nu}{E} & 0 & 0 & 0 \\ -\frac{\nu}{E} & -\frac{\nu}{E} & \frac{1}{E} & 0 & 0 & 0 \\ 0 & 0 & 0 & \left(1+\nu\right)/E & 0 & 0 \\ 0 & 0 & 0 & 0 & \left(1+\nu\right)/E & 0 \\ 0 & 0 & 0 & 0 & 0 & \left(1+\nu\right)/E \end{bmatrix} \begin{bmatrix} \sigma_{11} \\ \sigma_{22} \\ \sigma_{33} \\ \sigma_{12} \\ \sigma_{23} \\ \sigma_{13} \end{bmatrix} \tag{4.70}$$

where only two material properties are necessary to characterize the mechanical behavior; *E*, elastic modulus and ν, Poisson's ratio. For the damaged and pseudo-undamaged states Hooke's law takes the following forms

$$\begin{aligned} \boldsymbol{\sigma} &= \tilde{\mathbf{C}}_{EL}\boldsymbol{\varepsilon}_e \\ \tilde{\boldsymbol{\sigma}} &= \mathbf{C}_{EL}\tilde{\boldsymbol{\varepsilon}}_e \end{aligned} \tag{4.71}$$

respectively, where $\tilde{\mathbf{C}}_{EL}$ is the degraded elastic stiffness tensor.

In the hypothesis of strain equivalence it is assumed that the elastic strain tensor observed in the damaged state is equated to that observed in the pseudo-undamaged state ($\boldsymbol{\varepsilon}_e = \tilde{\boldsymbol{\varepsilon}}_e$) [40]. Using the effective stress [Eq. (4.65)] we find the degraded elastic stiffness tensor as

$$\tilde{\mathbf{C}}_{EL} = \frac{1}{2}\left[\mathbf{M} : \mathbf{C}_{EL} + \mathbf{C}_{EL} : \mathbf{M}\right] \tag{4.72}$$

In the hypothesis of strain-energy equivalence the strain-energy of the damage state is equated to that of the pseudo-undamaged state [201]. Using both the effective stress and strain [Eq. (4.65)] the following is found

$$\tilde{\mathbf{C}}_{EL} = \mathbf{M} : \mathbf{C}_{EL} : \mathbf{M} \tag{4.73}$$

More complex forms of the $\mathbf{M}$ and $\tilde{\mathbf{C}}_{EL}$ have been proposed in literature [14,40,204,205].

Experiments have been conducted to compare the strain and strain-energy hypotheses. It has been found that mechanical degradation is strongly dependent on the dominant microstructural damage mechanism [206-208]. Possible damage mechanisms include: constrained cavity nucleation and growth, continuum cavity growth, super-plastic void growth, and ductile void growth [209]. It has been observed that just before fracture the stiffness

degrades by 50 to 100% dependent on the ductility of the subject material. Just before fracture, damage is the following

$$\omega_{cr} = \frac{A_0 - A_{net,cr}}{A_0} \tag{4.74}$$

where ω_{cr} and $A_{net,cr}$ are the critical damage and reduced area respectively. This suggests that critical damage should be less than unity and is a function load rate and temperature $\omega_{cr}(\dot{\sigma},T)$. Predicting rupture becomes highly inaccurate. To overcome this issue the following assumptions about damage are made

- Isotropic and scalar
- Critical damage is always unity
- It is possible for stiffness to be greater than zero just before fracture

The most important feature of the proposed approach is the introduction of the degradation factor, *m* that changes the damage-area equation [Eq. (4.74)] to

$$m\omega = \frac{A_0 - A_{net}}{A_0} \quad m \le 1 \quad 0 \le \omega \le 1 \tag{4.75}$$

This assumption is important because it infers that the effective stress reaches some critical value before fracture occurs. Penny found that a critical effective stress exists between the ultimate tensile σ_{UTS} and yield strength σ_{YS} of most materials [210]. In the proposed approach the critical effective stress becomes

$$\begin{aligned} \tilde{\sigma}_{cr} &= \frac{\sigma}{1-m} \\ m(T) &\propto \sigma_{UTS}(T) \end{aligned} \tag{4.76}$$

where the degradation factor, *m*, is proportional to the ultimate tensile strength a function of temperature.

The hypothesis of strain equivalence furnishes an elastic degradation of

$$\tilde{E} = E(1 - m\omega) \tag{4.77}$$

And the hypothesis of strain-energy equivalence provides

$$\tilde{E} = E(1 - m\omega)^2 \tag{4.78}$$

It is clear that stiffness just before fracture is not zero and stiffness after fracture is zero; therefore, a step-function must be introduced to represent this near instantaneous loss of stiffness. The strain and strain-energy degraded stiffness's becomes

Strain Equivalence

$$\tilde{E} = \begin{cases} E(1 - m\omega) & 0 \le t < t_r \\ 0 & t \ge t_r \end{cases} \tag{4.79}$$

Strain-Energy Equivalence

$$\tilde{E} = \begin{cases} E(1 - m\omega)^2 & 0 \le t < t_r \\ 0 & t \ge t_r \end{cases} \tag{4.80}$$

The selection of the either the strain or strain-energy hypothesis should be based on the response of the subject material. An analytical exercise of both approaches [Eqs. (4.79)-(4.80)] is provided in Figure 4.12 where the Y axis is normalized Young's modulus.

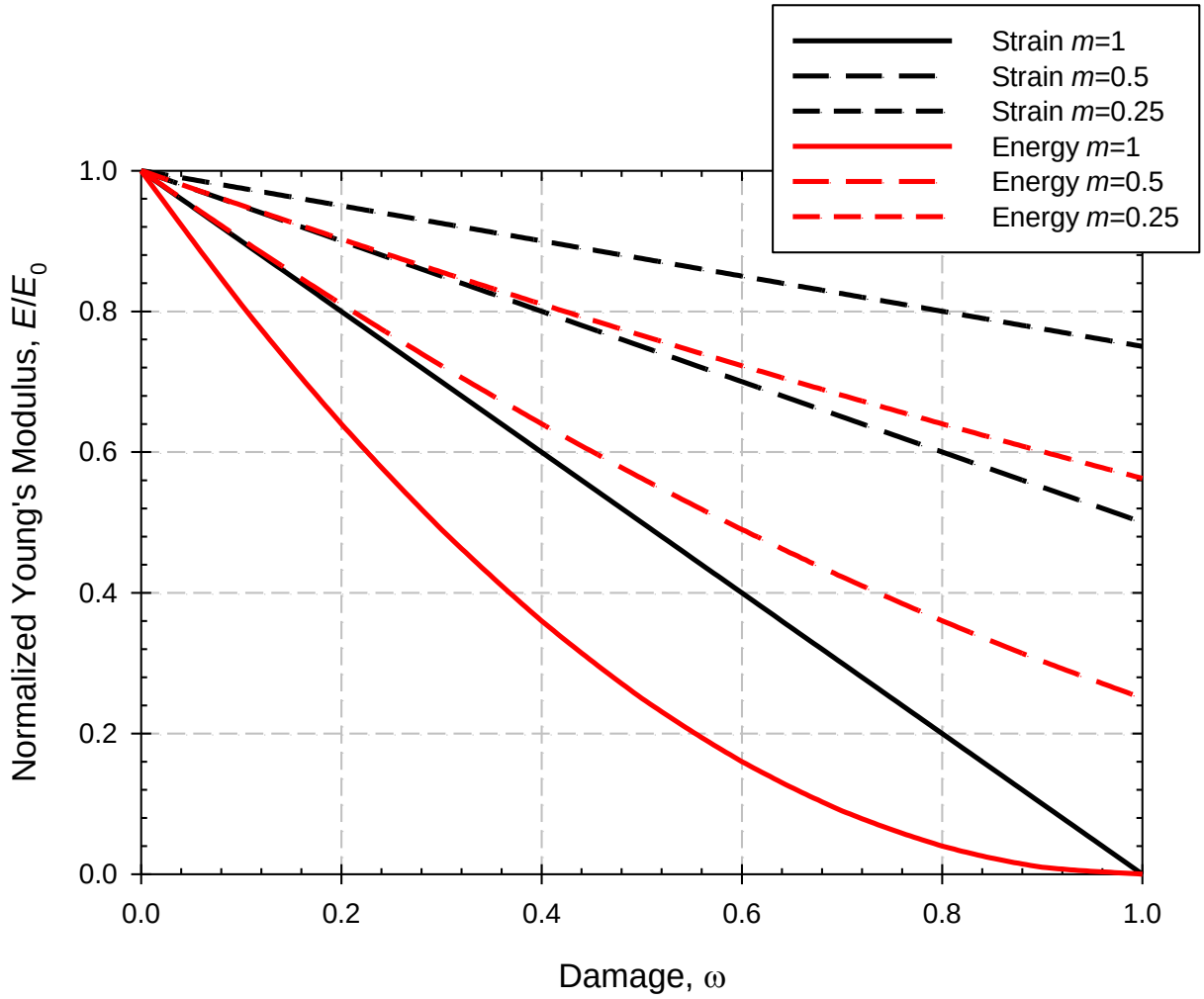

Figure 4.12 - Analytical exercise of proposed degradation equations

The mechanical degradation factor, *m* can be obtained in a number of ways. For strain equivalence, rearranging the effective stress produces

Strain Equivalence

$$m = 1 - \left(\frac{\sigma}{\tilde{\sigma}_{cr}} \right)$$
$$\tilde{\sigma}_{cr} = \sigma_{UTS} \tag{4.81}$$

where the critical effective stress can be assumed equal to the ultimate tensile strength. For both strain and strain-energy hypothesis, measuring stiffness just before rupture, $\tilde{E}_{cr}$, and rearranging [Eqs. (4.79-(4.80)] gives

Strain Equivalence
$$m = 1 - \left(\frac{\tilde{E}_{cr}}{E} \right) \tag{4.82}$$

Strain-Energy Equivalence
$$m = 1 - \left(\frac{\tilde{E}_{cr}}{E} \right)^{1/2} \tag{4.83}$$

Using the assumption that damage is isotropic and scalar the elastic stiffness tensor becomes the following

$$\begin{bmatrix} \varepsilon_{11} \\ \varepsilon_{22} \\ \varepsilon_{33} \\ \varepsilon_{12} \\ \varepsilon_{23} \\ \varepsilon_{13} \end{bmatrix} = \begin{bmatrix} \frac{1}{\tilde{E}} & -\frac{\nu}{\tilde{E}} & -\frac{\nu}{\tilde{E}} & 0 & 0 & 0 \\ -\frac{\nu}{\tilde{E}} & \frac{1}{\tilde{E}} & -\frac{\nu}{\tilde{E}} & 0 & 0 & 0 \\ -\frac{\nu}{\tilde{E}} & -\frac{\nu}{\tilde{E}} & \frac{1}{\tilde{E}} & 0 & 0 & 0 \\ 0 & 0 & 0 & (1+\nu)/\tilde{E} & 0 & 0 \\ 0 & 0 & 0 & 0 & (1+\nu)/\tilde{E} & 0 \\ 0 & 0 & 0 & 0 & 0 & (1+\nu)/\tilde{E} \end{bmatrix} \begin{bmatrix} \sigma_{11} \\ \sigma_{22} \\ \sigma_{33} \\ \sigma_{12} \\ \sigma_{23} \\ \sigma_{13} \end{bmatrix} \tag{4.84}$$

where only two material properties are necessary to characterize the mechanical behavior; $\tilde{E}$, degraded Young's modulus and ν, Poisson's ratio. Historically, the average Young's modulus has been used as a cumulative damage equation

$$D_i = 1 - E_i / E_0 \tag{4.85}$$

where E_0 and E_i are the initial and current respectively [212]. Numerous authors have studied the degradation of Young's modulus [213-219].

4.3 **Summary of Constitutive Model**

The proposed constitutive model is completed. The model is multistage, able to model the primary, secondary, and tertiary creep regimes. The damage evolution equation mitigates stress- and as a results mesh-dependence. A representative stress accounts for anisotropic cavity damage induced by multiaxial stress. The strain and strain-energy equivalence approach to mechanical degradation has been created to model mechanical degradation more accurately. The constitutive model equations are collected and listed in Table 4.3.

Table 4.3 – Summary of the Unified Mechanical Model for Creep

Title	Equation
Creep Strain Rate	$\dot{\varepsilon}_{cr} = \dot{\varepsilon}_{pr} + \dot{\varepsilon}_{sc}$ $\dot{\varepsilon}_{cr} = B\sinh\left(\sigma/\sigma_p\right)\exp\left(-qt\right) + A\sinh\left(\sigma/\sigma_s\right)\exp\left(\lambda\omega^{3/2}\right)$
Damage Evolution	$\dot{\omega} = \frac{M\left[1-\exp\left(-\phi\right)\right]}{\phi}\sinh\left(\frac{\sigma_{rep}}{\sigma_t}\right)^{\chi}\exp\left(\phi\omega\right)$
Microstructural Evolution	$\frac{A_p}{A_{p,cr}} = \frac{\rho}{\rho_{cr}} = \sin(\frac{3}{2}\omega)$
Representative (triaxial/multiaxial) Stress	$\sigma_{rep} = \alpha\sigma_1 + (1-\alpha)\sigma_{vm}$
Mechanical Degradation	(Strain) $\tilde{E} = E(1-m\omega)$ (Strain-Energy) $\tilde{E} = E(1-m\omega)^2$

A description of the material constants associate with each equation is provided below

Table 4.4 – Primary creep constants

Name	Symbol	Units
Primary Creep coefficient	B	hr^{-1}
" " mechanism transition	σ_p	*MPa*
" " exhaustion rate	q	hr^{-1}

Table 4.5 – Secondary creep constants

Name	Symbol	Units
Secondary Creep coefficient	A	hr^{-1}
" " mechanism transition	σ_s	*MPa*
Natural logarithm of the final over minimum strain rate	λ	unitless

Table 4.6 – Damage constants

Name	Symbol	Units
Tertiary creep-damage coefficient	M	hr^{-1}
" " mechanism transition	σ_t	*MPa*
" " exponent	χ	*unitless*
" " trajectory constant	ϕ	*unitless*
mechanical degradation factor	m	*unitless*

Table 4.7 – Representative Stress Constants

Name	Symbol	Units
Multiaxial rupture parameter	α	unitless

4.4 **FEM Implementation**

The proposed constitutive model is implemented into the finite element analysis (FEA) software ANSYS®. The ANSYS® program has an open architecture that allows linking of customized FORTRAN routines and subroutines, called user-programmable features (UPF's). The usermat3d UPF allows the user to implement any 3D material constitutive law. For every Newton-Raphson iteration and every material integration point the USERMAT UPF is called. At the beginning of a time increment, the current stresses, strains, and state variables are inputs. The USERMAT must then provide updated stresses, inelastic strains, state variables, and the material Jacobian matrix as outputs [220]. The stress increment is determined using the radial return technique. The inelastic strain vector is determined from the multiaxial extension of the isotropic model. The material Jacobian matrix is determined through derivation. The following sections detail how to obtain these terms.

4.4.1 Multiaxial Form

It is necessary to convert the scalar isotropic constitutive model into a multiaxial form. This is required to model the general deformation of a three-dimensional body. Borrowing from the plastic potential theory, the creep potential hypothesis suggests that some creep-potential controls creep-flow

$$d\varepsilon_{ij,cr} = d\varepsilon_{cr}\frac{d\psi(\boldsymbol{\sigma})}{d\sigma_{ij}} \tag{4.86}$$

where $d\varepsilon_{cr}$ is the equivalent creep strain increment [221]. In the case of creep, the yield surface is zero such that the potential function is equal to the selected equivalent stress.

In the current study Hill's anisotropic equivalent stress will be used [59]. Hill's anisotropic yield criterion is an extension of the von Mises yield criterion that allows for anisotropic yield of materials

$$\sigma_{\text{Hill}} = \sqrt{\mathbf{s}^T \mathbf{M} \mathbf{s}}$$

$$\mathbf{s} = VEC(\boldsymbol{\sigma})$$

$$\mathbf{M} = \begin{bmatrix} G+H & -H & -G & 0 & 0 & 0 \\ -H & F+H & -F & 0 & 0 & 0 \\ -G & -F & F+G & 0 & 0 & 0 \\ 0 & 0 & 0 & 2N & 0 & 0 \\ 0 & 0 & 0 & 0 & 2L & 0 \\ 0 & 0 & 0 & 0 & 0 & 2M \end{bmatrix} \tag{4.87}$$

where σ_{Hill} is Hill's equivalent stress, **s** is the Cauchy stress vector, and **M** is the Hill compliance tensor consisting of the *F*, *G*, *H*, *L*, *M*, and *N* unitless material constants [170]. Hill's equivalent stress reverts to von Mises when

$$F = G = H = \frac{1}{2}$$

$$L = M = N = \frac{3}{2} \tag{4.88}$$

Using Hill's potential function and the creep potential hypothesis, a general flow rule of the proposed isotropic constitutive model is produced

$$d\varepsilon_{cr,i} = \dot{\varepsilon}_{cr} \Delta t \frac{\mathbf{M}\mathbf{s}}{\sigma_{Hill}}$$

$$\dot{\varepsilon}_{cr} = B \sinh\left(\sigma_{Hill}/\sigma_p\right) \exp\left(-qt\right) + A \sinh\left(\sigma_{Hill}/\sigma_s\right) \exp\left(\lambda \omega^{3/2}\right) \tag{4.89}$$

where is the equivalent creep strain rate listed in Table 4.3.

4.4.2 Radial Return Mapping Technique

Creep is considered an incompressible process [222] where

- volumetric stress has no effect on the creep strain
- stress has no effect on volumetric creep strain

Using the above and the assumption of isotropy, the stress-strain law can be separated into spherical and deviatoric invariants

$$\begin{Bmatrix} \Delta p \\ \Delta \sigma_e \end{Bmatrix} = \begin{bmatrix} K & 0 \\ 0 & 3G \end{bmatrix} \begin{Bmatrix} \Delta \varepsilon_v \\ \Delta \varepsilon_e - \Delta \varepsilon_e^{cr} \end{Bmatrix} \tag{4.90}$$

where $\Delta\varepsilon$ is the elastic strain increment, $\Delta\varepsilon^{cr}$ is the creep strain increment, and K and G are the bulk and shear modulus respectively [223]. The deviatoric stress σ_e is equal to the equivalent stress σ_{Hill}. The term is Δp volumetric (hydrostatic) stress. In incremental form the equation becomes

$$\begin{aligned} p &= p_0 + K\Delta\varepsilon_v \\ \sigma_e &= \sigma_{e,0} + 3G\left(\Delta\varepsilon_e - \Delta\varepsilon_e^{cr}\right) \end{aligned} \tag{4.91}$$

where 0 denotes the initial value. To find the updated values of spherical p and equivalent σ_e stress the method of successive approximation is used. In this method, a problem is solved by a series of approximations which converge to a solution. An elastic predictor is used as the approximation

$$\begin{aligned} p^* &= p_0 + K\Delta\varepsilon_v \\ \sigma_e^* &= \sigma_{e,0} + 3G\Delta\varepsilon_e^{cr} \end{aligned} \tag{4.92}$$

where * denotes the predictor value. By rearranging [Eqs. (4.91),(4.92)] the updated stress becomes

$$\begin{aligned} p &= p^* \\ \sigma_e &= \sigma_e^* - 3G\Delta\varepsilon_e^{cr} \end{aligned} \tag{4.93}$$

The volumetric stress does not change. For the equivalent stress, by moving everything to the right hand side, a function that can be solved by iteration is produced

$$F\left(\sigma_e\right) = \sigma_e - \sigma_e^* + 3G\Delta\varepsilon_e^{cr} = 0 \tag{4.94}$$

Using the Newton-Raphson method gives

$$\left(\sigma_e\right)_{n+1} = \left(\sigma_e\right)_n - \frac{F_n}{\left(\frac{dF}{d\sigma_e}\right)_n} \tag{4.95}$$

where *n* is the iteration count. The convergence criterion follows

$$\begin{aligned} \left|F_{n+1} - F_n\right| &< \delta \\ \left|\left(\sigma_e\right)_{n+1} - \left(\sigma_e\right)_n\right| &< \delta \end{aligned} \tag{4.96}$$

where δ is the desired accuracy. The updated stress vector can be found using the following

$$\sigma_{ij} = pI_{ij} + \frac{\sigma_e}{\sigma_e^*} S_{ij}^* \tag{4.97}$$

where I_{ij} is the identity tensor, S_{ij}^* is the elastic predictor deviatoric stress tensor, and σ_{ij} is the Cauchy stress. The elastic predictor stresses can be obtained from

$$\sigma_i^* = C_{EL,ij}\left(\varepsilon_{EL,j} + \Delta\varepsilon_j^* - \varepsilon_{IN,j}\right) \tag{4.98}$$

where $C_{EL,ij}$ is the elastic stiffness matrix and $\Delta\varepsilon_j^*$ is the given strain increment.

4.4.3 Material Jacobian Matrix

The total strain rate, $\dot{\boldsymbol{\varepsilon}}_{tot}$, is a summation of elastic and creep strain rates, $\dot{\boldsymbol{\varepsilon}}_{e}$ and $\dot{\boldsymbol{\varepsilon}}_{cr}$ respectively

$$\dot{\boldsymbol{\varepsilon}}_{tot} = \dot{\boldsymbol{\varepsilon}}_{e} + \dot{\boldsymbol{\varepsilon}}_{cr} \tag{4.99}$$

The rate-based Hooke's law (the relationship between $\dot{\sigma}$ the Cauchy stress rate and $\dot{\boldsymbol{\varepsilon}}_{e}$ the elastic strain rate) takes the following form

$$\dot{\sigma} = \mathbf{C}_{EL}\dot{\boldsymbol{\varepsilon}}_{e} = \mathbf{C}_{EL}\left(\dot{\boldsymbol{\varepsilon}}_{tot} - \dot{\boldsymbol{\varepsilon}}_{cr}\right) \tag{4.100}$$

where $\mathbf{C}_{EL}$ is the elastic stiffness matrix.

The material constitutive response (the relationship between $\dot{\sigma}$ the Cauchy stress and $\dot{\boldsymbol{\varepsilon}}_{tot}$ the total strain rate) is

$$\dot{\sigma} = \mathbf{C}_{TOT}\dot{\boldsymbol{\varepsilon}}_{tot} \tag{4.101}$$

where $\mathbf{C}_{TOT}$ is the total stiffness matrix better known as the "material Jacobian matrix". In "implicit" FEM, the material Jacobian matrix is needed to solve using Newton-Raphson at every integration point and each global iteration [224]. Mathematical manipulation furnishes

$$\begin{aligned} \dot{\sigma} &= \mathbf{C}_{TOT}\dot{\boldsymbol{\varepsilon}}_{tot} \\ \dot{\sigma} &= \mathbf{C}_{EL}\dot{\boldsymbol{\varepsilon}}_{e} + \mathbf{C}_{CR}\dot{\boldsymbol{\varepsilon}}_{cr} \\ \mathbf{C}_{TOT} &= \mathbf{C}_{EL} + \mathbf{C}_{CR} \end{aligned} \tag{4.102}$$

above demonstrates that $\mathbf{C}_{TOT}$ the material Jacobian matrix can be decomposed into elastic and creep stiffness matrices, $\mathbf{C}_{EL}$ and $\mathbf{C}_{CR}$ respectively.

The material Jacobian matrix is a vital part of the equilibrium equations used in FEM [220]. The material Jacobian can be described as a partial derivative

$$\mathbf{C}_{TOT} = \frac{\partial \sigma_i}{\partial \varepsilon_j} \tag{4.103}$$

where $\partial \sigma_i$ is the change in the ith stress at the end of the time increment caused by the jth strain $\partial \varepsilon_j$ [225]. A closed-form solution to $\mathbf{C}_{EL}$ the elastic stiffness matrix always exists. A closed-form solution to $\mathbf{C}_{CR}$ the creep stiffness matrix may or may not exist. If a closed-form solution exists, it greatly reduces computational costs.

To that end, inverting the creep stiffness matrix, $\mathbf{C}_{CR}$, will furnish the creep compliance matrix, $\mathbf{S}_{CR}$, as follows

$$\mathbf{S}_{CR} = \left(\mathbf{C}_{CR}\right)^{-1} = \frac{\partial \varepsilon_i}{\partial \sigma_j} \tag{4.104}$$

The partial derivative of the proposed constitutive model (Table 4.3) can be found manually or by using symbolic computational algorithms. A partial derivative of a variable function is a derivative with respect to a constant such that

$$\mathbf{S}_{CR} = \frac{d\Delta \varepsilon_{cr,i}(\boldsymbol{\sigma})}{d\sigma_j} \tag{4.105}$$

introducing the proposed model furnishes

$$\begin{aligned} \mathbf{S}_{CR} &= \frac{d\Delta \varepsilon_{pr}\left(\sigma_{Hill}\right)}{d\sigma_j} + \frac{d\Delta \varepsilon_{sc}\left(\sigma_{Hill}\right)}{d\sigma_j} \\ \mathbf{S}_{CR} &= \mathbf{S}_{PR} + \mathbf{S}_{SC} \end{aligned} \tag{4.106}$$

where $\mathbf{S}_{PR}$ and $\mathbf{S}_{SC}$ are the primary and secondary-tertiary parts of the creep stiffness matrix. A closed-form solution for both was found using the symbolic computation. The matrices were simplified to the following

$$\mathbf{S}_{SC} = \Delta\varepsilon_{sc}\frac{\mathbf{M}}{\sigma_{Hill}} - \Delta\varepsilon_{sc}\frac{(\mathbf{M\sigma})(\boldsymbol{\sigma}\mathbf{M})^{\mathrm{T}}}{\sigma_{Hill}^{3}} + \frac{A}{\sigma_s}\cosh\left(\frac{\sigma_{Hill}}{\sigma_s}\right)\exp\left(\lambda\omega^{3/2}\right)\Delta t\frac{(\mathbf{M\sigma})(\boldsymbol{\sigma}\mathbf{M})^{\mathrm{T}}}{\sigma_{Hill}^{2}}$$
$$\mathbf{S}_{PR} = \Delta\varepsilon_{pr}\frac{\mathbf{M}}{\sigma_{Hill}} - \Delta\varepsilon_{pr}\frac{(\mathbf{M\sigma})(\boldsymbol{\sigma}\mathbf{M})^{\mathrm{T}}}{\sigma_{Hill}^{3}} + \frac{B}{\sigma_p}\cosh\left(\frac{\sigma_{Hill}}{\sigma_p}\right)\exp\left(-qt\right)\Delta t\frac{(\mathbf{M\sigma})(\boldsymbol{\sigma}\mathbf{M})^{\mathrm{T}}}{\sigma_{Hill}^{2}} \quad (4.107)$$

where both matrices are symmetric and non-singular. To obtain the stiffness matrix the compliance tensors must be inverted

$$\mathbf{C}_{CR} = \left(\mathbf{S}_{CR}\right)^{-1} = \left(\mathbf{S}_{PR} + \mathbf{S}_{SC}\right)^{-1} \quad (4.108)$$

In the current study, Gaussian elimination is used to find the inverse.

CHAPTER FIVE: UNIFIED MECHANICAL MODEL FOR CREEP-FATIGUE

5.1 Introduction

While the creep constitutive model developed in the previous chapter is able to fully describe the creep deformation and damage process under constant load; it is unable to model monotonic tension and cyclic viscoplasticity observed during fatigue. Under creep-fatigue both creep and cyclic viscoplasticity contribute to the evolution of a material. This necessitates the development of a unified mechanical model for creep fatigue able to model:

- primary, secondary, and tertiary creep
- monotonic and cyclic viscoplasticity
- hardening, softening, and saturation
- damage and rupture prediction
- mechanical and microstructural degradation

In this "unified" mechanical model all inelastic strains are derived from a single viscous function. Creep and yielding viscoplasticity are not independent of each other; rather the state variables of the viscous function evolve such that both phenomena can be modeled.

The development of the unified mechanical model involves many steps. First appropriate state variable must be selected. Next, a viscous function must be found which models the secondary creep behavior and incorporates steady-state values of the state variables. Then, the primary creep, monotonic tensile, and cyclic behavior can be model by converting the state variables into evolving functions. Then, coupled CDM-based creep and fatigue equations must

be developed to model tertiary and post-cyclic stress saturation behavior towards prediction of rupture. Finally, the influence of damage on the mechanical properties and microstructure of the material must be investigated.

5.2 **Proposed Constitutive Model**

Considerable effort has gone towards the development of unified viscoplasticity constitutive models [68,226]; however, only recently have researchers begun incorporating continuum damage evolution equations [227-229].

The identification of appropriate state variables is key to the development of a viscoplasticity model capable of modeling the complex phenomena associated with inelastic deformation under transient mechanical loading. While the fundamental mechanisms which contribute to deformation are coupled at multiple time- and length- scales it is necessary to limit the complexity (depth of characterization) of the proposed model for brevity and simplicity of implementation; however, considerable effort is expended to correlate macro-scale behavior to microstructural mechanisms.

In the proposed model, the classical assumption of a static yield surface is not used. Instead, the yield surface is replaced by isotropic and kinematic equilibrium surfaces where plastic flow is resisted until some rate-dependent equilibrium stress is reached. Another assumption is that all forms of rate-dependent inelastic strain are inseparable, such that non-recoverable strains due to creep, plasticity, etc. evolve from a single viscous function. The total strain rate, $\dot{\varepsilon}$, becomes

$$\dot{\varepsilon} = \dot{\varepsilon}_E + \dot{\varepsilon}_{IN} \tag{5.1}$$

where $\dot{\varepsilon}_E$ and $\dot{\varepsilon}_{IN}$ are the elastic and inelastic strain rates respectively. The inelastic strain rate is a viscous function which must include state variables to model:

- isotropic hardening (uniform expansion of the equilibrium surface)
- kinematic hardening (translation of the equilibrium surface the "Bauschinger" effect)
- cyclic hardening, softening, and saturation
- creep damage due to the nucleation and growth of cavities are grain boundaries
- fatigue/plastic damage due to climb and slip of dislocations

Towards these goals an inelastic viscous function of the following form is proposed

$$\dot{\varepsilon} = f(\sigma, R, D) \cdot g(T) \cdot h(\omega_c, \omega_f) \tag{5.2}$$

where σ, R, and D are the applied, rest (kinematic), and drag (isotropic) stresses, T is the temperature, and ω_c and ω_f are the creep and fatigue/plastic damage respectively. In this study the model is limited to isothermal conditions such that $g(T)$ equals unity.

5.2.1 Hybrid Viscoplasticity Constitutive Model

As discussed in section 2.3.1, a number of viscoplasticity constitutive model have been developed to model the complex phenomena observed at high temperature. A series of studies [68,226,230-232] have been conducted to compare models developed by authors such as Bodner 1975 [71], Hart 1976 [233], Miller 1976 [70,234-237], Chaboche 1977 [238], Robinson 1978 [239], Krempl 1980 [72,240], Walker 1981 [241], etc. It has been found that most viscoplasticity constitutive models are initial developed to model a particular set of boundary conditions such as

monotonic tension, strain-controlled fatigue, stress-controlled fatigue, and then extended to model other phenomena such as ratcheting, relaxation, and creep. This extrapolation often results inaccuracy. Miller's MATMOD [70,234-237] equations on the other hand were developed to model monotonic, cyclic, and creep deformation and sets forth a methodology to obtain material parameters analytically from these experimental data sets. Unfortunately, the original MATMOD equations [236-237] do not replicate the nonlinear cyclic hysteresis loop of experimental data well and the more modern MATMOD equations [234] are too complex for easy determination of material parameters. The Walker model [241] produces an excellent fit to most cyclic hysteresis loops with the ability to model nonlinear asymmetry; however, the original equations produce purely fictitious creep curves above the apparent yield strength of the subject material. When an initial value of the rest stress is set, the Walker model produces fictitious negative inelastic strain rates upon loading. The Walker model incorporates strain directly in the drag stress equation. This results in the inelastic strain rate becoming sensitivity to the time increment; thus relatively small time-steps are required for stability. This is an unacceptable property especially when simulating long term creep (>10,000 hours). It is desirable to develop a hybrid model which incorporates the monotonic, cyclic, creep deformation data sets and is able to model them at high fidelity across a wide range of applied conditions while overcoming the issues found in the legacy models.

First, the $f(\sigma, R, D) \cdot g(T)$ components of the viscous function must be found. Miller found that the viscoplasticity viscous function can be consider equivalent to a secondary creep viscous function used in traditional creep constitutive models. Miller uses the Garofalo 1965[34] hyperbolic-sine function as follows

$$\dot{\varepsilon}_{sc} = Bg(T)\left[\sinh\left(A\sigma_c\right)\right]^n \tag{5.3}$$

where B and n are the secondary creep coefficient and exponent, $g\left(T\right)$ is a temperature-dependent variable, and A is the secondary creep mechanism-transition ratio.

In the previous chapter the proposed creep constitutive model uses the 1943 McVetty [160] hyperbolic-sine function

$$\dot{\varepsilon}_{sc} = A_0 \sinh\left(\frac{\sigma_c}{\sigma_s}\right) \tag{5.4}$$

where A_0 is the secondary creep coefficient and σ_s is the secondary creep mechanism-transition stress. This form produces the best fit to minimum creep rate versus stress data as presented in the previous chapter. Following Gilman [66] and Rice [67], the rest and drag stresses are introduced into [Eq. (5.4)], and with considerations for Millers form [236-237], the hybrid viscous function becomes the following

$$\dot{\varepsilon}_{IN} = A_0 \sinh\left(\frac{|\sigma - R|}{D}\right)\mathrm{sgn}(\sigma - R) \tag{5.5}$$

where A_0 is the secondary creep coefficient, and R and D are the rest and drag stress respectively. The function $\mathrm{sgn}(x)$ is the sign of a real number x

$$\mathrm{sgn}(x) = \begin{cases} -1 & for \quad x < 0 \\ 0 & for \quad x = 0 \\ 1 & for \quad x > 0 \end{cases} \tag{5.6}$$

Let it be assumed that both viscous functions [(5.4)] and [(5.5)] are exercised for a creep test. At the time step where the secondary creep regime has been reached ($t > t_{ss}$), the inelastic strain rate becomes a constant equal to the minimum creep strain rate. Both the hybrid and McVetty viscous

functions become equal. This necessitates that the rest and drag stress become steady state values, R_{ss} and D_{ss} respectively where $\dot{R} \approx 0$ and $\dot{D} \approx 0$. Simplification furnishes the following "stress ratio" equation

$$\frac{\sigma_c - R_{ss}}{D_{ss}} = \frac{\sigma_c}{\sigma_s} \tag{5.7}$$

where σ_c is the applied stress. This relationship must be enforced to produce the constant minimum creep strain rate observed during the secondary creep regime in a creep testing and the ultimate tensile strength of monotonic tension.

The above relationship suggests that the evolution of the rest and drag stresses take the form of a rate-dependent equilibrium surface. Armstrong and Frederick [242] proposed that nonlinear kinematic hardening should be described as

$$\dot{\underset{\sim}{\mathbf{X}}} = \frac{2}{3} C \dot{\underset{\sim}{\varepsilon}}^p - \underset{\sim}{\mathbf{X}} \dot{p} \tag{5.8}$$

where C is a constant. This rate-dependent equilibrium surface evolves from the difference between work-hardening, $2/3 C \dot{\underset{\sim}{\varepsilon}}^p$ and (thermally-activated) dynamic recovery, $\underset{\sim}{\mathbf{X}} \dot{p}$ mechanics. Most legacy constitutive models have hardening laws can be regressed to a form of the Armstrong and Frederick rule [68]. The development of appropriate rest and drag stress rate-dependent equilibrium equations is key to the accurate prediction of static and transient phenomena. Towards that goal, modified components of legacy constitutive models (listed at the begin of this section) are used to build the rest and drag stress equations of the hybrid model while following the Armstrong and Frederick rule.

In literature, Walker model is observed to produce an excellent fit to the cyclic hysteresis loop data of superalloys compared to other legacy constitutive models [230-231]. This transient phenomena is mostly modeled by the kinematic hardening evolution equation equivalent to the rest stress as follows

$$\text{Walker} \qquad \begin{aligned} \dot{R} &= \left(n_1 + n_2\right)\dot{\varepsilon}_{IN} - \left(R - R_0 - n_1\varepsilon_{IN}\right)\dot{G} \\ \dot{G} &= \left(n_3 + n_4 \exp\left[-n_5\left|\varepsilon_{IN}\right|\right]\right)\left|\dot{\varepsilon}_{IN}\right| + n_6\left|\frac{R}{R_s}\right|^{m-1} \end{aligned} \tag{5.9}$$

Unfortunately the kinematic hardening law is ill-defined. When R_0 is set to greater than zero fictitious negative inelastic strain rates are produced when upon initial loading. The inclusion of dependence on the inelastic strain, ε_{IN} results in time-step size dependence of the material constants. Static phenomena (such as creep) cannot be model when the rest stress is dependent on the inelastic strain. The nine material constants exhibit low dependencies suggesting that the model is ill-defined. To produce a high quality fit to both static and transient phenomena, the rest stress evolution equations of Walker most be heavily modified to the point of novelty. In the hybrid model, the novel rest stress evolution equation, $\dot{R}$ becomes

$$\begin{aligned} \dot{R} &= c_1\dot{\varepsilon}_{IN} - \left(R - Q\right)\left[\left(c_2 + c_d\right)\left|\dot{\varepsilon}_{IN}\right|\right] \\ c_d &= c_3 \exp\left[-c_4\left(R - Q\right)\operatorname{sgn}\left(\sigma - R\right)\right] \end{aligned} \tag{5.10}$$

where c_1, c_2, c_3, c_4 and Q are material constants. The $\dot{R}$ equation removes four superfluous constants form the Walker model [Eq. (5.9)]. The term $c_1\dot{\varepsilon}_{IN}$ models work hardening. The portion c_d is a form of the variable work hardening coefficient original proposed by Krieg [243], then modified by Miller [244] to model "normal" and "anomalous" Bauschinger's effect where

"anomalous" effects include local reversals in curvature of the hysteresis loops. It is again modified and implemented in $\left(c_2 + c_d\right)\left|\dot{\varepsilon}_{IN}\right|$ as a dynamic recovery term. The term Q replaces R_0 (allowing R_0 to always equal zero). This eliminates the fictitious inelastic strain rates upon loading. The value Q represents the initial anisotropy of the yield surface where when there is no pre-existing anisotropy equals zero. Inelastic strain does not appear in the model, thus time-step size and static phenomena problems are overcome. The hybrid rest stress evolution equation can be regressed into a specialized form of the Armstrong and Frederick nonlinear kinematic hardening rule [242].

In literature, the drag stress equation of Miller's model [236-237] is observed to control isotropic hardening, softening, and saturation through coupling the rest and drag stress terms within the drag stress equation.

Miller $$\dot{D} = H_2\left|\dot{\varepsilon}_{IN}\right|\left[c_2 + \left|R\right| - \left(A_2/A_1\right)D^3\right] - H_2 c_2 B\theta'\left[\sinh\left(A_2 D^3\right)\right]^n \tag{5.11}$$

This coupling is only possible through the nature of the form of the rest and drag stress equations themselves. In the case of the hybrid model rest stress, the coupling method results in a overly complex drag stress equation. As an alternative, the drag stress equation of Krieg, Swearengen, and Rhode's [245] and the equation by James [230] are evaluated.

Krieg $$\dot{D} = A_4\dot{\varepsilon}_{IN} - A_5\left(D - D_0\right)^n \tag{5.12}$$

James $$\dot{D} = C_4\left|\dot{\varepsilon}_{IN}\right| - C_5 D \tag{5.13}$$

The Krieg equation is unable to model saturation due to the lack of a traditional dynamic recovery term and due to the way inelastic strain rate is used. The James equation exhibits

saturation but the drag stress continuously evolves in the absence of plasticity due to the $C_5 D$ term. To produce a high quality fit to isotropic hardening, softening, and saturation, a hybrid drag stress incorporating components of the Miller, Krieg, and James model is developed to the point of novelty. In the hybrid model, the novel drag stress evolution equation, $\dot{D}$ becomes

$$\dot{D} = \left[\left(c_5 - c_7 D_0^{\,3} \right) - c_6 \left(D - D_0 \right)^3 \right] \left| \dot{\varepsilon}_{IN} \right| \tag{5.14}$$

where c_5, c_6, and c_7 are material constants. The terms $\left(c_5 - c_7 D_0^{\,3} \right)$ is a work hardening term which controls hardening/softening while the term $c_6 \left(D - D_0 \right)^3$ is a dynamic recovery term which controls saturation. Miller [236-237] suggested that during warm-working experiments (where specimen are warm-worked to approximately 100% strain) the rest stress remains relatively small while the drag stress evolves. A semi-linear relationship exists between the warm-working stress and the resulting room temperature yield strength at a ratio of 1 to 3 for 304 stainless steel. By replacing the stress in the viscous function [Eq. (5.5)] with the yield strength and setting *R*=0, it is observed that stress to drag stress carries an exponent of 3. This exponential is introduce into the drag stress evolution equation. Cyclic saturation is model through the dynamic recovery term. When dynamic recovery, $c_6 \left(D - D_0 \right)^3$ overcomes the linear work hardening the drag stress rate becomes zero. Cyclic hardening and softening can be model through the relationship in the $\left(c_5 - c_7 D_0^{\,3} \right)$ term where a positive net value results in hardening and a negative net value results in softening. This suggests that if the initial drag stress is greater than some saturation value ($D_0 > D_0^*$) then softening will occur. The speed of saturation depends

on the evolving ratio between the hardening and dynamic recovery terms. The term $\left|\dot{\varepsilon}_{IN}\right|$ is used to enforce accumulation of the drag stress only during yielding and without regard to asymmetry.

The initial value of the drag stress, D_0 must exist as a value greater than zero. Miller developed a phenomenological calculation which can be used to "estimate" D_0 from monotonic data [236-237]. Let it be assumed that a single time step is used to reach the 0.2% yield strength at 0.002 strain offset, D_0 does not change significantly, inelastic strain rates are equal to the mechanical values, and the quantity Q is zero. Under these conditions the following approximations are made

$$\begin{aligned} &\sigma = Y \\ &\dot{\varepsilon}_{IN} \approx \dot{\varepsilon}_0 \\ &\varepsilon_0 = \dot{\varepsilon}_0 \Delta t = 0.002 \\ &R = c_1 \varepsilon_0 \\ &D = D_0 \end{aligned} \tag{5.15}$$

introducing the above terms into the viscous function [Eq. (5.5)] and solving for D_0 produces the following “initial drag stress for displacement control” as

$$D_0 = \frac{Y - c_1 0.002}{\operatorname{asinh}\left(\frac{\dot{\varepsilon}_0}{A_0}\right)} \tag{5.16}$$

where Y is the 0.2% yield strength and $\dot{\varepsilon}_0$ is the corresponding tensile-test strain rate. This value can be considered approximately equal to the "characteristic" drag stress of the material [66]. A more complex form of the initial drag stress can be calculated when less assumption are made; however, it increases the accuracy of modeling monotonic behavior at the expensive of fatigue and creep. An “initial drag stress for load control” still needs to be developed.

The rest and drag stress become steady-state (R_{ss}, D_{ss}) in a creep test when the secondary (steady-state) regime is reach and in a monotonic tensile test when the ultimate tensile strength is reached. The steady-state rest stress can be calculated by taking the rest stress rate [Eq. (5.10)] setting it equal to zero and solving for R_{ss}

$$0 = c_1 - \left(R_{ss} - Q\right)\left(c_2 + c_3 \exp\left[-c_4\left(R_{ss} - Q\right)\right]\right) \tag{5.17}$$

where a nonlinear solver can be used to solve for R_{ss} and assumes $\operatorname{sgn}\left(\sigma - R\right)$ equals unity. The steady-state drag stress can be calculated by taking the drag stress rate [Eq. (5.14)] setting it equal to zero and solving for the "real portion" of D_{ss}

$$D_{ss} = \left[\frac{c_5 - c_7 D_0^{\,3}}{c_6}\right]^{1/3} + D_0 \tag{5.18}$$

where a direct solution for D_{ss} is found. For a creep test, the time at which the secondary (steady-state) creep regime is reached occurs when the current "stress ratio" equals the steady-state "stress ratio" of [Eq. (5.7)]

$$\frac{\sigma_c - R(t)}{D(t)} = \frac{\sigma_c - R_{ss}}{D_{ss}} \tag{5.19}$$

where σ_c is the applied creep stress. For a monotonic tensile test, the ultimate tensile strength is reached at the steady-state "stress ratio". The ultimate tensile strength is not implicit stated within the equations. It can be calculated analytically through manipulation of the viscous function. Replacing σ, R and D with UTS, R_{ss} and D_{ss} in the viscous function [Eq. (5.5)] and solving for UTS produces

$$UTS = R_{ss} + D_{ss}\,\text{asinh}\left(\frac{\dot{\varepsilon}_0}{A_0}\right) \tag{5.20}$$

where UTS is the ultimate tensile strength and $\dot{\varepsilon}_0$ is the corresponding tensile-test strain rate. The above equation can be used to obtain rest and drag stress constants that produce an appropriate ultimate tensile strength for the subject material.

The hybrid viscoplasticity constitutive model is summarized below

$$\begin{aligned}
\dot{\varepsilon}_{IN} &= A_0 \sinh\left(\frac{|\sigma - R|}{D}\right)\text{sgn}(\sigma - R) \\
\dot{R} &= c_1\dot{\varepsilon}_{IN} - (R - Q)\left[(c_2 + c_d)|\dot{\varepsilon}_{IN}|\right] \\
c_d &= c_3 \exp\left[-c_4 (R - Q)\,\text{sgn}(\sigma - R)\right] \\
\dot{D} &= \left[\left(c_5 - c_7 D_0^{\,3}\right) - c_6 (D - D_0)^3\right]|\dot{\varepsilon}_{IN}|
\end{aligned} \tag{5.21}$$

where $A_0, c_1, c_2, c_3, c_4, c_5, c_6, Q$ and Y are material constants. The rest stress is a kinematic hardening law which controls transient phenomena, initial yield surface asymmetry, and "normal" and "anomalous" Bauschinger's effect. The drag stress is a isotropic hardening law which controls monotonic hardening, isotropic cyclic hardening and softening, and saturation. Drag and rest stress are not physical stress but represent the expansion and translation of equilibrium surfaces.

An analytical exercise of the hybrid model is performed for creep and fatigue type mechanical tests. A schematic of the change in ε_{IN}, R and D during a simulated creep test is provided in Figure 5.1. The inelastic strain depicts the primary and secondary creep regimes of creep deformation. The rest and drag stress saturate to equilibrium quickly. According to [Eq. (5.7)], the secondary creep regime is reached when both the rest and drag stress are fully

saturated. It should be noted that in the simulation, the drag stress appears to soften towards saturation instead of hardening. This behavior can be attributed to the fictitious low applied strain rate used to approximate an initial drag stress under creep. A schematic of the change in R, D and σ during a simulated softening and hardening fatigue test is provided in Figure 5.2 and Figure 5.3 respectively. In both figures asymmetry is observed in the rest stress where the constant Q is indentified as the average value of the rest stress during a cycle. The nonlinearity of the rest stress evolution is greatly influenced by the c_d term. Cyclic hardening and softening are controlled by the evolution of the drag stress towards a saturation value. During cyclic hardening (Figure 5.2) the drag stress evolves from a low value to the higher saturation value. During cyclic softening (Figure 5.3) the drag stress evolves from a high value to a lower saturation value. Cyclic hardening and softening are clearly observable in the stress graph of each figure.

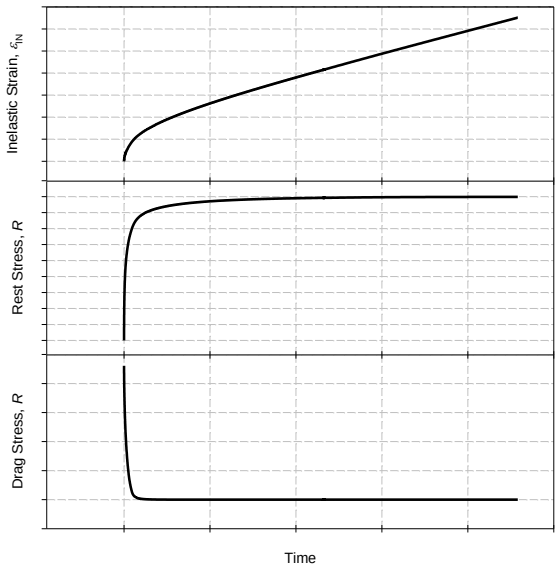

Figure 5.1 - Schematic of the change in ε_{IN}, R and D during a simulated creep test

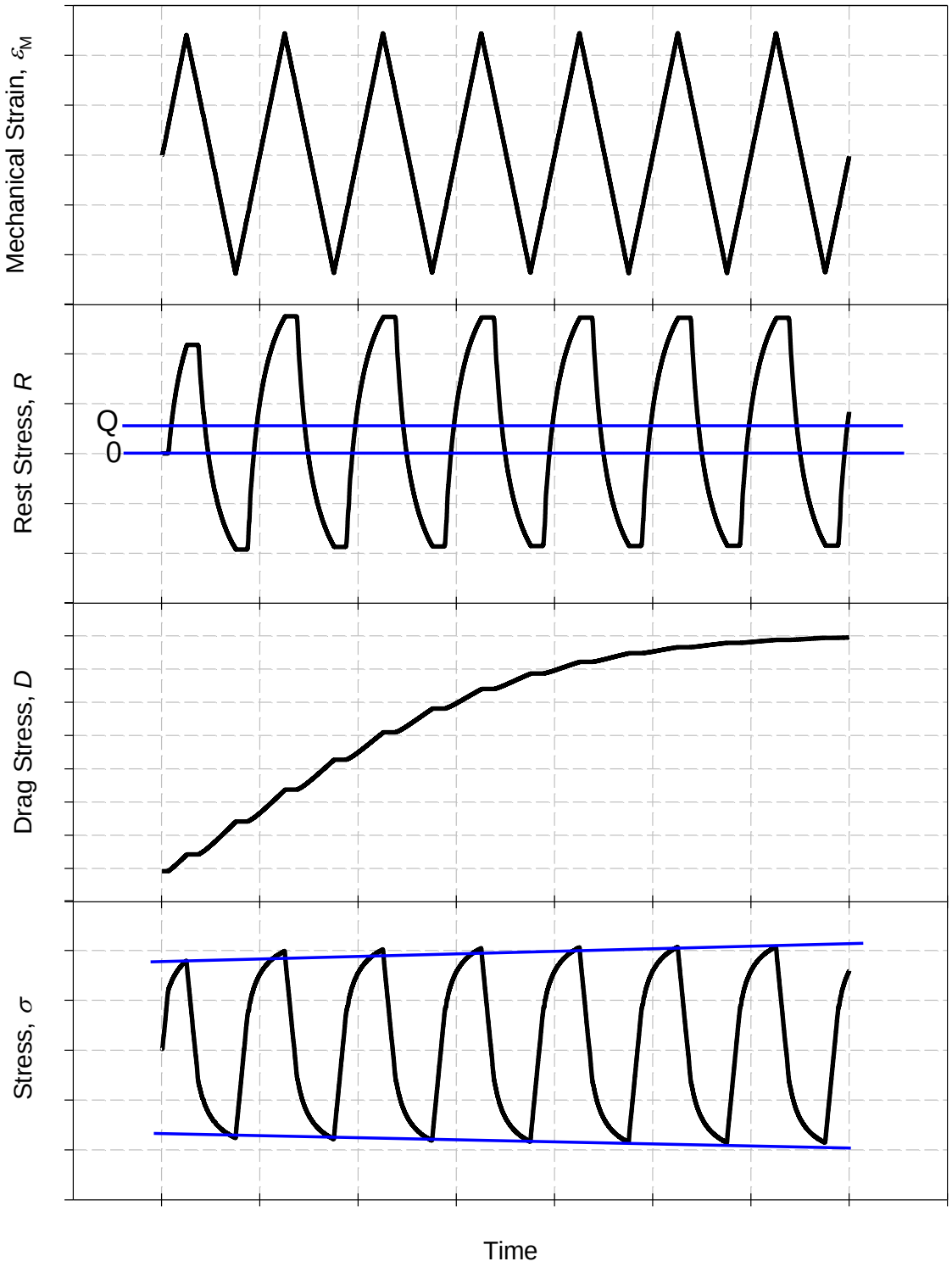

Figure 5.2 - Schematic of the change in R, D and σ during a simulated hardening fatigue test

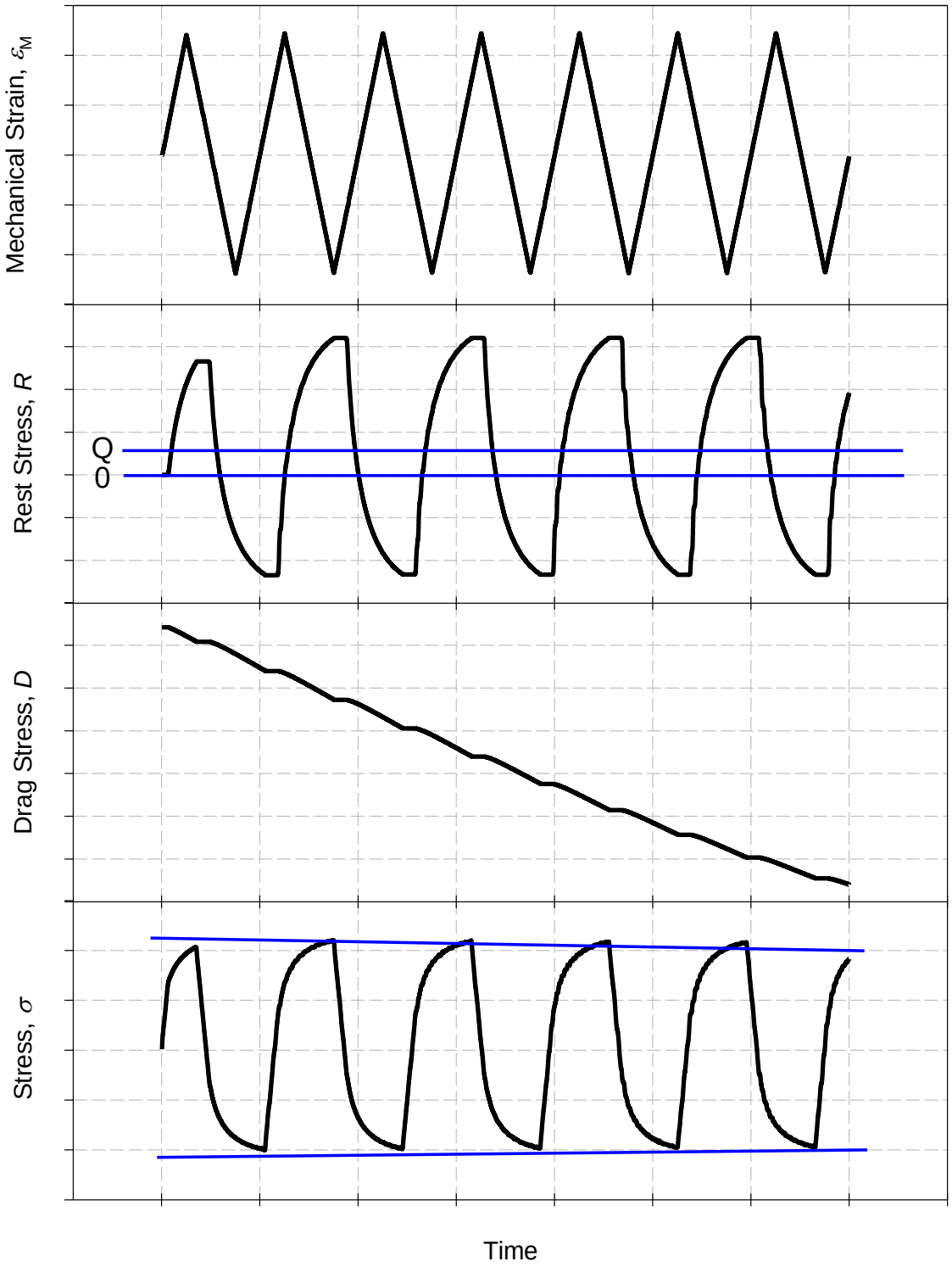

Figure 5.3 - Schematic of the change in R, D and σ during a simulated softening fatigue test

5.2.2 Numerical Optimization

In determination of the material constants of the hybrid constitutive model, the secondary creep and monotonic behavior can be incorporated through analytical techniques [Eq. (5.5)] and [Eq. (5.16)] respectively; however, the complexity of the transient phenomena (primary creep and cyclic behavior) necessitates numerical optimization. Previous work in the Mechanics of Materials Research Group at the University of Central Florida by Hogan et al. produced the uSHARP 1.0 a local optimization software [246]. The software was extended by DeMarco and colleagues resulting in uSHARP 2.0 a global optimization software [247]. Both versions of the software offer a convenient method by which the constants of a viscoplasticity constitutive model can be determined; however, these software required enormous computational time to obtain the optimal constants. Towards, reducing the computational time required to converge to an optimal set of constants, uSHARP 3.0 multithreaded software is developed for this study.

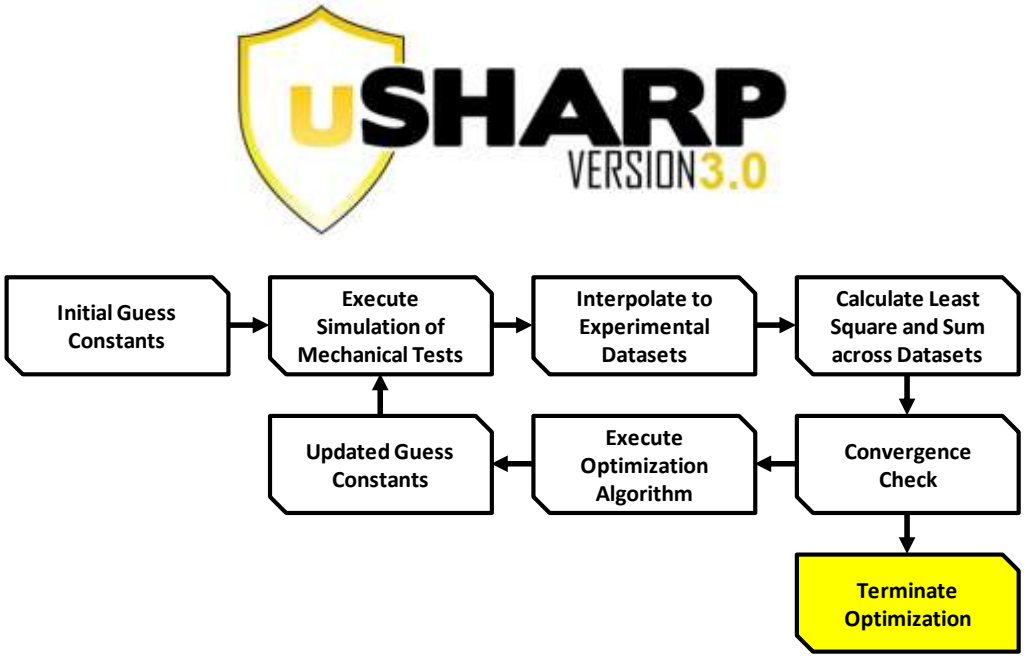

Figure 5.4 – General Framework of uSHARP 3.0

uSHARP 3.0 takes the general framework depicted in Figure 5.4. It has been auto-parallelized to generate a multithreaded code for loops, which enables parallel execution on a multiprocessing system. This enables the software to take advantage of multi-CPU, multi-core, and cluster computing solutions. An initial guess set of constants must be selected by the user. Next simulations are conducted of the mechanical tests under consideration. Afterwards, interpolation to the experimental datasets is conducted. Then a least squares calculation is performed and summed across the datasets under consideration to produce an objective value. The least squares objective function follows

$$SUM = \frac{\sum_{i=1}^{m} W(i)\left[\frac{100\left(\varepsilon_{FEM,i} - \varepsilon_{EXP,i}\right)}{\varepsilon_{EXP,\max}}\right]^2}{m} \tag{5.22}$$

where $\varepsilon_{FEM,i}$ and $\varepsilon_{EXP,i}$ are the strain values obtained by FEM simulation and experimental testing, respectively and $W(i)$ is a weight function vector. The parameter m is the total number of data points resulting from an individual simulation used to determine the least squares value. The integer n represents the number of datasets under evaluation. The weight function vector, $W(i)$ is filled with unity for creep and 50 for fatigue. This is done to produce comparable least square values between the two types of tests such that the optimization converges to constants which match both types of tests equally. A convergence check is performed. If convergence has not been reached then the optimization algorithm is executed which produces a new set of guess constants. This procedure is repeated until convergence has been reached. The optimization algorithm is selectable such that local or global optimization can be performed.

In the previous versions of uSHARP the mechanical tests are simulated externally. A batch file is executed which runs the ANSYS general-purpose finite element analysis (FEA) software. ANSYS requires two things to perform the simulation. First, the constitutive equations under considerations must be implemented into ANSYS. The equations are written into a Fortran subroutine (user-programmable feature) in ANSYS and then either a new executable (exe) file is compiled or a dynamic-link library (.dll) file is created to incorporate the modified code. Secondly, a input file in the ANSYS Parametric Design Language (APDL) must be written to provide the guess constants, geometry, and boundary conditions to the ANSYS solver. This approach using ANSYS has a high cost in terms of the time required to converge to optimal constants. The ANSYS executable must be executed and terminated multiple times. Running a simulation produces multiple arrays and temporary files which must be written and erased from random-access memory and read/write storage. As ANSYS is often run as a client software with license files available through a server, extended interruptions of internet can cause the uSHARP optimization software to crash. The only advantage of the ANSYS approach is that non-uniform geometry (notched specimen, multi-element bodies) can be more easily considered. It is highly desirable to develop an internal FORTRAN subroutine that is able to simulate the mechanical tests as it would greatly reduce the computational overhead involved in interfacing with ANSYS. An advantage of such an approach is scale and portability. As a standalone application, it could be executed across multiple computers within a network or executed remotely in the cloud. It could possibly be used to deal with situations where a vast number of datasets must be evaluated quickly.

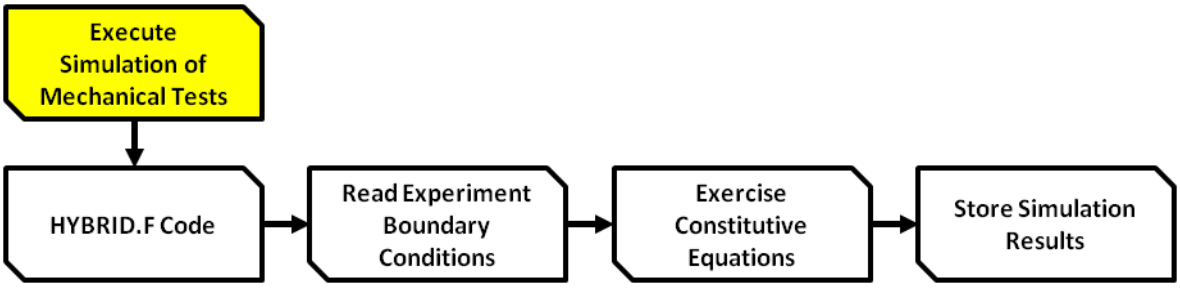

Figure 5.5 - Operation of the MATMOD Fortran Subrountine

Towards that goal, an internal Fortran code was developed for uSHARP 3.0. The resulting "HYBRID.F" subroutine, is outlined in Figure 5.5. This routine is an 1D isotropic finite element routine able to exercise constitutive equations to simulate a mechanical test. The mechanical test is assumed to have been conducted on a uniform specimen such that a 1D calculation can be performed to evaluate the properties. The recorded applied boundary conditions from the mechanical test (experiment) are imported into the routine. These boundary conditions are used in the 1D calculation to produce the simulation results. These results are then return to the main uSHARP routine. This procedure is relatively simple for load control tests where the applied load is used to directly evaluate the constitutive equations. However, for displacement controlled experiments, the following equation must be solved for stress before the constitutive equations can be evaluated

$$0 = \frac{\sigma}{E} + \dot{\varepsilon}_{IN}\left(\sigma\right)\Delta t + \varepsilon_{IN} - \varepsilon_{M} \tag{5.23}$$

where ε_M is the applied mechanical strain. Newton's Method is used to solve this equation. Convergence is meet when

$$\left|\sigma_{i+1} - \sigma_i\right| < 10^{-5} \tag{5.24}$$

or when the maximum number of iterations 50 is exceed. The HYBRID.F subroutine only works for 1D isotropic conditions. A majority of mechanical tests are performed on uniform specimen where 1D calculations are possible. In the future a more complex version of HYBRID.F could be developed to incorporate, notched specimen using the analytical solution of the notched geometry; however, this is not necessary for the present study.

The Corana et al. implementation of the simulated annealing multimodal algorithm was selected as the optimization algorithm in this study [248]. It is a robust global optimizer which has the capability to explore a function's entire surface by both uphill and downhill moves. This capability allows it to effectively climb out of local minima when necessary. The method is suitable for problems with a high number of variables (tens of thousands) . The simulated annealing algorithm is motivated by metallurgy. Consider a material heated above the re-crystallization temperature. The cooling rate will greatly influences the resulting thermodynamic free energy of the material. A quenched material might not escape the local minima energy state. A slow cooled material is more likely to reach a lower energy state. Slow cooling is used in the simulated annealing algorithm to control the probability of accepting worse solutions in a solution space [249]. As temperature decreases, the probability is reduced, resulting in more evaluation of the function in areas where the global minima should be present. This allows for a transition from evaluating the "gross behavior" to evaluating the finer "wrinkles" within a function.

The nature of the simulated annealing algorithm suggests that slowing the temperature reduction will result in a lower global minima. Slowing the temperature reduction has an added

impact of increasing the number of evaluations of the function. uSHARP 2.0, when used to evaluate the current study, produced approximately 1,000 evaluations per day. Using uSHARP 3.0, this has been increased to greater than 1,000,000 evaluations per day. Thus uSHARP 3.0 allows a slower temperature reduction which will produce a lower global minima and can converge to that minima faster.

A number of internal parameters are key to obtaining the global minima while minimizing the total evaluations needed [249]. The initial temperature, T_i must be set high enough to allow an evaluation of the "gross behavior" of the model within the solve space. As temperature decreases the probability of a downhill move is reduced leading to evaluations of the "wrinkles" within a function. An initial temperature, T_i, that is too high will result in excess evaluations while a value that is too low will results in convergence at a local minima. After N_S times N evaluations, 50% of all moves are accepted. The terms N_S and N represent the number of steps through N and the number of unknown variables respectively. This step is repeated N_T times. Temperature is therefore reduced when $N \cdot N_S \cdot N_T$ evaluations have occurred in the following manor

$$T_i = T_{i-1} \cdot r_T \tag{5.25}$$

where r_T is the temperature reduction factor commonly set to 0.85 units. Decreasing the temperature reduction factor, r_T will result in a quicker transition from "gross behavior" to an evaluation of "wrinkles" in the function. Assuming that the quantity $N \cdot N_S \cdot N_T$ is large enough to identify the potential global minima sites quickly, the value of r_T can be decreased to improve

speed of convergence. The term N_S is commonly set to 20 while the recommended value for N_T is $\max(5N,100)$. The term N_S is often not adjusted. The term N_T can be reduced to a quantity much less than $5N$ without significantly hindering global optimization; however, close evaluation of the behavior at intermediate temperature reductions are important. Convergence is controlled by the constants *EPS* and *NEPS*. Convergence is reached when the final function value of the last *NEPS* temperature reductions (including the current) change by less than *EPS*. *EPS* and *NEPS* are often set to 1E-05 and 4 respectively.

The uSHARP 3.0 software, requires that initial guess constants be input by the user. It is desirable to obtain initial guess constants that closely fit the experimental data. This allows the simulated annealing algorithm to identify the most promising area within the solve space early on and gives the opportunity to evaluate it in comparison to other local minima more often. The best methodology to find initial guess constants is to perform 1D calculations of the constitutive model in comparison to creep experimental data. The constants A_0 and D_0 are given from secondary creep and monotonic test data. The drag stress evolution, $\dot{D}$ can be set to zero, as Gilman found that drag stress represents a macroscopic constants called the "characteristic" drag stress [66]. Thus the initial values of c_5, c_6 and c_7 are zero. For simplification set c_4 to zero and c_3 to unity such that c_d becomes unity. Assume *Q* is zero. The simplified model becomes

$$\dot{\varepsilon}_{IN} = A_0 \sinh\left(\frac{|\sigma - R|}{D_0}\right)\mathrm{sgn}(\sigma - R) \tag{5.26}$$

$$\dot{R} = c_1\dot{\varepsilon}_{IN} - (R)\left[(c_2 + 1)|\dot{\varepsilon}_{IN}|\right] \tag{5.27}$$

Rearranging the simplified viscous function [Eq.(5.26)] and solving for *R*. Using experimental data an analytical approximation of the rest stress, R^* (under load control) can be obtain as

$$R^* = \sigma - \left| D_0 \operatorname{asinh}\left(\frac{\dot{\varepsilon}_{IN}}{B} \right) \right| \tag{5.28}$$

Now consider the condition where the secondary creep regime has been reached such that the rest stress evolution becomes $\dot{R} \approx 0$. Take [Eq. (5.27)], set to zero, and solve for c_2

$$c_2 = \frac{c_1}{R_{ss}} \frac{\dot{\varepsilon}_{IN}}{\left| \dot{\varepsilon}_{IN} \right|} - 1 \tag{5.29}$$

where R_{ss} equal to R^* at $t = t_{ss}$. Using the above relationship c_1 can be manually adjust until the minimum creep strain rate of the 1D calculation fits to creep experimental data. Initial guess constants for c_5, c_6 and c_7 can be obtained by curve fitting the normalized drag stress to the normalized peak stress during a fatigue test; however, it is acceptable to set all equal to zero. An example of curve fitting to obtain initial guess constants is provided in Figure 5.6.

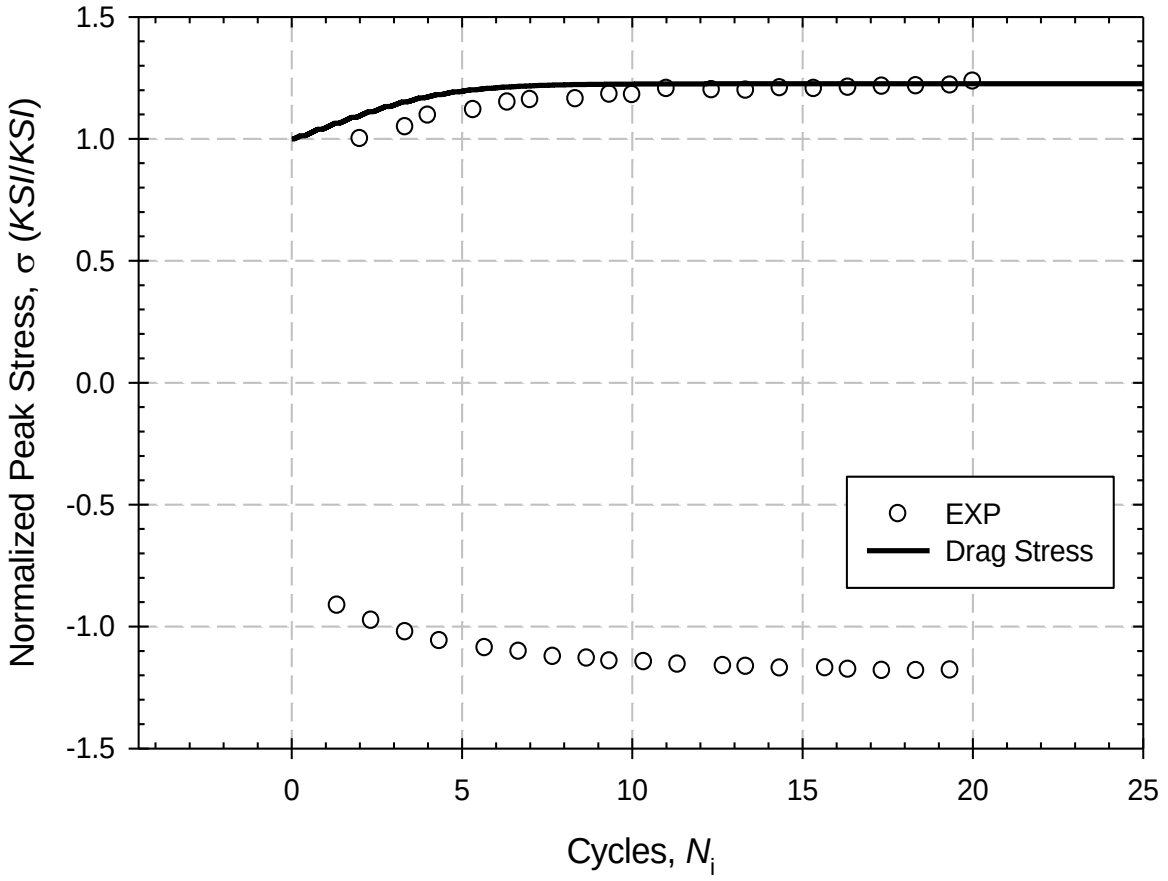

Figure 5.6 - Normalized peak stress used to determine initial guess constants for the drag stress evolution

Table 5.1 – Parameters of 1% and 1.4% fatigue tests

Parameter	Units	1%	1.4%
$\Delta\varepsilon_T$	*%*	1	1.4
f	*Hz*	*0.5*	--
$\dot{\varepsilon}_0$	*1/s*	*0.001*	--
E	*KSI*	21313.89	21059.85
v		0.29	--
Y	*KSI*	36.886	40.163
N		*694*	495

To demonstrate the capabilities and limitations of the model, simulations of creep, monotonic tension, and fatigue experiments must be compared to experimental data. Creep curves of 304 stainless steel at 300 and 320 *MPa* at 600°C are available from literature as depicted in Figure 4.5 [129]. Note, the significant scatter of the creep observe in the duplicate tests. Unfortunately, the author of the article does not include the 0.2% yield strength of the specimen nor the displacement rate used to initial load the material. Because the initial drag stress [Eq. (5.16)] has two unknowns, the yield strength is set equal to that of a fatigue test and the displacement rate becomes a variable which must be optimized. A method to back calculate the yield strength of the creep tests is provided later. The parameters associated with the fatigue tests are listed in Table 5.1. The yield strength of the 1% fatigue test was used for the initial drag stress of the creep simulations. The creep and fatigue data come from different studies; therefore, it can be assumed that the mechanical behavior will exhibit scatter. This is due to different chemical composition, industrial processing, and product types between the two studies. Nevertheless, an attempt is made to optimize across both studies to demonstrate the capabilities of the hybrid constitutive model.

Table 5.2 – Simulated annealing settings

Material Constant	Value
N	8
r_T	0.5
N_S	20
N_T	N
T	100
EPS	1E-3
$NEPS$	4

The uSHARP 3.0 software was configured to accept each dataset of the available experimental data. Optimization was attempted for each individual dataset, and was also performed on all four datasets simultaneously. This was done so that the capabilities of the hybrid model can be evaluated in the absence and presence of scatter (due to the stochastic nature of mechanical behavior). The upper and lower bounds of the possible material constants are zero and 1E5 units respectively. The eight material constants $c_1, c_2, c_3, c_4, c_5, c_6, c_7$ and Q are optimized for all datasets while a special $\dot{\varepsilon}_0$ is optimized for the two creep datasets to produce an initial drag stress, D_0 using the yield strength, Y of the CF01 dataset. The special $\dot{\varepsilon}_0$ is used because the actual yield strength and applied stress rate of the creep tests are unknown. The upper and lower bounds of the special $\dot{\varepsilon}_0$ are fixed between unity and zero strain per second to promote optimization of the datasets. The creep datasets also use the young's modulus, and Poisson's ratio of the CF01 dataset. The simulated annealing algorithm is configured using the settings listed in Table 5.2. When optimization was performed on each individual dataset, it was observed that the simulated annealing algorithm produce numerically unstable fits to experimental data where the optimal material constants carried low dependencies. Further operation of USHARP prove that the hybrid model requires at least one creep and fatigue dataset to produce valid optimized constants. This can be attributed to a requirement of knowledge of both the static and transient nature of the subject material. Due to the stochastic nature of mechanical behavior, any mechanical test repeated under the exact same boundary conditions while produce a probabilistic response. An attempt is made to obtain a single set of constants for

the collection of datasets. The goodness of fit will demonstrate the models ability to handle a probabilistic response. The simulated annealing algorithm was configured using the settings listed in Table 5.2. Temperature reduction occurred every 1620 evaluations. Convergence occurred at a final temperature of 0.11921E-04 with a total of 38881 evaluations. Of the 38881 evaluations, 18129 were accepted and 300 out of bounds. The initial least square sum was 10454.61 while the final sum reached 936.25 units. The optimal constants of the hybrid model for 304 stainless steel at 600°C are listed in Table 5.3. The sum of the least square for each dataset are provided in Figure 5.7. It is observed that the creep datasets converge to a low least square value. This can be attributed to the static boundary conditions. The fatigue datasets converge towards a higher value which is logical considering the dynamic boundary conditions. The least square values produced in the attempt to optimize all datasets are substantially larger than those producing when optimizing each dataset individual. This can be attributed to the stochastic nature of mechanical behavior and requirement of the constitutive equations to accommodate both static and transient phenomena simultaneously. Examining Figure 5.7 it is clear that the simulated annealing algorithm works for multiple datasets; however, better settings could be found to reduce the number of evaluations performed before convergence is reached. The results of the 300 and 320 *MPa* creep deformation data are provided in Figure 5.8 and Figure 5.9 respectively. Both simulated datasets fit within the bounds of the experimental data. The minimum creep strain rate is simulated perfectly while the primary creep strain is slightly under predicted. The current version of the hybrid model lack the ability to model the tertiary creep regime. This will be remedied in the next section. The simulated results for the fatigue test at $\Delta\varepsilon_T = 1\%$ and 600°C are provided in Figure 5.10. It is observed that the hybrid model slightly

under-predicts the monotonic behavior of the material. This can be attributed to the simplifying assumptions made in the initial drag stress approximation [Eq. (5.16)]. The model captures the shape of the hysteresis but under predicts the amount of hardening before saturation. The simulated results for the fatigue test at $\Delta\varepsilon_T = 1.4\%$ and 600°C are provided in Figure 5.11. It is observed again, the hybrid model slightly under-predicts the monotonic behavior of the material. The model captures the shape of the hysteresis but under predicts the amount of softening. The cyclic stress saturation data of the $\Delta\varepsilon_T = 1\%$ and $\Delta\varepsilon_T = 1.4\%$ fatigue tests are provided in Figure 5.12 and Figure 5.13 respectively. Specimen CF03 shows very slow saturation atypical for 304SS under the applied conditions. Normally, much less softening is observed and saturation occurs quickly. Disregarding this irregularity, the hybrid model approximates the hardening, softening, and saturation behavior fairly well when compared to the abilities of other constitutive models [230]. The hybrid model lack the ability to model the rapid softening that occurs at the end of the fatigue tests. This will be remedied in the next section. The current hybrid constitutive model is able to produce most of the static and transient phenomena associated with creep and fully-reversed fatigue tests. The hybrid model with creep damage is used to simulate a monotonic tensile test at $\dot{\varepsilon} = 0.001/s$ and 600°C as depicted in Figure 5.14. The large and small figures are cross-head and extensometer displacement respectively. A good prediction of the experimental data is obtained. The simulation produced the same ultimate tensile strength as the prediction [Eq. (5.20)] equation. A small negative slope is observed beyond the UTS that can be attributed to rest and drag stress contributions to softening. A plastic damage model is needed to better fit the softening observed in monotonic data. Optimization was performed with only creep

and fatigue experimental data available yet the hybrid model was able to produce a good fit to monotonic experimental data.

Table 5.3 – Simulatenously optimized constants for the hybrid model

Material Constant	Units	Initial Guess	Final Value
A_0	*1/s*	N/A	1.464E-12
c_1	*KSI*	2000	5838.3
c_2		72	239.64
c_3		0	511.96
c_4	KSI^{-1}	0	0.86806E-01
c_5	*KSI*	0	11.876
c_6	KSI^{-2}	0	1087.4
c_7	KSI^{-2}	0	5.0569
Q	*KSI*	0	2.1772
$\dot{\varepsilon}_0$	*1/s*	0.000833	0.49118E-08
$\dot{\varepsilon}_0^*$	*1/s*	N/A	0.000833

* the simulation strain rate for the 300 and 320 MPa creep tests

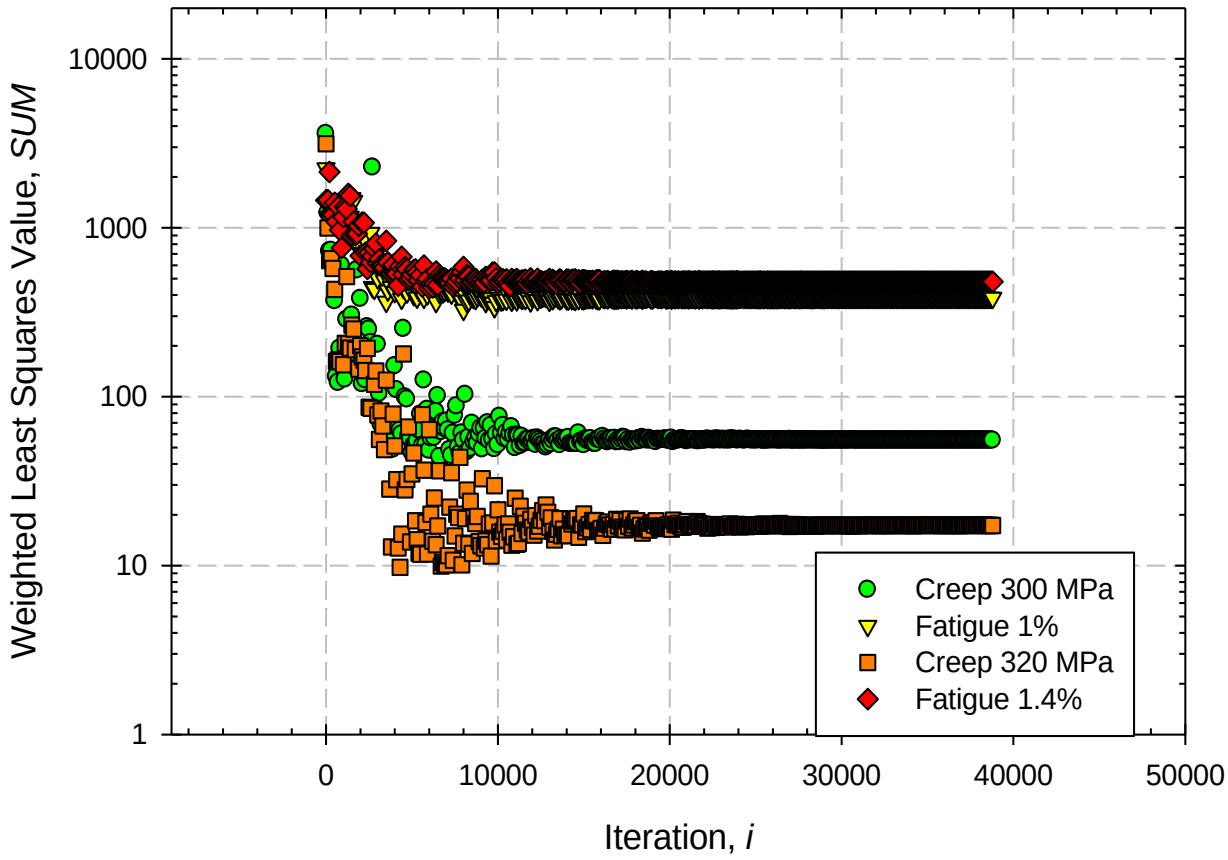

Figure 5.7 – Least square values during simulatenous optimization

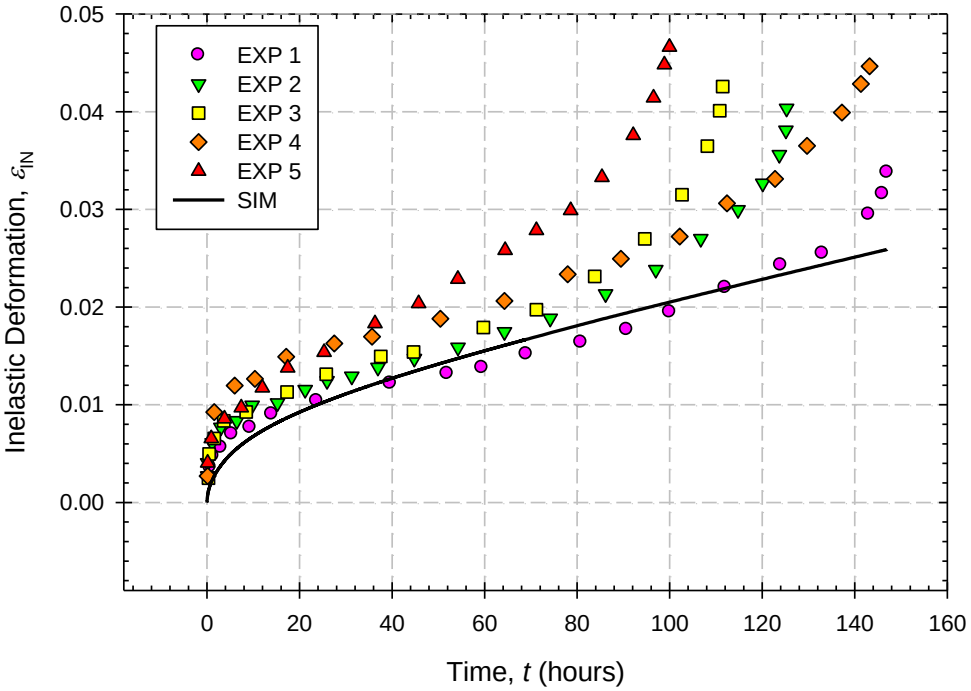

Figure 5.8 – Simultaenously simulated creep at 300 MPa and 600°C

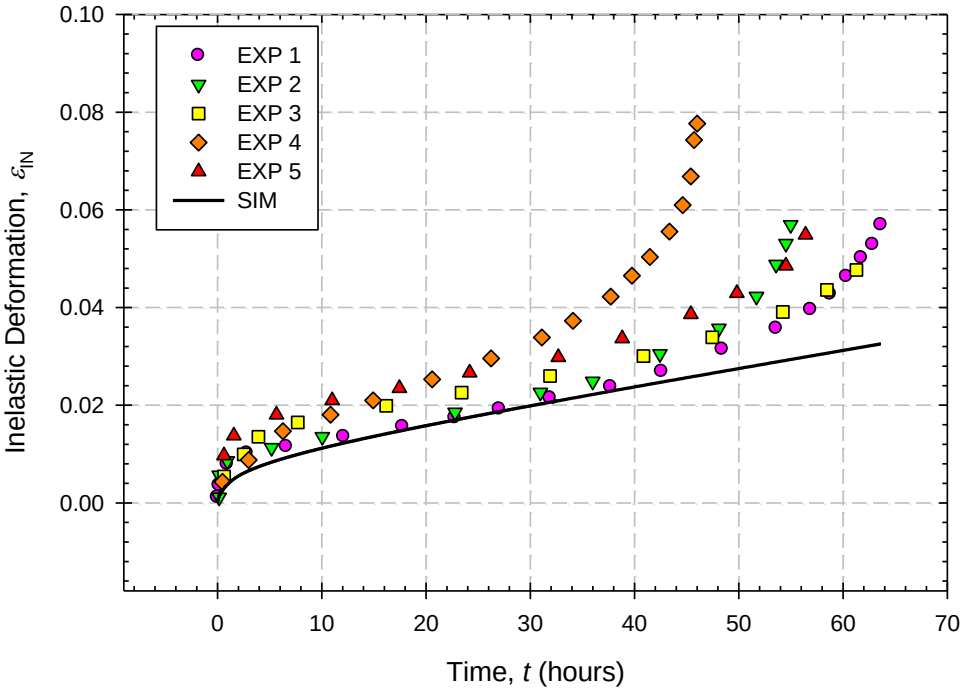

Figure 5.9 – Simultaenously simualted creep at 320 MPa and 600°C

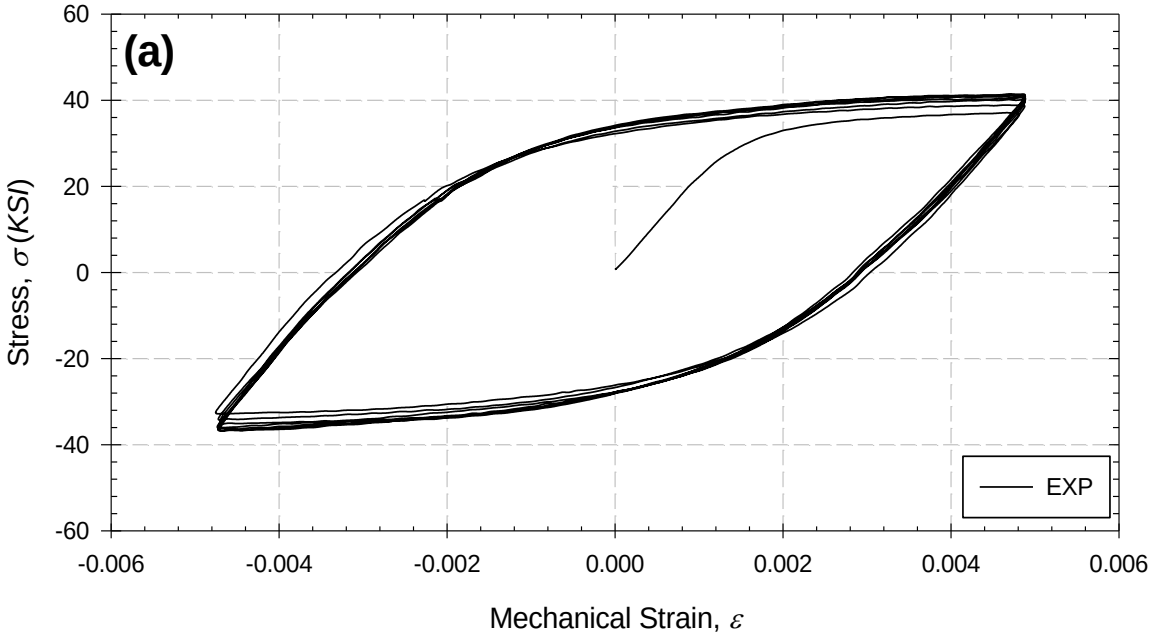

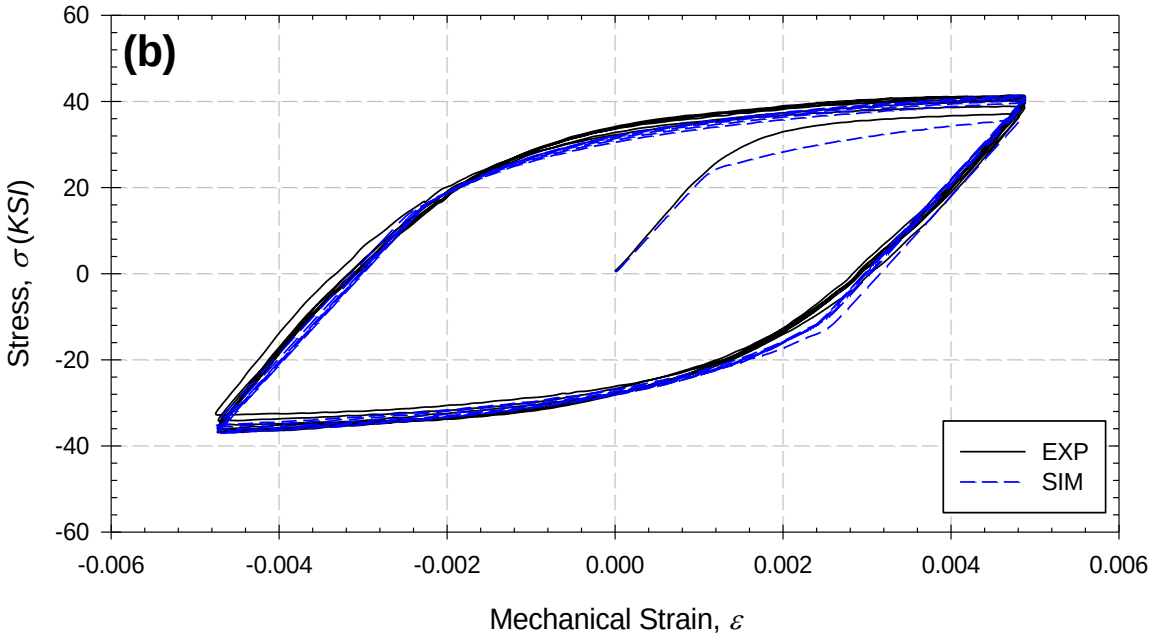

Figure 5.10 – Simultaenously simulated stress-strain curve $\Delta\varepsilon_T = 1\%$ fatigue test at 600°C: (a) experiment (b) simulated

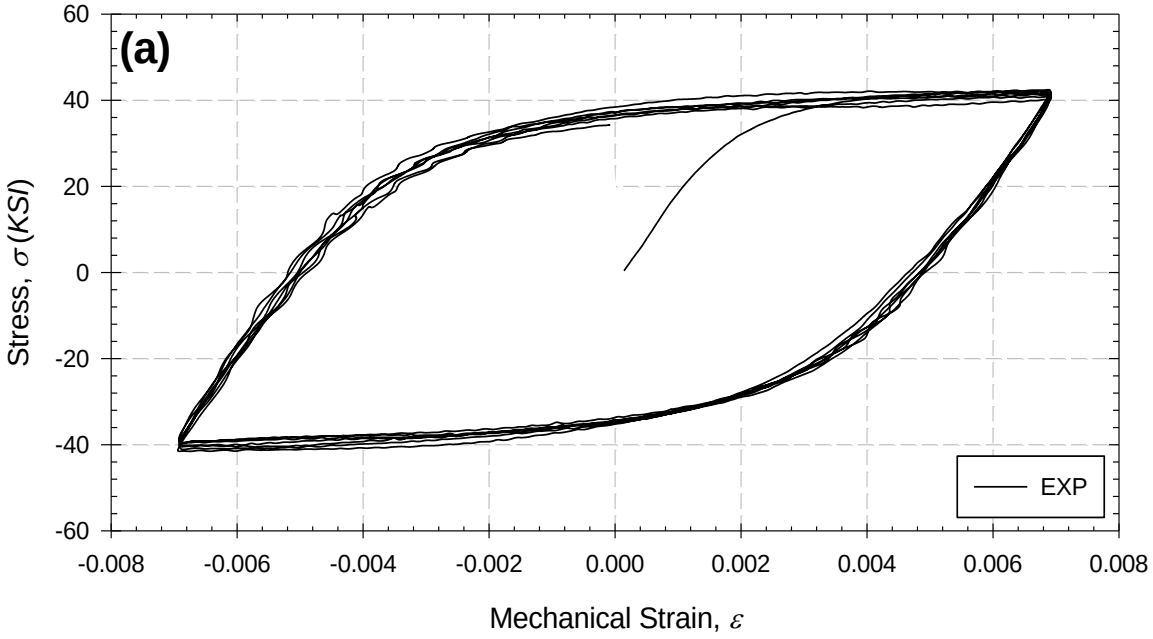

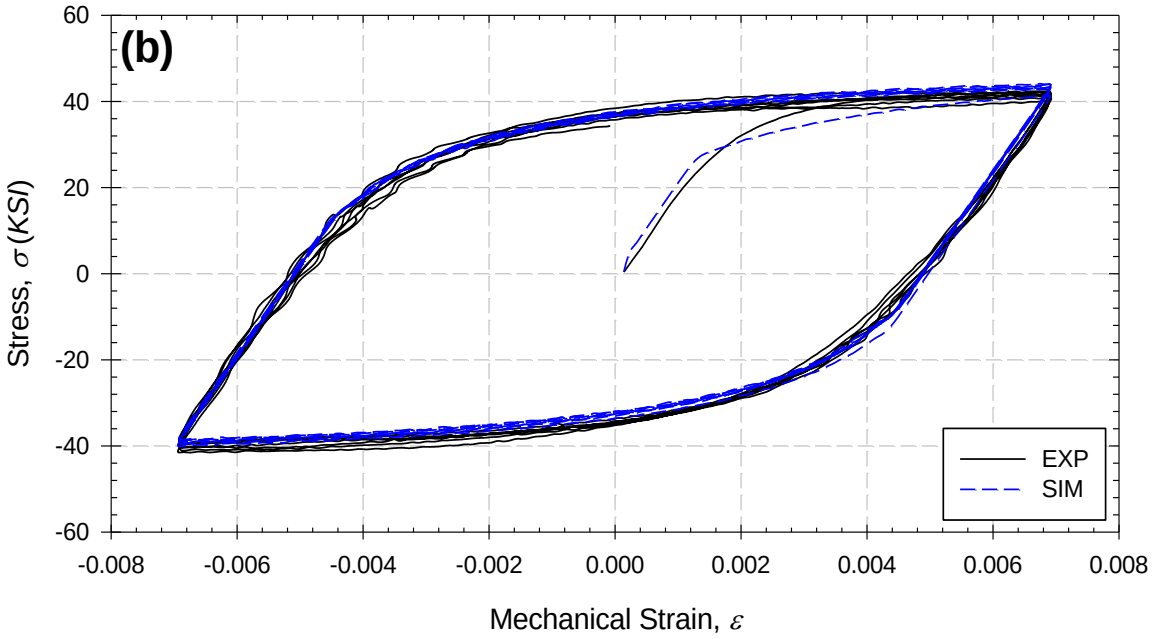

Figure 5.11 – Simultaenously simulated stress-strain curve $\Delta\varepsilon_T = 1.4\%$ fatigue test at 600°C: (a) experiment (b) simulated

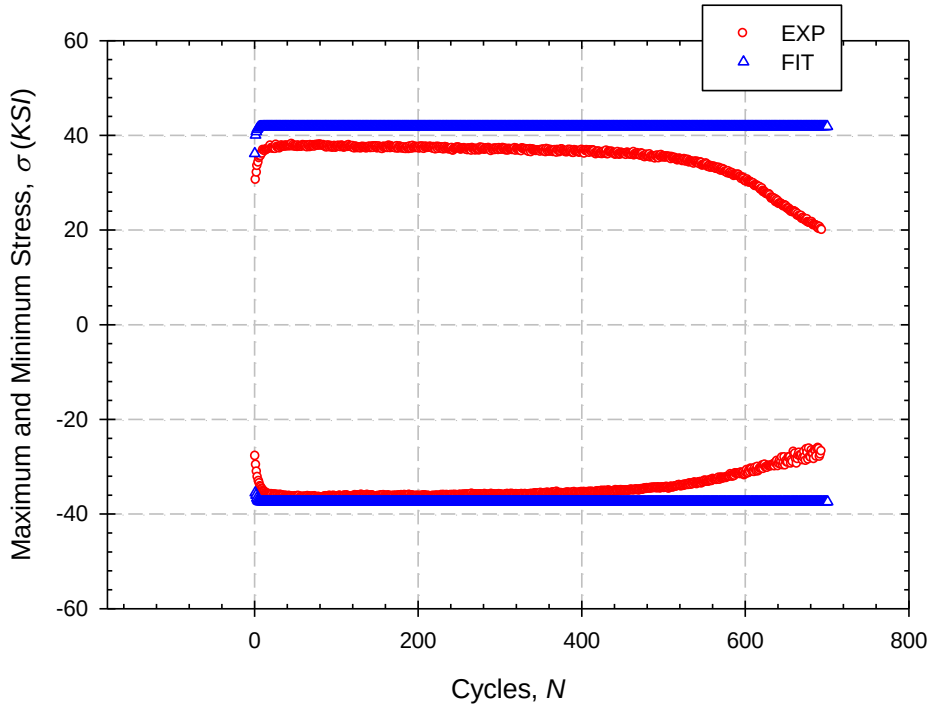

Figure 5.12 – Simultaenously simulated cyclic stress saturation of $\Delta\varepsilon_T = 1\%$ fatigue test

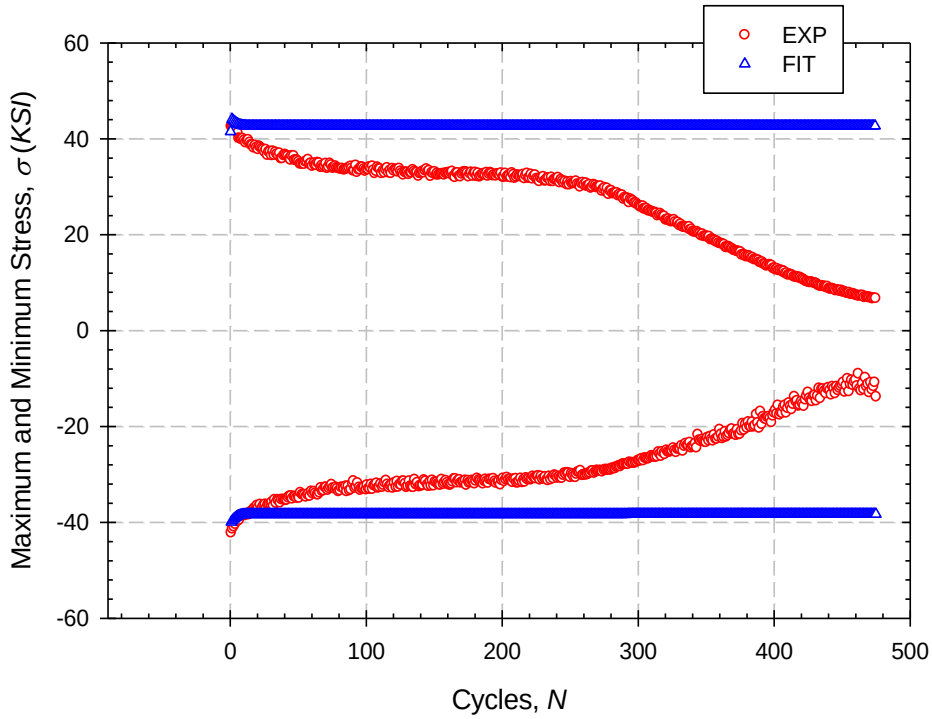

Figure 5.13 – Simultaenously simulated cyclic stress saturation of $\Delta\varepsilon_T = 1.4\%$ fatigue test

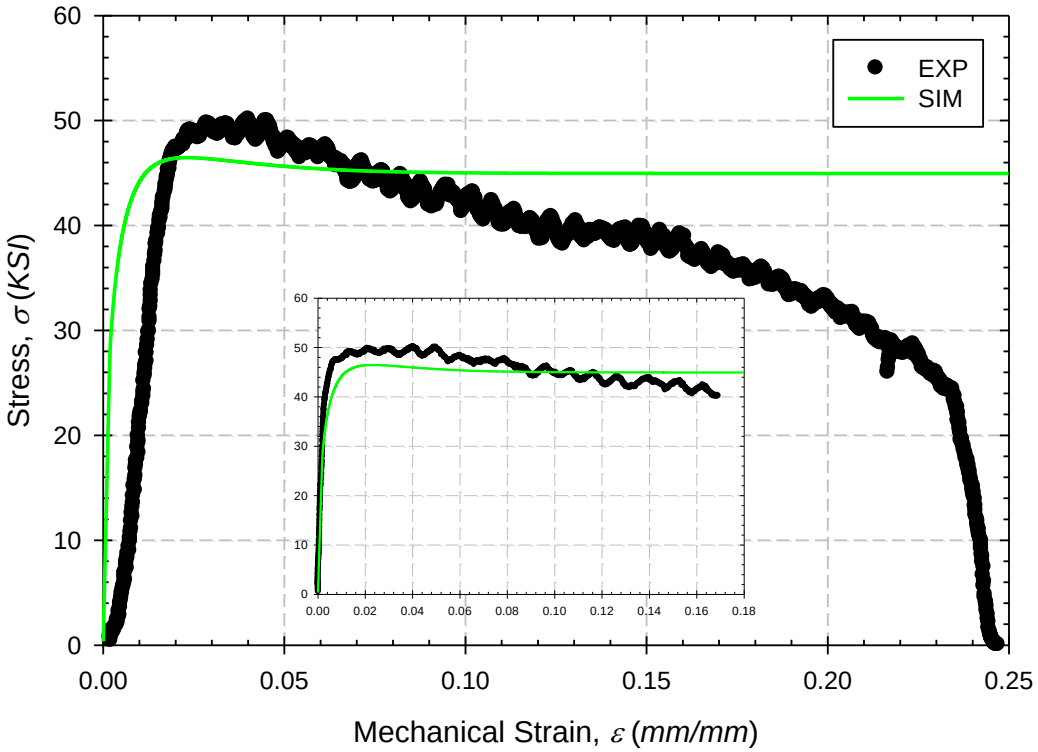

Figure 5.14 - Monotonic Tensile simulated at $\dot{\varepsilon} = 0.001/s$ and 600°C using the hybrid model (large-crosshead, small extensometer)

5.2.3 Damage Evolution and Microstructural Degradation

Under the conditions of creep-fatigue, in general, three microstructural mechanisms cause the accumulation of damage and plastic strain: the nucleation and growth of internal and grain boundary cavitation, the slip and climb of dislocations, and the formation of persistent slip bands during cyclic loading. These microstructural mechanisms are strongly correlate to creep, plastic/ductile, and fatigue damage, ω_c, ω_p, and ω_f respectively. The purpose of the damage evolution equations are to model the softening phenomena observed in mechanical tests and track the evolution of microstructural defects. These damage terms can be associated with the observable softening phenomena apparent in creep, monotonic tensile, and fatigue tests as depicted in Figure 5.15. During creep, softening is observed in the creep deformation history. Creep damage is represented by homogenous nucleation, growth, and coalescences of cavities near the end of life. A large number of micro-voids nucleate on grain boundaries. Creep damage produces the tertiary creep regime. During monotonic tension, plastic/ductile softening is observed after the ultimate tensile strength has been exceeded. This plastic-ductile damage is represented by the rapid (when compared to creep damage) nucleation, growth, and coalescences of microvoids [250]. Plastic damage produces necking in monotonic specimen and is often characterized by some critical plastic strain or stress. During strain-controlled fatigue, softening occurs in the stress amplitude in cycles proceeding cyclic-stress saturation. This fatigue damage occurs due to crack nucleation, growth, and fast fracture where cycling creates striations and extension of the crack length.

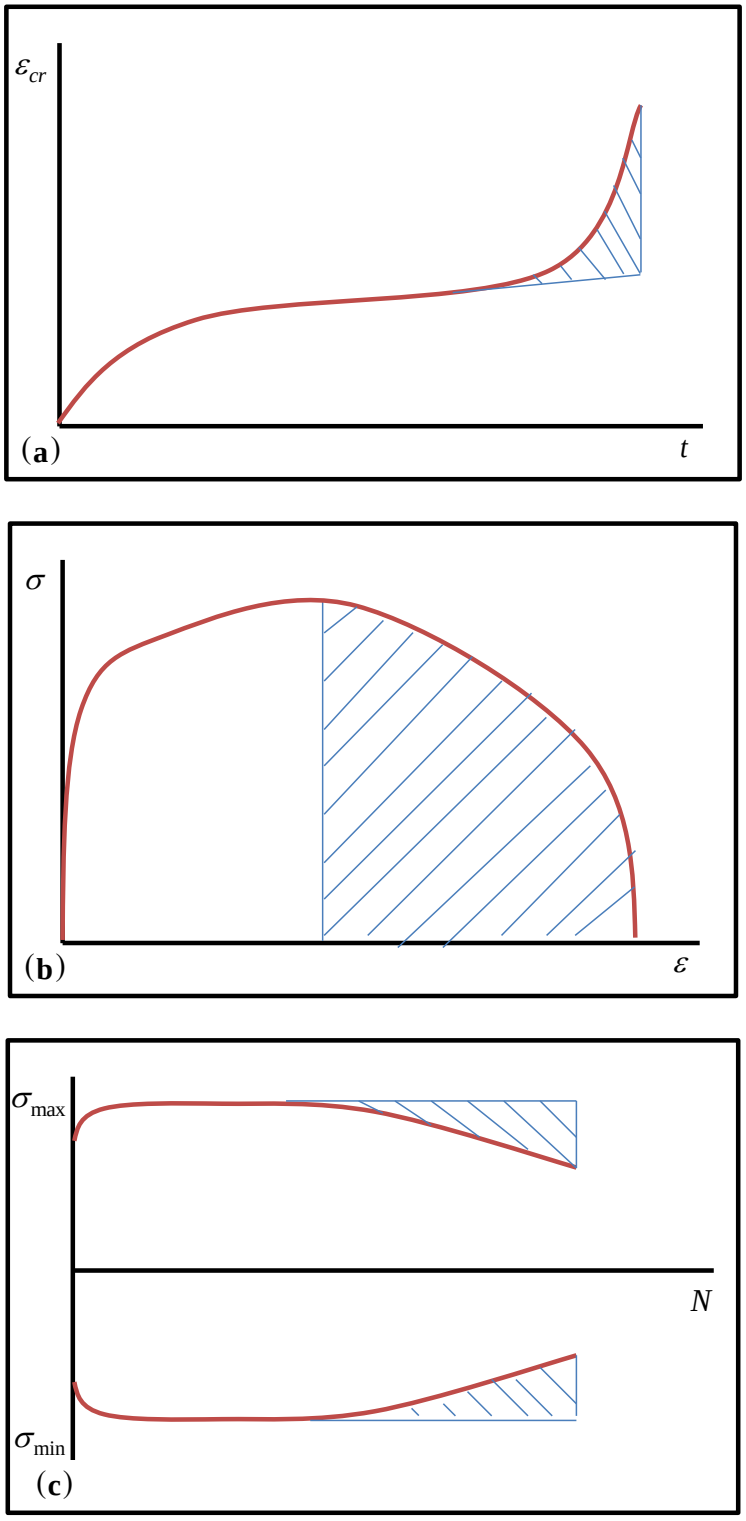

Figure 5.15 - Schematic of softening observed in (a) creep (b) monotonic tension (c) and fatigue

To model these softening phenomena the hybrid model viscous function must be extended as follows

$$\dot{\varepsilon} = f(\sigma, R, D)\, g(T)\, h\left(\omega_c, \omega_f, \omega_p\right) \tag{5.30}$$

where the function *h* describes how creep and plastic/fatigue damage influence the strain rate. Oxidation damage does not appear in an explicit form but is considered as an inseparable portion of the creep, plastic/ductile, and fatigue terms.

Iino studied the plastic zone around notched specimen of 304 stainless steel under creep and high-cycle fatigue conditions at elevated temperature [251-254]. High cycle fatigue tests were chosen over low-cycle fatigue because high-cycle fatigue tests are less susceptible to the creep effect. The recrystallization technique was used to observe the plastic zones [252,253].

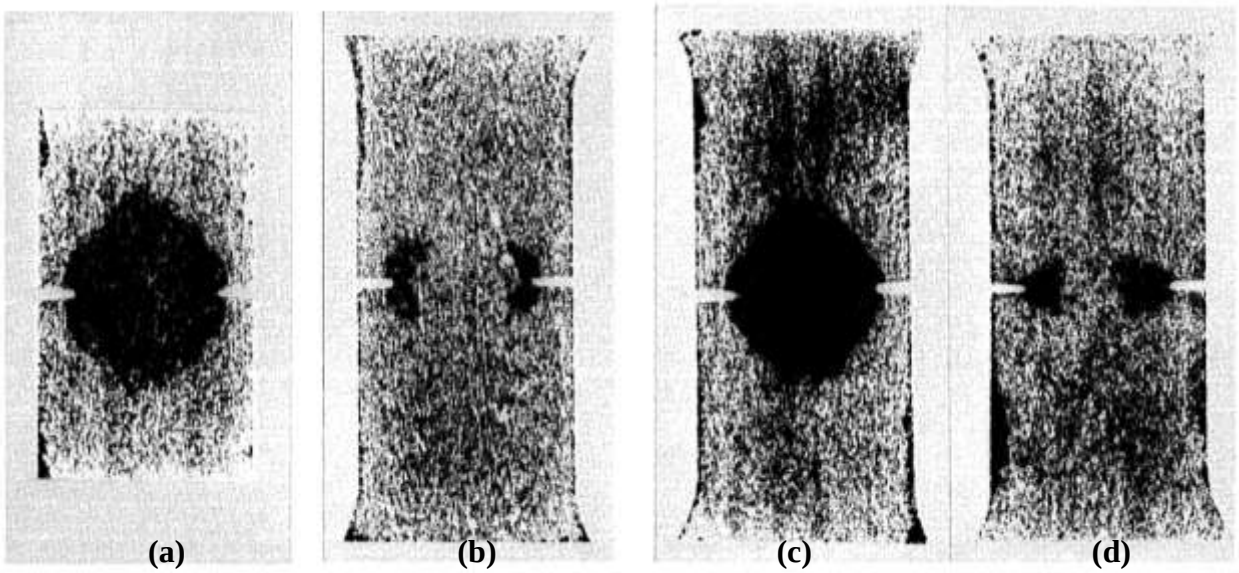

Figure 5.16 – Macroscopic recrystallization zone of 304 stainless steel at 650°C creep (a) 130MPa, t=2hr (b) 105 *MPa* and fatigue, t=5 *hr* (c) 130 MPa, *R*=7/130, 300cpm, t=0.6hr (d) 105 *MPa*, *R*=7/105, 300 *cpm*, t=1.5 *hr* [251]

In this technique, a specimen which has experienced some load history is annealed at high temperature for 24 hours. The microstructure after annealing will show that recrystallization takes place only in regions where plastic strain has exceeded some threshold (for 304SS between -196 to 850°C, $\varepsilon_p = 0.02$ and above 950°C $\varepsilon_p = 0.06$) [254]. The recrystallization technique reveals both the plastic zone (regions of recrystallization) and the amount of plastic deformation within a body (intensity of recrystallization). Comparing the macroscopic recrystallization of creep and high-cycle fatigue tests at approximately the same time, Iino found that the plastic zones are of comparable size as depicted in Figure 5.16 [251]. If the plastic zone indicates a region of damage and the creep and fatigue plastic zones are of comparable size, then creep and fatigue damage can be assumed to have one-to-one mapping where

$$\omega = \omega_c + \omega_f + \omega_p \tag{5.31}$$

This theory has been utilized by various researchers to produce good results for several materials [46]. It should be noted, that one-to-one mapping does not correspond to the physical nature of damage (i.e. slip and climb, cavitation). Only the net mechanical degradation induced by each mechanism is added together. Iino found that while the plastic zones of creep and high-cycle fatigue are of similar size, the gradient of plastic strain (intensity of recrystallization) is not the same with notch cracks initiating faster under fatigue [251]. This suggests that each damage mechanism influences the viscous function differently

$$h\left(\omega_c, \omega_p, \omega_f\right) = h_1\left(\omega_c\right) h_2\left(\omega_p\right) h_3\left(\omega_f\right) \tag{5.32}$$

Under Iino's boundary conditions the variation of fatigue damage $\partial\omega_f$ with an infinitesimal variation of stress $\partial\sigma(t)$ is larger than the variation of creep damage (under the same maximum stress, R=0) at a given time

$$\partial\omega_f > \partial\omega_c \tag{5.33}$$

where creep and fatigue tests have a interruption time delta of 1.4-3.6 hours equal to an additional 2.7E04 to 6.48E04 cycles (assuming plastic damage is negligible). This suggests that the frequency of cycling loading controlled by the applied strain rate, $\dot{\varepsilon}$ significantly accelerates the initiation of cracks. Under fatigue, plasticity is highly localized near the crack tip, while under creep, plasticity is more distributed. This can be attributed to the microstructural mechanisms associated with each behavior. Fatigue damage is primarily a dislocation process where dislocations move towards low energy free surfaces and form fine and coarse slip bands. Under cyclic loading the slip bands create intrusions and extrusions, with intrusions becoming stress concentrations (potential crack initiation sites) [51]. The collective motion of dislocations is the microstructural principal behind rate-dependent plastic flow embodied by the isotropic and kinematic hardening variables. Fatigue damage exhibits a damage surface (where the endurance limit must be exceed before damage accumulates). The above suggests that fatigue damage evolution is dependent on stress, stress rate, rest and drag stresses, temperature, current damage, and fatigue limit as follows

$$\dot{\omega}_f = f\left(\sigma, \dot{\sigma}, R, D, T, \omega, \sigma_f\right) \tag{5.34}$$

While plastic/ductile and creep damage have a similar fundamental microstructural mechanism (void formation), plastic/ductile damage occurs under dynamic loading (subject to isotropic and

kinematic hardening), exhibits a damage surface (critical strain or stress must be exceeded) and at a higher intensity in a short period of time. This necessitates that the plastic/ductile damage evolution be dependent on stress, stress rate, rest and drag stresses, temperature, current damage, and UTS as follows

$$\dot{\omega}_p = f\left(\sigma, \dot{\sigma}, R, D, T, \omega, UTS\right) \tag{5.35}$$

Creep damage is primarily a cavitation process where cavities form inside grains and along weakened grain boundaries. Cavities are unable to migrate but grow in radius eventually coalescing. Clearly, dislocations become localized early while cavities are more distributed and coalesce towards the end of life. In the unified mechanical model for creep (Chapter Four), it has been demonstrate that creep damage evolution is dependent on stress, temperature, and the current damage state.

$$\dot{\omega}_c = f\left(\sigma, T, \omega\right) \tag{5.36}$$

The evolution of creep damage and the associated microstructural cavitation were demonstrate to interface with the viscous function in the following manor

$$\begin{aligned} h &= \exp\left(\lambda \omega^{3/2}\right) \\ \dot{\omega} &= \frac{M\left[1-\exp\left(-\phi\right)\right]}{\phi} \sinh\left(\frac{\sigma}{\sigma_t}\right)^{\chi} \exp\left(\phi\omega\right) \\ \frac{A_p}{A_{p,cr}} &= \frac{\rho}{\rho_{cr}} = \sin(\frac{3}{2}\omega) \end{aligned} \tag{5.37}$$

where these equations produced an excellent correlation to creep data at 300 and 320 *MPa* as depicted in Figure 4.9. Due to similarities between the viscous function in the previous chapter and that of the hybrid model it is reasonable to introduce the creep damage model into the hybrid viscoplasticity constitutive model as follows

$$
\begin{aligned}
\dot{\varepsilon}_{IN} &= A_0 \sinh\left(\frac{|\sigma - R|}{D}\right)\operatorname{sgn}(\sigma - R)\exp\left(\lambda_c \omega_c^{3/2}\right) \\
\dot{R} &= c_1 \dot{\varepsilon}_{IN} - (R - Q)\left[\left(c_2 + c_d\right)|\dot{\varepsilon}_{IN}|\right] \\
c_d &= c_3 \exp\left[-c_4 (R - Q)\operatorname{sgn}(\sigma - R)\right] \\
\dot{D} &= \left[\left(c_5 - c_7 D_0^{\,3}\right) - c_6 \left(D - D_0\right)^3\right]|\dot{\varepsilon}_{IN}| \\
\dot{\omega}_c &= \frac{M_c\left[1 - \exp\left(-\phi_c\right)\right]}{\phi_c}\sinh\left(\frac{\sigma}{\sigma_t}\right)^{\chi_c}\exp\left(\phi_c \omega\right)
\end{aligned}
\tag{5.38}
$$

The above represents a hybrid model with creep damage. The creep damage evolution, $\dot{\omega}_c$ is a function of the total damage ω term [Eq. (5.31)]. The rupture prediction material constants M, σ_t and χ and damage-interface λ term do not change and are given subscript *c* to denote creep. The constant ϕ can exhibit a slight change. This is associated with time-scale issues where the size of the average time-increment affects the precision of the creep damage evolution equation. This can become a serious problem when studying long-term creep and high cycle fatigue. The creep damage constants are optimized at the time-scale of creep and while fatigue damage constants are optimized at the fatigue time-scale; therefore, the precision of each damage model is preserved when phenomena is most dominant.

This partial model will help determine the form of the fatigue damage evolution equation. The hybrid model with creep damage can be used to analytical extract the fatigue damage. This is done by comparing the results of the hybrid model with creep damage to experimental data and recording the remaining error where the error represents fatigue damage. The amount of damage related to fatigue damage at rupture can be simply found as

$$
t = t_r \quad 1 = \omega_c + \omega_f \quad \omega_f = 1 - \omega_c \tag{5.39}
$$

when the critical stress to activate plastic/ductile damage is not exceeded.

Using the creep damage constants listed in Table 4.2, the hybrid model with creep damage is used to simulate creep under 300 and 320 MPa at 600°C depicted in Figure 5.17 and Figure 5.18 respectively. It is clear that the model produces reasonable results when compared with the experimental data. The primary, secondary, and tertiary regime regimes are well represented. Ductility is slightly over-predicted but not to the point of impossibility considering the scatter in experimental data. Next, the hybrid model with creep damage is used to simulate fatigue under $\Delta\varepsilon_T = 1\%$ and 1.4% at 600°C as depicted in Figure 5.19 and Figure 5.20 respectively. It is observed that the creep damage law has minimal impact on the fatigue behavior. It has been previously stated that fatigue damage is a highly localized process that occurs early in a material while creep damage is a homogenous damage which occurs later in life. Creep damage does not have a chance to develop due to the intensity of the fatigue damage in the experimental data. This suggests that fatigue damage is the dominant mechanism attributed to cyclic softening in the current dataset at 600°C. It should be noted that this relationship is temperature-dependent, such that increasing the temperature will reduce the dominance of the fatigue damage and enhance creep damage. The hybrid model with creep damage is used to simulate a monotonic tensile test at $\dot{\varepsilon} = 0.001/s$ and 600°C as depicted in Figure 5.21. Creep damage has no visible influence on the mechanical evolution during the current monotonic test. It is reasonable to project that creep damage becomes highly influential at lower strain rates, where the extended runtime allows cavity growth, homogenization, and coalescence. A parametric study on the influence of applied strain rate will be provided in the next chapter.

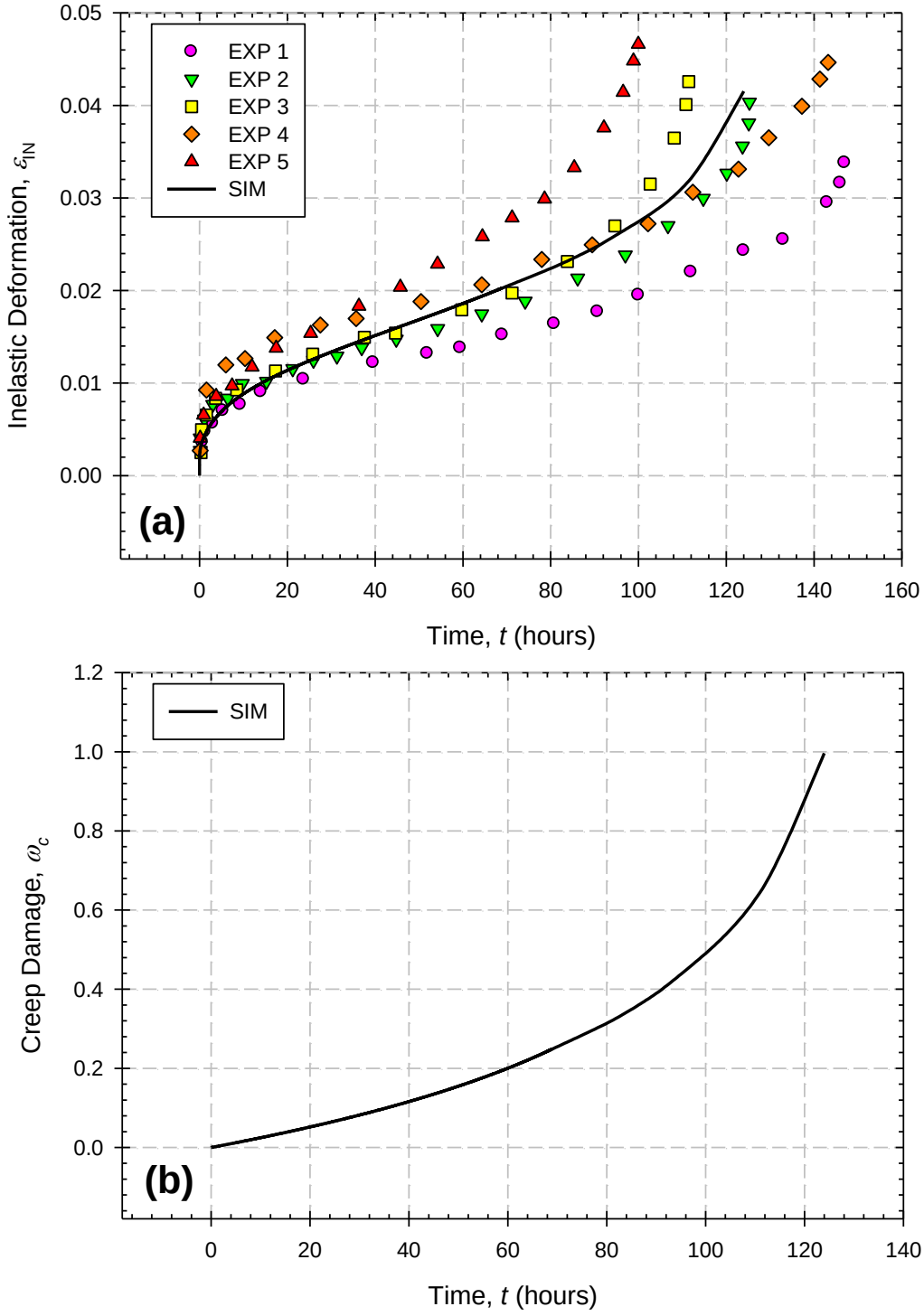

Figure 5.17 – Simulated (a) creep deformation and (b) damage at 300 MPa and 600°C using the hybrid model with creep damage

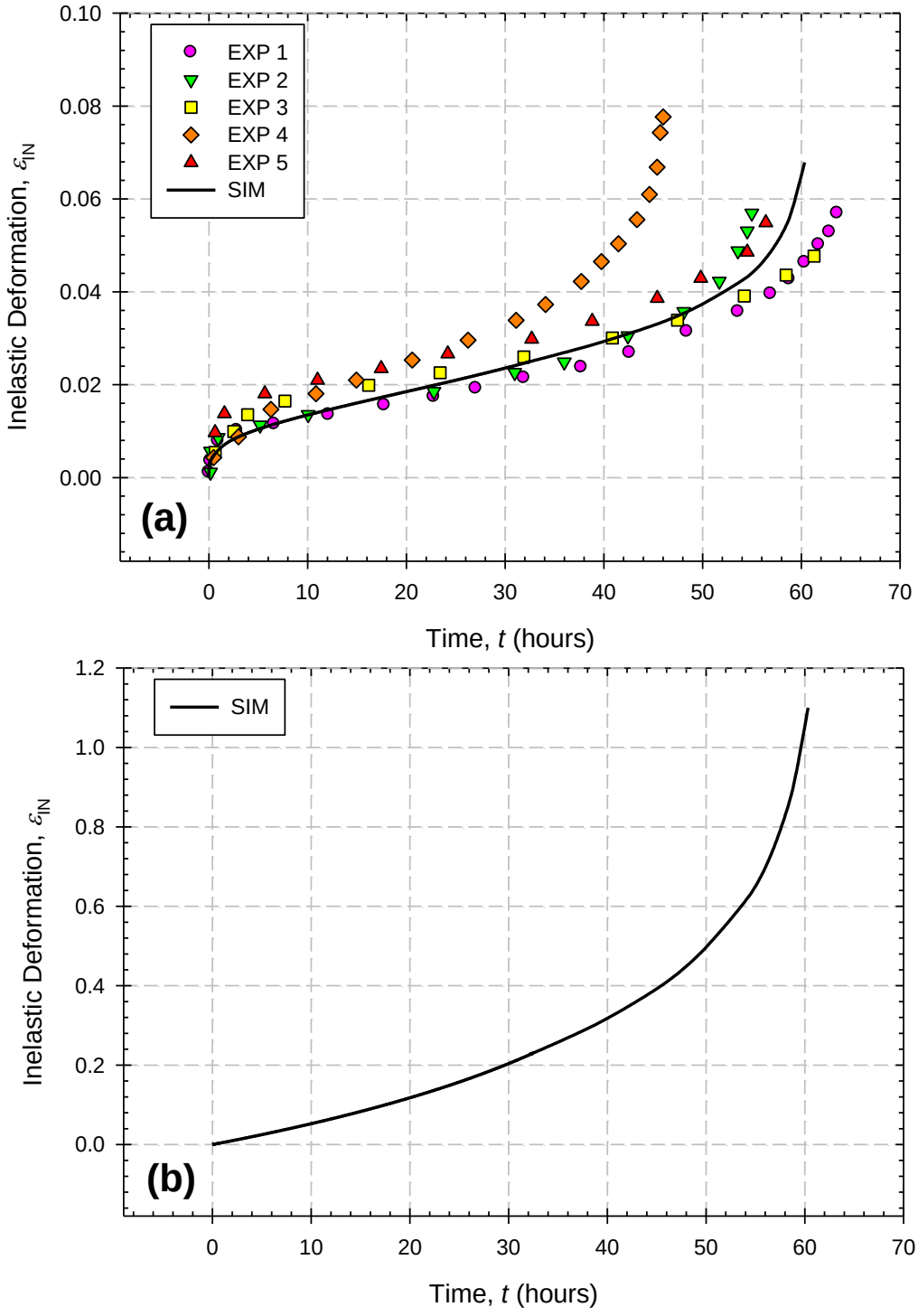

Figure 5.18 – Simulated (a) creep deformation and (b) damage at 320 MPa and 600°C using the hybrid model with creep damage

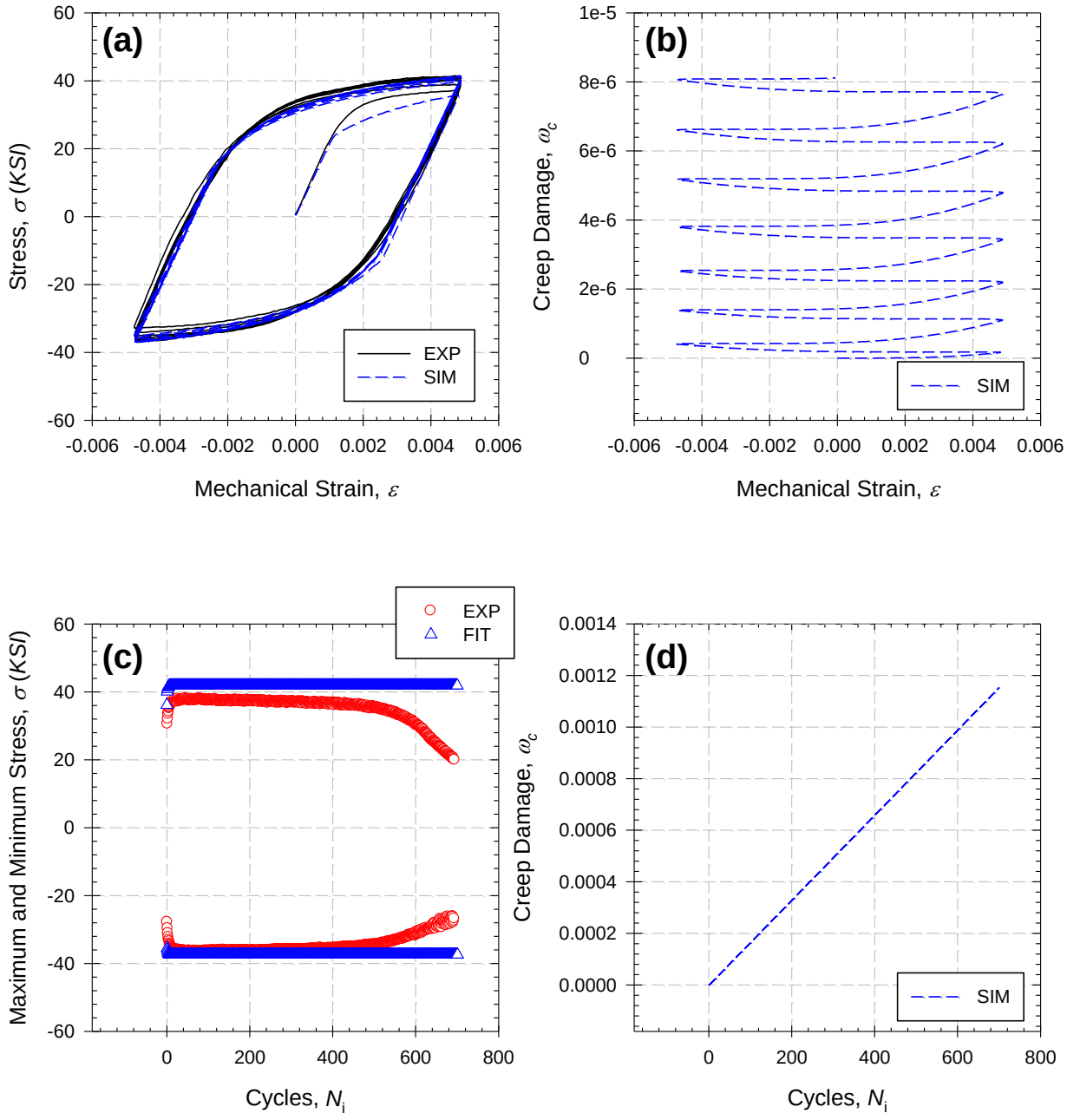

Figure 5.19 - Simulated fatigue tests $\Delta\varepsilon_T = 1\%$ and 600°C (a) stress-strain (b) damage-strain (c) cyclic stress-cycles and (d) damage-cycles using the hybrid model with creep damage

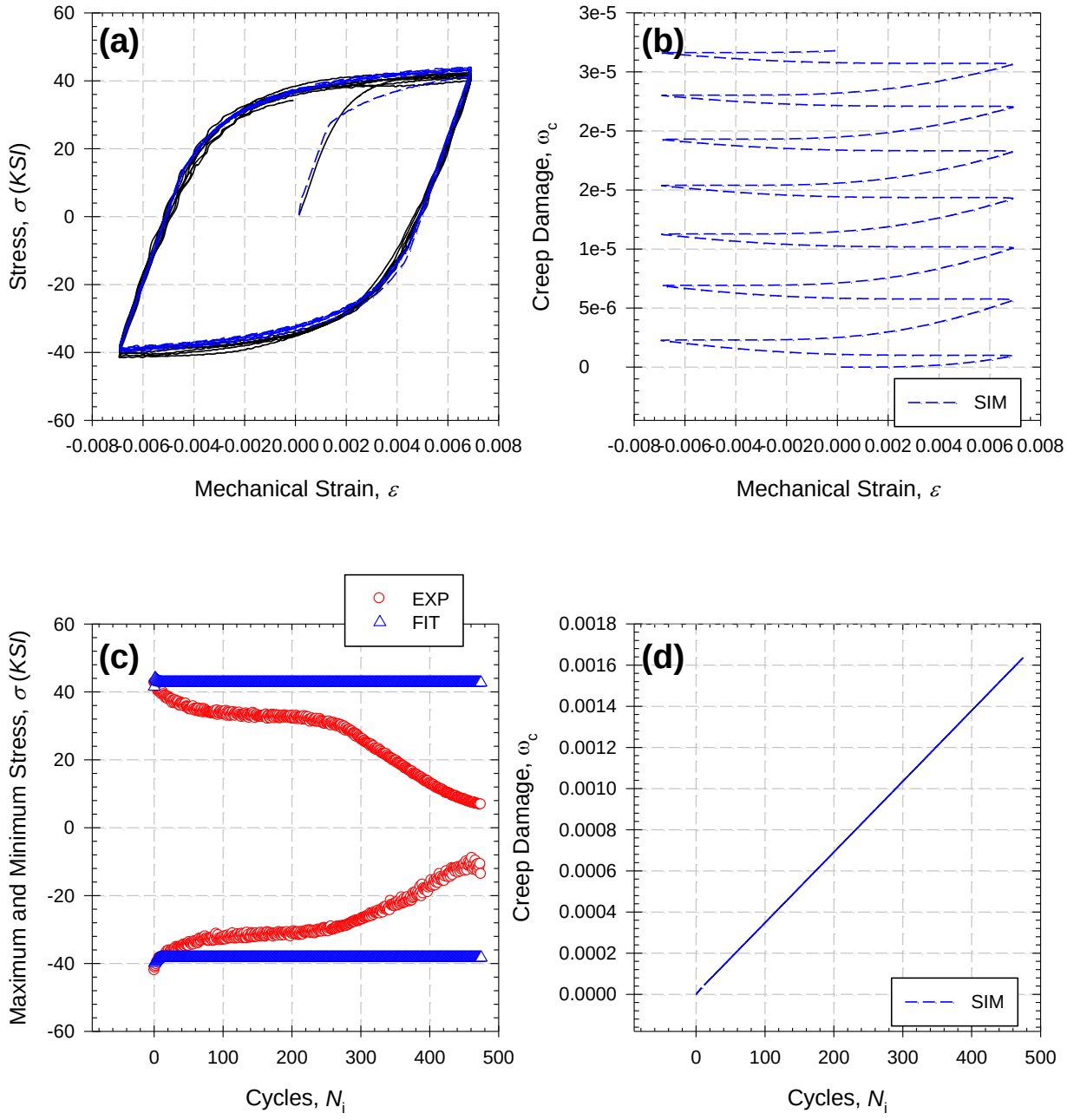

Figure 5.20 - Simulated fatigue test $\Delta\varepsilon_T = 1.4\%$ and 600°C (a) stress-strain (b) damage-strain (c) cyclic stress-cycles and (d) damage-cycles using the hybrid model with creep damage

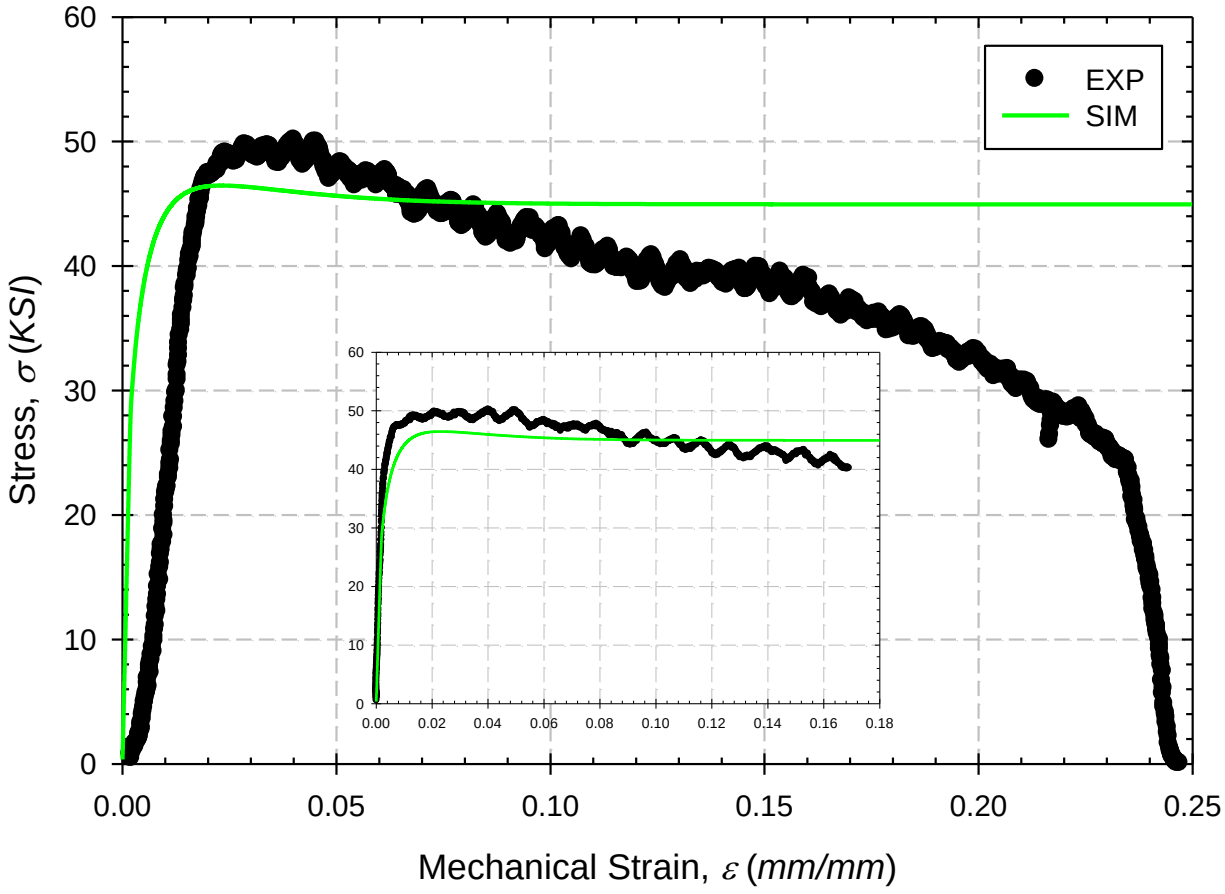

Figure 5.21 - Monotonic Tensile simulated at $\dot{\varepsilon} = 0.001/s$ and 600°C using the hybrid model with creep damage (large-crosshead, small extensometer)

It has been shown that the creep damage can be implemented in the hybrid model to produce the tertiary creep regime observed in creep deformation data without negatively impacting the ability to model fatigue behavior. The next step is to develop plastic/ductile and fatigue damage laws which produce the ductile and cyclic stress softening observed in mechanical testing. Towards, development of a plastic/ductile and fatigue damage law, an extensive literature review of existing continuum damage mechanics-based fatigue damage laws was conducted in section 2.3.2. Review papers by Fatemi and Yang show that a considerable effort has been expended in the development of fatigue damage models [73,212]. While many researchers have focused on, life-curve modifications methods, crack growth methods, and energy-based methods relatively few have investigate the continuum damage mechanics approach. One of the most commonly implemented CDM-based fatigue models was developed by Chaboche and Lesne as follows

$$\frac{d\omega}{dN} = D^{\alpha(\sigma_M,\bar{\sigma})}\left[\frac{\sigma_M - \bar{\sigma}}{M(\bar{\sigma})}\right]^{\beta} \qquad M(\bar{\sigma}) = M_0(1 - b\bar{\sigma}) \tag{5.40}$$

where α, β, M_0 and b are material constants, σ_M is the maximum stress, and $\bar{\sigma}$ is the mean stress [255]. This model has been extended to account for the stress ratio [256,257], fatigue limit [258], and frequency [259]. The classical CDM model is an excellent design tool which can provided life prediction for stable, sequential, and random stress or strain loading conditions; however, to model the constitutive response due to fatigue damage the equation must be interfaced with constitutive equations. Recently, a number of authors have attempted to develop unified viscoplasticity models with CDM-based fatigue damage [93,227]. In a model by Yang and Wei [93] the sum of the plastic, creep, and fatigue damage are interfaced with the

viscoplasticity constitutive model; however, evolution of isotropic and kinematic hardening internal variables is not considered. The fatigue limit is also not considered. Chow [227] developed a multiaxial unified viscoplasticity model where only plastic and fatigue damage are considered. The obstacles observed in literature will be overcome in the present work.

The development of the fatigue damage equation requires two components

- An equation describing how fatigue damage evolves
- An equation describing how fatigue damage interfaces with the viscous function

In the later, considering the work by Iino [251-254], it is observed that the gradient of the plastic zone under a fatigue test is much higher than during creep suggesting the general *h* function described in [Eq. (5.32)]. The following *h* function is proposed

$$h = \exp\left(\lambda_c \omega_c^{3/2} + \lambda_p \omega_p + \lambda_f \omega_f^{3/2}\right) \tag{5.41}$$

where λ_c, λ_p and λ_f are the damage-viscous function interface terms.

In the former, it is assumed that fatigue damage can be represented by the softening that occurs after cycle-stress saturation is reached. Literature shows that the stress range can be used as accumulative damage equation

$$D_i = 1 - \Delta\sigma_i / \Delta\sigma_0 \tag{5.42}$$

where $\Delta\sigma_0$ and $\Delta\sigma_i$ are the initial and current stress range [260,213]. A normalized analytical damage, D^*, derived from the stress amplitude is more appropriate and is described as follows

$$D_i^* = 1 - \frac{\Delta\sigma_i}{\Delta\sigma_0} \Big/ 1 - \frac{\Delta\sigma_f}{\Delta\sigma_0} \tag{5.43}$$

where $\Delta\sigma_i$ is the current stress amplitude, $\Delta\sigma_0$ is the cyclic saturated stress amplitude, and $\Delta\sigma_f$ is the final stress amplitude before rupture. This damage includes contributions from creep and fatigue damage. The stress amplitude can be separate into peak stresses $\sigma_{\max}$ and $\sigma_{\min}$ such that two damage curves are produced

$$D^*_{\max,i} = 1 - \frac{\sigma_{\max,i}}{\sigma_{\max,0}} \Big/ 1 - \frac{\sigma_{\max,f}}{\sigma_{\max,0}} \cdot \quad D^*_{\min,i} = 1 - \frac{\sigma_{\min,i}}{\sigma_{\min,0}} \Big/ 1 - \frac{\sigma_{\min,f}}{\sigma_{\min,0}}, \tag{5.44}$$

This allows damage to be predicted with respect to time instead of cycle number at the cost of scatter between the $D^*_{\max,i}$ and $D^*_{\min,i}$ curves respectively. Scatter is observed in materials that exhibit pre-existing asymmetry which results in asymmetric evolution of maximum and minimum peak stresses. Equation (5.44) is exercised for the 1% and 1.4% fatigue tests, with the results plotted in Figure 5.22. It is observed in the 1% fatigue tests Figure 5.22(a) that fictitious large values of analytical damage appear before cyclic saturation is reached due to initial hardening. After saturation, damage exponentially grows with a similar trajectory to creep damage (examining Figure 5.17 and Figure 5.18 in comparison). In the cases of the 1.4% fatigue test, Figure 5.22(b) fictitious large and negative values of analytical damage appear before cyclic saturation is reached due to initial softening. An almost linear damage evolution is observed beyond this point, dissimilar to the 1% fatigue test. Both behaviors can be modeled using a damage rate equation that includes an exponential function of the current damage state.

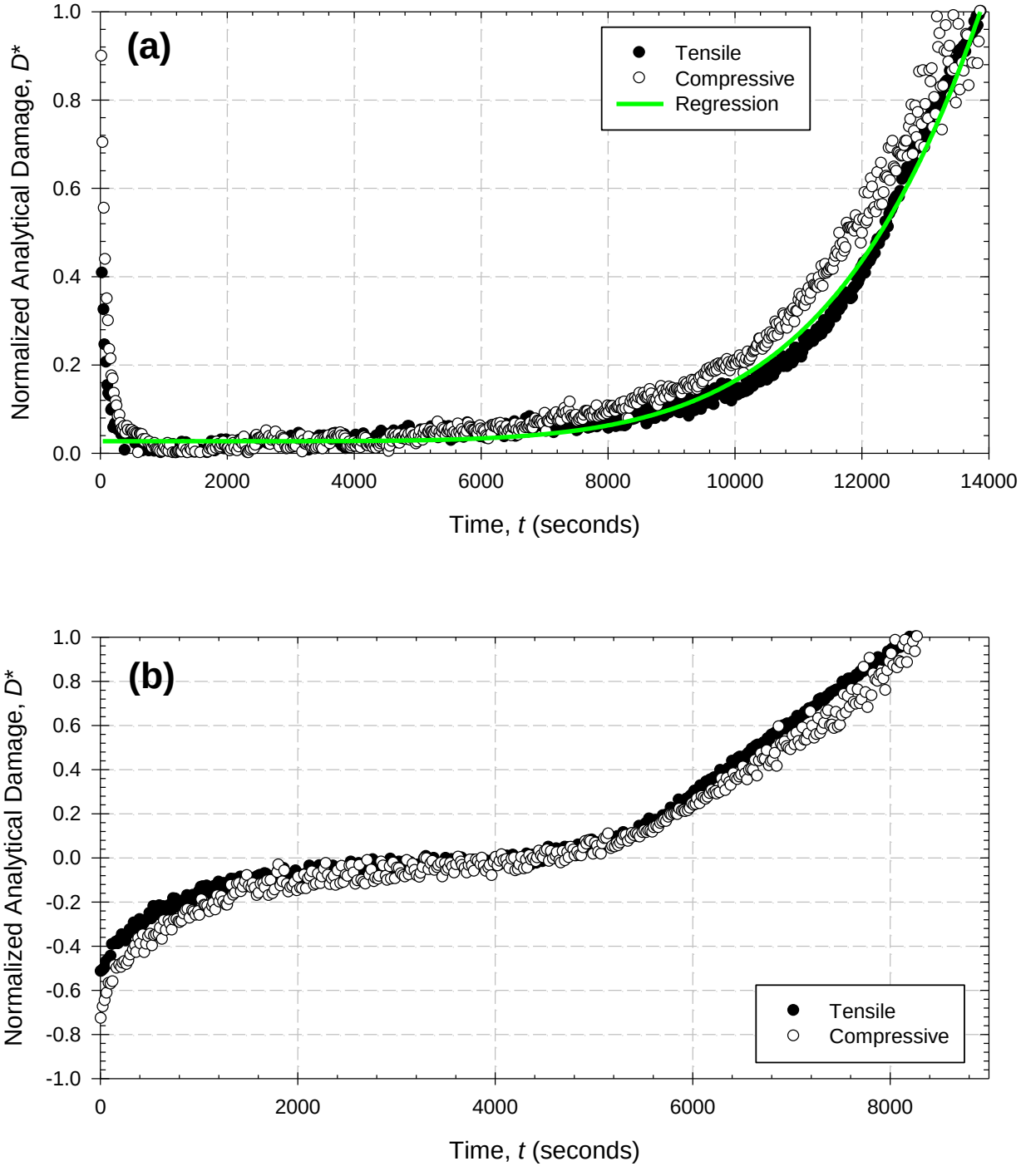

Figure 5.22 - Analytical damage using peak stresses (a) 1% and (b) 1.4% strain range fatigue tests at $\dot{\varepsilon} = 0.001/s$ and 600°C

As discussed in the background (section 2.4), the activation of creep and fatigue damage depend on the applied boundary conditions (see Figure 2.9 and Figure 2.10).This is also true for plastic/ductile damage. Under isothermal temperature and when temperature is above the creep activation limit, creep will always be active, as long as stress is greater than zero $\sigma > 0$. Fatigue damage is active when the fatigue limit is exceeded (a criterion of $\Delta\sigma > \sigma_f$) and only during transient boundary conditions ($|\dot{\sigma}| > 0, \quad |\dot{\varepsilon}| > 0$). Plastic damage is active when the ultimate tensile strength has been exceed ($\sigma \geq UTS$ and remains active thereafter $t \geq t_{uts}$) and only during transient boundary conditions ($|\dot{\sigma}| > 0, \quad |\dot{\varepsilon}| > 0$). In the presence of load or displacement holds ($\dot{\sigma} = 0, \quad \dot{\varepsilon} = 0$), the only active damage mechanism is creep. In the absence of load, there is no damage ($\dot{\sigma} = \dot{\varepsilon} = 0$). Schematics of the mechanical response of metal subject to various applied boundary conditions are provided in Figure 5.23 and Figure 5.24. Using the schematics a special activation term is developed to enable fatigue and plastic/ductile damage when transient boundary conditions are observed. The transient activation equation, $\psi = f(\dot{\sigma}, \dot{\varepsilon})$, takes the following form

$$\psi = \text{sgn}\left[\text{sgn}\left(|\dot{\sigma}|\right)\text{sgn}\left(|\dot{\varepsilon}|\right)\right], \quad \text{sgn}(x) = \begin{cases} -1 & x < 1 \\ 0 & x = 0 \cdot \\ 1 & x > 1 \end{cases} \tag{5.45}$$

The activation equation can be extended for anisotropic materials by using Hill's analogy or by replacing the scalar stress and strain rates with vectors.

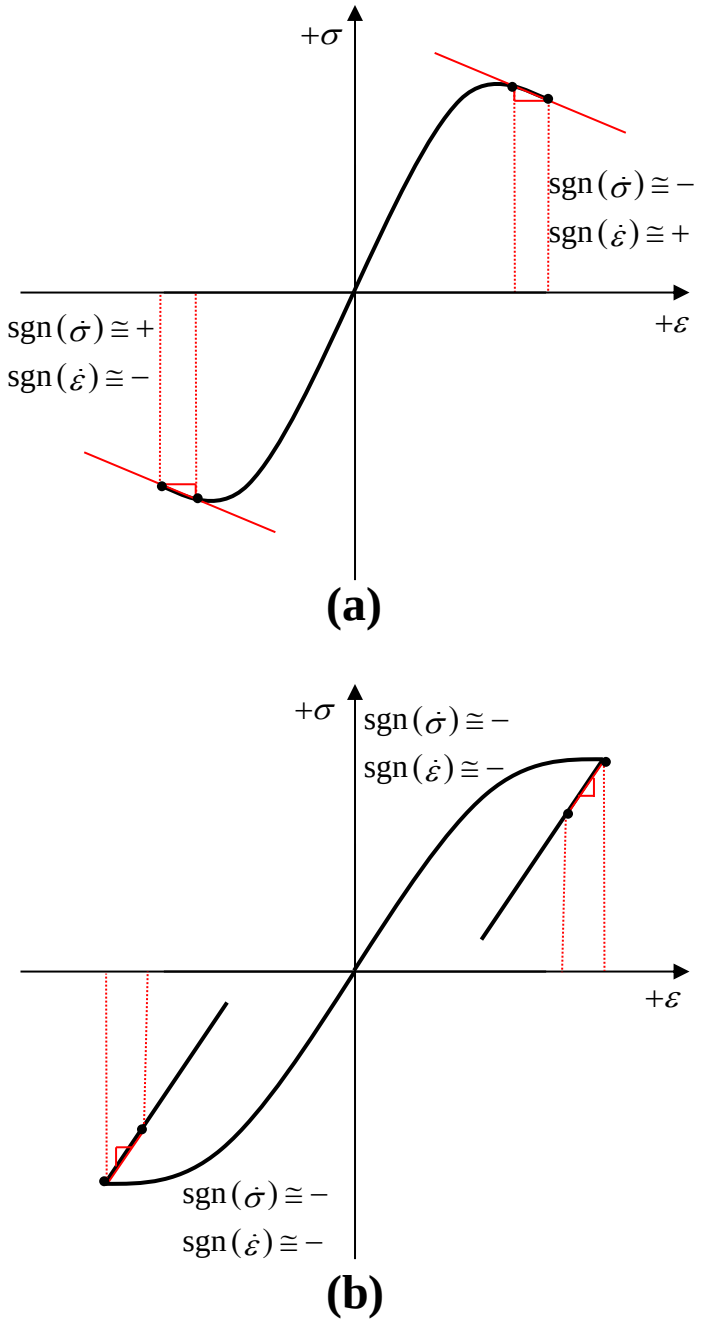

Figure 5.23 - Schematic of hybrid model response under (a) tensile and compressive monotonic tension (b) and tensile and compressive unload during fatigue

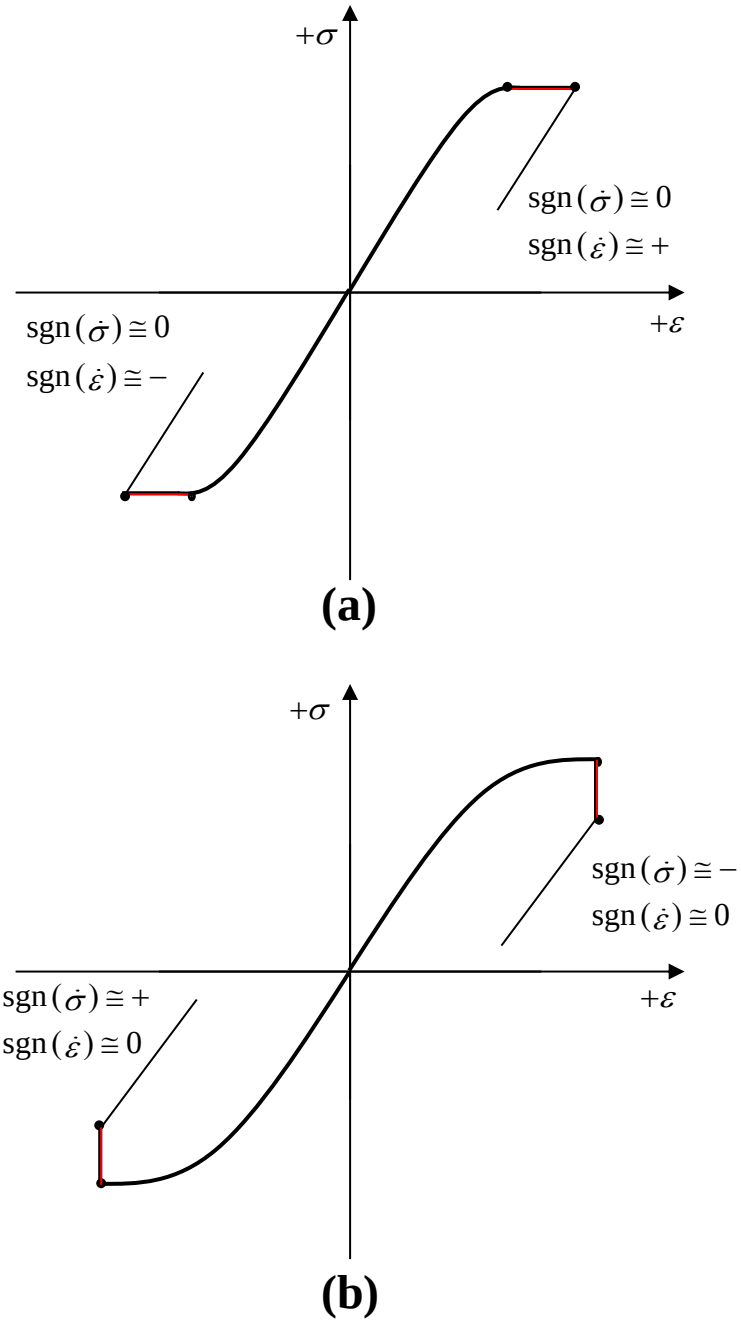

Figure 5.24 - Schematic of hybrid model response under (a) load-controlled tensile hold (b) and displacement-controlled tensile hold

In the current study, the fatigue damage law is proposed as follows

$$\dot{\omega}_f = \frac{1-\exp\left(-\phi_f\right)}{\phi_f} A_0 \sinh\left(\frac{\sigma - R}{D}\right)^{\chi_f} \exp\left(\phi_f \omega\right) \cdot \psi \tag{5.46}$$

where ϕ_f is the damage trajectory constants of the fatigue damage. Similar to the damage trajectory constant of the creep damage model [Eq. (4.35)], the fatigue version controls size of the variation of $\partial\omega_f(t)$ with an infinitesimal variation of stress $\partial\sigma(t)$. When ϕ_f is increased, the stress sensitivity of the damage model increases. The irreversible portion of the viscous function [Eq. (5.5)] is used to build the damage law, similar to the technique used by Gurson [250]. This was done, because indefinite integration of the above equation under the conditions of fatigue results in a complex solution which cannot be easily used to predict rupture time a priori. Using the inelastic strain rate reduces complexity.

A simple fatigue damage criterion is proposed as follows

$$\sigma \geq \frac{\sigma_f}{2}, \quad \sigma \geq \frac{\sigma_{UTS}}{4} \tag{5.47}$$

where σ is an equivalent stress (such as von Mises) and σ_f is the fully reversed fatigue limit. The fatigue limit is assumed to equal 50% of the ultimate tensile strength. Asymmetry of the fatigue damage criterion can be assumed by incorporating an anisotropic equivalent stress such as Hill's anisotropic analogy [59] or by determine a fatigue limit vector which can be converted into an equivalent fatigue limit. The ultimate tensile strength can be found using [Eq. (5.20)].

Two separate optimizations must be performed to obtain:

- The coefficient of the fatigue-damage/viscous-function interface λ_f
- The fatigue damage constants, ϕ_f and χ_f

The former is obtained by using the regressed analytical fatigue damage (of Figure 5.22) to replace fatigue damage in the *h* function [Eq. (5.41)] of the viscous function [Eq. (5.5)]. The constant λ_f is optimized by comparing the final peak stress before rupture of the 1% fatigue experimental data (Figure 5.19c) to the simulated. The least square function for the final peak stress takes the following form

$$SUM = \left[\frac{100\left(\sigma_{EXP} - \sigma_{SIM}\right)}{\sigma_{EXP}} \right]^2 \tag{5.48}$$

where σ_{EXP} and σ_{SIM} are the experimental and simulated final peak stresses respectively. The regressed analytical damage equation follows

$$D^* = 0.02714 + 1.37 \cdot 10^{-25} t^6 \tag{5.49}$$

The simulated annealing algorithm settings of Table 5.2 were used with the exception that only one constants λ_f (*N*=1) is optimized. The lower *LB* and upper bound *UB* of λ_f is restricted to 0 and 100 units respectively. The initial guess value was set to equivalent to the λ_1 constant. The final *SUM* was 1.13860E-05 units with the least squares evolution depicted in Figure 5.25. A total of 321 evaluations where conducted with 121 accepted and 0 rejected. The final temperature is 0.305175E-02 units. The optimal value of λ_f is 17.332 shown in Table 5.4.

To obtain the later, using the newly discovered λ_f, USHARP 3.0 is reconfigured to optimize ϕ_f and χ_f of the fatigue damage evolution [Eq. (5.46)] to the analytical damage data for the 1% fatigue test depicted in Figure 5.22(a). The simulated annealing algorithm settings of Table 5.2 were used with the exception that two constants (*N*=2) are optimized. The initial guess constants where set equivalent to those of the creep damage law (Table 4.2). The lower *LB* and

upper bound, initial guess and final values are provided in Table 5.4. The final *SUM* was 8.626256 units with the least squares evolution depicted in Figure 5.26. A total of 1681 evaluations where conducted with 594 accepted and 22 rejected. The final temperature is 0.953674E-04 units.

The results of monotonic, creep, and fatigue simulations (with creep and fatigue damage enabled) are provided in Figure 5.27 to Figure 5.31. Examining the results of the creep simulations (Figure 5.27 and Figure 5.28), it is observed that fatigue damage has negligible influence on the damage evolution rate. The fatigue component is only active during the load ramping phase of the creep tests where the stress has exceeded. Examining the monotonic tensile test (Figure 5.29), it is observed that fatigue damage has negligible influence on the stress-strain curve. The post ultimate tensile strength softening suggests that a plastic/ductile damage equation is required. In the 1% fatigue simulation (Figure 5.30), the model is able to closely predict the stress range softening which occurs after cyclic saturation. Using a critical damage of unity, it is found that the model accurately predicts the cycles to failure for both 1 and 1.4% fatigue tests. The model does not accurately predict the cyclic stress softening observed in the 1.4% fatigue test (Figure 5.31). This can be attributed to the atypical mechanical behavior produced in this particular specimen.

Table 5.4 – Optimal fatigue damage constants

Material Constant	Units	Lower Bound	Upper Bound	Initial Guess	Final Value
ϕ_f		1	25	22.790	19.376
χ_f		0	1	0.95704	0.91691
λ_f		0	100	3.586404	17.332

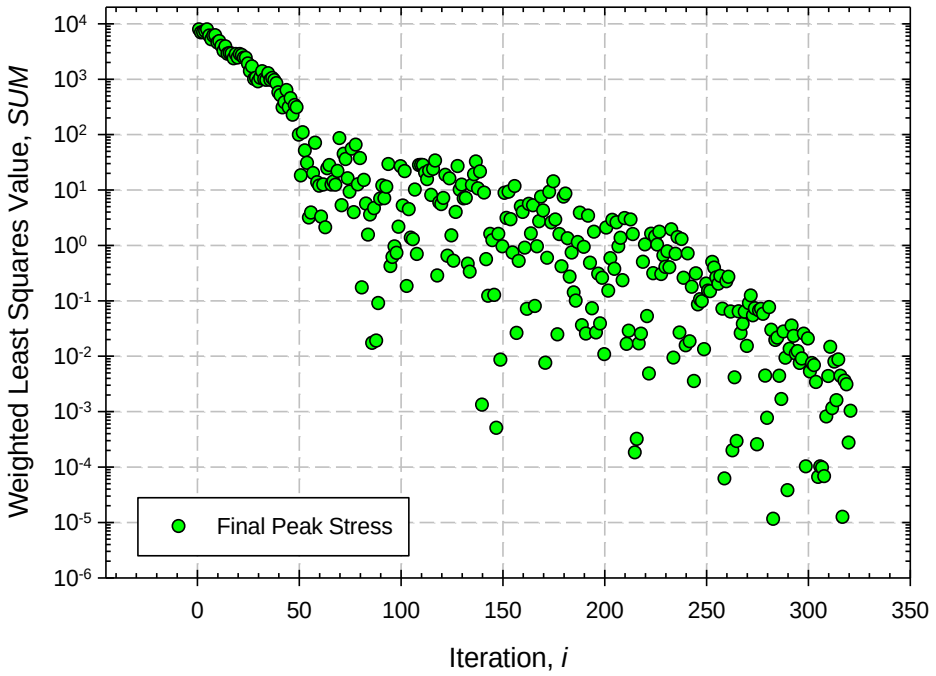

Figure 5.25 - Least square values during optimization of the λ_p constant

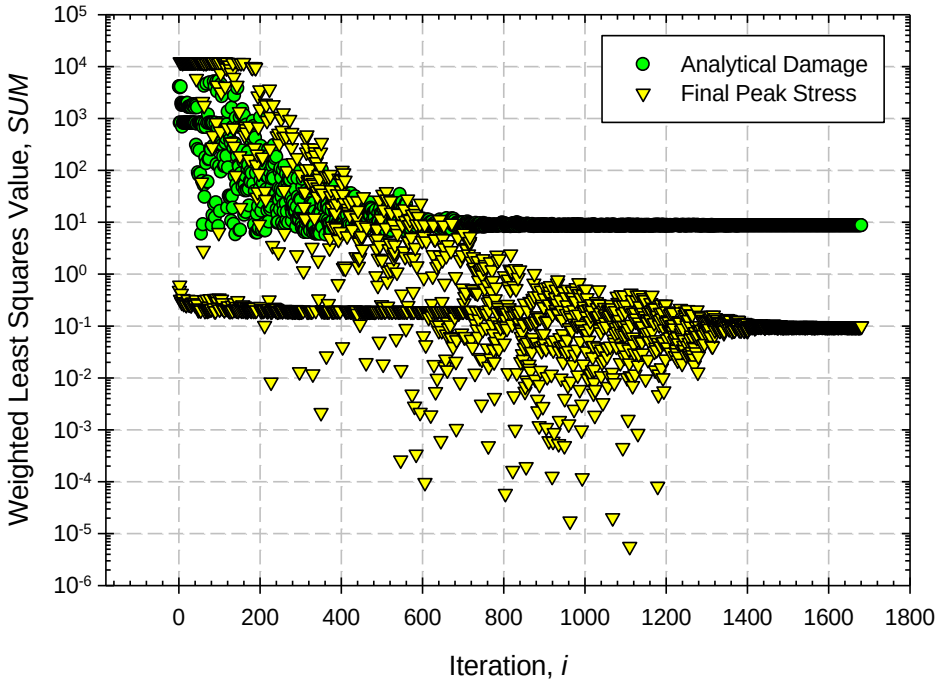

Figure 5.26 - Least square values during optimization of ϕ_f and χ_f constants

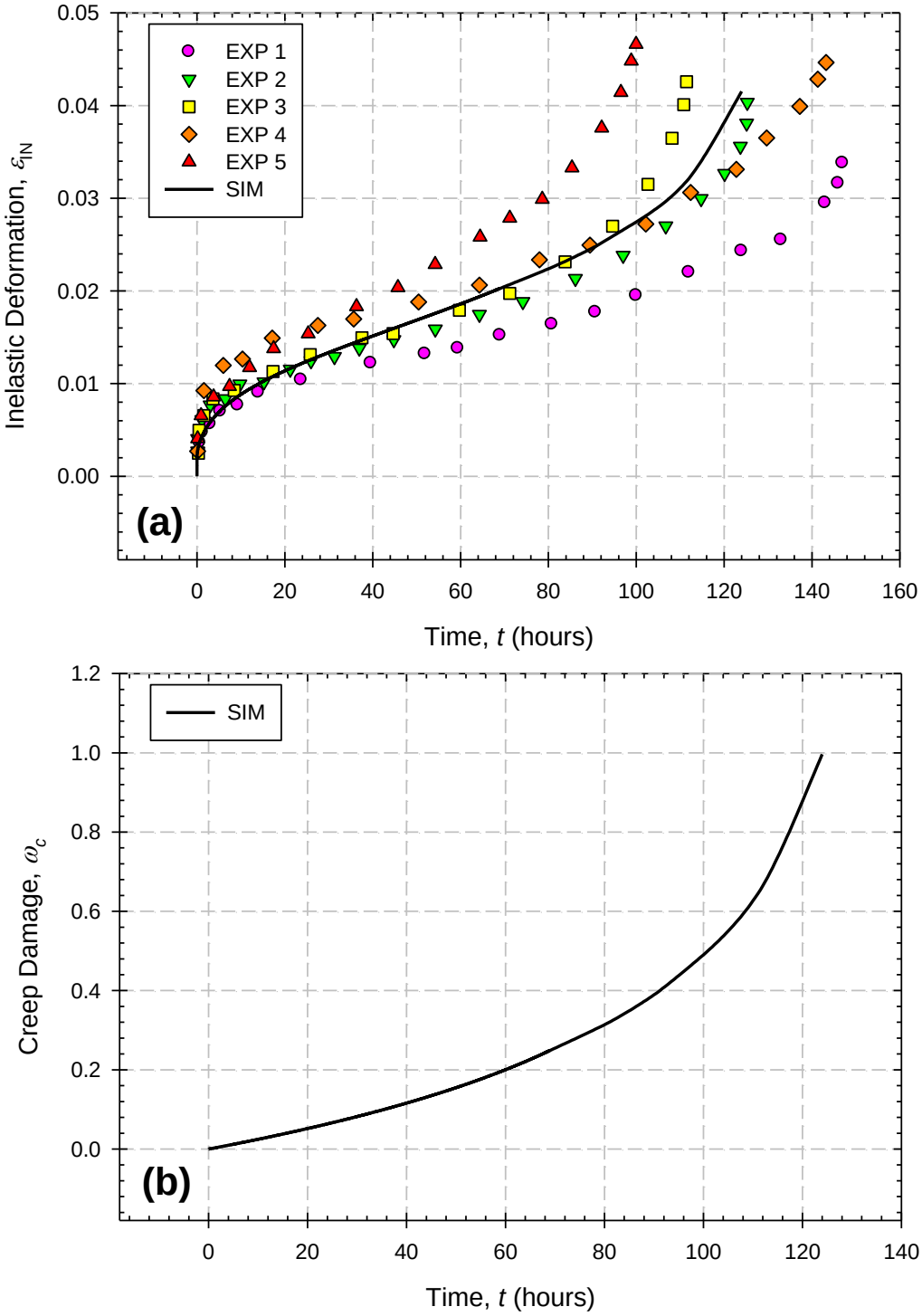

Figure 5.27 - Simulated (a) creep deformation and (b) damage at 300 MPa and 600°C using the hybrid model with creep and fatigue damage

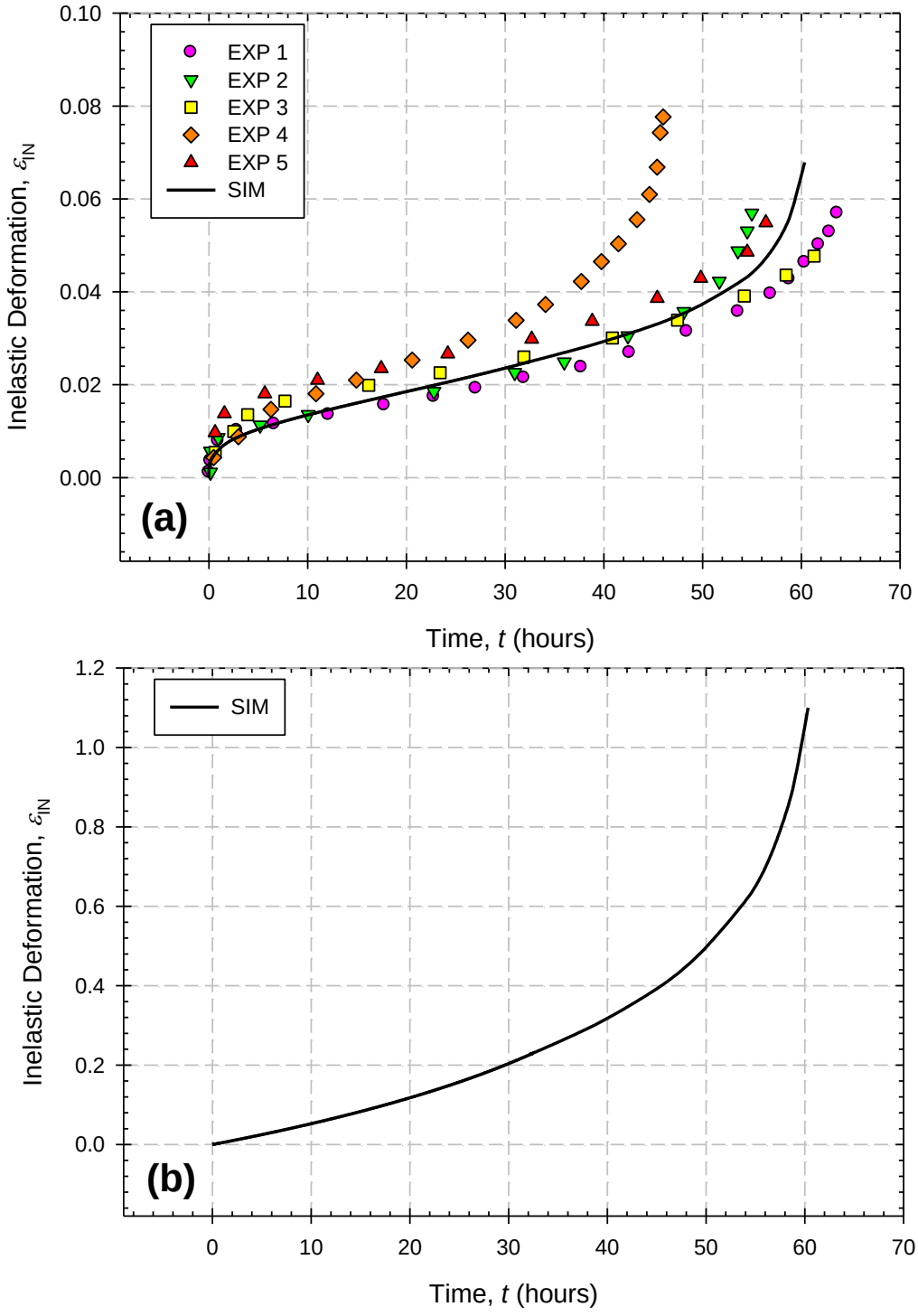

Figure 5.28 - Simulated (a) creep deformation and (b) damage at 320 MPa and 600°C using the hybrid model with creep and fatigue damage

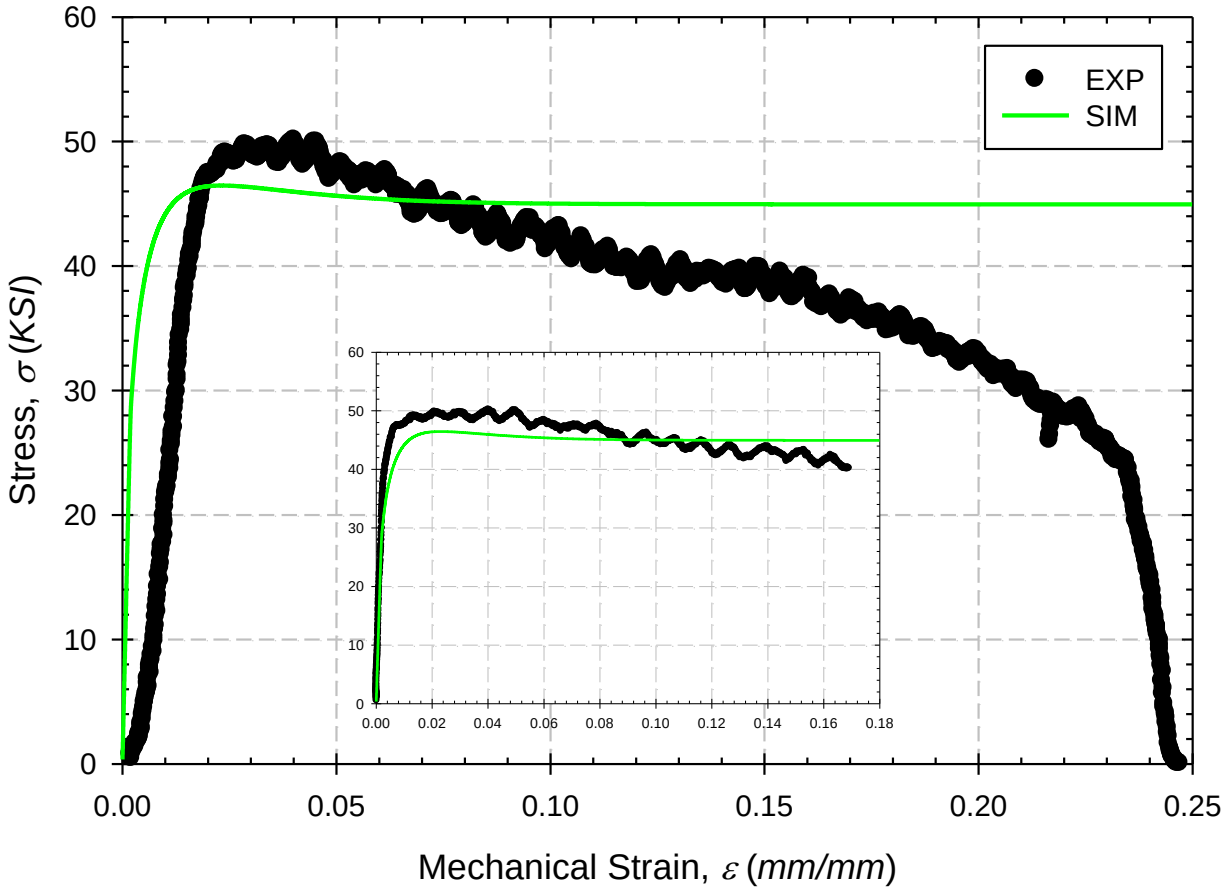

Figure 5.29 - Monotonic Tensile simulated at $\dot{\varepsilon} = 0.001/s$ and 600°C using the hybrid model with creep and fatigue damage (large-crosshead, small extensometer)

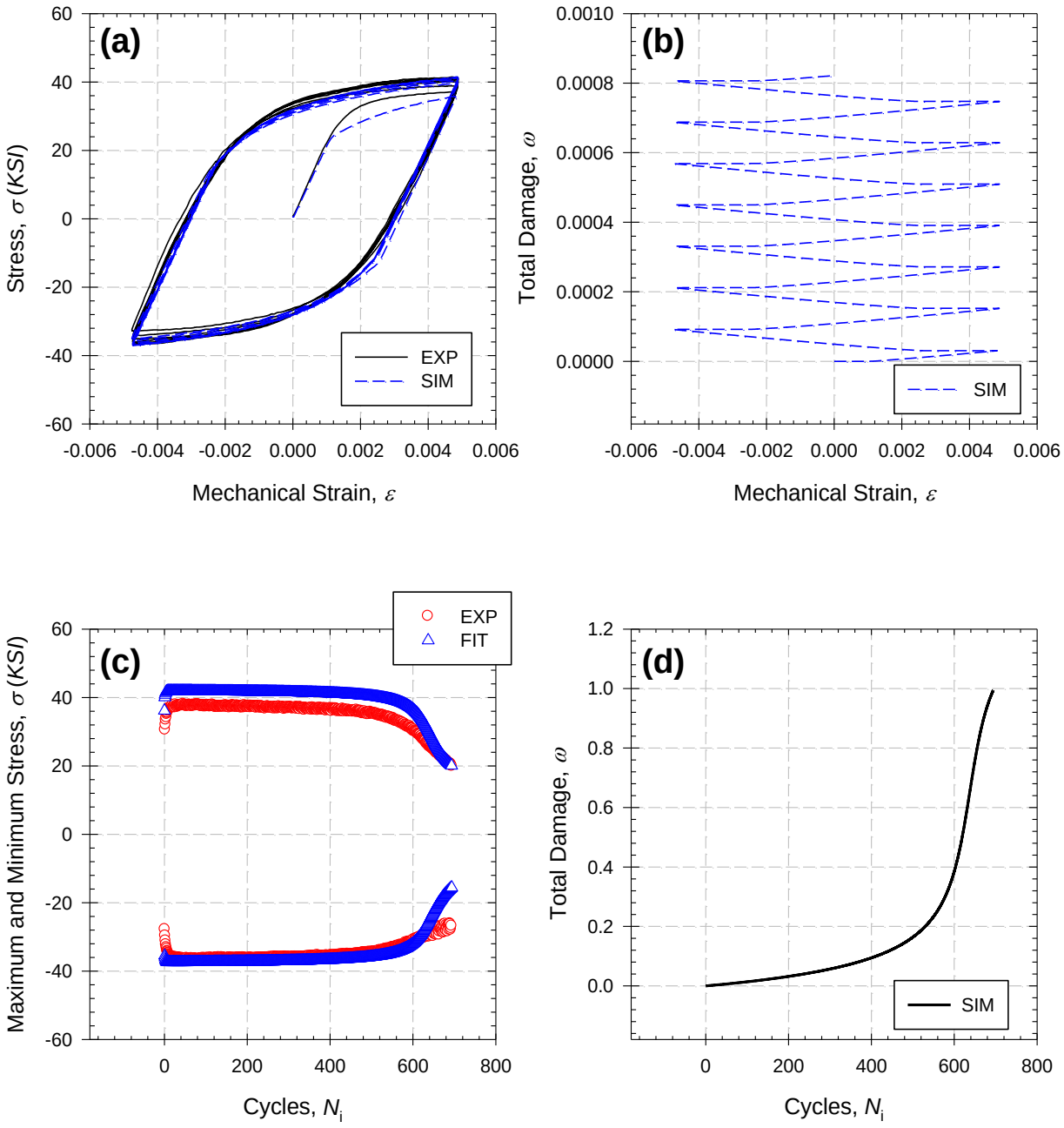

Figure 5.30 - Simulated fatigue tests $\Delta\varepsilon_T = 1\%$ and 600°C (a) stress-strain (b) damage-strain (c) cyclic stress-cycles and (d) damage-cycles using the hybrid model with creep and fatigue damage

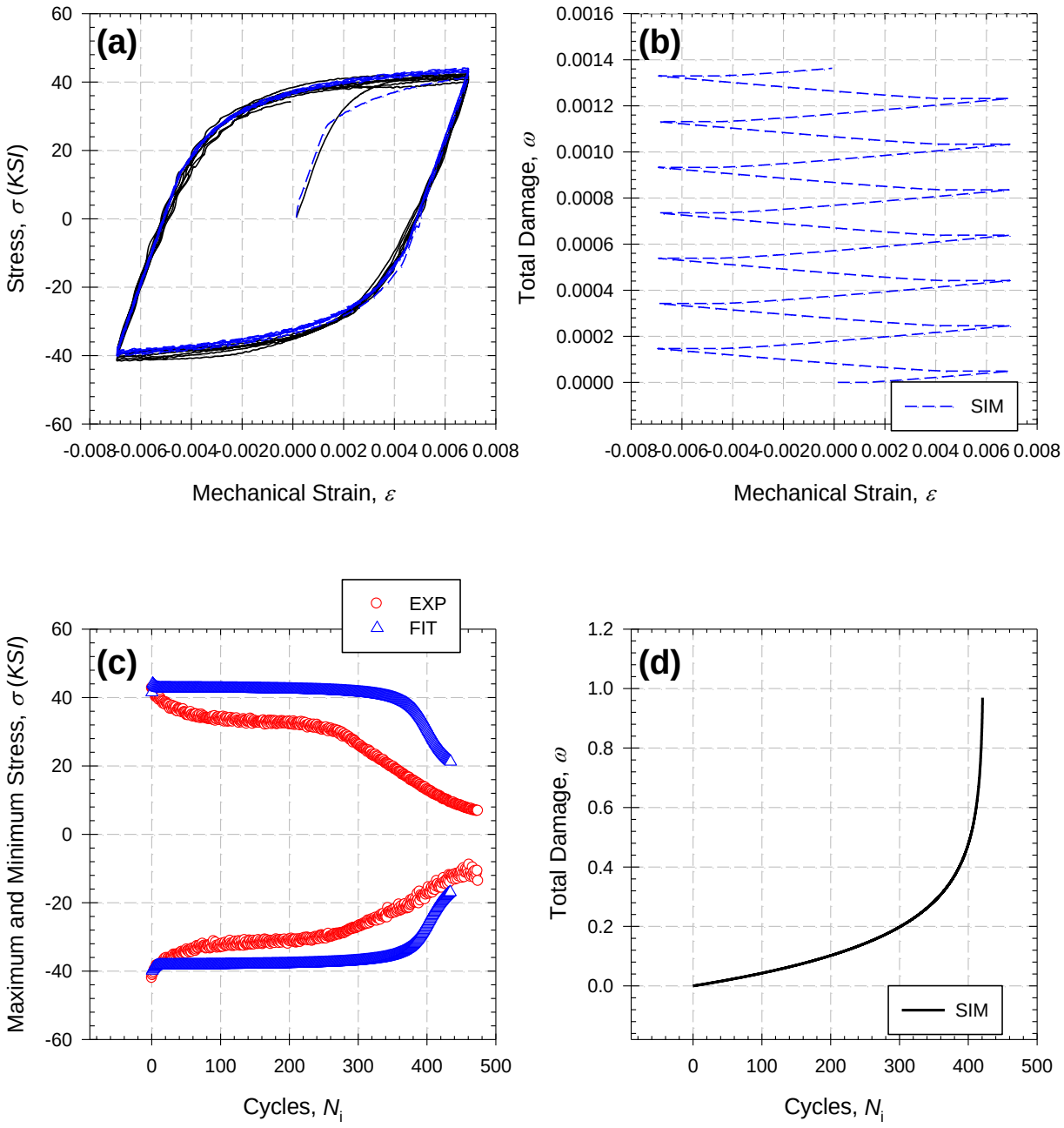

Figure 5.31 - Simulated fatigue tests $\Delta\varepsilon_T = 1.4\%$ and 600°C (a) stress-strain (b) damage-strain (c) cyclic stress-cycles and (d) damage-cycles using the hybrid model with creep and fatigue damage

An analytical value of plastic/ductile damage must be determined from monotonic data. Consider the evolution of the engineering stress after the ultimate tensile strength has been reached. The material continuously softens to zero stress at rupture. A normalized analytical damage, derived from stress is described as follows

$$D_i^* = 1 - \frac{\sigma_i}{\sigma_{UTS}} \tag{5.50}$$

where σ_{UTS} is the ultimate tensile strength and σ_i is the current stress. Equation (5.50) is exercised using the available monotonic data with the results plotted in Figure 5.32. Fictitious values of damage are produced before the ultimate tensile strength is reached.

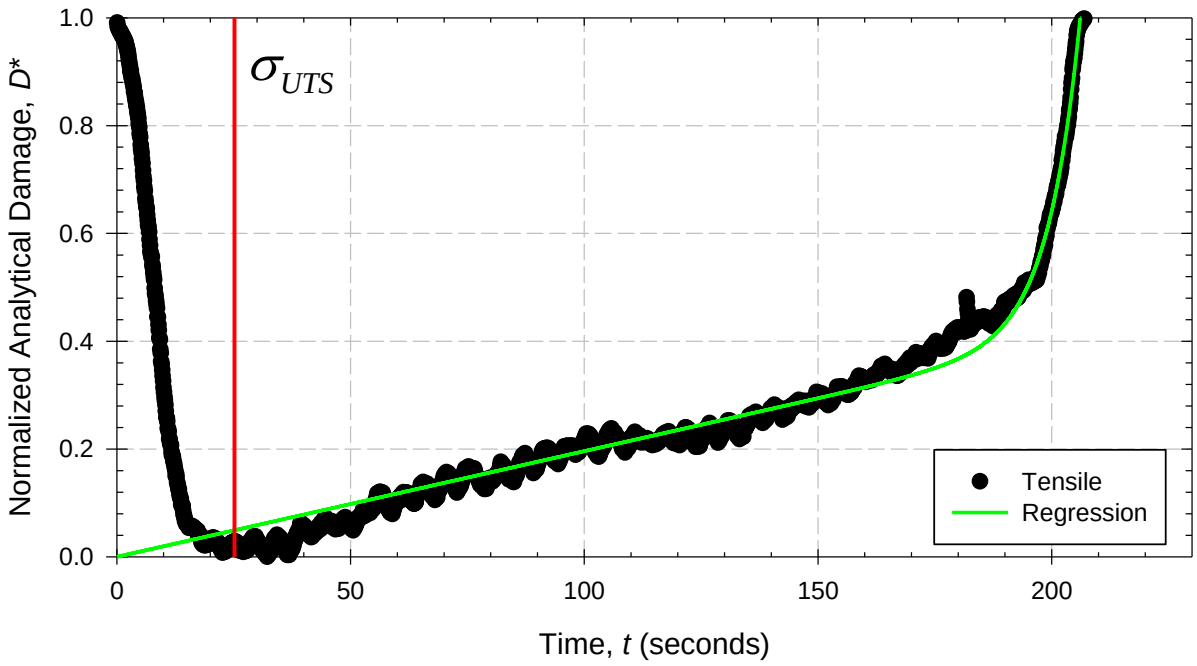

Figure 5.32 - Analytical damage of monotonic damage using ultimate tensile strength

In the current study, the plastic/ductile damage law is proposed as follows

$$\dot{\omega}_p = \frac{1-\exp\left(-\phi_p\right)}{\phi_p} A_0 \sinh\left(\frac{\sigma - R}{D}\right)^{\chi_p} \exp\left(\phi_p \omega\right) \cdot \psi \tag{5.51}$$

where ϕ_p is the damage trajectory constants of the plastic/ductile damage. The plastic/ductile damage evolution, $\dot{\omega}_p$ is a function of the total damage ω term [Eq. (5.31)].

The key to predicting the onset of plastic/ductile damage is indentifying the material constants and/or internal state variable associated with the onset of ductile softening. Traditional methods involve using yield surfaces or critical strain to predict the onset and accumulation of plastic/ductile damage [250,261]. In the current study, it is postulated that plastic/ductile damage doesn't arise until the ultimate tensile strength has been exceeded such that

$$\sigma \geq UTS \tag{5.52}$$

where σ is an equivalent stress and *UTS* is the ultimate tensile strength. Once the plastic/ductile damage surface is violated, plastic/ductile damage can occur at anytime $t \geq t_{uts}$ but only when transient boundary conditions are applied given by ψ . An approximation of the *UTS* can be analytically calculated using [Eq. (5.20)].

For the plastic/ductile damage, two optimizations must be performed for:

- The coefficient of the fatigue-damage/viscous-function interface λ_p
- The fatigue damage constants, ϕ_p and χ_p

The former is obtained by using the regressed analytical plastic/ductile damage (of Figure 5.32) to replace plastic/ductile damage in the *h* function [Eq. (5.41)] of the viscous function [Eq.

(5.5)]. The constant λ_p is optimized by comparing the experimental final stress to the simulated. The least square function for the final stress takes the following form

$$SUM = \left[\frac{100\left(\sigma_{EXP} - \sigma_{SIM}\right)}{\sigma_{EXP}} \right]^2 \tag{5.53}$$

where σ_{EXP} and σ_{SIM} are the experimental and simulated final stresses respectively. In the real world, the final stress is zero; however, to avoid divide by zero the time step just before zero stress is reached is selected. The regressed analytical damage equation follows

$$D^* = 0.00196 \cdot t + 9.395 \cdot 10^{-12} t^{0.02265 \cdot t} \tag{5.54}$$

as depicted in Figure 5.32. The simulated annealing algorithm settings of Table 5.2 were used with the exception that only one constants λ_p (N=1) is optimized. The lower *LB* and upper bound *UB* of λ_p is restricted to 1 and 50 units respectively. The initial guess value was set to equivalent to 25 units. The final *SUM* was 4.9275107 units with the least squares evolution depicted in Figure 5.33. A total of 441 evaluations where conducted with 190 accepted and 4 rejected. The final temperature is 0.476837E-04 units. The optimal value of λ_p is 38.806 listed in Table 5.5.

To obtain the later, using the newly discovered λ_p, USHARP 3.0 is reconfigured to optimize ϕ_p and χ_p of the plastic/ductile damage evolution [Eq. (5.51)] to the regressed analytical damage [Eq. (5.54)]. The simulated annealing algorithm settings of Table 5.2 were used with the exception that two constants (N=2) are optimized. The initial guess constants where set equivalent to those of the fatigue damage law (Table 5.4). The lower *LB* and upper bound *UB*, initial guesses, and final values are provided in Table 5.5. The final *SUM* was

30.72955 units with the least squares evolution depicted in Figure 5.34. A total of 2001 evaluations where conducted with 758 accepted and 0 rejected. The final temperature is 0.5960464E-05 units.

The results of creep, monotonic, and fatigue simulations are provided in Figure 5.35 to Figure 5.39. In the monotonic simulation (Figure 5.37) the large figure is the cross head displacement, while the small figure is the displacement recorded using an extensometer. The optimization was conducted using simulated boundary conditions that produce a constant strain rate of $\dot{\varepsilon} = 0.001/s$. The scatter observed in the experimental data is due to inaccuracy in temperature control. The induction heating control exhibited temperature oscillations which produce fluttering records of displacement. The plastic/ductile damage model produces a reasonable prediction of elongation. An interesting feature of the constitutive model is that the stress cannot soften below the value of the steady-state rest stress, R_{ss}. Both the creep (Figure 5.35 and Figure 5.36) and fatigue behavior (Figure 5.38 and Figure 5.39) are unchanged due to plastic/ductile softening condition not being exceeded. The plastic damage successfully models the monotonic behavior of the subject material.

Table 5.5 – Optimal plastic damage constants

Material Constant	Units	Lower Bound	Upper Bound	Initial Guess	Final Value
ϕ_p	*unitless*	1	100	19.376	50.786
χ_p	*unitless*	1	100	1.1	1.2042
λ_p	*unitless*	1	50	25	38.806

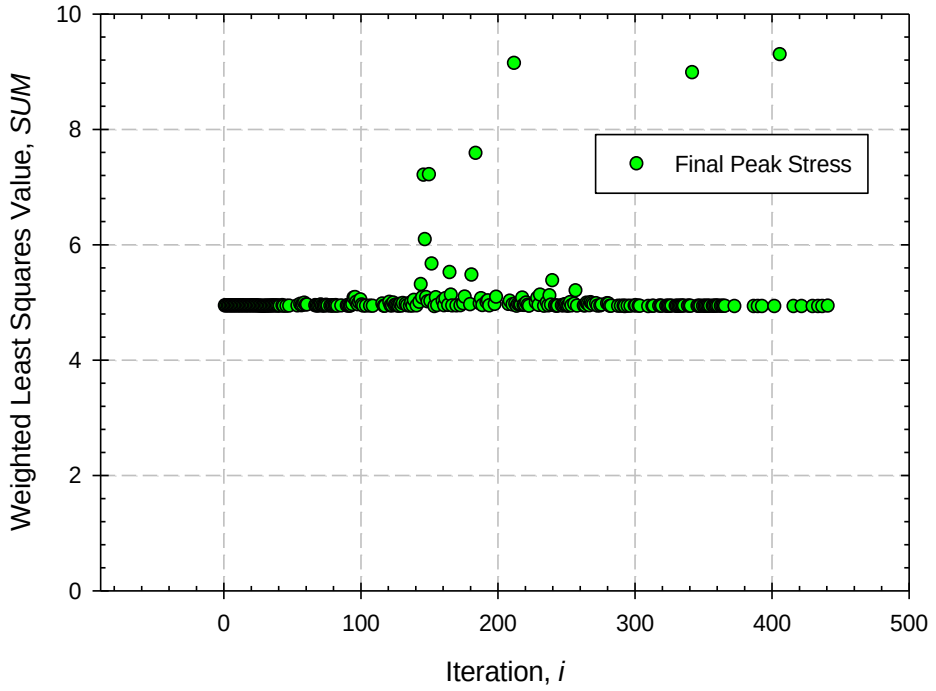

Figure 5.33 - Least square values during optimization of the λ_p constant

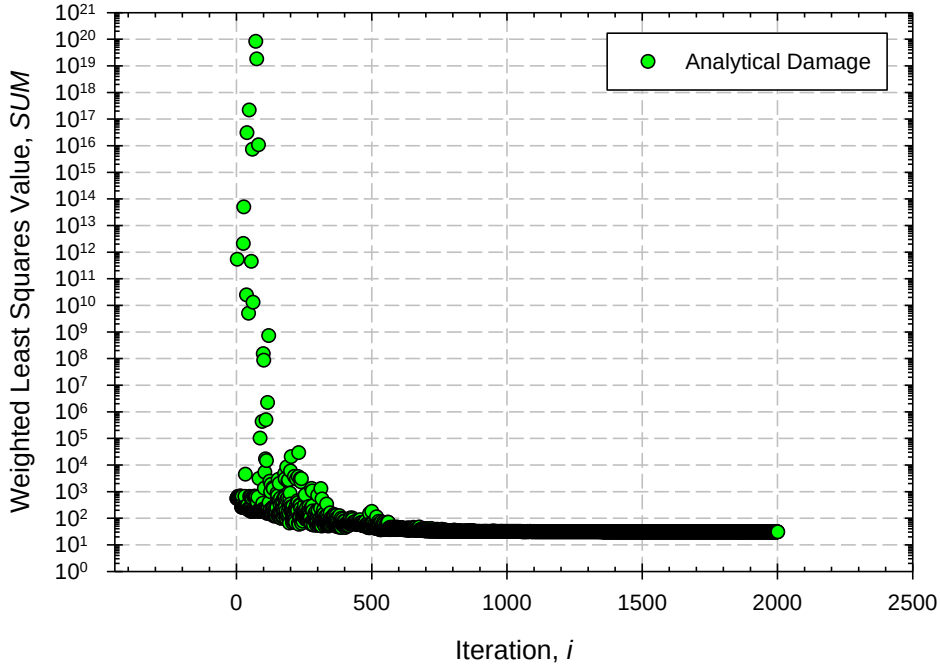

Figure 5.34 - Least square values during optimization of ϕ_p and χ_p constants

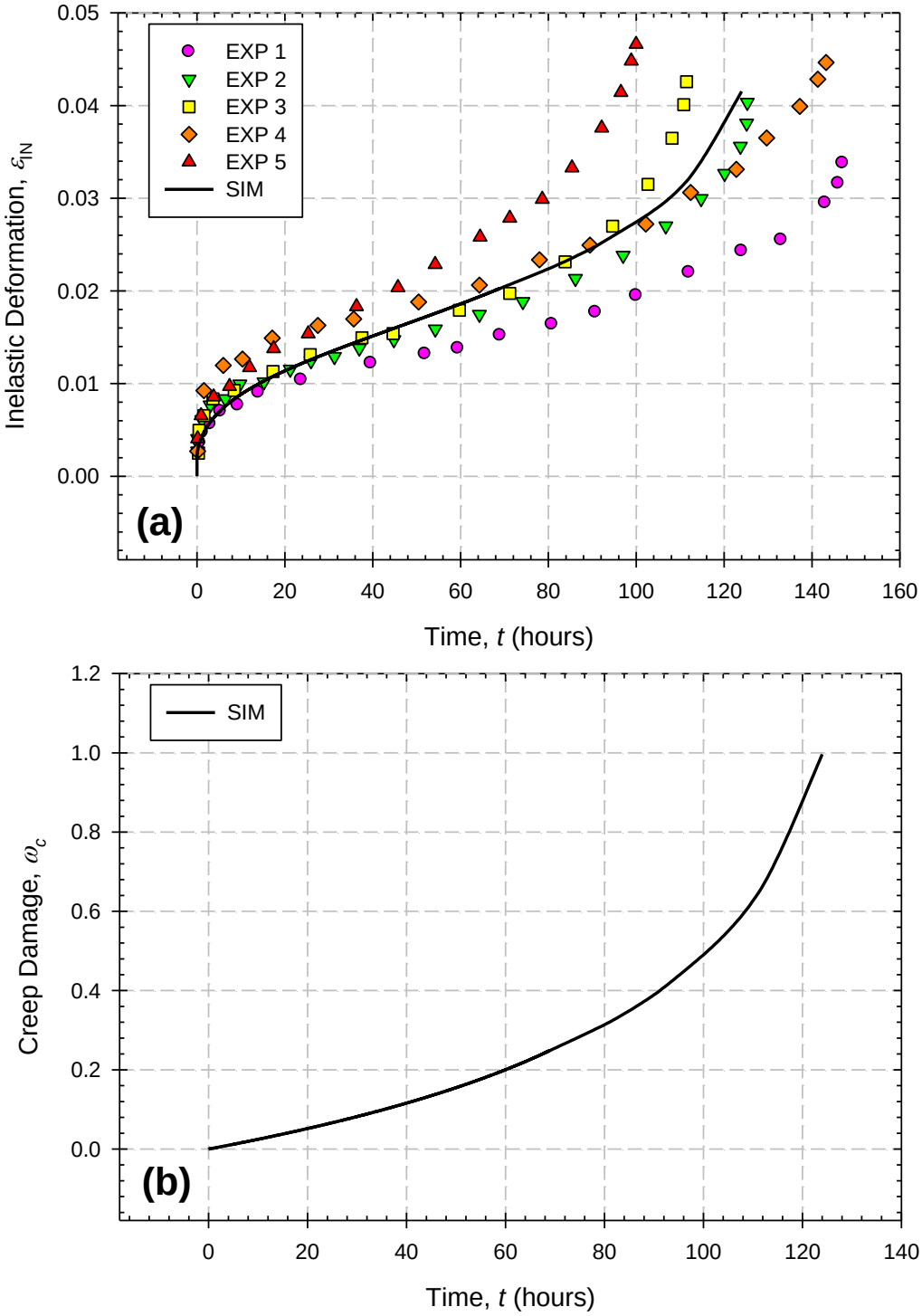

Figure 5.35 - Simulated (a) creep deformation and (b) damage at 300 MPa and 600°C using the finalized hybrid model

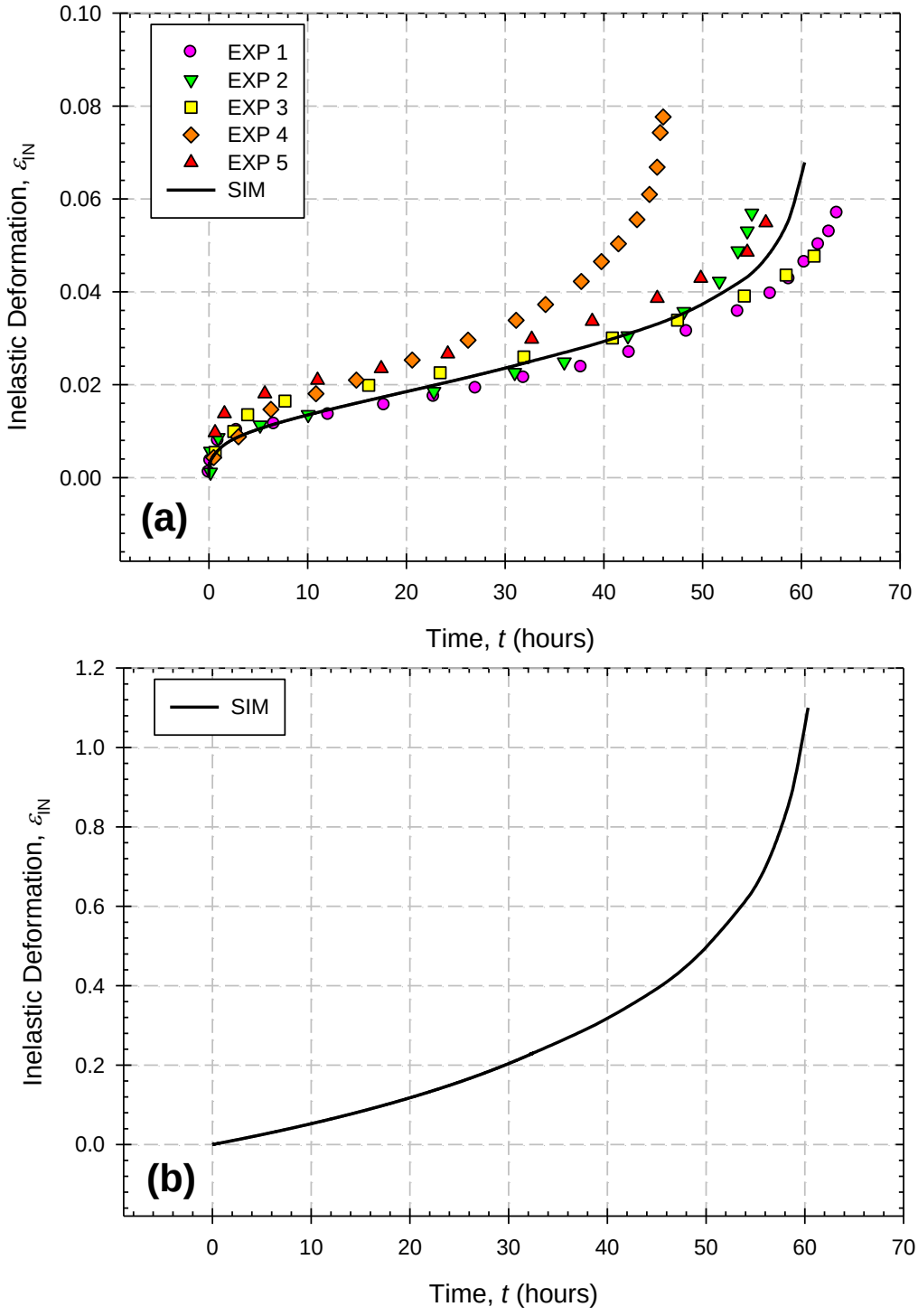

Figure 5.36 - Simulated (a) creep deformation and (b) damage at 320 MPa and 600°C using the finalized hybrid model

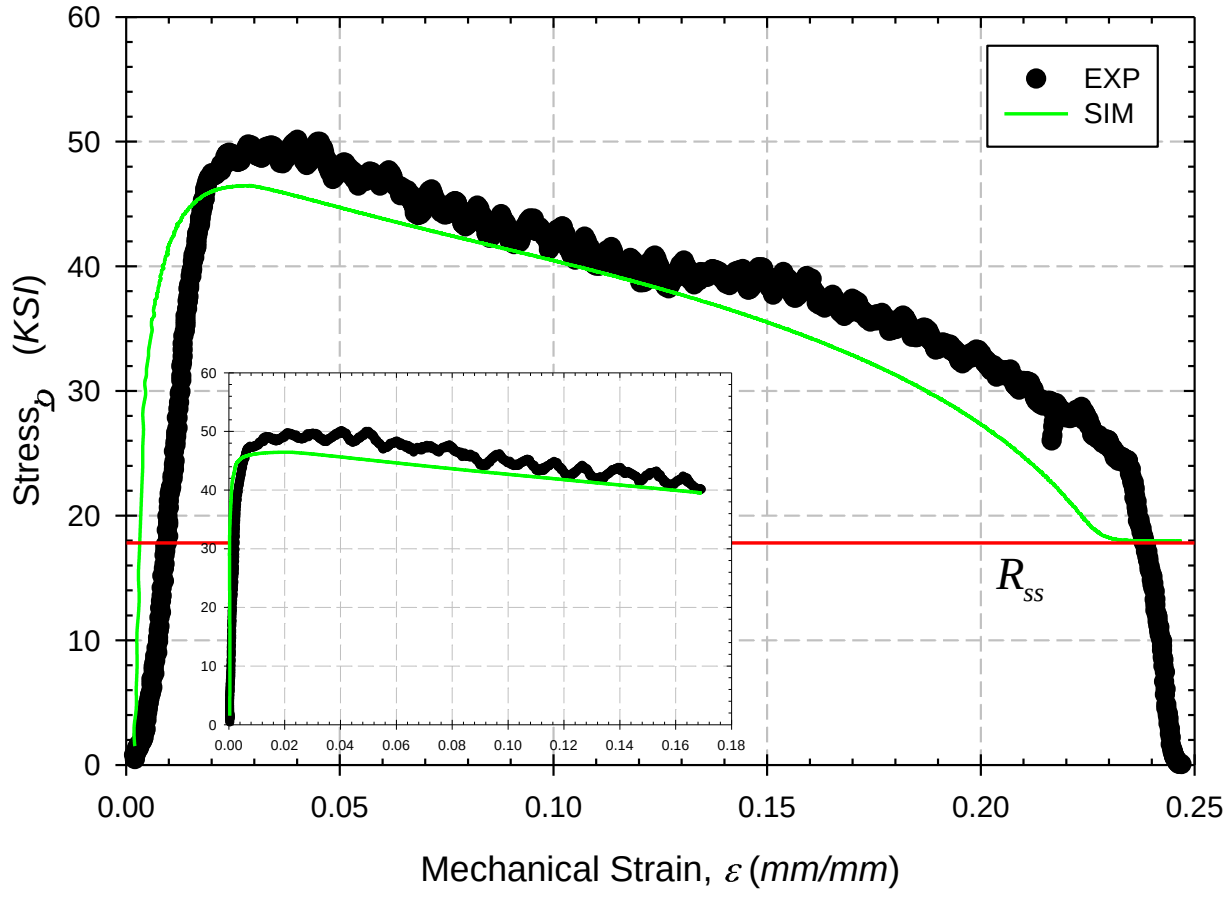

Figure 5.37 - Monotonic Tensile simulated at $\dot{\varepsilon} = 0.001/s$ and 600°C using the finalized hybrid model (large-crosshead, small extensometer)

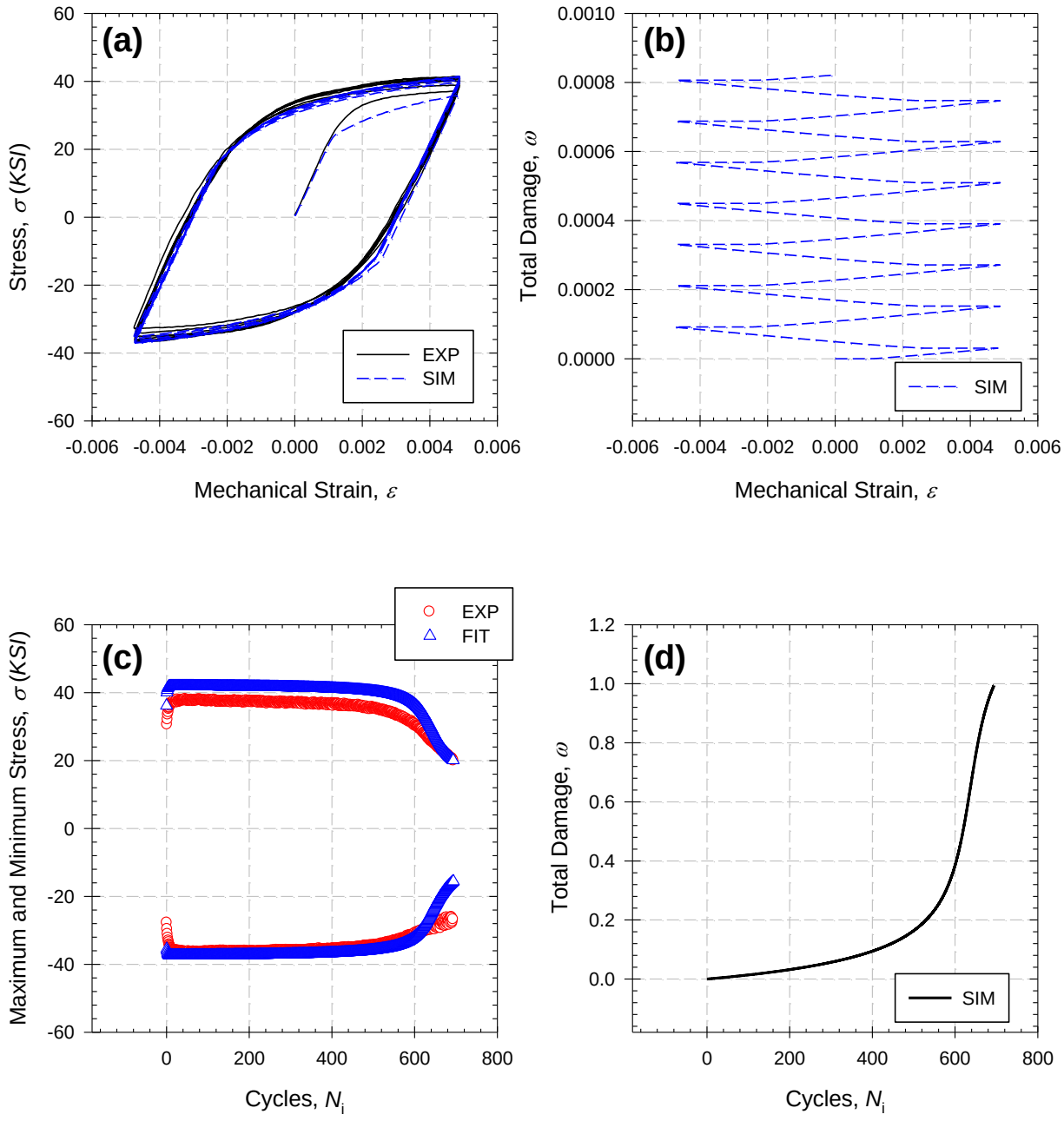

Figure 5.38 - Simulated fatigue tests $\Delta\varepsilon_T = 1\%$ and 600°C (a) stress-strain (b) damage-strain (c) cyclic stress-cycles and (d) damage-cycles using the finalized hybrid model

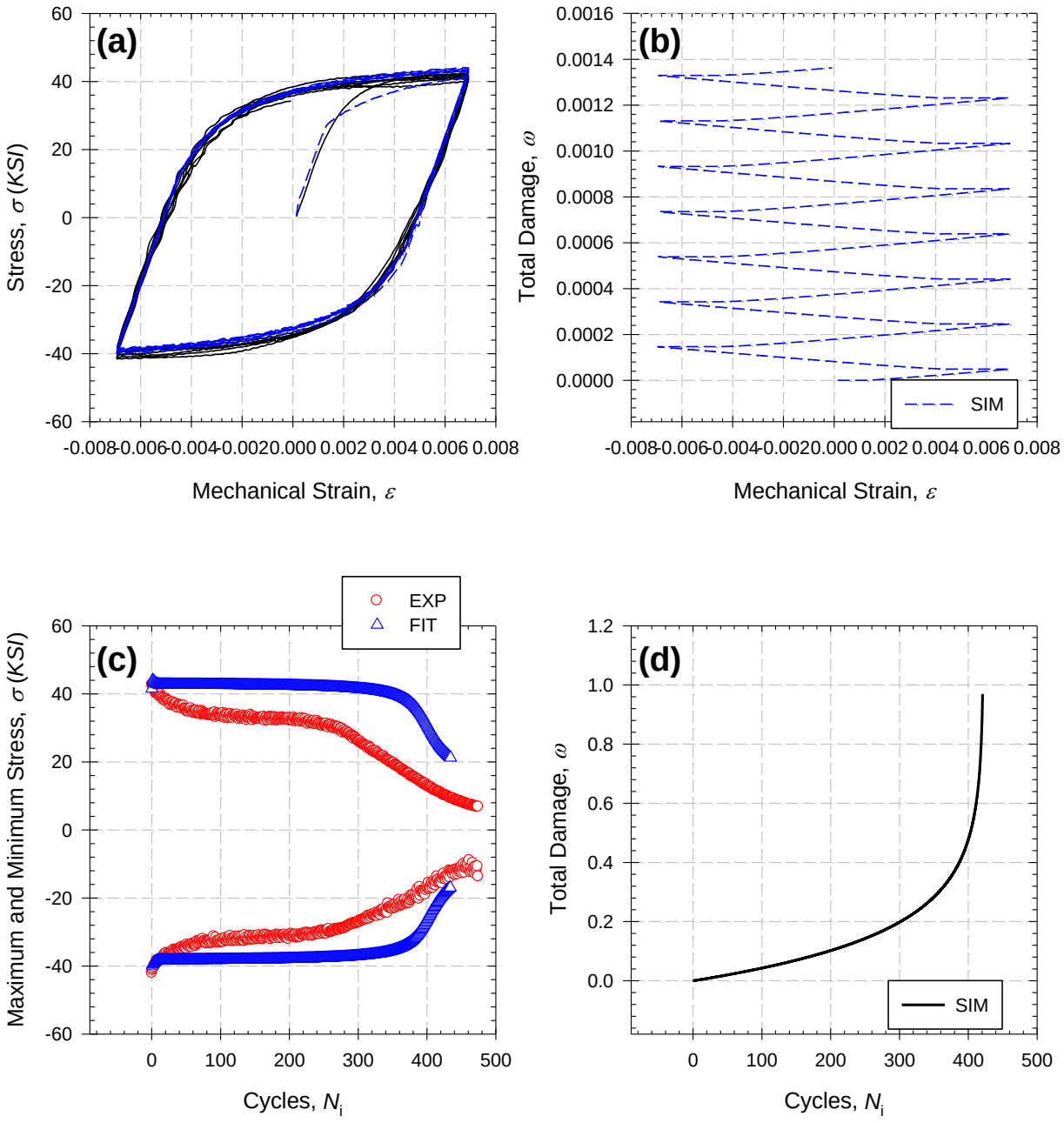

Figure 5.39 - Simulated fatigue tests $\Delta\varepsilon_T = 1.4\%$ and 600°C (a) stress-strain (b) damage-strain (c) cyclic stress-cycles and (d) damage-cycles using the finalized hybrid model

The multiple possible combination of damage for creep, monotonic, and fatigue conditions now follow. During a creep test, creep damage is always active. Fatigue damage becomes active when $\sigma \geq UTS/4$ but remains very small and only occurs during the primary creep regime. Fatigue damage disappears at constant stress (due to the unit step function) thus fatigue damage can only occur during transient loading. Plastic/ductile damage does not occur becomes the stress rate is zero.

During a monotonic test, creep damage is always active. The amount of creep damage is dictated by the applied strain rate where decreasing the strain rate increases the accumulated creep damage. Fatigue damage is active when $\sigma \geq UTS/4$ but remains very small due to the size of the fatigue damage constants. Plastic/ductile damage is active when the ultimate tensile strength is exceeded.

During a fatigue test, three possibilities exist. In all three, creep damage is always active. In the first option, $\sigma < UTS/4$ and $\sigma < \sigma_{UTS}$ are such that no fatigue or plastic/ductile damage occur. In the second option, $\sigma \geq UTS/4$ and $\sigma < \sigma_{UTS}$ fatigue damage occurs with negligible plastic/ductile damage. In the third option, $\sigma \geq UTS/4$ and $\sigma > \sigma_{UTS}$ both fatigue and plastic/ductile damage occur.

Both the fatigue and plastic/ductile damage equations include the irreversible portion of the viscous function [Eq. (5.5)]. Indefinite integration cannot be used to predict fatigue or monotonic rupture time a priori; therefore, the equation must be numerically optimized to determine appropriate material constants.

The importance of tracking the microstructural evolution cannot be overlooked. In the previous chapter, the cavity area density, ρ (number of cavities within a set area) and the A_p - Parameter (number of cavitated grain-boundaries) were correlated to the CDM damage variable [Eq. (4.49)] repeated below

$$\frac{A_p}{A_{p,cr}} = \frac{\rho}{\rho_{cr}} = \sin(\frac{3}{2}\omega) \tag{5.55}$$

The above equation remains valid where total damage [Eq. (5.31)] controls evolution. The creep and plastic/ductile damage components of total damage correlate directly to the above equation. The fatigue damage is a dislocation process which causes the formation of external cracks. When the external cracks are treated as external cavities the above microstructural evolution equation remains valid.

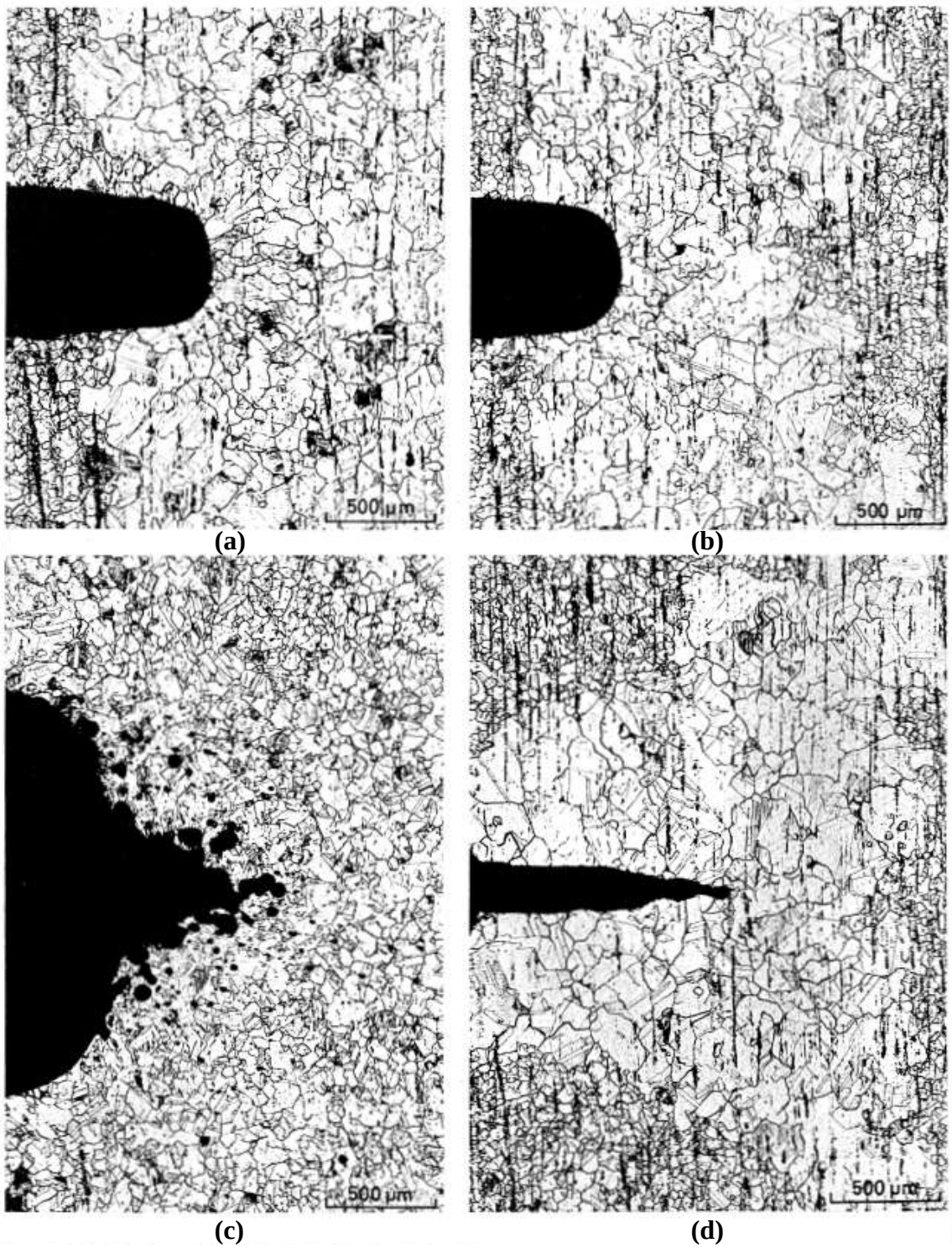

Figure 5.40 - Micrographs of re-crystallized structures for notched creep and fatigue specimen (a)-(c) creep, (d) fatigue (a) 130 *MPa t*=2 *hr* (b) 105 *MPa t*=5 *hr* (c) 105 *MPa t*=54 *hr* (d) *N*=25000 300 *cpm t*=1.4 *hr* [251]

5.2.4 Notch Strengthening and Weakening

Iino studied the high temperature cracking of 304 stainless steel in the presence of a notch [251]. Micrographs of notched creep (a-c) and fatigue (d) specimen where taken as depicted in Figure 5.40. Comparing the observation time associated with (c) and (d) it is clear that cracks initiate and grows earlier in the fatigue specimen than the creep specimen and damage is localized at the crack tip. This is indicative of transgranular cracking. In the creep specimen cracks initiation and grow after a homogenous field of cavities nucleate, grow, and begin to coalesce about the crack tip. This is indicative of intergranular cracking. Comparing the crack tips of (c) and (d) it is observed that fatigue has a notched sharpening effect while creep has a notch blunting effect. In the proposed model, the notch sharpening effect during fatigue is taken into account by the fatigue damage trajectory constant ϕ_f which controls the variation of fatigue damage $\partial\omega_f(t)$ with respect to an infinitesimal variation of stress $\partial\sigma(t)$ (i.e. the damage gradient near the notch tip). The relatively larger ϕ_f causes fatigue damage to be highly localized at stress concentrations. An equivalent stress based on distortion energy theory (von Mises) drives fatigue damage evolution. The constants λ_f controls how fatigue-damage enhances the inelastic strain rate. The relatively large value of λ_f induces high plasticity localized near the crack tip. The notch blunting effect during creep is taken into account by the creep damage trajectory constant ϕ_c which controls the variation of fatigue damage $\partial\omega_c(t)$ with respect to an infinitesimal variation of stress $\partial\sigma(t)$ (i.e. the damage gradient near the notch tip). The relatively small ϕ_c causes creep damage to be more distributed in the presences of stress concentrations. The Sdobyrev representative stress [Eq. (4.53)] is used to decrease the equivalent

stress of the creep damage evolution equations [Eqs. (5.38)] to replicate the notch strengthening where the presence of a notch increases creep rupture life [192]. The λ_c constant controls how creep damage enhances the inelastic strain rate. The relatively small value of λ_c cause's intermediate plasticity in the vicinity of the crack tip.

5.2.5 Mechanical Degradation

The same framework outlined in section 4.2.5 is repeated. The individual creep, plastic, and fatigue damages be linearly summed in the following form

$$\omega = \omega_c + \omega_p + \omega_f \tag{5.56}$$

Total damage can then be introduced into either the hypothesis of strain equivalence or the hypothesis of strain-energy equivalence as follows

$$\begin{aligned} &\text{(Strain)} && \tilde{E} = E(1 - m\omega) \\ &\text{(Strain-Energy)} && \tilde{E} = E(1 - m\omega)^2 \end{aligned} \tag{5.57}$$

where E is the initial young's modulus, $\tilde{E}$ is the current young's modulus, and m is the mechanical degradation factor. The mechanical degradation factor, m is assumed equal to 0.25 units. The simulations conducted in the previous section used the hypothesis of strain equivalence. All results depicted in the plots in the previous section demonstrate that the inclusion of stiffness degradation is key to predicting stress saturation and cycles to failure.

Table 5.6 – Summary of the Unified Mechanical Model for Creep-Fatigue (Hybrid Model)

Title	Equation
Viscous Function	$\dot{\varepsilon}_{IN} = A_0 \sinh\left(\frac{\lvert\sigma - R\rvert}{D}\right)\operatorname{sgn}(\sigma - R)\exp\left(\lambda_c\omega_c^{3/2} + \lambda_p\omega_p + \lambda_f\omega_f^{3/2}\right)$
Rest Stress	$\dot{R} = c_1\dot{\varepsilon}_{IN} - (R-Q)\left[(c_2 + c_d)\lvert\dot{\varepsilon}_{IN}\rvert\right]$ $c_d = c_3\exp\left[-c_4(R-Q)\operatorname{sgn}(\sigma - R)\right]$
Drag Stress	$\dot{D} = \left[\left(c_5 - c_7 D_0^{\,3}\right) - c_6\left(D - D_0\right)^3\right]\lvert\dot{\varepsilon}_{IN}\rvert$
Initial Drag Stress	$D_0 = \frac{Y(\dot{\varepsilon}_0) - c_1 0.002}{\operatorname{asinh}\left(\frac{\dot{\varepsilon}_0}{A_0}\right)}$
Total Damage	$\omega = \omega_c + \omega_f + \omega_p$
Creep Damage	$\dot{\omega}_c = \frac{M_c\left[1-\exp(-\phi_c)\right]}{\phi_c}\sinh\left(\frac{\sigma_{rep}}{\sigma_t}\right)^{\chi_c}\exp(\phi_c\omega)$
Representative Stress	$\sigma_{rep} = \alpha\sigma_1 + (1-\alpha)\sigma_{vm}$
Transient Activation	$\psi = \operatorname{sgn}\left[\operatorname{sgn}(\lvert\dot{\sigma}\rvert)\operatorname{sgn}(\lvert\dot{\varepsilon}\rvert)\right],\quad \operatorname{sgn}(x) = \begin{cases} -1 & x < 1 \\ 0 & x = 0 \cdot \\ 1 & x > 1 \end{cases}$
Fatigue Damage	$\dot{\omega}_f = \frac{1-\exp(-\phi_f)}{\phi_f}A_0\sinh\left(\frac{\sigma - R}{D}\right)^{\chi_f}\exp(\phi_f\omega)\cdot\psi$
Fatigue Damage criterion	$\sigma \geq \frac{\sigma_f}{2},\quad \sigma \geq \frac{UTS}{4},\quad UTS = R_{ss} + D_{ss}\operatorname{asinh}\left(\frac{\dot{\varepsilon}_0}{A_0}\right)$
Plastic/Ductile Damage	$\dot{\omega}_p = \frac{1-\exp(-\phi_p)}{\phi_p}A_0\sinh\left(\frac{\sigma - R}{D}\right)^{\chi_p}\exp(\phi_p\omega)\cdot\psi,\quad \sigma \geq UTS$
Normalized A_p-Parameter Evolution	$\frac{A_p}{A_{p,cr}} = \frac{\rho}{\rho_{cr}} = \sin\left(\frac{3}{2}\omega\right)$
Mechanical Degradation	(Strain) $\quad \tilde{E} = E(1-m\omega)$ (Strain-Energy) $\quad \tilde{E} = E(1-m\omega)^2$

5.3 **Summary of Constitutive Model**

The proposed constitutive model is completed. The hybrid constitutive model with creep, plastic/ductile, and fatigue damage is able to model the hardening and softening observed in creep, monotonic, and fatigue experiments. The CDM-based damage laws produce an a posteriori prediction of rupture time via iterative execution of the constitutive equations. A representative stress accounts for anisotropic cavity damage induced by multiaxial stress for both creep and plastic/ductile damage laws. The Normalized A_p-parameter is related to the cavitation driven creep and plastic/ductile damage. The strain and strain-energy equivalence approach to mechanical degradation has been created to model mechanical degradation more accurately. The constitutive model equations are collected and listed in Table 5.6. A description of the material constants associate with each equation is provided in Table 5.7 through Table 5.13.

Table 5.7 - Viscous function constants

Name	Symbol	Units
Secondary creep coefficient	A_0	s^{-1}
Natural logarithm of the final over minimum strain rate during creep	λ_c	*unitless*
Coefficient of the fatigue-damage/viscous-function interface	λ_f	*unitless*
Coefficient of the plastic-damage/viscous-function interface	λ_p	*unitless*

Table 5.8 - Fatigue damage constants

Name	Symbol	Units
Fatigue limit	σ_f	*mm/mm*
Fatigue damage trajectory constant	ϕ_f	*unitless*
" " exponent	χ_f	*unitless*

Table 5.9 - Drag stress constants

Name	Symbol	Units
1st work hardening coefficient	c_5	*KSI*
2nd work hardening coefficient	c_7	KSI^{-2}
Dynamic recovery coefficient	c_6	KSI^{-2}
Initial drag stress	D_0	*KSI*
Yield strength	*Y*	*KSI*
Ultimate Tensile Strength	*UTS*	*KSI*

Table 5.10 - Creep damage constants

Name	Symbol	Units
Tertiary creep-damage coefficient	M_c	s^{-1}
" " mechanism transition	σ_t	*KSI*
" " exponent	χ_c	*unitless*
Damage trajectory constant	ϕ_c	*unitless*
Mechanical degradation factor	*m*	*unitless*

Table 5.11 - Representative stress constant

Name	Symbol	Units
Multiaxial rupture parameter	α	*unitless*

Table 5.12 - Plastic/ductile damage constants

Name	Symbol	Units
Plastic/ductile damage trajectory constant	ϕ_p	*unitless*
" " exponent	χ_p	*unitless*

Table 5.13 - Rest stress constants

Name	Symbol	Units
Work hardening coefficient	c_1	*KSI*
1st dynamic recovery coefficient	c_2	*unitless*
2nd dynamic recovery coefficient	c_3	*unitless*
3rd dynamic recovery coefficient	c_4	KSI^{-1}
initial anisotropy of the yield surface	*Q*	*KSI*

5.4 **FEM Implementation**

The same technique outlined in the previous chapter will be used for the finalized hybrid model. The constitutive equations will be programmed into an ANSYS usermat3d UPF file. The stress increment is determined using a 3D radial return technique. The inelastic strain vector is determined from the multiaxial extension of the isotropic model. The material Jacobian matrix is determined through derivation. The following sections detail how to obtain these terms.

5.4.1 Multiaxial Form

The development of a multiaxial form can be conducted in two ways:

- The conversion of the isotropic model until a general multiaxial extension
- The conversion into an anisotropic model able to account for kinematic yield surface distortions

The first case only requires that the viscous function be converted into a vector. Borrowing from the plastic potential theory, the creep potential hypothesis suggests that some creep-potential controls creep-flow

$$d\varepsilon_{ij,cr} = d\varepsilon_{cr} \frac{d\psi(\boldsymbol{\sigma})}{d\sigma_{ij}} \tag{5.58}$$

where $d\varepsilon_{cr}$ is the equivalent creep strain increment [221]. In the case of creep, the yield surface is zero such that the potential function is equal to the selected equivalent stress.

In the current study Hill's anisotropic equivalent stress will be used [59]. Hill's anisotropic yield criterion is an extension of the von Mises yield criterion that allows for anisotropic yield of materials

$$\sigma_{\text{Hill}} = \sqrt{\mathbf{s}^T \mathbf{M} \mathbf{s}}$$

$$\mathbf{s} = VEC(\boldsymbol{\sigma})$$

$$\mathbf{M} = \begin{bmatrix} G+H & -H & -G & 0 & 0 & 0 \\ -H & F+H & -F & 0 & 0 & 0 \\ -G & -F & F+G & 0 & 0 & 0 \\ 0 & 0 & 0 & 2N & 0 & 0 \\ 0 & 0 & 0 & 0 & 2L & 0 \\ 0 & 0 & 0 & 0 & 0 & 2M \end{bmatrix} \tag{5.59}$$

where σ_{Hill} is Hill's equivalent stress, **s** is the Cauchy stress vector, and **M** is the Hill compliance tensor consisting of the *F, G, H, L, M,* and *N* unitless material constants [170]. Hill's equivalent stress reverts to von Mises when

$$F = G = H = \frac{1}{2}$$

$$L = M = N = \frac{3}{2} \tag{5.60}$$

Using Hill's potential function and the creep potential hypothesis, a general flow rule of the proposed isotropic constitutive model is produced

$$d\varepsilon_{IN,i} = A_0 \sinh\left(\frac{|\sigma_{Hill} - R|}{D}\right) \text{sgn}(\sigma - R) \exp\left(\lambda_c \omega_c^{3/2} + \lambda_p \omega_p + \lambda_f \omega_f^{3/2}\right) \Delta t \frac{\mathbf{Ms}}{\sigma_{Hill}} \tag{5.61}$$

In the cases of yield surface distortions, the kinematic hardening variable must be converted in to a vector. Helling and Miller [70] and Kagawa and Asada [235] show that major modifications to the viscous function and rest stress equation of most viscoplastic constitutive models must be performed to produce an appropriate response. A multiaxial form of the hybrid model is provided in Table 5.14 (only the modified equations listed) where $\overline{\dot{\varepsilon}_{IN}}$, $\overline{(\sigma - R)}$, **M,** and σ_{Hill}

are the equivalent inelastic strain rate, equivalent over stress, Hill's compliance tensor, and Hill's equivalent stress respectively. For simplicity the term Q is consider a scalar. No proof is provided to suggest that Q should not become a Q_i vector. Multiple experiments and numerical optimization must be performed to make a determination. This is outside the scope of this study.

Table 5.14 – Multiaxial Unified Mechanical Model for Creep-Fatigue (The Hybrid Model)

Title	Equation
Viscous Function	$\varepsilon_{IN,i} = \bar{\dot{\varepsilon}}_{IN} \dfrac{M_{ij}\left(\sigma_j - R_j\right)}{\overline{(\sigma - R)}}$ $\bar{\dot{\varepsilon}}_{IN} = A_0 \sinh\left(\dfrac{\overline{(\sigma - R)}}{D}\right) \exp\left(\lambda_c \omega_c^{3/2} + \lambda_p \omega_p + \lambda_f \omega_f^{3/2}\right)$ $\overline{(\sigma - R)} = \sqrt{\left(\sigma_i - R_i\right) M_{ij} \left(\sigma_j - R_j\right)}$
Rest Stress	$\dot{R}_i = c_1 \dot{\varepsilon}_{IN,i} - \left(R_i - Q\right)\left[\left(c_2 + c_{d,i}\right)\bar{\dot{\varepsilon}}_{IN}\right]$ $c_{d,i} = c_3 \exp\left[-c_4 \left(R_i - Q\right) \dfrac{M_{ij}\left(\sigma_j - R_j\right)}{\overline{(\sigma - R)}}\right]$
Drag Stress	$\dot{D} = \left[\left(c_5 - c_7 D_0^{\,3}\right) - c_6 \left(D - D_0\right)^3\right] \bar{\dot{\varepsilon}}_{IN}$
Representative stress	$\sigma_{rep} = \alpha \sigma_1 + (1 - \alpha)\overline{(\sigma - R)}$
Plastic/Ductile Damage	$\dot{\omega}_p = \dfrac{1 - \exp\left(-\phi_p\right)}{\phi_p} A_0 \sinh\left(\dfrac{\overline{(\sigma - R)}}{D}\right)^{\chi_p} \exp\left(\phi_p \omega\right) \cdot \psi$
Fatigue Damage	$\dot{\omega}_f = \dfrac{1 - \exp\left(-\phi_f\right)}{\phi_f} A_0 \sinh\left(\dfrac{\overline{(\sigma - R)}}{D}\right)^{\chi_f} \exp\left(\phi_f \omega\right) \cdot \psi$

5.4.2 Radial Return Mapping Technique

For one dimensional viscoplasticity, the radial return mapping function is simplified to

$$F\left(\sigma_e\right) = \sigma_e - \sigma_e^* + E\Delta\varepsilon_{IN} = 0 \tag{5.62}$$

where the isotropic viscous function [Eq. (5.61)] is used. The updated stress vector is obtained using the same method developed in the previous chapter (see section 4.4.2). This is a method similar to the original work by Wilson [262]. For three dimensional viscoplasticity the entire stress vector must be solved [263]. The trial stress vector, $\boldsymbol{\sigma}_{n+1}^*$ becomes

$$\boldsymbol{\sigma}_{n+1}^* = \boldsymbol{\sigma}_n + \mathbf{C}_{EL}\Delta\boldsymbol{\varepsilon} \tag{5.63}$$

where $\boldsymbol{\sigma}_n$ is the given stress at step n, $\mathbf{C}_{EL}$ is the elastic stiffness matrix, and $\Delta\boldsymbol{\varepsilon}$ is the strain increment provided by the parent FEM code. The updated stress can be calculated using the following

$$\boldsymbol{\sigma}_{n+1} = \boldsymbol{\sigma}_{n+1}^* - \mathbf{C}_{EL}\Delta\boldsymbol{\varepsilon}_{IN,n+1} \tag{5.64}$$

where $\Delta\boldsymbol{\varepsilon}_{IN,n+1}$ is the inelastic strain increment calculated using the updated $\boldsymbol{\sigma}_{n+1}$ stress. By moving everything to the right hand side, a function that can be solved by iteration is produced

$$\mathbf{F}_m\left(\boldsymbol{\sigma}_{n+1}\right) = \boldsymbol{\sigma}_{n+1} - \boldsymbol{\sigma}_{n+1}^* + \mathbf{C}_{EL}\Delta\boldsymbol{\varepsilon}_{IN,n+1} = 0 \tag{5.65}$$

Using the Newton-Raphson method gives

$$\left(\boldsymbol{\sigma}_{n+1}\right)_{m+1} = \left(\boldsymbol{\sigma}_{n+1}\right)_m - \left(\frac{d\mathbf{F}_m}{d\boldsymbol{\sigma}_{n+1}}\right)^{-1}\mathbf{F}_m \tag{5.66}$$

where m is the iteration count. The derivative of F_m is provided below

$$\frac{d\mathbf{F}_m}{d\boldsymbol{\sigma}_{n+1}} = 1 + \mathbf{C}_{EL}\left(\frac{d\Delta\boldsymbol{\varepsilon}_{IN,n+1}}{d\boldsymbol{\sigma}_{n+1}}\right) = 1 + \mathbf{C}_{EL}\mathbf{S}_{IN,n+1} \tag{5.67}$$

where $\mathbf{S}_{IN,n+1}$ is the inelastic compliance matrix. The inverse of the derivative becomes

$$\left(\frac{d\mathbf{F}_m}{d\boldsymbol{\sigma}_{n+1}}\right)^{-1} = \left(1 + \mathbf{C}_{EL}\mathbf{S}_{IN,n+1}\right)^{-1} \tag{5.68}$$

The convergence criterion follows

$$\begin{aligned} &\left|\mathbf{F}_{m+1} - \mathbf{F}_m\right| < \delta \\ &\left|\left(\boldsymbol{\sigma}_{n+1}\right)_{m+1} - \left(\boldsymbol{\sigma}_{n+1}\right)_m\right| < \delta \end{aligned} \tag{5.69}$$

where δ is the desired accuracy.

5.4.3 Material Jacobian Matrix

The material Jacobian can be described as a partial derivative

$$\mathbf{C}_{TOT} = \frac{\partial\sigma_i}{\partial\varepsilon_j} = \mathbf{C}_{EL} + \mathbf{C}_{IN} \tag{5.70}$$

where $\partial\sigma_i$ is the change in the ith stress at the end of the time increment caused by the jth strain $\partial\varepsilon_j$ [225]. A closed-form solution to $\mathbf{C}_{EL}$ the elastic stiffness matrix always exists. A closed-form solution to $\mathbf{C}_{IN}$ the inelastic stiffness matrix may or may not exist. If a closed-form solution exists, it greatly reduces computational costs.

To that end, inverting the inelastic stiffness matrix, $\mathbf{C}_{IN}$, will furnish the inelastic compliance matrix, $\mathbf{S}_{IN}$, as follows

$$\mathbf{S}_{IN} = \left(\mathbf{C}_{IN}\right)^{-1} = \frac{\partial \varepsilon_{IN,i}}{\partial \sigma_j} \tag{5.71}$$

The partial derivative of the viscous function can be found manually or by using symbolic computational algorithms. The partial derivative of a variable function is a derivative with respect to a constant such that

$$\mathbf{S}_{IN} = \frac{d\Delta\varepsilon_{IN,i}(\boldsymbol{\sigma})}{d\sigma_j} \tag{5.72}$$

Using the multiaxial form of the hybrid constitutive model (Table 5.14), the incremental inelastic strain is introduced, derivation performed, and the resulting condensed matrix provided below

$$\begin{aligned}\mathbf{S}_{PR} &= \Delta\varepsilon_{IN}\frac{\mathbf{M}}{\sigma_{Hill}} - \Delta\varepsilon_{IN}\frac{(\mathbf{M}\boldsymbol{\sigma})(\boldsymbol{\sigma}\mathbf{M})^{\mathrm{T}}}{\sigma_{Hill}^3} \\ &+ \frac{A_0}{D}\cosh\left(\frac{\overline{(\sigma - R)}}{D}\right)\exp\left(\lambda_c\omega_c^{3/2} + \lambda_p\omega_p + \lambda_f\omega_f^{3/2}\right)\Delta t\frac{(\mathbf{M}\boldsymbol{\sigma})(\boldsymbol{\sigma}\mathbf{M})^{\mathrm{T}}}{\sigma_{Hill}^2}\end{aligned} \tag{5.73}$$

the matrix is symmetric and non-singular. To obtain the stiffness matrix the compliance tensors must be inverted

$$\mathbf{C}_{IN} = \left(\mathbf{S}_{IN}\right)^{-1} \tag{5.74}$$

In the current study, Gaussian elimination is used to find the inverse.

CHAPTER SIX: FINITE ELEMENT SIMULATIONS

6.1 **Introduction**

This chapter presents and discusses finite element simulations produced using the unified mechanical model for creep-fatigue. The simulations are conducted to demonstrate the capabilities of the unified mechanical model in comparison to experimental data and parametrically exercise the model to characterize the response under service like conditions. A series of simulations are conducting using the isotropic form of the model as summarized in Table 5.6. For convenience, the material constants developed in the previous chapter that will be used in the simulations are listed together in Table 6.1. The one dimensional simulations are conducting using the "HYBRID.F" 1D isotropic finite element code (provided in APPENDIX A:HYBRID.F) developed for the uSHARP 3.0 software using the isotropic constitutive equations (Table 5.6). The applied boundary conditions are stored as an array and feed into "HYBRID.F" which determines the updated stress [see section 5.4.2], strain, and internal variables at each time interval. Simulations based on service-like conditions are performed to evaluate the capabilities of the model under the typical boundary conditions are industrial gas turbine may undergo. These tests include; creep, continuous strain cycling, strain-hold cycling, continuous stress cycling, and stress-hold cycling. Simulations based on atypical load histories are performed to evaluate the unified mechanical model under unusually combinations of load to determine if the model lacks the ability to model certain phenomena. These tests include: creep to cycling, cycling to creep, stepped creep, and sequential fatigue blocks and creep.

Table 6.1 – Viscous function constants

Name	Symbol	Value	Units
Secondary creep coefficient	A_0	1.464E-12	s^{-1}
Natural logarithm of the final over minimum strain rate during creep	λ_c	3.586404	*unitless*
Coefficient of the fatigue-damage/viscous-function interface	λ_f	17.332	*unitless*
Coefficient of the plastic-damage/viscous-function interface	λ_p	38.306	*unitless*
Work hardening coefficient	c_1	5838.3	*KSI*
1st dynamic recovery coefficient	c_2	239.64	*unitless*
2nd dynamic recovery coefficient	c_3	511.96	*unitless*
3rd dynamic recovery coefficient	c_4	0.86806E-01	KSI^{-1}
Initial anisotropy of the yield surface	Q	2.1772	*KSI*
1st work hardening coefficient	c_5	11.876	*KSI*
2nd work hardening coefficient	c_7	5.0569	KSI^{-2}
Dynamic recovery coefficient	c_6	1087.4	KSI^{-2}
Initial drag stress	D_0	*	*KSI*
Young's Modulus	E	*	*KSI*
Mechanical degradation factor	m	0.25	*unitless*
Yield strength	Y	*	*KSI*
Ultimate Tensile Strength	UTS	*	*KSI*
Tertiary creep-damage coefficient	M_c	5.272E-10	s^{-1}
" " mechanism transition	σ_t	12.676080	*KSI*
" " trajectory constant	ϕ_c	3.703911	*unitless*
" " exponent	χ_c	3.09	*unitless*
Multiaxial rupture parameter	α	0.75	*unitless*
Fatigue limit	σ_f	$0.5UTS$	*mm/mm*
Fatigue damage trajectory constant	ϕ_f	19.376	*unitless*
" " exponent	χ_f	0.91691	*unitless*
Plastic/ductile damage trajectory constant	ϕ_p	50.786	*unitless*
" " exponent	χ_p	1.2042	*unitless*

* varies based on the experiment

6.2 **Service-Like Conditions**

Creep deformation and damage continuously accumulate when a material is subject to a temperature above the creep limit. It is important to demonstrate the capability of the unified mechanical model to accurately predict the creep deformation and rupture. Towards, those goals a series of creep simulations are conducted. First the creep rupture prediction [Eq. (4.32)] is evaluated and compare to available experimental data. The results are plotted in Figure 6.1 and show that the model accurately predicts the available creep rupture data at 600°C for 304SS. When compared to temperatures above and below 600°C it is clear the extrapolated prediction at low stress follows the general trend for 304SS. The high stress extrapolations are not accurate with life predict above the ultimate tensile strength. This error is due to the fact that the creep damage law does not model plastic damage but a separate equation is used [Eq. (5.51)]. When plastic damage is enabled, the high stress behavior is better prediction with rapid rupture once the UTS is reached. Additional experiments should be conducted to better demonstrate and calibrate the creep damage model for stress rupture.

A series of creep deformation simulations at 220, 240, 260, 280, 300, and 320 MPa and 600°C are performed and plotted in Figure 6.2. The unified mechanical model produces the appropriate primary, secondary, and tertiary creep responses for all stress levels. The primary creep strain increases with stress. The minimum creep strain rate observed in the secondary creep regime increases as stress increases. The amount and rate of tertiary creep strain increases with stress. The damage evolution and normalized cavity area density plots show that damage evolves to a critical value at any stress level. Stiffness is observed to degrade as typical of metals.

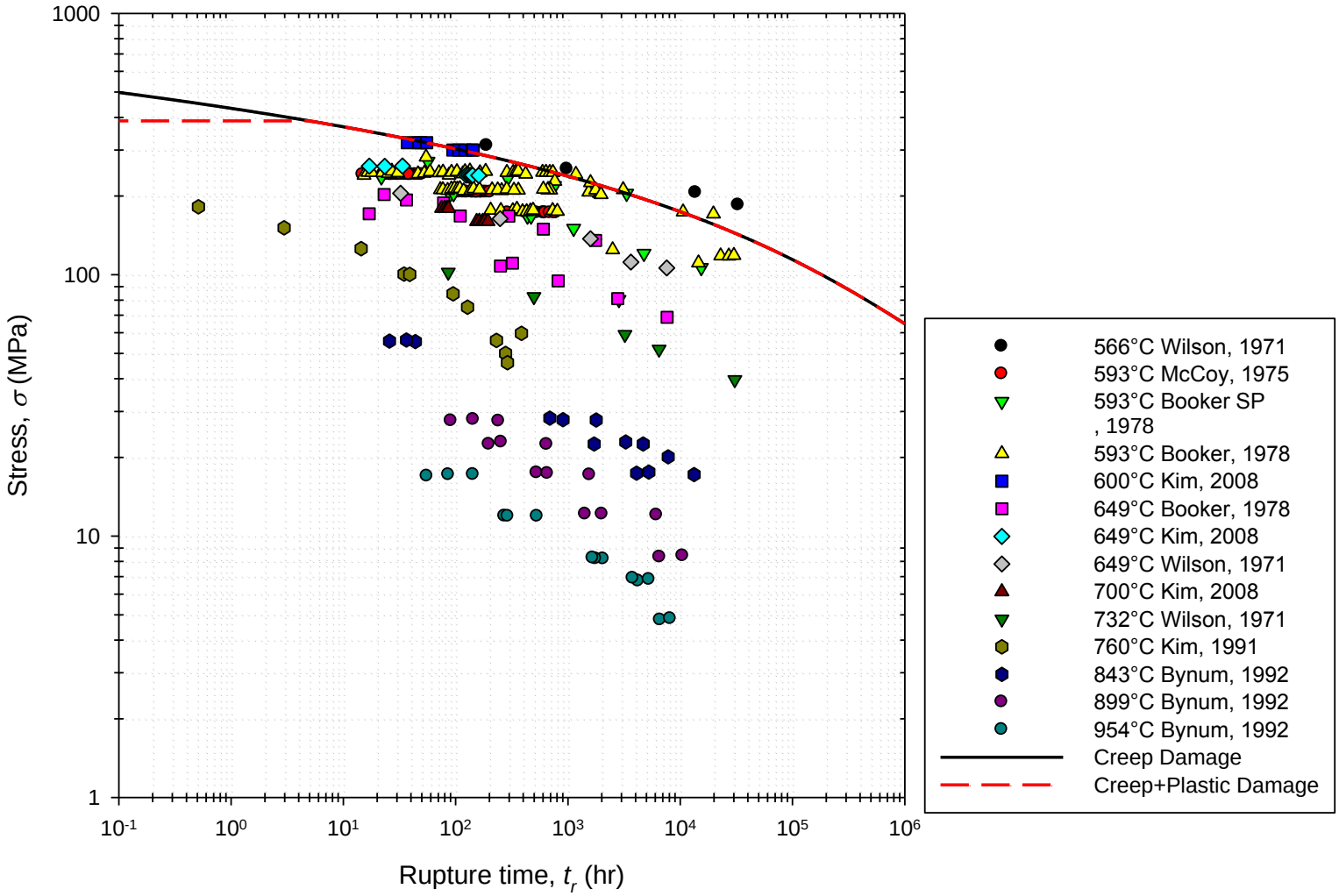

Figure 6.1 - Parametric Exercise of the Creep Rupture Prediction

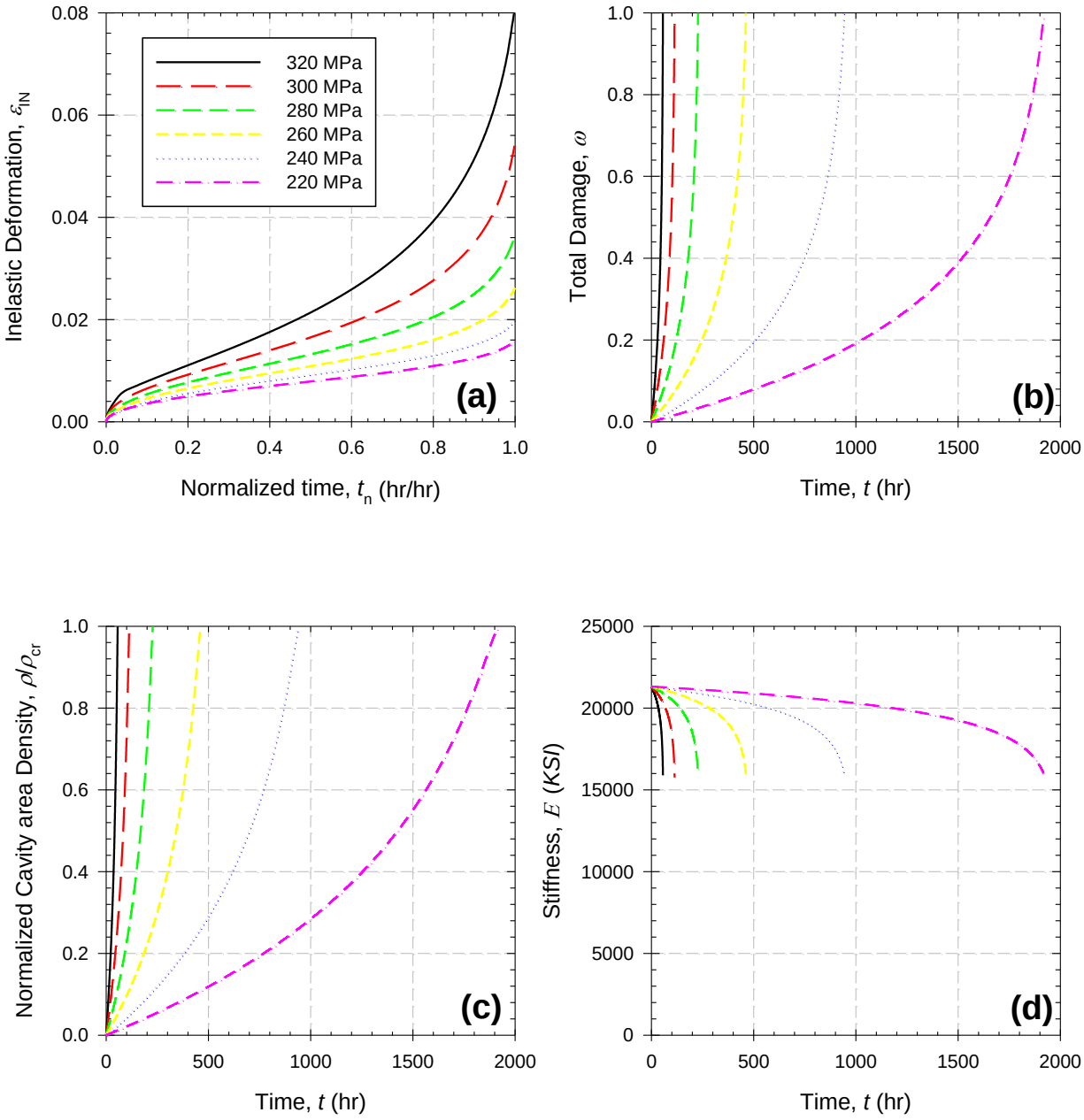

Figure 6.2 - Isotropic Creep at 50, 100, 150, 200, 250, 300, 320 *MPa* (a) deformation (b) total damage (c) normalized cavity area density (d) stiffness

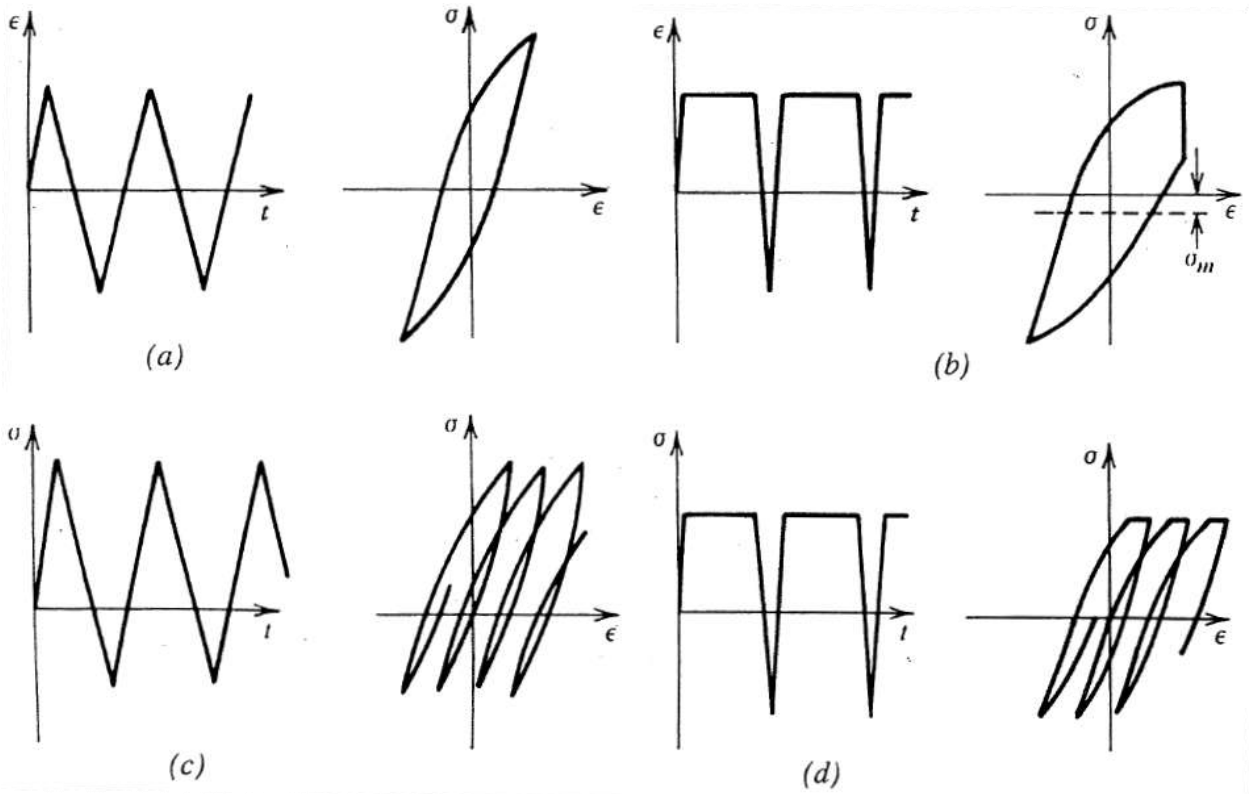

Figure 6.3 - Schematic of service-like hysteresis loops (a) continous strain cycling (b) strain-hold cycling (c) continous stress cycling (d) stress-hold cycling [264]

Table 6.2 – Monotonic properties of the fatigue tests

Strain Range, $\Delta\varepsilon$ %	Hold Time, t_h *s*	Young's Modulus, *E* *KSI*	Yield Strength, *Y* *KSI*	Ultimate Tensile Strength, *UTS** *KSI*
1	0	21313.89	36.886	46.19043
1	*60*	15641.96549	30.1597	40.624418
1.4	*0*	21059.85327	40.163	47.362529
1.4	60	23034.0935	48.2939	59.615004
stepped		20821.34352	35.5987	45.25925

* obtained using the analytical equation [Eq. (5.20)]

Gas turbine superalloys are subject to complex load histories; the simplest of which consists of isothermal temperature with mixed transient and constant mechanical loading. These dynamic boundary conditions make modeling the constitutive response of components using traditional modeling techniques difficult. It is necessary to demonstrate the capabilities of the unified mechanical model to predict the constitutive response under typical boundary conditions. Coffin developed a schematic of the hysteresis loops observed during creep-fatigue under various mechanical loads, depicted in Figure 6.3[264]. These hysteresis loops consists of (a) continuous strain, (b) strain-hold (c) continuous stress, and (d) stress-hold cycling. The unified mechanical model was developed and calibrated based on type (a) experimental data, the results of which are presented in Figure 5.38 and Figure 5.39. Compared to the experimental data the unified mechanical model is able to accurately predict the constitutive response and rupture under continuous strain cycling. The next step is to examine the unified mechanical models performance when modeling strain-hold cycling. Experimental fatigue data for 304SS at 600°C subject to 60s tensile strain holds for $\Delta\varepsilon_T = 1\%$ and $\Delta\varepsilon_T = 1.4\%$ at $\dot{\varepsilon}_0 = 0.001/s$ were obtained. The monotonic properties are listed in Table 6.2. Simulations of both $\Delta\varepsilon_T = 1\%$ and $\Delta\varepsilon_T = 1.4\%$ fatigue tests were conducted with the results provided in Figure 6.4(a)-(d) and Figure 6.5(a)-(d) respectively. Examining the resulting hysteresis loops (a) it is clear that the model is able to capture the strain hardening that occurs during transient loading and the stress relaxation that occurs during strain holds. Examining the cyclic stress-life data (b), it is observed that he model produces an expect fit to $\Delta\varepsilon_T = 1.4\%$ but a terrible fit to $\Delta\varepsilon_T = 1\%$. This is believed to be due to either the specimen being defective or human error when conducting the mechanical test. When life is compared between the continuous strain and strain-hold fatigue tests, it is observed that the strain-hold

$\Delta\varepsilon_T = 1.4\%$ tests exhibits a large reduction in life that is not observed in the $\Delta\varepsilon_T = 1\%$ test. At the test frequency with the 60s hold time, this dramatic reduction in life is not expected to occur because creep damage will not be dominant. With this consideration, it can be said the unified mechanical model performs well in modeling strain hold cycling.

An equation which approximates the initial drag stress for load control has not been developed yet. The problem was briefly discussed in the previous chapter (section 5.2.1). Under displacement control, the approximation is based on the conditions of a strain-controlled monotonic tensile test. For load control, the approximation is that of a stress-controlled monotonic tensile test. Let it be assumed that a single time step is used to reach the 0.2% yield strength at 0.002 strain offset, that D_0 does not change significantly and the quantity Q is zero. Under these conditions the following approximations are made

$$\begin{aligned} &\sigma = Y \\ &\dot{\varepsilon}_{IN} \approx \dot{\varepsilon}_{\min} \\ &\varepsilon_0 = \dot{\varepsilon}_{\min}\Delta t = 0.002 \\ &R = c_1\varepsilon_0 \\ &D = D_0 \end{aligned} \tag{6.1}$$

The minimum creep strain rate, $\dot{\varepsilon}_{\min}$ can be calculated using the secondary creep law [Eq. (5.4)] and replacing constant stress with the yield strength

$$\dot{\varepsilon}_{\min} = A_0 \sinh\left(\frac{Y}{\sigma_s}\right) \tag{6.2}$$

where A_0 and σ_s are material constants. Introducing the above conditions into the viscous function [Eq. (5.5)] and solving for D_0 produces the "initial drag stress for load control" as

$$D_0 = \frac{\sigma_s \left(Y - c_1 0.002 \right)}{Y} \tag{6.3}$$

where Y is the 0.2% yield strength at $\dot{\sigma}$, the applied tensile-test stress rate. Using this approach, the yield strength of the 300 and 320 MPa creep tests is calculated as 40.13236 *KSI*. This value compares well to those obtained from the displacement controlled fatigue tests. For the following load-controlled simulations the above method is used.

In the case of continuous stress cycling and stress-hold cycling, experimental data is not available. It is still however necessary to examine how the unified mechanical model performs under these conditions. Towards that goal continuous stress cycling simulation is performed with the following boundary conditions $\sigma_{\max} = 40 ksi$, $R = -1$, $\dot{\sigma} = 0.04 ksi/s$ using the material constants listed in Table 6.1 where Q=2.1772 units. The simulations are conducted using a Young's modulus of E = 21313.89 *KSI*, yield strength of Y = 40.13236 *KSI*, and the ultimate tensile strength is *UTS* = 51.0166061851541 *KSI*. The plot depicted in Figure 6.6 shows that negative ratcheting occurs where during the fully reversed cycle more compressive inelastic strain accumulates than tensile. This behavior does not occur naturally in 304SS; therefore, either the constitutive model is inaccurate or one of the material constants needs further optimization. The later is true. The initial asymmetry of the yield surface constant Q is the culprit for the error. The constants Q is a persistent value which controls asymmetry of the yield surface. To further evaluate the influence of Q, continuous stress cycling simulations with Q equal to -2.1772 and 0 are performed and plotted in Figure 6.7 and Figure 6.8 respectively. The effect of Q on the yield surface is depicted in Figure 6.9. When $Q > 0$ the yields surface is initially translated in the positive direction; therefore, yield occurs at a lower stress in compression than tension. This

results in an accumulation of more compressive strain then tensile during fully reversed stress cycling. When $Q < 0$ the yield surface is initially translated in the negative direction; therefore, yield occurs at a lower stress in tension than compression. This results in an accumulation of more tensile strain then compressive during fully reversed stress cycling. When $Q = 0$, the yield surface is symmetric. The strain controlled experimental data (Figure 5.38-5.39, and Figure 6.4-6.5) suggests that $Q > 0$ because yield appears to occur at a lower stress in compression. Literature shows that under load-control, ratcheting strain is always positive under fully reversed cycling; suggesting that $Q \leq 0$. Because ratcheting is an important process that often occurs in gas turbine components subject to creep-fatigue; perhaps the constant Q should be reoptimized to better predict the ratcheting process.

The final set of experimental data available for this study is a stepped-strain range test conducted at $\dot{\varepsilon}_0 = 0.001/s$ and 600°C. The purpose of this type of test is to generate the stabilized stress amplitude at multiple strain ranges in order to determine the cyclic stress-strain curve [265]. A simulation of this test is performed with the results plotted in Figure 6.10 using the monotonic properties listed in Table 6.2 and *Q*=2.1772 units. Examining the results it is observed that the model perfectly predicts the strain hardening during compression and under predicts the strain hardening during tension. The simulation is performed again for *Q* equal to 0 and -2.1772, with results plotted in Figure 6.11(a) and (b) respectively. With *Q*=-2.1772, the model under predicts the strain hardening during compression and perfectly predicts the strain hardening during tension (the exact opposite of Q=2.1772). With *Q*=0, the model only slightly under predicts the strain hardening in tension. This suggests that the previously optimized *Q* should be reoptimized to the stepped-strain data to produce the appropriate response.

To obtain a better value of *Q* the USHARP 3.0 is reconfigured to compare the simulated stress to the experimental stress of the stepped-strain fatigue test. The simulated annealing algorithm settings of Table 5.2 are used. The lower *LB* and upper bound *UB* are -2.1772 to 0 respectively. The final *SUM* was 32.39493 units with the least squares evolution depicted in Figure 6.12. A total of 401 evaluations where conducted with 177 accepted and 101 rejected. The final temperature is 0.1907349E-03 units. The optimal *Q* value is found to be -0.12140 units. The UTS is recalculated to 48.71801 *KSI*. A comparison plot of the stepped strain experimental data and optimized simulation is provided in Figure 6.13. The reoptimized *Q* produced a higher quality fit to the experimental data. The results of a load-controlled simulation (depicted in Figure 6.14) shows that the unified mechanical model produces an appropriate ratcheting strain accumulation. Changing the *Q* constant does not negatively impact the ability to model the strain-controlled experiments. The change translates the hysteresis loops but does not change the cycles to rupture significantly (<0.5%).

Finally, a stress-hold cycling simulation is performed with the following boundary conditions $\sigma_{\max} = 40ksi$, $R = -1$, $\dot{\sigma} = 0.04ksi/s$ with $t_h = 3.333$ hours hold using the material constants listed in Table 6.1 where the reoptimized *Q*=-0.12140 is used. The plot depicted in Figure 6.15 shows an excellent representation of mixed cycling ratcheting and creep deformation which would likely occur in 304SS. It can be said with the modification made to the *Q* constant, the unified mechanical model successfully, models the most basic of service-like conditions an industrial gas turbine component could face when under creep-fatigue.

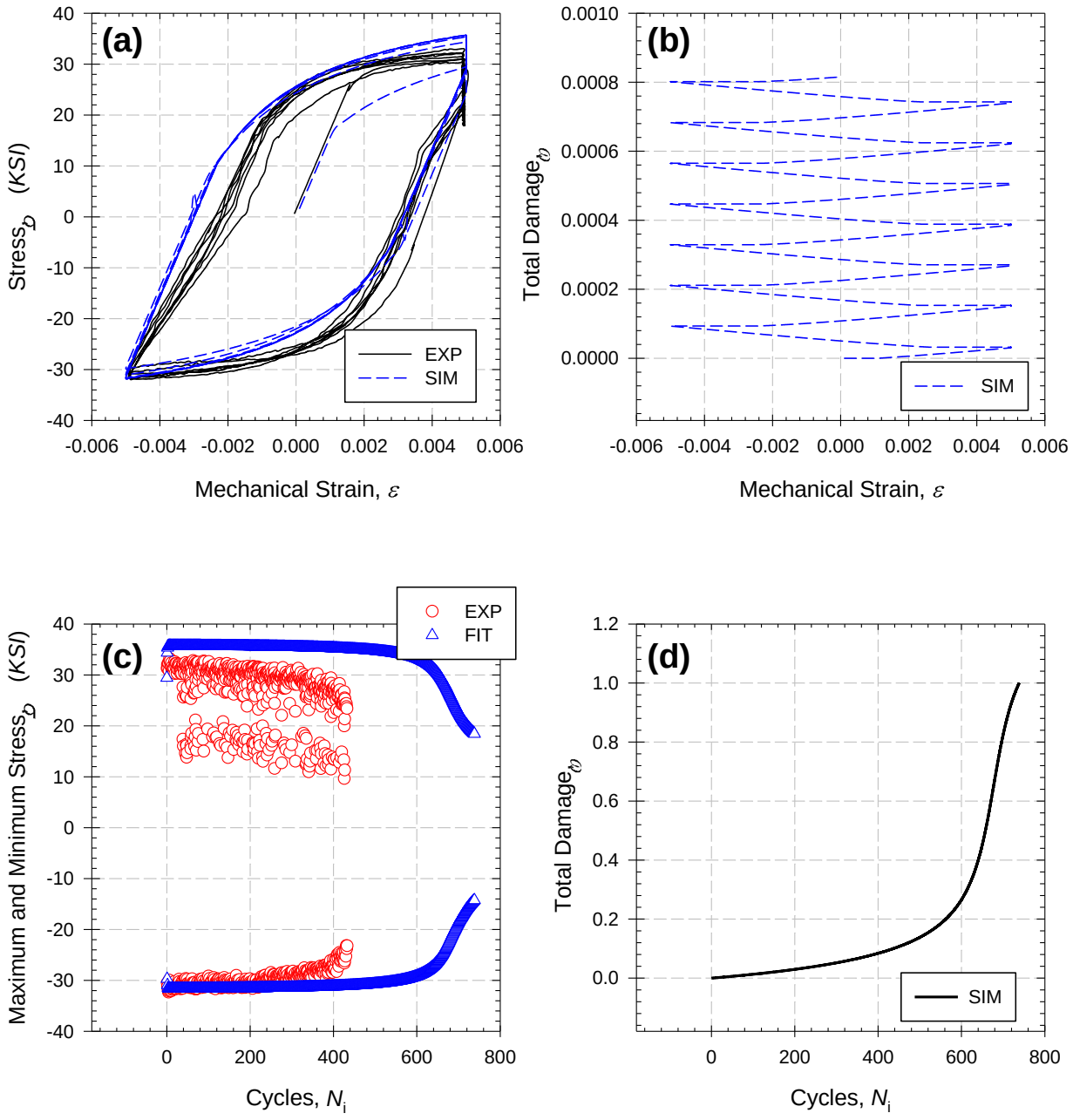

Figure 6.4 - Simulated fatigue tests $\Delta\varepsilon_T = 1\%$ with 60s tensile hold at 600°C (a) stress-strain (b) damage-strain (c) cyclic stress-cycles and (d) damage-cycles

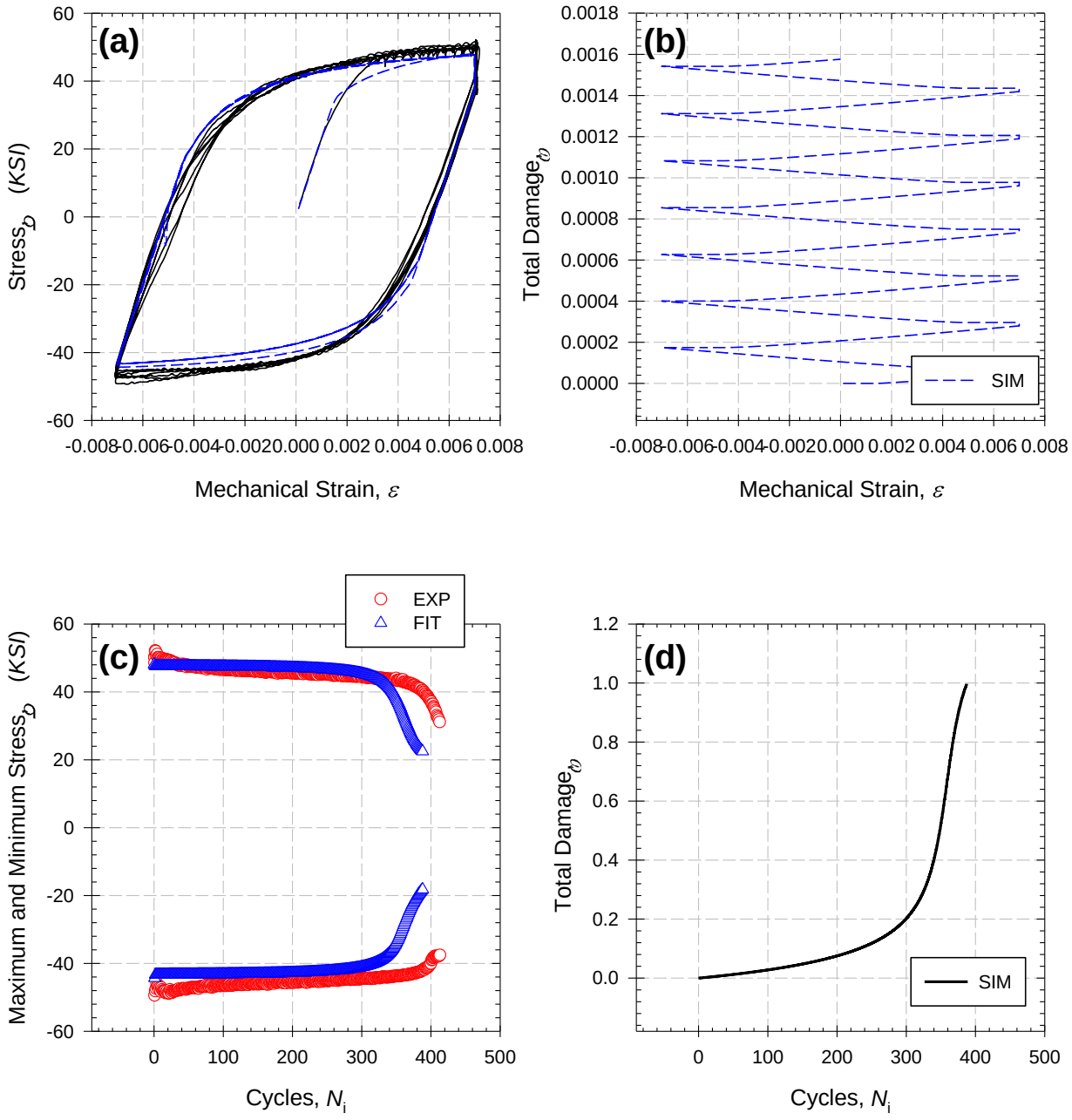

Figure 6.5 - Simulated fatigue tests $\Delta\varepsilon_T = 1.4\%$ with 60s tensile hold at 600°C (a) stress-strain (b) damage-strain (c) cyclic stress-cycles and (d) damage-cycles

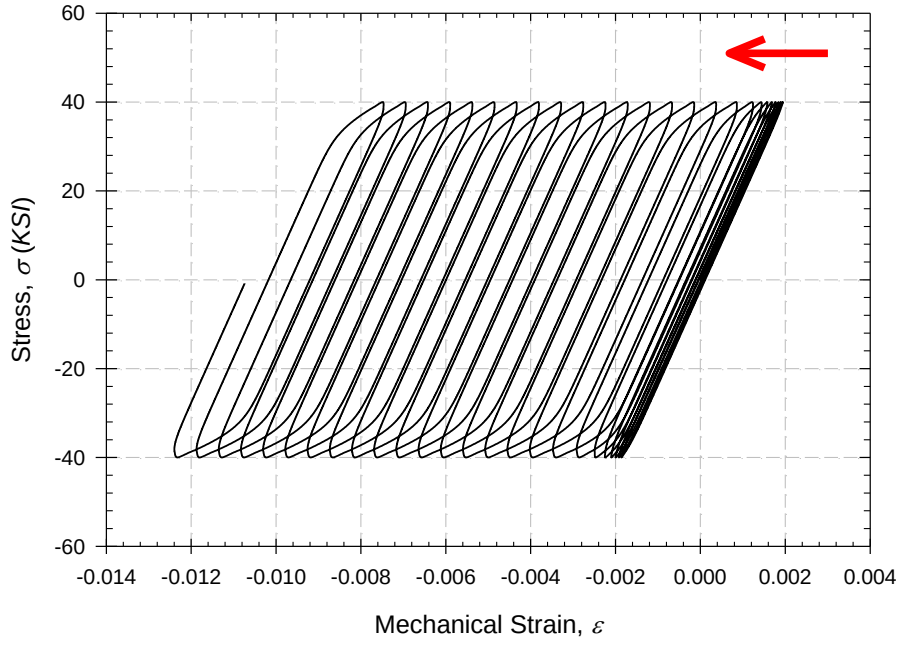

(a)

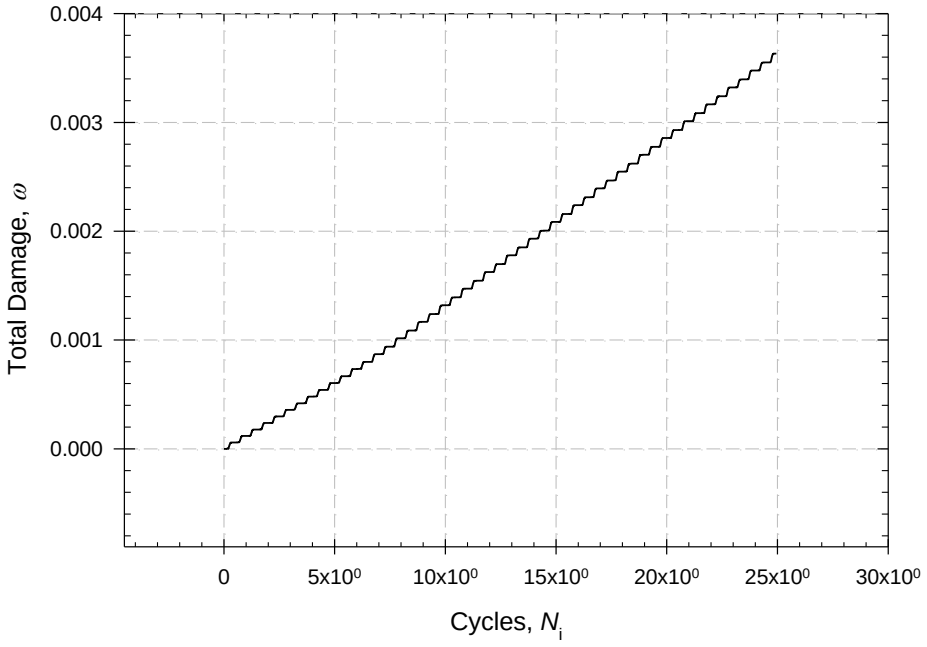

(b)

Figure 6.6 - Simulation of load-controlled fatigue at $\sigma_{\max} = 30ksi$, $R = -1$, $\dot{\sigma} = 0.03ksi/s$ (a) stress-strain (b) total damage-cycles with Q=2.1772

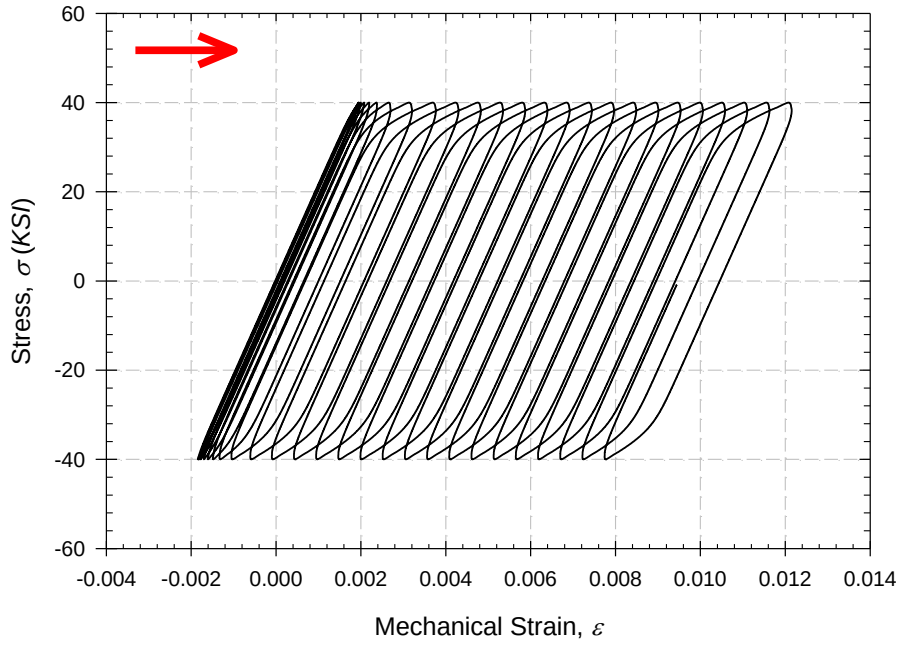

(a)

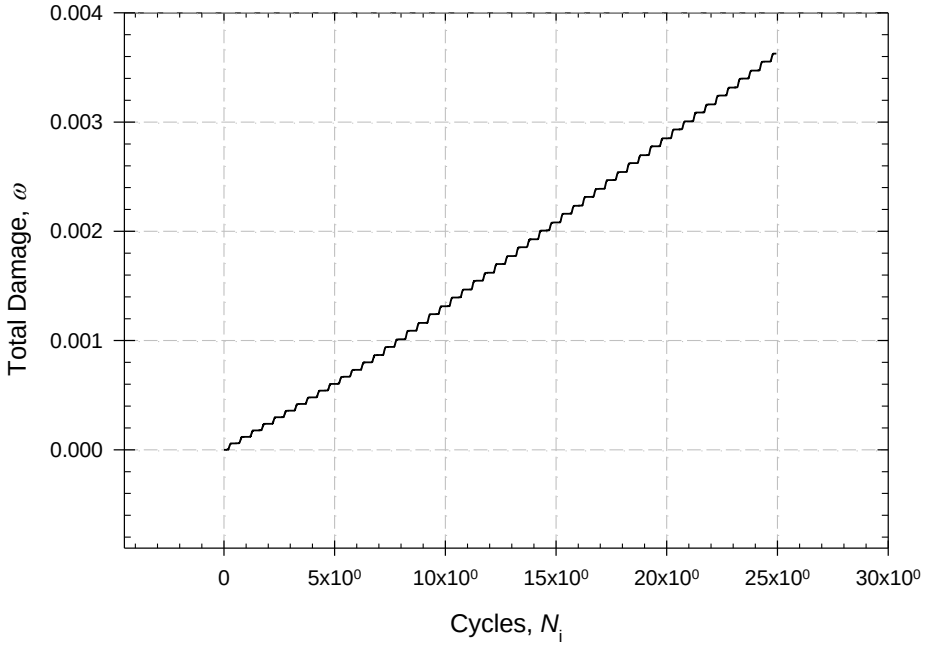

(b)

Figure 6.7 - Simulation of load-controlled fatigue at $\sigma_{\max} = 30ksi$, $R = -1$, $\dot{\sigma} = 0.03ksi/s$ (a) stress-strain (b) total damage-cycles with Q=-2.1772

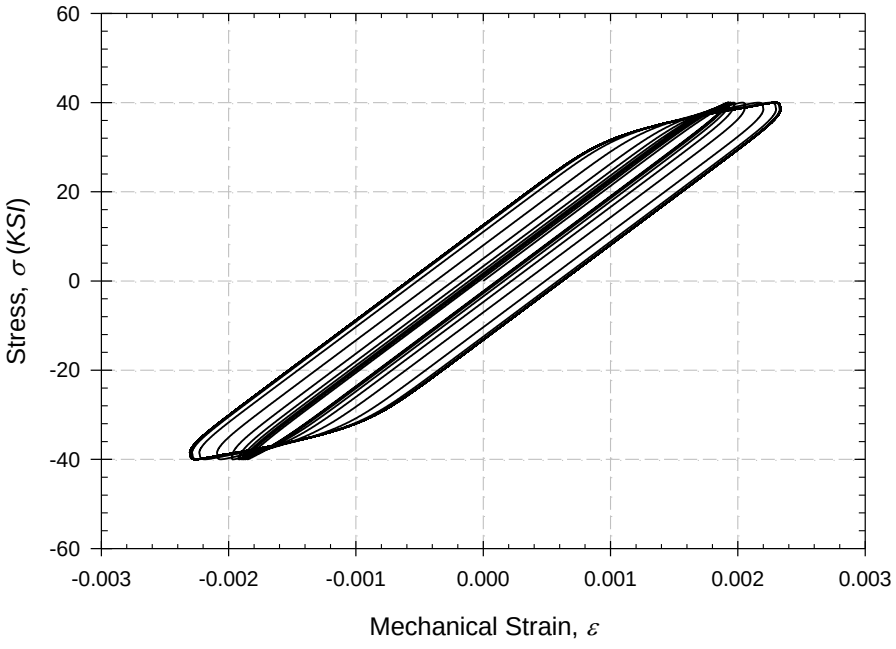

(a)

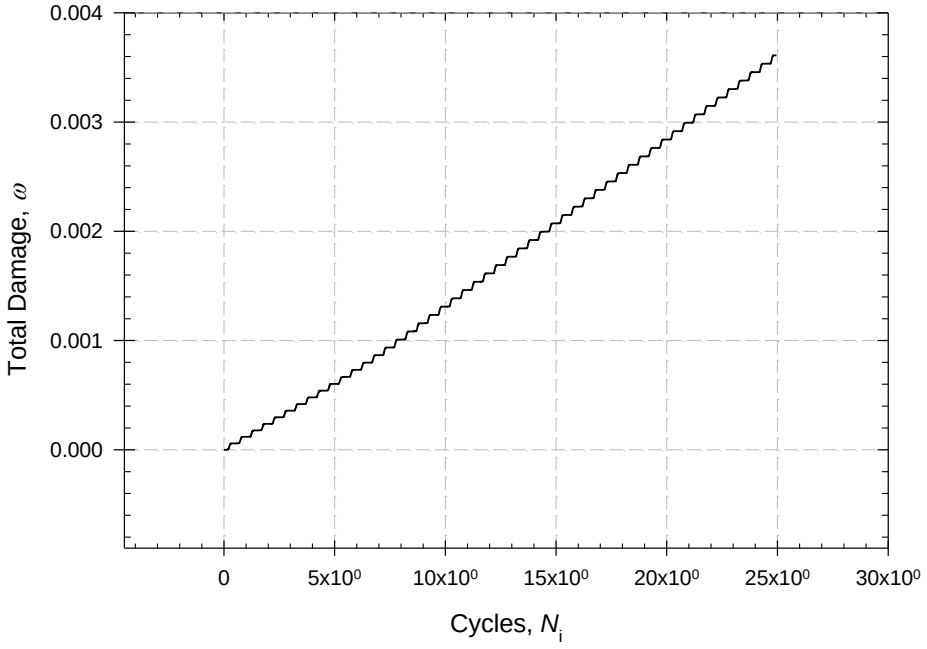

(b)

Figure 6.8 - Simulation of load-controlled fatigue at $\sigma_{\max} = 30ksi$, $R = -1$, $\dot{\sigma} = 0.03ksi/s$ (a) stress-strain (b) total damage-cycles with Q=0

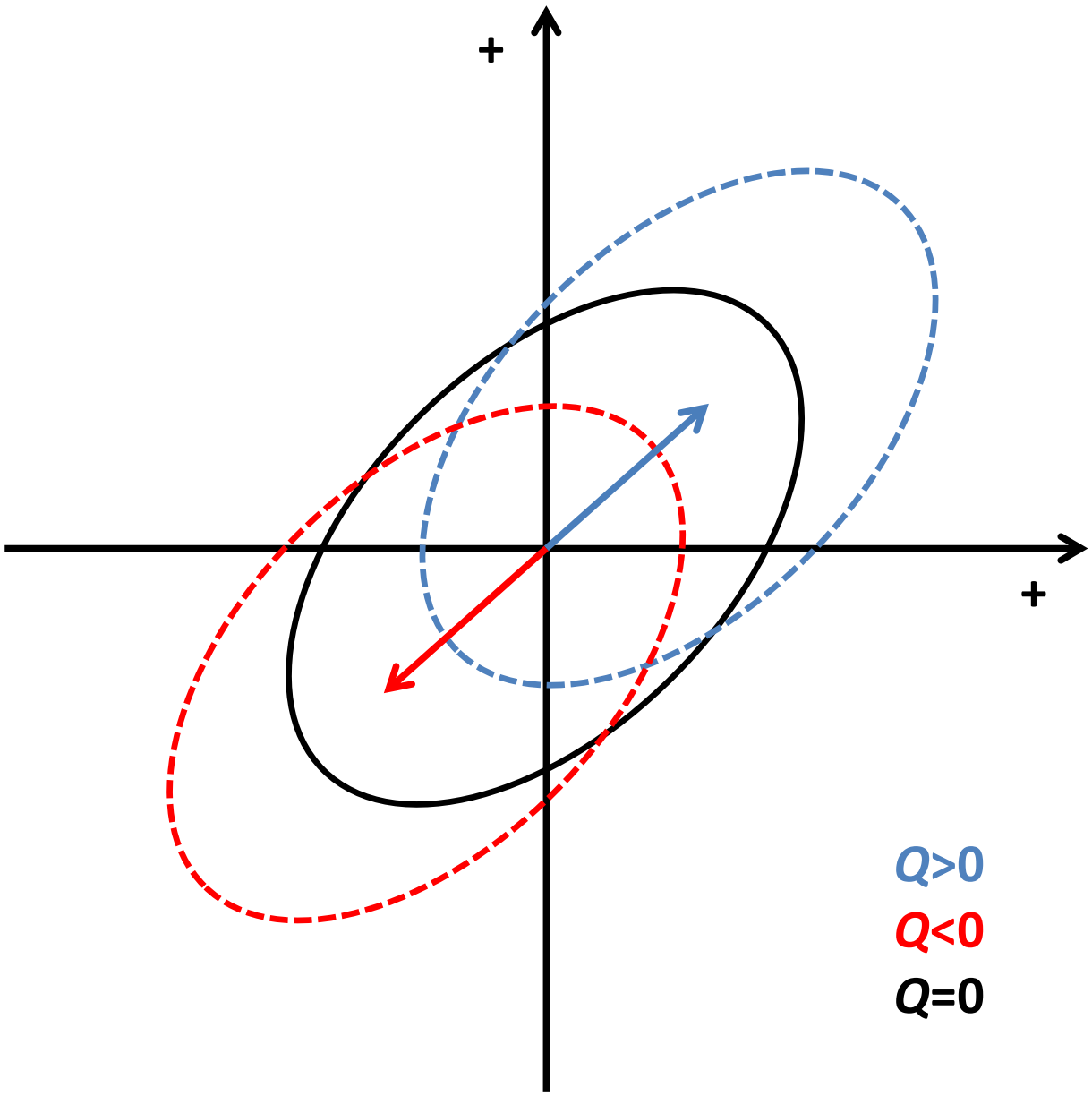

Figure 6.9 - Schematic of yield surface translation due to Q

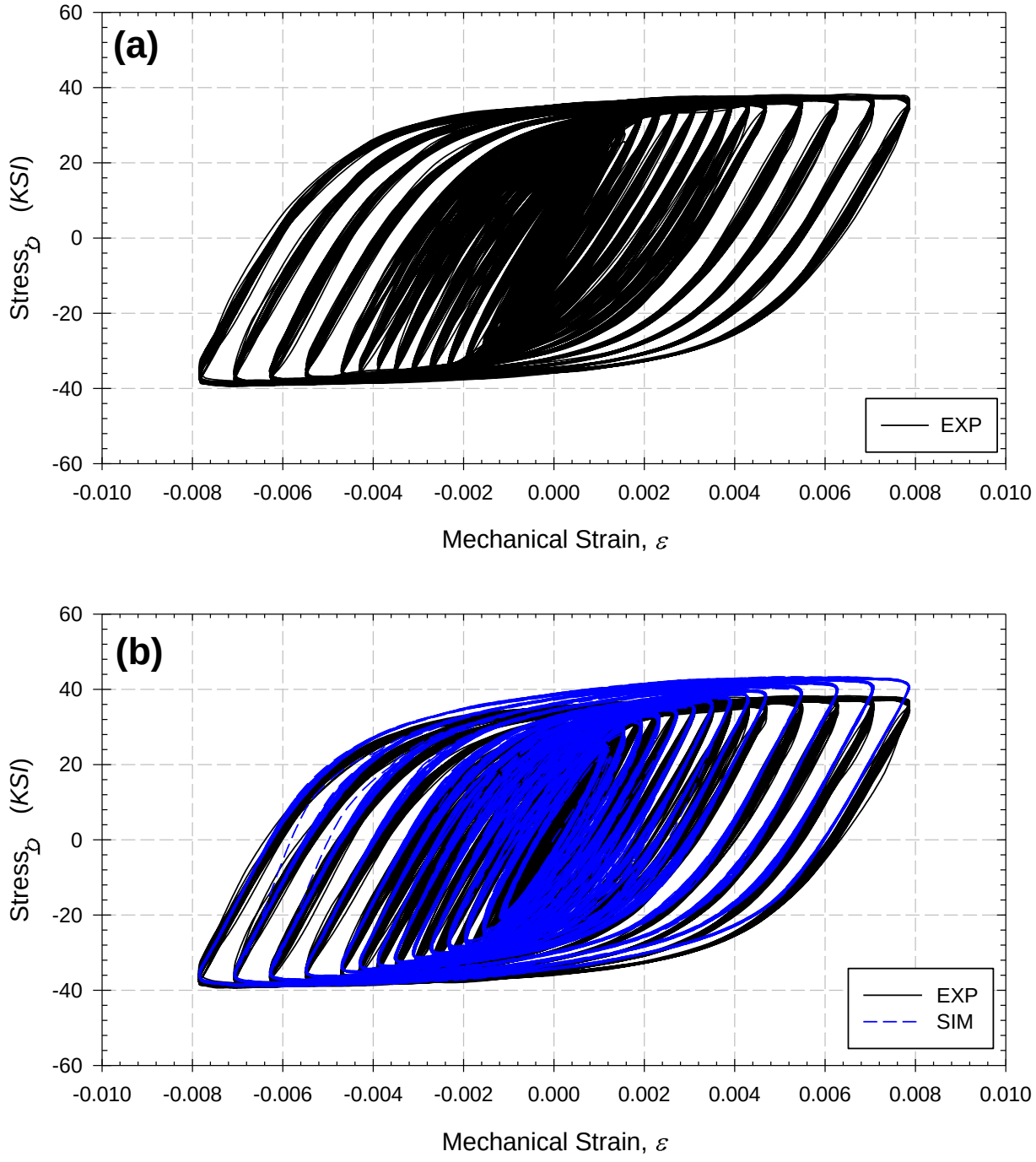

Figure 6.10 - Cyclic stress-strain curve (stepped strain range) of 304SS at 600°C (a) experiment (b) simulation Q=2.1772

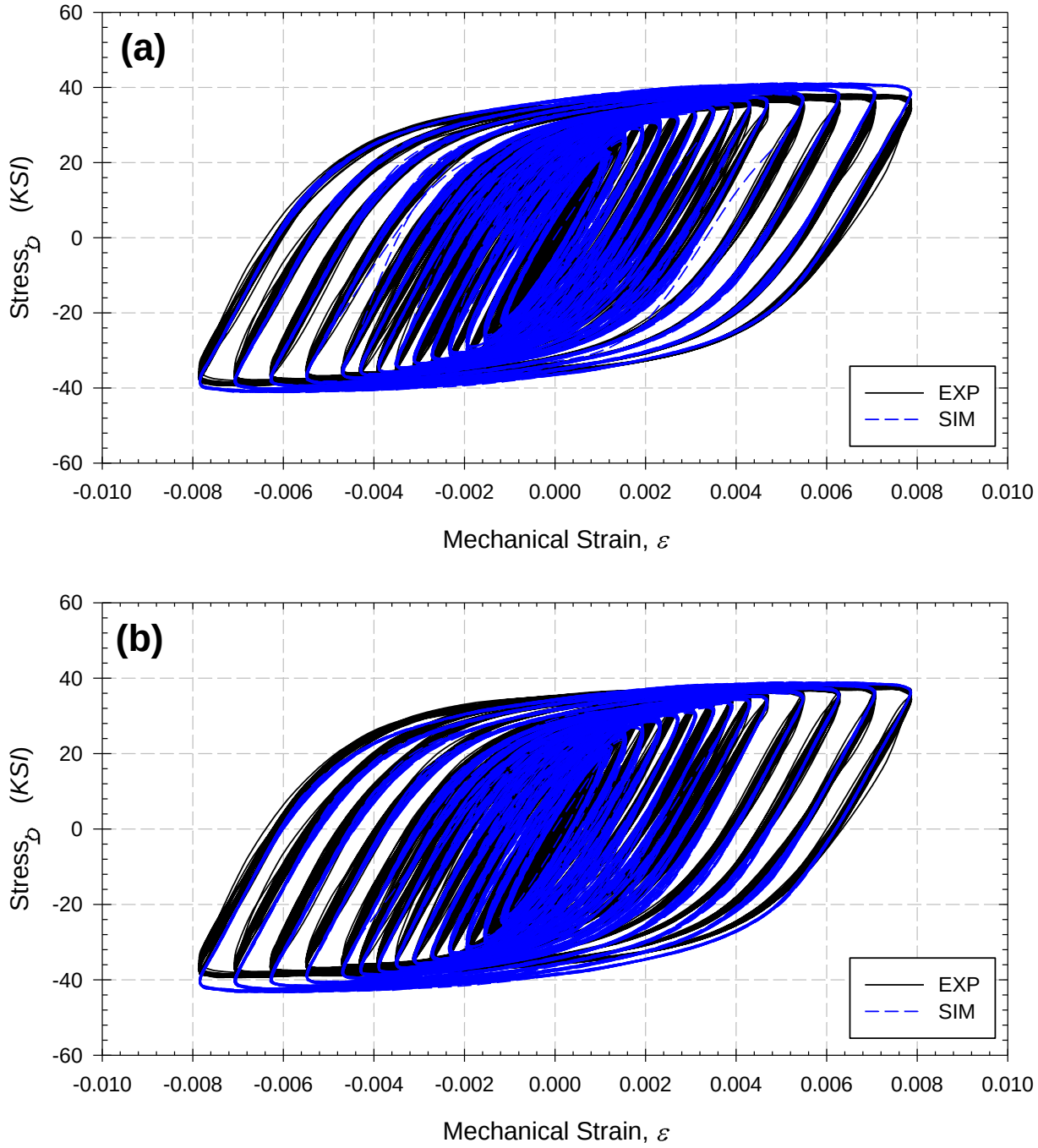

Figure 6.11 - Cyclic stress-strain curve (stepped strain range) of 304SS at 600°C (a) Q=0 (b) Q=-2.1772

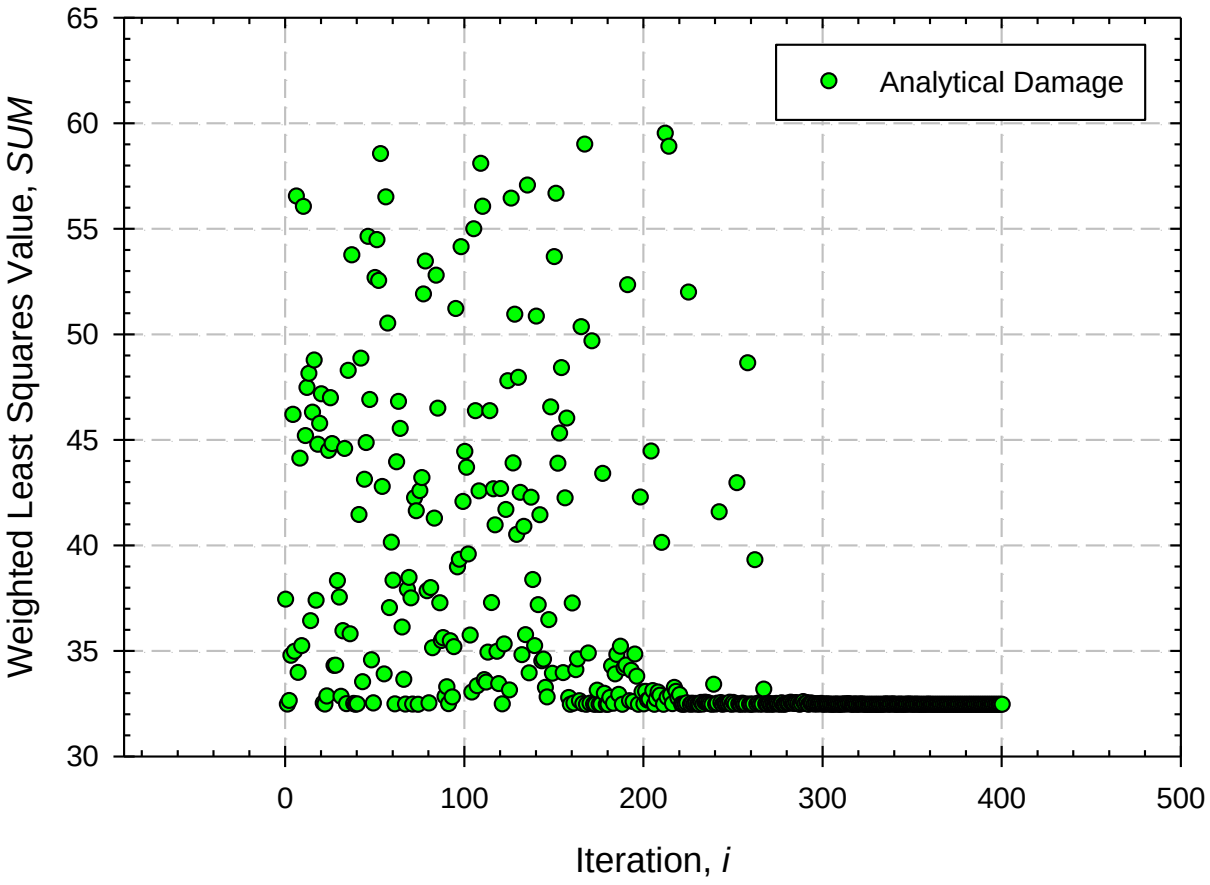

Figure 6.12 - Least square values during optimization of the Q constant

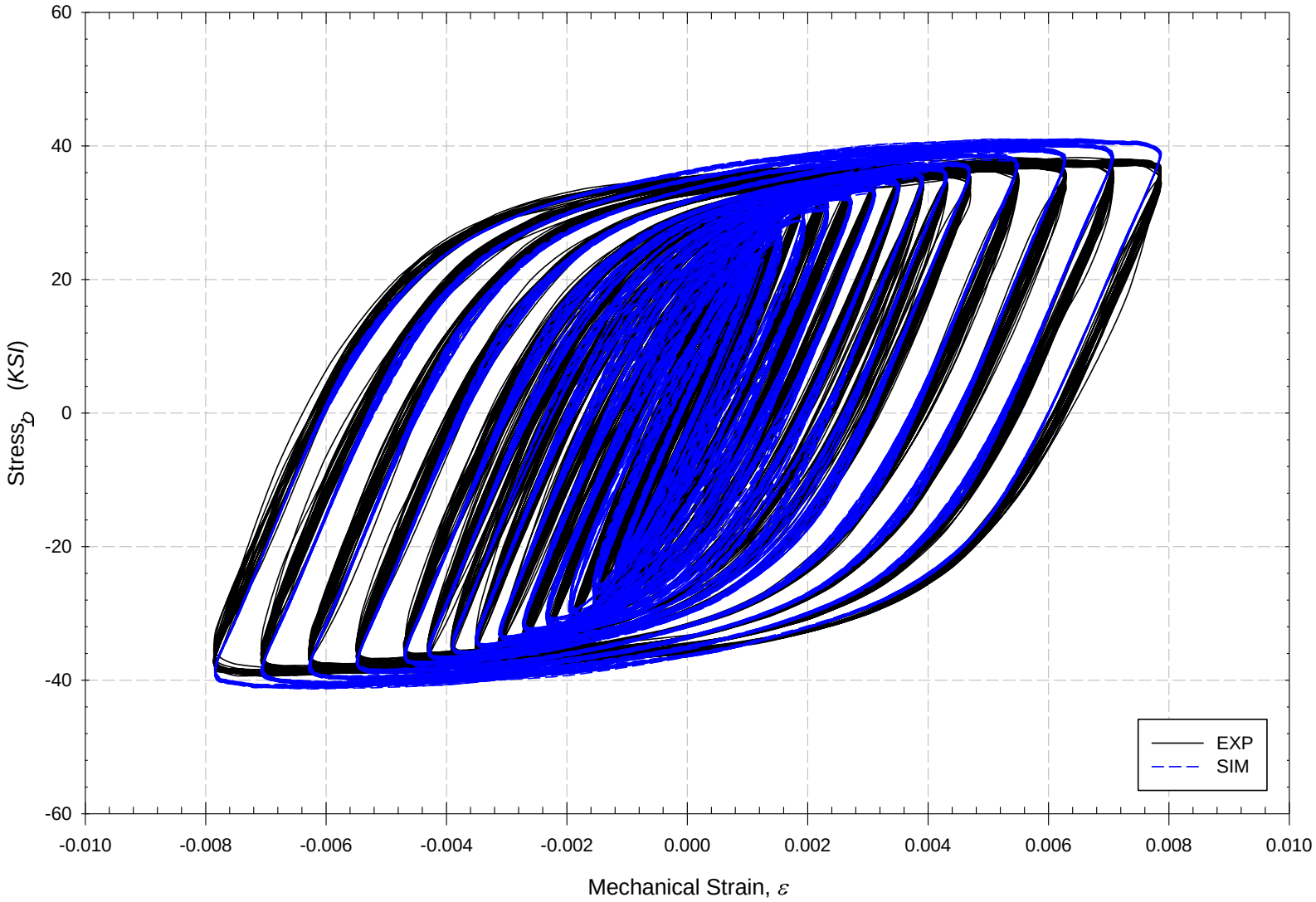

Figure 6.13 - Cyclic stress-strain curve (stepped strain range) of 304SS at 600°C using the reoptimized Q=-0.12140

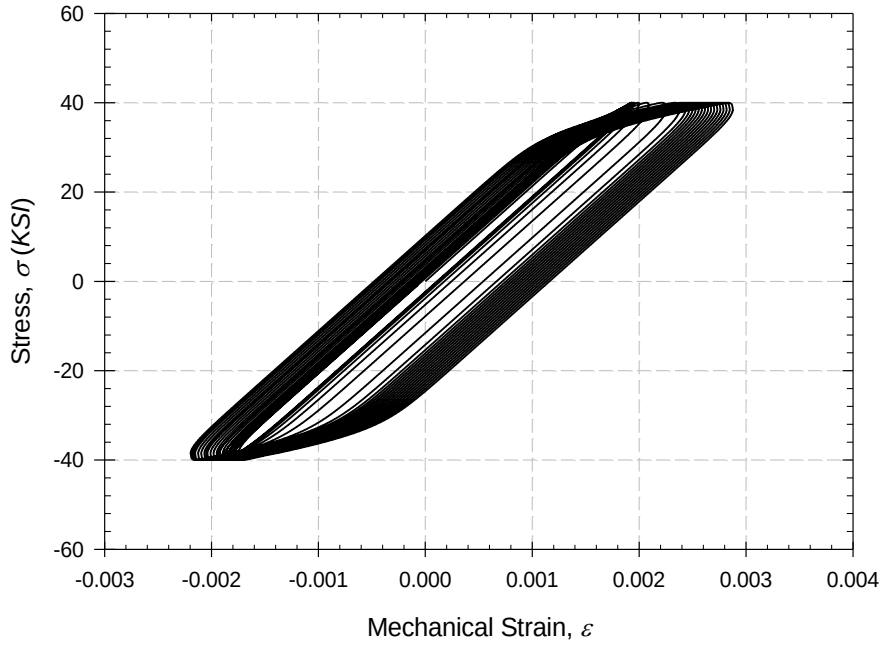

(a)

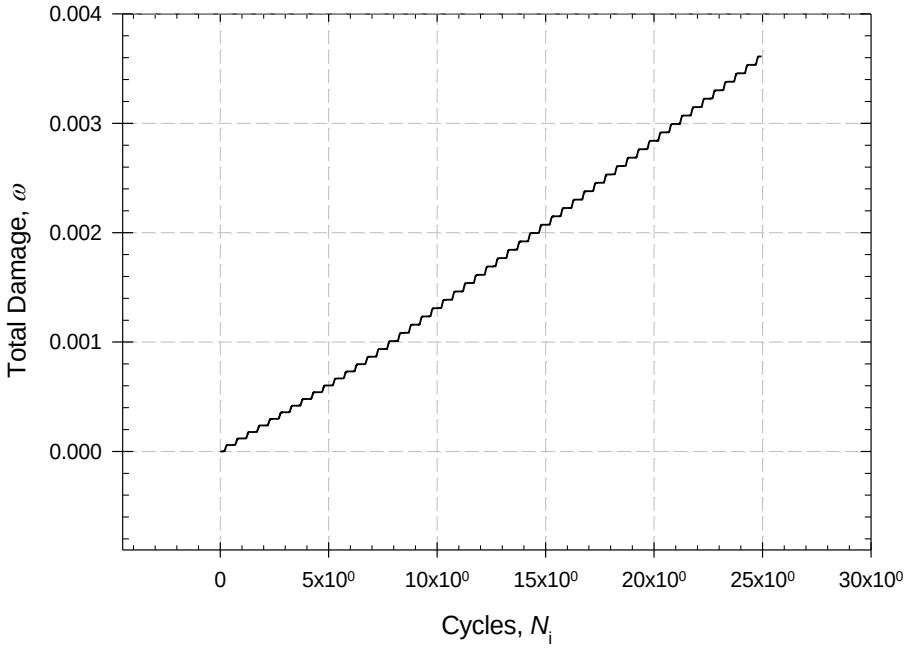

(b)

Figure 6.14 - Simulation of load-controlled fatigue at $\sigma_{\max} = 40ksi$, $R = -1$, $\dot{\sigma} = 0.04 ksi/s$ (a) stress-strain (b) total damage-cycles with *reoptimized Q*= -0.12140

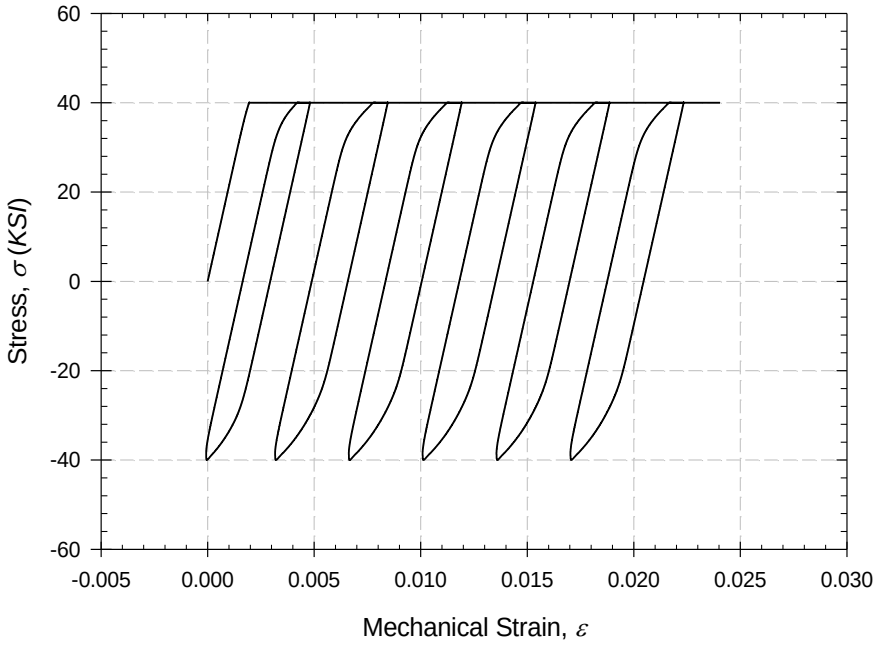

(a)

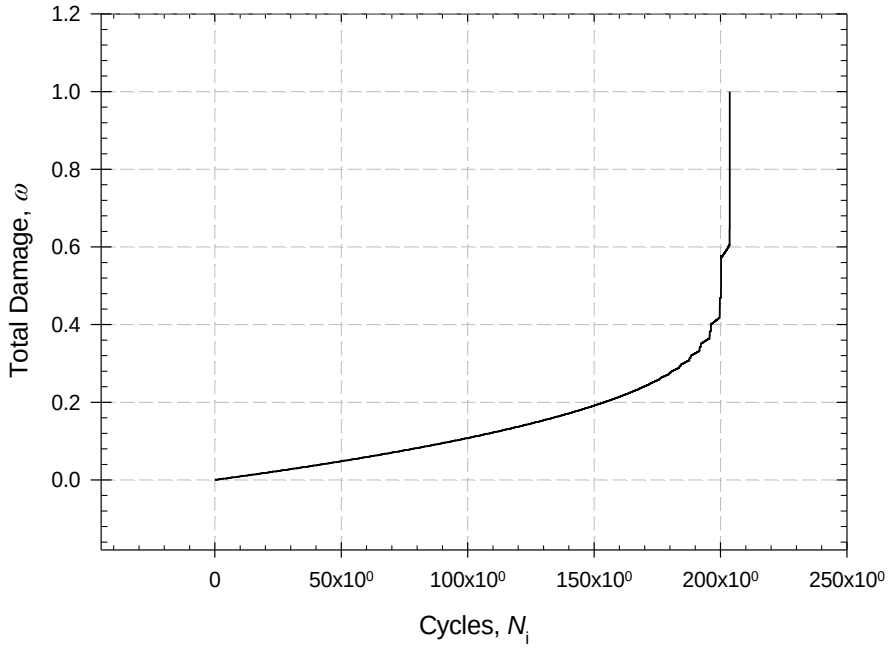

(b)

Figure 6.15 - Simulation of load-controlled fatigue at $\sigma_{\max} = 40ksi$, $R = -1$, $\dot{\sigma} = 0.04 ksi/s$ with 3.333 hour holds (a) stress-strain (b) total damage-cycles with *reoptimized Q*= -0.12140

6.3 **Atypical Load Histories**

The unified mechanical model is exercised for a number of atypical load histories as depicted in Figure 6.16 to demonstrate the models ability to deal with complex load histories and the interactive effects of creep, plastic, and fatigue damage on the constitutive response.

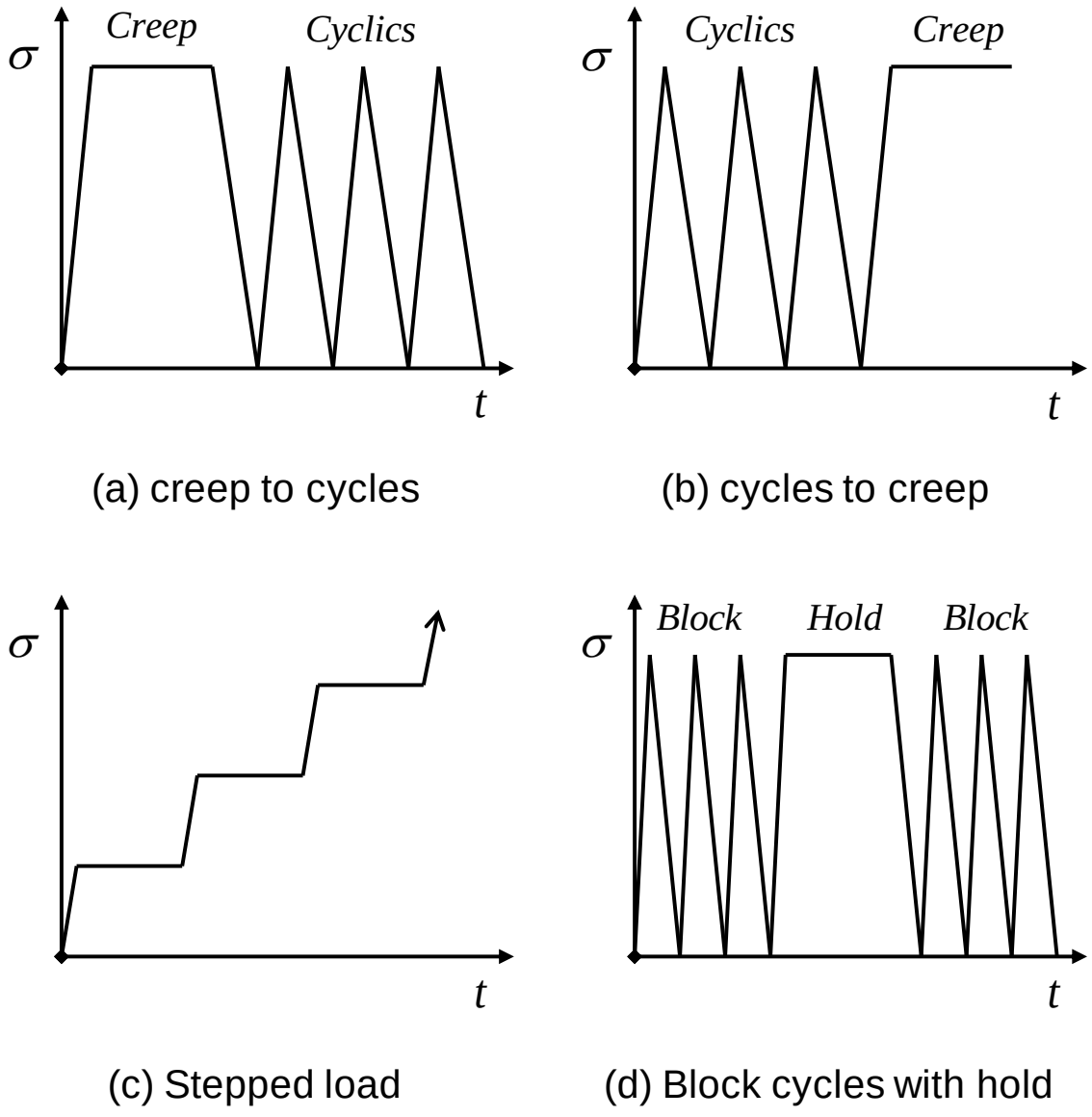

Figure 6.16 - Schematic of Atypical Load Histories

A single set of material properties are used for the atypical load histories. The unified mechanical model properties listed in Table 6.1 are used with the exception that the reoptimized Q=-0.12140 is used. The simulations are conducted using a Young's modulus of E = 21313.89 *KSI*, yield strength of Y = 40.13236 *KSI*, and the ultimate tensile strength is *UTS* = 48.71801 *KSI*.

A $\sigma_{\max}$ =40 *KSI* creep and $\Delta\sigma$ =40 *KSI*, $\dot{\sigma}$ =0.04 *KSI*/*s*, pulsating tensile fatigue simulations are performed for comparison as depicted in Figure 6.17a and b respectively. The creep simulation reached rupture at 265.556 hours with creep damage as the dominant damage mechanism. The pulsating tensile simulation rupture at 3592.5 cycles or 1995.83 hours with fatigue damage as the dominant damage mechanism. Fatigue damage does not become dominant until near the end of life.

The first atypical load history simulated (Figure 6.16a) is a creep test followed by pulsating tensile cycling R=0 the results of which are depicted in Figure 6.18. The peak stress is $\sigma_{\max}$ =40 *KSI*, the stres range $\Delta\sigma$ =40 *KSI*, and the stress rate, $\dot{\sigma}$ =0.04 *KSI*/*s*. The purpose of the first load history is to examine how prior creep damage influences fatigue cycles to failure. The creep test is held for 150 hours followed by continuous cycling until rupture. Compared to a pure creep simulation, the creep to cycles simulation produced a much longer life, a 168.464% increase. Creep damage evolves throughout the simulation, but the rate is greatly reduced when cycling beings. The inelastic strain rate dramatically reduces when cycling begins. Compared to pure cycling, the creep to cycles simulation produces a much shorter life, a 64.279% decrease. Fatigue damage does not appreciably accumulate until near the end of life and becomes the

dominant damage mechanism. This large period of minimal fatigue damage can be associated with the cycles necessary for the fatigue crack to nucleate and initiate.

The second atypical load history simulated (Figure 6.16b) is pulsating tensile cycling R=0 followed by creep the results of which are depicted in Figure 6.19. The purpose of this load history is to examine how prior cycling influence creep rupture time. The peak stress is $\sigma_{\max}$ =40 *KSI*, the stres range $\Delta\sigma$ =40 *KSI*, and the stress rate, $\dot{\sigma}$ =0.04 *KSI*/*s*. Cycling occurs for N_i =3000 cycles followed by a creep held until rupture. Compared to a pure creep simulation, the creep to cycles simulation produced a much longer life, a 561.714% increase. Creep damage is the dominant damage mechanism. the inelastic strain rate dramatically increases when creep loading begins. Compared to pure cycling, the creep to cycles simulation produces a much shorter life, a 11.955% decrease. Fatigue damage is minimal.

The third atypical load history simulated (Figure 6.16b) is an stepped isostress method (SSM) creep tests with the stress rate, $\dot{\sigma}$ =0.04 *KSI*/*s* the results of which are depicted in Figure 6.20. The purpose of the third load history is to examine how the primary creep and secondary creep regime change as the stress level is increased. The stress starts at 40 *KSI* and increases in 1.6 *KSI* increments at a stress rate of $\dot{\sigma}$ =0.04 *KSI*/*s* every $t_h = 5$ hours. The unified mechanical model produces the appropriate response when compared to results of SSM in literature for various materials [266]. A near instantaneous increase in the strain is associated with increased primary creep strain. The minimum creep strain rate increases due to the applied stress. Given SSM experimental data to rupture, it may be possible to determine the viscous function constants A_0 and σ_s and the creep damage constants M, σ_t and χ respectively.

The fourth atypical load history simulated (Figure 6.16b) is mixed sequential creep-fatigue test where 500 cycles blocks are interrupted with 40 hours of creep. The tests is performed with $\sigma_{\max} =$=40 *KSI*, $\Delta\sigma$=40 *KSI*, $\dot{\sigma}$=0.04 *KSI*/*s* the results depicted in Figure 6.21. The purpose of the third load history is to examine how damage evolves during mixed loading conditions. It is observed that the inelastic strain rate continuously increases and decreases in during creep and cycling respectively. It is possible that the reduction in inelastic strain rate during fatigue can be associated with the transgranular cracking process. For a majority of life, creep damage is dominant. At the end of life, fatigue damage rapidly evolves and becomes dominant. Again, this large period of minimal fatigue damage can be associated with the cycles necessary for the fatigue crack to nucleate and initiate.

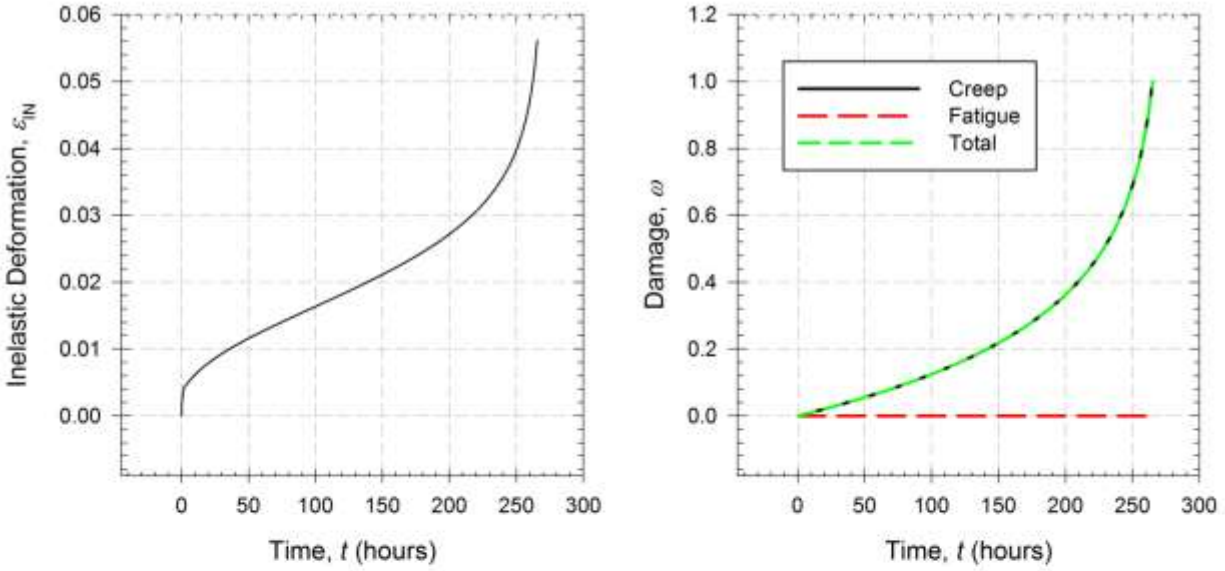

(a)

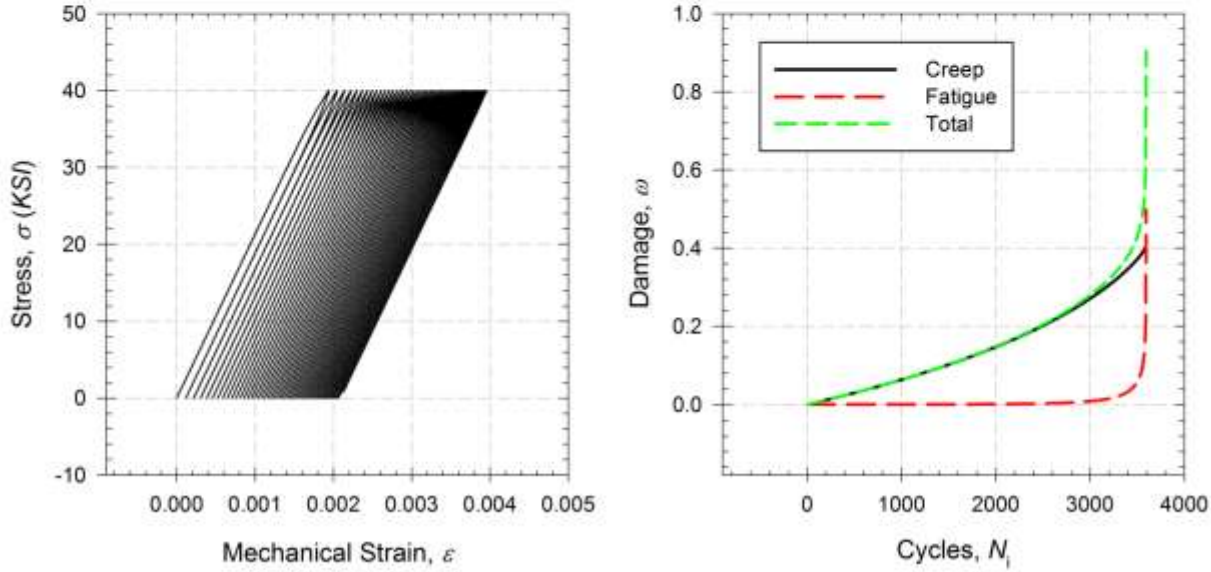

(b)

Figure 6.17 - Simulation of (a) creep and (b) pulsating tensile fatigue test with $\Delta\sigma$ =40 *ksi*, $\dot{\sigma}$ =0.04 *ksi/s*

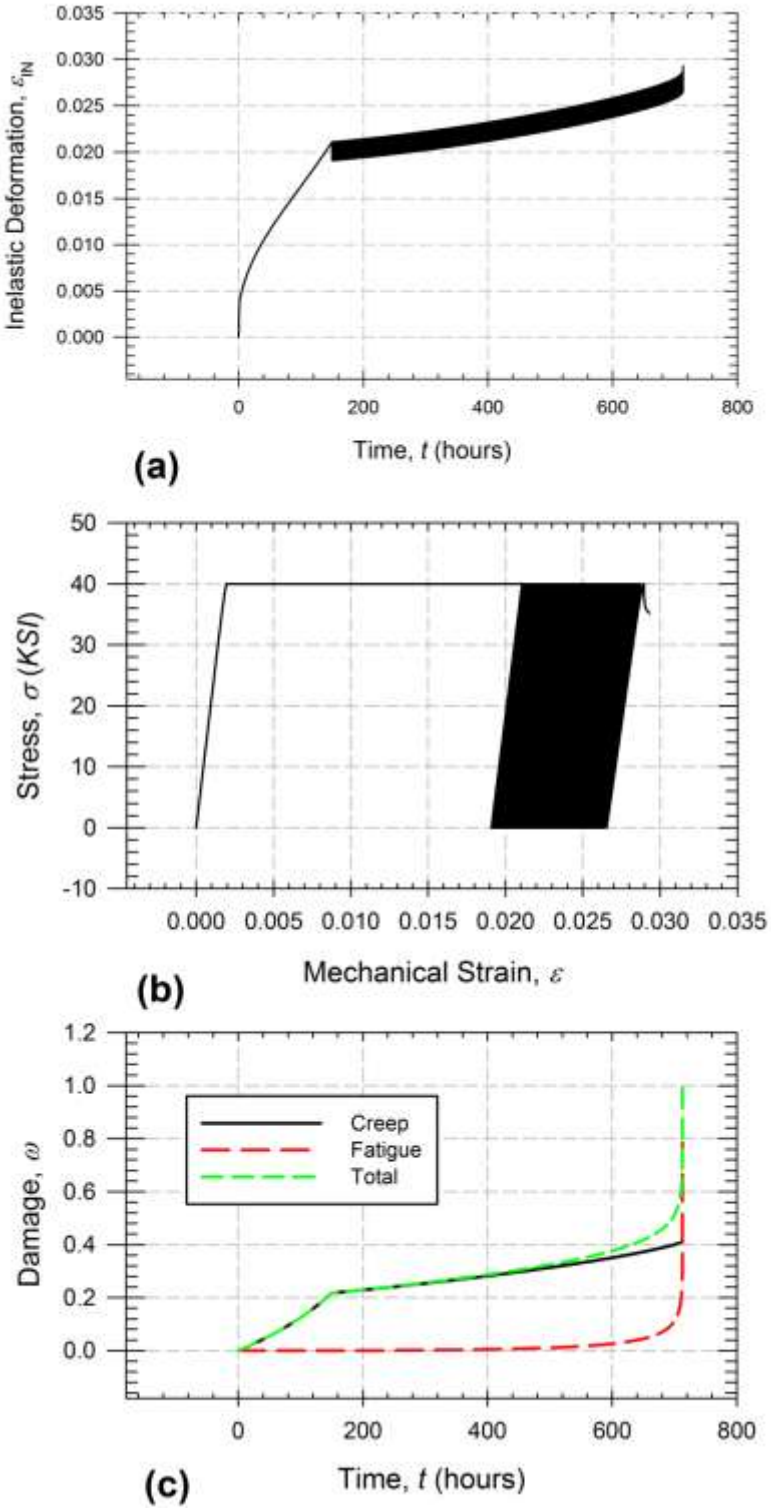

Figure 6.18 - Creep for 150 hours followed by pulsating tensile cycling to rupture (a) deformation (b) stress-strain (c) damage

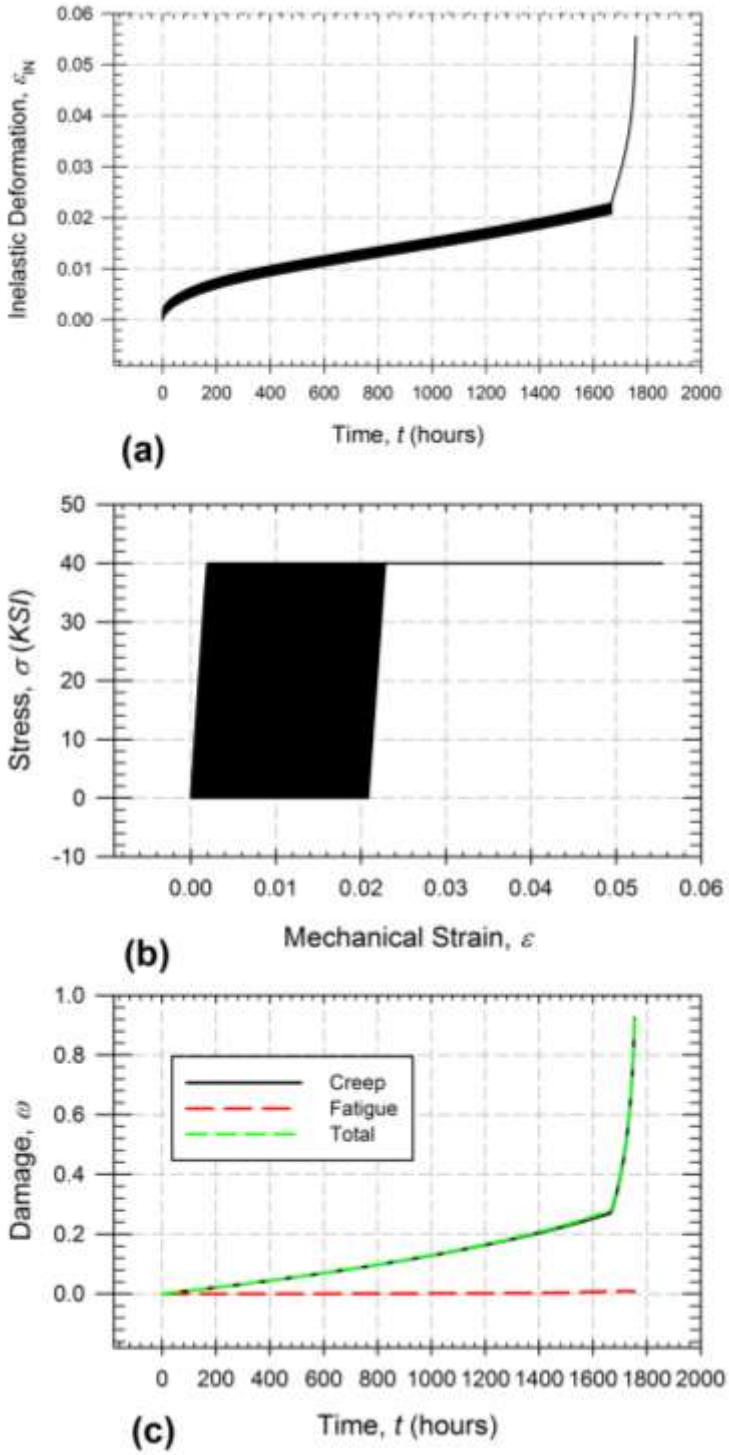

Figure 6.19 - Pulsating tension for 3000 cycles followed by creep to rupture (a) deformation (b) stress-strain (c) damage

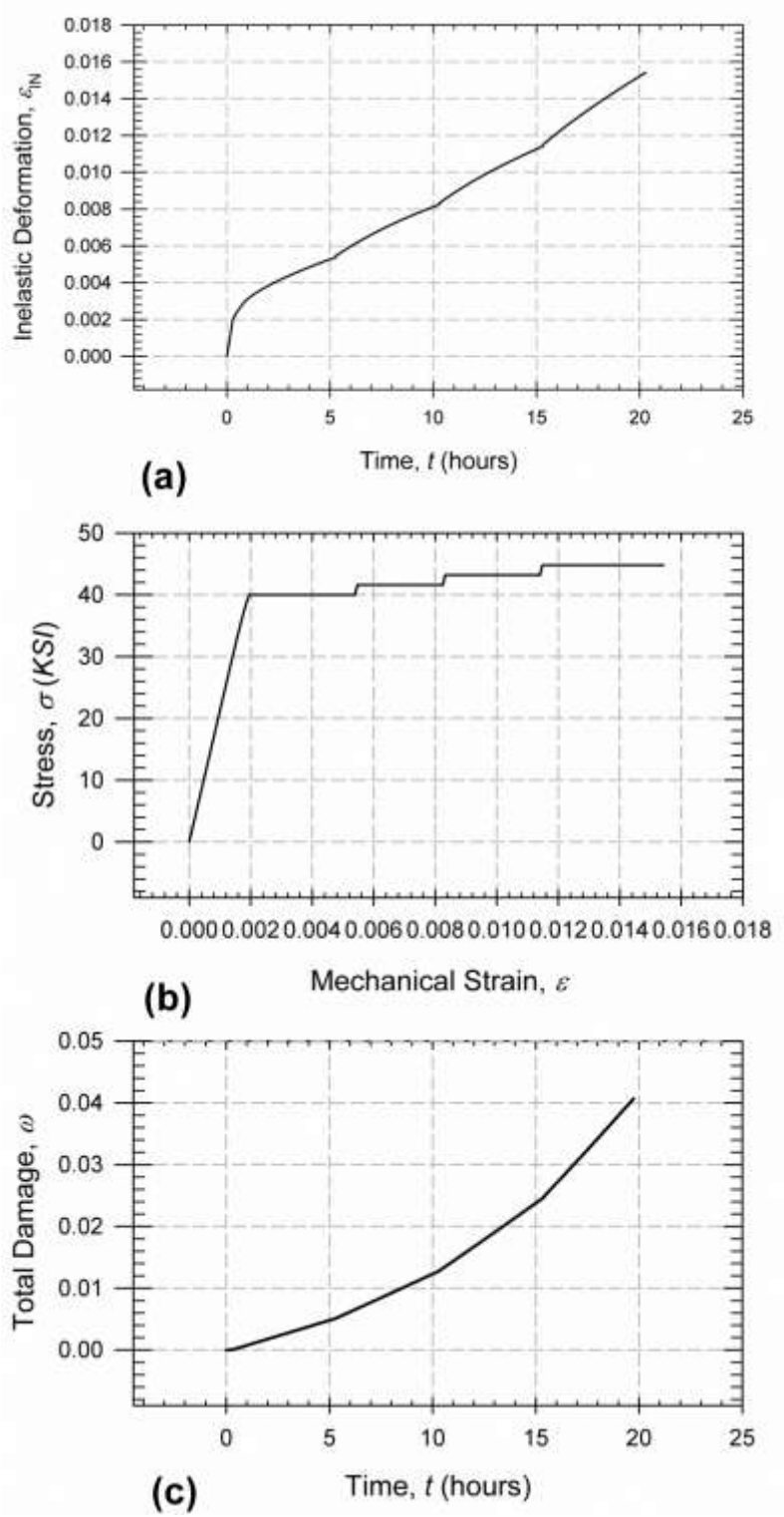

Figure 6.20 - Stepped isostress method (SSM) creep tests (a) deformation (b) stress-strain (c) damage

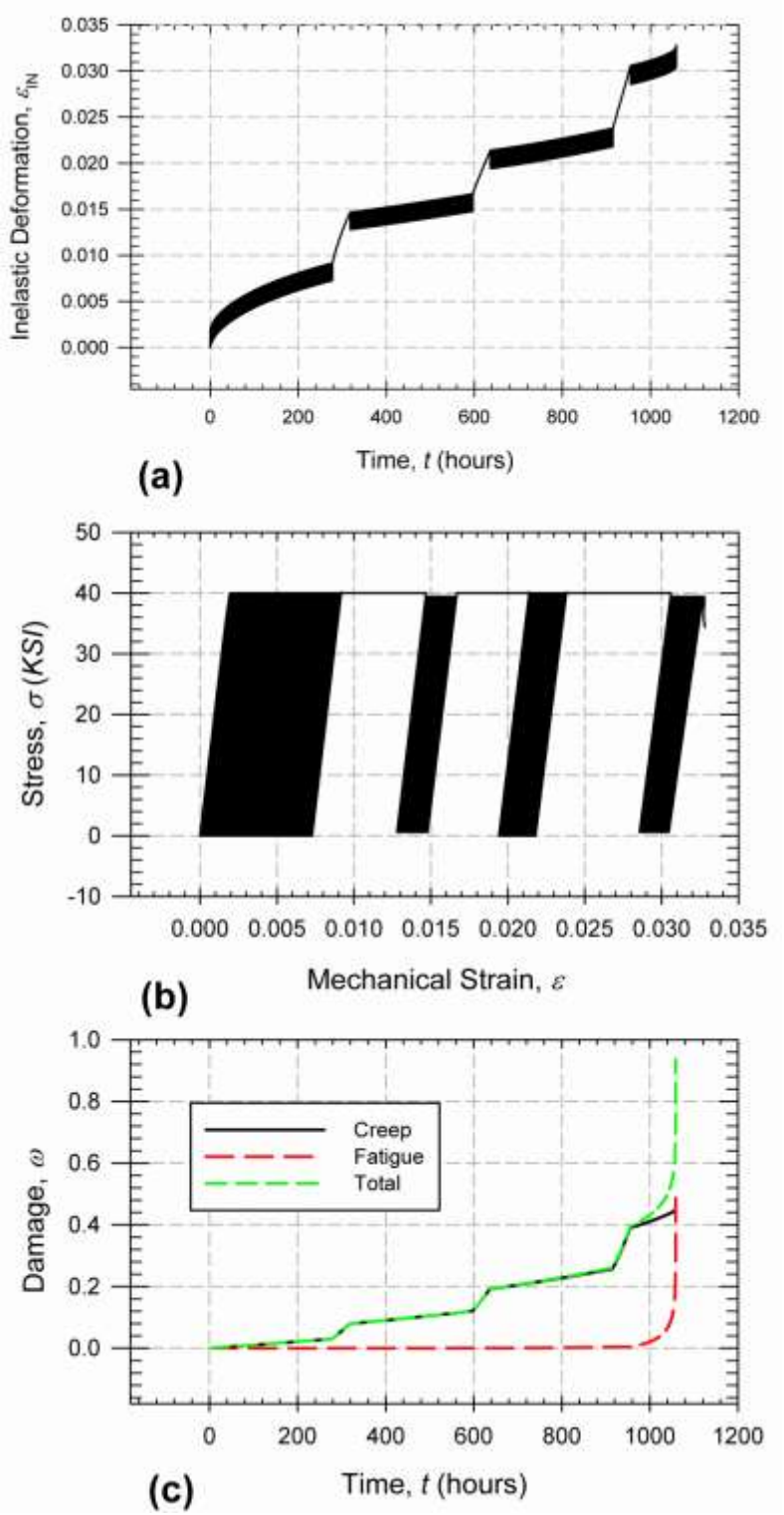

Figure 6.21 - Mixed sequential fatigue test (a) deformation (b) stress-strain (c) damage

CHAPTER SEVEN: CONCLUSIONS AND FUTURE WORK

7.1 **Conclusions**

A novel unified mechanical model for the creep-fatigue of a gas turbine superalloy has been developed. A hybrid constitutive model which incorporates continuum damage mechanics has been derived, analytically and numerically fit to experimental data, and proven to model the constitutive response of the subject material. A linearly-coupled continuum damage mechanics law for creep, fatigue, and plasticity/ductility has been derived which allows the monitoring of microstructural damage through a body under consideration. A mechanical degradation equation is implemented to allow the reduction of the stiffness of a body until a crack is produced within that body. Progress interaction of the constitutive, damage, and mechanical degradation provide a method by which crack initiation, propagation, and rupture can be predicted in a body. Extensive parametric simulations of the unified mechanical model have been performed to validate the applicability of the unified model. It has been proven that the novel unified mechanical model for creep-fatigue of a gas turbine superalloy meets the research objectives stated in the introduction.

7.2 **Future Work**

While considerable effort has been expended in the completion of this dissertation, the scale of the unified mechanical model precluded inclusion of additional experiments, numerical implementations, derivations which could enhance the capabilities of the unified mechanical model. Below are listed topics of future work pertaining to the improvement of the unified mechanical model:

Implement the Unified Mechanical Model in a Commercial FEM Code

While, the model has been implemented in a custom 1D FEM code; implementation in a commercial FEM software, would demonstrate that the model could be used by practicing engineers in industry who are familiar with commercial software. This is a important future topic because it can lead to adaptation of the unified mechanical model within industry or at the least, collaboration between academia and industry.

Evaluate the Multiaxial and Anisotropic Form

Multiaxial equations for the unified mechanical model for creep-fatigue were derived but not evaluated. An anisotropic form was suggested by using Hill's anisotropic analogy. A series of creep, fatigue, and monotonic tensile tests for an anisotropic superalloy should be conducted and compared to simulations using the anisotropic multiaxial equations. The result of these simulations would prove useful in determining the unified mechanical models ability to model the mechanical behavior of directionally solidified turbine blades under service.

Conduct Creep-Fatigue Cracking Experiments

The current study has emphasized the constitutive response and rupture prediction using the unified mechanical model. A lack of creep-fatigue crack initiation and propagation data precluded the evaluation of crack growth using the CDM-based damage variables. A series of experiments which produce crack quantities for a superalloy would demonstrate the capabilities (or lack thereof) of the unified mechanical model in predicting crack growth. The inclusion of variables such as mean stress and notched geometry would further evaluate the model and provide opportunity for improvement. Possible improvements include using an alternative damage quantity to better predict crack growth [267].

Optimize the Constant Determination Process

In the current study, a significant number of experiments are required to determine the material properties of the unified mechanical model for creep-fatigue. The determination process involves a series of numerical optimization for sets of constants associated with each experiment. The determination process could be simplified by developing "specialized" mechanical tests which exercise the material over a wide range of boundary conditions. This would reduce the number of experiments needed and thus reduce the costs associated with calibrating the unified mechanical model for creep-fatigue for any particular material.

Simplify the Unified Mechanical Model for Creep-Fatigue

As depicted in Table 5.6, the unified mechanical model for creep-fatigue includes many internal state variables which require a significant number of material parameters. This becomes a serious problem when simulations are needed under non-isothermal conditions. Simplify the unified mechanical model would improve the chance of the model being adopted by industry. Possible avenues of simplification include:

- developing a singular damage law for creep, fatigue, and plastic/ductile damage
- total damage interfaces with the viscous function instead of each individual damage mechanism.

7.3 **Alternative Topics**

Considerable literature review has been performed in the conduction of this study. During this process, a number of alternative topics where evaluated and have potential as future work. Towards the execution of these alternative topics, grant-formatted abstract have been constructed and are provided below

Multiscale Energy-Based Model of Metals Subject to Irreversible Processes

As our world becomes more complicated and the demands on materials increase, multiple active failure mechanisms have become the norm. This is particularly the case for anisotropic superalloys subject to dynamic thermomechanical fatigue where a combination of creep, fatigue, and oxidation cause degradation. As a response there arose unified viscoplasticity constitutive models that incorporate multiple strain hardening and softening mechanisms to model

complicated history. Unfortunately, numerous experiments are needed to identify the history of the internal variables which represent each mechanism. These phenomenological internal variables must be functionalized then introduced into the viscous function to describe the constitutive response. The practical implementation of these constitutive models is exceptionally difficult. It is hypothesized that energy or entropy can be used to replace the phenomenological internal variables which represent physical mechanisms. Barasan and Nie [268] have shown that entropy can be used to represent the damage mechanics of solids. Biegler and Mehrabadi [269] developed an energy-based anisotropic constitutive model for rate-independent solids subject to damage. Energy is an excellent multiscale parameter. At the atomic-scale there exists bond and dislocation energy, at the micro-scale there is grain boundary energy, at the meso-scale grain size, distribution, and morphology create unit cells with unique strain energy release rates, and at the macro-scale strain-energy represents the maximum energy per unit volume before failure. It is my desire to develop a multiscale energy-based constitutive model to represent the multiple irreversible processes in solids which lead to failure. To achieve this goal, I will collaborate with faculty at the university to purchase commercial licenses for software necessary for finite element simulations. While this project is both accessible to undergraduate and graduate level researchers, I will also seek a post doc collaborator through the NSF Fellowships for Transformative Computational Science using CyberInfrastructure (CI TraCS). For large simulations, I will work with the National Center for Supercomputing Applications (NCSA) at the University of Illinois at Urbana-Champaign to complete complex jobs.

Keywords**:** Multiscale, Energy-Based, Anisotropic, Constitutive Model, Damage, Life Prediction, Thermomechanical Fatigue (TMF), Oxidation

Stochastic CDM Model for the Prediction of Initial/Current Damage Distribution

Traditionally solids are modeled as homogenous volumes with uniform strength; however, in practice materials exhibit a non-uniform distribution of strength. Defects of unknown scale, dimension, geometry, and position make the strength, deformation, and rupture of solids a statistical variable [270]. The manufacture of solids is a stochastic process, where the damage state of the "product" is based on both predictable actions and some randomness. The distribution of initial damage can be uniform or localized [271]. Processes such as solidification, aging, surface machining, environment, etc. can influence the state of damage. Damage is a multi-scale problem where crystallographic defects on all scales influence the bulk constitutive response [272]. In some cases, extremely heterogeneous materials exist where a high order of multiscale complexity leads to enormous computational costs. For example, metallic woven wire mesh; on the wire-scale individual wires exhibit different residual deformations (due to the drawing and weaving process) and coefficients of friction, on the meso-scale weave pattern and orientation influence contact friction, and on the macro-scale miss-weaves, rips, tears, and the environment influence damage accumulation [273]. A multiscale model of such a material would require large-scale parallel multi-body dynamics computation to deal with the interaction of these variables. For in vivo biological materials it can be difficult to quantify the defects and mechanical properties accurately and at multiple scales. Clearly, in some cases it is necessary to take a phenomenological approach to degradation. In continuum damage mechanics, the solid is assumed to be initially undamaged and evolve to a ruptured state ($0 \le \omega \le 1$). The evolution of

damage is deterministic. As an alternative, I plan to develop stochastic CDM models to represent the probabilistic natural of damage within solids. The macro-scale properties will be extracted using traditional mechanical testing and stochastically implemented in the constitutive model. Both an a priori and a posteriori approach to predict the initial damage distribution will be conducted. The a priori approach involves predicting the initial damage distribution (intensity and location) via global numerical optimization to a given constitutive response. The a posteriori approach involves acquiring an X-ray microtomograph (μ-CT**)** of the initial undamaged material and replicating that distribution in simulation. To achieve this goal, partnerships with various industries could be formed to investigate methods by which the current damage state of an in-service part could be determined via simulation.

Keywords**:** stochastic, continuum damage mechanics, a priori, a posteriori, initial damage distribution, in-service, damage state, microtomography

APPENDIX A: HYBRID.F

```
!-------------------------------------------------------!
! THIS FUNCTION IS A 1D EVALUATION OF THE HYBRID MODEL    !
! CONSTITUTIVE EQUATIONS FOR STRESS AND STRAIN-CONTROL    !
!-------------------------------------------------------!

subroutine HYBRID(X,N,ANSTIME,ANSDATA,NDIMA,set1,set2,PRNTR)

IMPLICIT NONE

  INTEGER*4 N,I,J
  INTEGER*4 NDIMA
  INTEGER*4 set1, set2
  REAL PRNTR

  REAL ANSTIME(NDIMA),ANSDATA(NDIMA),X(N)
  DOUBLE PRECISION b,n0,c1,c2,c3,c4,c5,c6,c7,c8,cd,rate,D_sat,sgn, conv
  DOUBLE PRECISION Q, E1,E2
  DOUBLE PRECISION young,poisson,yield,dtime, tmp, var, temp1, temp2, tmp2
  DOUBLE PRECISION R_rate(NDIMA), D_rate(NDIMA),
E_rate(NDIMA),R(NDIMA),D(NDIMA)
  DOUBLE PRECISION E(NDIMA), EM(NDIMA), STRESS(NDIMA), NSTRESS, OSTRESS, F,
FP
  DOUBLE PRECISION W(NDIMA), W_rate(NDIMA), M,chi,phi,sig_t, hfunc, lamda
  DOUBLE PRECISION MF,phiF,chiF, lamdaF, WF(NDIMA), W_rateF(NDIMA), Ffd,
STR_rate
  DOUBLE PRECISION WT(NDIMA), md, Ravg(NDIMA), UTS, ACTIVE
  DOUBLE PRECISION WP(NDIMA), W_rateP(NDIMA), phiP, chiP, lamdaP, Tuts, Fpd
!-------------------------------------------------------!
! SET MATERIAL CONSTANTS                                 !
!-------------------------------------------------------!
if(PRNTR.eq.1) then

    X(1)=-2.1772

endif

b=0.000000000001464
n0=1

c1=5838.3
c2=239.64
c3=511.96
c4=0.86806E-01
c5=11.876
c6=1087.4
c7=5.0569
Q=-0.12140 !2.1772

lamda=3.586404
phi=3.703911
chi=3.09
M=5.272E-10
sig_t=12.676080
```

```
phiF=19.376
chiF=0.91691
MF=b
lamdaF=17.332
Ffd=46.1904300124828/4
if (set2.eq.1) Ffd=47.3625289632271/4

phiP=50.786
chiP=1.2042
lamdaP=38.806
Tuts=0

md=0.25

young=21313.89 !1% fatigue
poisson=0.29
yield=36.886 !1% fatigue

if (set2.eq.1) young=21059.85327 !1.4% fatigue
if (set2.eq.1) yield=40.1629311 !1.4% fatigue

!1% 60s
!Ffd=40.6244175248538/4
!Young=15641.96549
!yield=30.1597761

!1.4% 60s
!Ffd=59.6150047165328/4
!Young=23034.0935
!yield=48.29390197

!stepped
!Ffd=45.2592500158258/4
!Young=20821.34352
!yield=35.59864735

!30ksi load controlled *uses the 1% data
!Ffd=40.6244175248538/4
!Young=15641.96549
!yield=30.1597761

!young=15133       !Monotonic Tension
!yield=41.3928256  !Monotonic Tension
!Ffd=50.4231913605892/4 !Monotonic Tension

Ffd=48.7180061851541/4 ! Load Control
UTS=FFD*4*1 !.92
Ravg=0
ACTIVE=0

IF (set1.EQ.0) THEN
!-----------------------------------------------------------!
! CREEP LOOP  / Load Control                                !
!-----------------------------------------------------------!
```

```
yield=40.132363500546453487
rate=b*sinh(yield/4.035)
tmp=c1*0.002
D(1)=(yield-tmp)/asinh((rate/B)**(1/n0))
R(1)= 0
W(1)= 0
WF(1)= 0
WP(1)= 0
WT(1)= 0
D_Rate(1)=0
R_Rate(1)=0
W_rate(1)=0
W_rateF(1)=0
W_rateP(1)=0

dtime=ANSTIME(1)
str_rate=ANSDATA(1)/dtime

tmp=ANSDATA(1)-R(1)
var=1
hfunc=exp(lamda*W(1)**(1.5)+lamdaP*WP(1)**(1)+lamdaF*WF(1)**(1.5))
CALL NN(tmp,sgn)
E_rate(1)=b*sinh(abs(tmp)/D(1))**n0*sgn*hfunc
E(1)=E_rate(1)*dtime
EM(1)=ANSDATA(1)/(young*(1-md*WT(1)))+E(1)

W_rate(1)=M*(1-exp(-phi))/phi*sinh(abs(ANSDATA(1))/sig_t)**chi*exp(phi*WT(1))

temp1=(EM(1)-ANSDATA(1)/Young)/dtime
CALL NN(abs(temp1),temp1) !strain rate
CALL NN(abs(str_rate),temp2) !stress rate
Tuts=temp1*temp2
CALL NN(temp1*temp2,tuts)

W_rateF(1)=0
if (Tuts.gt.0) then
    if (abs(ANSDATA(1)).ge.Ffd) W_rateF(1)=MF*(1-exp(-
phiF))/phiF*sinh(abs(tmp)/D(1))**chiF*exp(phiF*WT(1))
endif
W_rateP(1)=0
if (abs(ANSDATA(1)).ge.UTS) ACTIVE=1
if (ACTIVE.ge.1) THEN
    IF (TUTS.gt.0) W_rateP(1)=MF*(1-exp(-
phiP))/phiP*sinh(abs(tmp)/D(1))**chiP*exp(phiP*WT(1))
endif

W(1)=W_rate(1)*dtime+W(1)
WF(1)=W_rateF(1)*dtime+WF(1)
WP(1)=W_rateP(1)*dtime+WP(1)
WT(1)=W(1)+WF(1)+WP(1)

!Simulation
do i=2,NDIMA
```

```
if (WT(i-1).gt.1.or.E(i-1).gt.1) then
R(i)=R(i-1)
D(i)=D(i-1)
E(i)=E(i-1)
W(i)=W(i-1)
WF(i)=WF(i-1)
WP(i)=WP(i-1)
WT(i)=WT(i-1)
goto 77
endif

dtime=ANSTIME(i)-ANSTIME(i-1)
str_rate=(ANSDATA(i)-ANSDATA(i-1))/dtime

tmp=ANSDATA(i)-R(i-1)
hfunc=exp(lamda*W(i-1)**(1.5)+lamdaP*WP(i-1)**(1)+lamdaF*WF(i-1)**(1.5))
CALL NN(tmp,sgn)
E_rate(i)=b*sinh(abs(tmp)/D(i-1))**n0*sgn*hfunc
cd=c3*exp(-c4*(R(i-1)-Q)*sgn)
R_rate(i)=c1*E_rate(i-1)-(R(i-1)-Q)*( (c2+cd)*abs(E_rate(i-1)))
D_rate(i)=(c5-c7*D(1)**3)*abs(E_rate(i-1))-c6*((D(i-1)-
D(1))**3)*abs(E_rate(i-1))

E(i)=E_rate(i)*dtime+E(i-1)
EM(i)=ANSDATA(i)/(young*(1-md*WT(i-1)))+E(i)

if(WT(i-1).ge.1) then
    W_rate(i)=0
    W_rateF(i)=0
    W_rateP(i)=0
    else
W_rate(i)=M*(1-exp(-phi))/phi*sinh(abs(ANSDATA(i))/sig_t)**chi*exp(phi*WT(i-
1))

temp1=(EM(i)-EM(i-1))/dtime
CALL NN(abs(temp1),temp1) !strain rate
CALL NN(abs(str_rate),temp2) !stress rate
Tuts=temp1*temp2
CALL NN(temp1*temp2,tuts)

W_rateF(i)=0
if (tuts.gt.0) then
    if (abs(ANSDATA(i)).ge.Ffd) W_rateF(i)=MF*(1-exp(-
phiF))/phiF*sinh(abs(tmp)/D(i-1))**chiF*exp(phiF*WT(i-1))
endif
W_rateP(i)=0
if (abs(ANSDATA(i)).ge.UTS) ACTIVE=1
if (ACTIVE.ge.1) THEN
    IF (TUTS.gt.0) W_rateP(i)=MF*(1-exp(-phiP))/phiP*sinh(abs(tmp)/D(i-
1))**chiP*exp(phiP*WT(i-1))
endif

endif
```

```
R(i)=R_rate(i)*dtime+R(i-1)
ravg(i)=(R_rate(i)*dtime)/(ANSTIME(i))+ravg(i-1)
D(i)=D_rate(i)*dtime+D(i-1)
W(i)=W_rate(i)*dtime+W(i-1)
WF(i)=W_rateF(i)*dtime+WF(i-1)
WP(i)=W_rateP(i)*dtime+WP(i-1)
WT(i)=W(i)+WF(i)+WP(i)

77 continue
!PRINT *,ANSTIME(I),' ',ANSDATA(i),' ',W(i),' ',WF(i)
enddo

!Store Results
if (PRNTR.eq.1) OPEN (UNIT=45, FILE='CREEP.TXT')
    do i=1,NDIMA
        IF (isnan(E(I))) THEN
            ANSDATA(I)=10
        ELSEIF (E(i).gt.1) then
            ANSDATA(I)=10
        ELSE
            ANSDATA(i)=EM(i)
        ENDIF

        !if (PRNTR.eq.1) WRITE (45,*) ANSDATA(i),' ', WT(i)
        if (PRNTR.eq.1) WRITE (45,*) W(i) ,' ',WF(i),' ',WT(i)
    enddo
if (PRNTR.eq.1) CLOSE (45)

ELSE

!-------------------------------------------------------------!
! FATIGUE LOOP    / Displacement Control                      !
!-------------------------------------------------------------!
!Initialize
rate=0.001
tmp=c1*0.002
D(1)=(yield-tmp)/asinh((rate/B)**(1/n0))
R(1)= 0
W(1)= 0
WF(1)= 0
WP(1)= 0
WT(1)= 0
D_Rate(1)=0
R_Rate(1)=0
W_rate(1)=0
W_rateF(1)=0
W_rateP(1)=0
Stress(1)= 0.658698669
if (set2.eq.1) stress(1)=0.368968822

dtime=ANSTIME(1)
str_rate=stress(1)/dtime

tmp=STRESS(1)-R(1)
```

```
var=1
hfunc=exp(lamda*W(1)**(1.5)+lamdaP*WP(1)**(1)+lamdaF*WF(1)**(1.5))
CALL NN(tmp,sgn)
E_rate(1)=b*sinh(abs(tmp)/D(1))**n0*sgn*hfunc
E(1)=E_rate(1)*dtime
EM(1)=Stress(1)/(young*(1-md*WT(1)))+E(1)

W_rate(1)=M*(1-exp(-phi))/phi*sinh(abs(Stress(1))/sig_t)**chi*exp(phi*WT(1))

temp1=(EM(1)-stress(1)/Young)/dtime
CALL NN(abs(temp1),temp1) !strain rate
CALL NN(abs(str_rate),temp2) !stress rate
Tuts=temp1*temp2
CALL NN(temp1*temp2,tuts)

W_rateF(1)=0
if (Tuts.gt.0) then
    if (abs(Stress(1)).ge.Ffd) W_rateF(1)=MF*(1-exp(-
phiF))/phiF*sinh(abs(tmp)/D(1))**chiF*exp(phiF*WT(1))
endif
W_rateP(1)=0
if (abs(Stress(1)).ge.UTS) ACTIVE=1
if (ACTIVE.ge.1) THEN
    IF (TUTS.gt.0) W_rateP(1)=MF*(1-exp(-
phiP))/phiP*sinh(abs(tmp)/D(1))**chiP*exp(phiP*WT(1))
endif

W(1)=W_rate(1)*dtime+W(1)
WF(1)=W_rateF(1)*dtime+WF(1)
WP(1)=W_rateP(1)*dtime+WP(1)
WT(1)=W(1)+WF(1)+WP(1)

!Simulation
do i=2,NDIMA

dtime=ANSTIME(i)-ANSTIME(i-1)
NSTRESS=Stress(i-1)

DO j=1,100
    OSTRESS=NSTRESS
    tmp=OSTRESS-R(i-1)
    CALL NN(tmp,sgn)
    hfunc=exp(lamda*W(i-1)**(1.5)+lamdaP*WP(i-1)**(1)+lamdaF*WF(i-1)**(1.5))
    E_rate(i)=b*sinh(abs(tmp)/D(i-1))**n0*sgn*hfunc

    F=OSTRESS/(young*(1-md*WT(i-1)))+E_rate(i)*dtime+E(i-1)-ANSDATA(i)

    CALL NN(tmp,sgn)
    CALL HH(tmp,temp1)
      CALL HH(tmp-1,temp2)

    FP=1/(young*(1-md*WT(i-1)))+2*(temp1-temp2)*b*hfunc*sinh(abs(tmp)/D(i-
1))**n0*dtime+(b*n0*hfunc*sgn*sgn*cosh(abs(tmp)/D(i-1))*sinh(abs(tmp)/D(i-
1))**(n0-1))*dtime/D(i-1)
```

```
    NSTRESS=OSTRESS-F/FP

    conv=abs(NSTRESS-OSTRESS)
    IF (conv.lt.1E-05) exit
ENDDO

STRESS(I)=NSTRESS

str_rate=(stress(i)-stress(i-1))/dtime

tmp=STRESS(I)-R(i-1)
hfunc=exp(lamda*W(i-1)**(1.5)+lamdaP*WP(i-1)**(1)+lamdaF*WF(i-1)**(1.5))
CALL NN(tmp,sgn)
E_rate(i)=b*sinh(abs(tmp)/D(i-1))**n0*sgn*hfunc
cd=c3*exp(-c4*(R(i-1)-Q)*sgn)
R_rate(i)=c1*E_rate(i-1)-(R(i-1)-Q)*( (c2+cd)*abs(E_rate(i-1)))
D_rate(i)=(c5-c7*D(1)**3)*abs(E_rate(i-1))-c6*((D(i-1)-
D(1))**3)*abs(E_rate(i-1))

E(i)=E_rate(i)*dtime+E(i-1)
EM(i)=Stress(i)/(young*(1-md*WT(i-1)))+E(i)

if(WT(i-1).ge.1) then
    W_rate(i)=0
    W_rateF(i)=0
    W_rateP(i)=0
    else
W_rate(i)=M*(1-exp(-phi))/phi*sinh(abs(Stress(i))/sig_t)**chi*exp(phi*WT(i-
1))

temp1=(EM(i)-EM(i-1))/dtime
CALL NN(abs(temp1),temp1) !strain rate
CALL NN(abs(str_rate),temp2) !stress rate
Tuts=temp1*temp2
CALL NN(temp1*temp2,tuts)

W_rateF(i)=0
if (tuts.gt.0) then
    if (abs(Stress(i)).ge.Ffd) W_rateF(i)=MF*(1-exp(-
phiF))/phiF*sinh(abs(tmp)/D(i-1))**chiF*exp(phiF*WT(i-1))
endif
W_rateP(i)=0
if (abs(Stress(i)).ge.UTS) ACTIVE=1
if (ACTIVE.ge.1) THEN
    IF (TUTS.gt.0) W_rateP(i)=F*(1-exp(-phiP))/phiP*sinh(abs(tmp)/D(i-
1))**chiP*exp(phiP*WT(i-1))
endif

endif

R(i)=R_rate(i)*dtime+R(i-1)
D(i)=D_rate(i)*dtime+D(i-1)
W(i)=W_rate(i)*dtime+W(i-1)
```

```
WF(i)=W_rateF(i)*dtime+WF(i-1)
WP(i)=W_rateP(i)*dtime+WP(i-1)
WT(i)=W(i)+WF(i)+WP(i)

!PRINT *,ANSTIME(i),' ',ratio(i)

enddo

!Store Results
if (PRNTR.eq.1) then
    if (set2.eq.0) then
        OPEN (UNIT=55, FILE='FATIGUE05.TXT')
    else
        OPEN (UNIT=55, FILE='FATIGUE07.TXT')
    endif
endif
    do i=1,NDIMA
        IF (isnan(STRESS(I))) THEN
            ANSDATA(I)=0
        ELSE
            ANSDATA(i)=STRESS(i)
        ENDIF

        if (PRNTR.eq.1) WRITE (55,*) ANSTIME(i),' ',ANSDATA(i),' ',WT(i)
    enddo
if (PRNTR.eq.1) CLOSE (55)

endIF

    RETURN
END
! Subroutine returns the sgn of the variable
      SUBROUTINE NN(Var,sgn)
        DOUBLE PRECISION  :: Var, sgn

      sgn=0.0

      If (Var .lt. 0.0) then
      sgn=-1.0
      ENDIF

      IF (Var .gt. 0.0) then
      sgn=1.0
      ENDIF

            RETURN
      END

! Subroutine is a heavyside function
      SUBROUTINE HH(Var,sgn)
        DOUBLE PRECISION    :: Var, sgn

      sgn=1/2
```

```
If (Var .lt. 0.0) then
sgn=0
ENDIF

IF (Var .gt. 0.0) then
sgn=1.0
ENDIF

      RETURN
END
```

LIST OF REFERENCES

[1] Viswanathan, R., and Scheirer, S. T., 2001, "Materials Technology for Advanced Land Based Gas Turbines," *Creep: proceedings of the international conference on creep and fatigue at elevated temperatures*, Tsukuba, Japan, No.01-201 (20010603), pp. 7-21.

[2] Reed, C. R., 2008, *The Superalloys: Fundamentals and Applications*, Cambridge University Press, Cambridge, UK.

[3] Mazur, Z., Luna-Ramirez, A., Juarez-Islas, J. A., and Campos-Amezcua, A., 2005, "Failure Analysis of a Gas Turbine Blade made of Inconel 738LC Alloy," *Engineering Failure Analysis*, **12**(3), pp 474-486.

[4] Pridemore, W. D., 2008, "Stress-Rupture Characterization in Nickel-Based Superalloy Gas Turbine Engine Components," *Journal of Failure Analysis and Prevention*, **8**(3), pp. 281-288.

[5] Schilke, P. W., Foster, A. D., Pepe, J. J., and Beltran, A. M., 1992, "Advanced Materials Propel Progress in Land-based Gas Turbines ," *Advanced Materials and Processes*, **141**(4), pp. 22-30.

[6] Misseijer, R. C., Thabit, T. I., and Mattheij, J. H. G., 1996, "Operational evaluation of patch repaired combustion gas turbine transition pieces," *Journal of Quality in Maintenance Engineering*, **2**(4), pp. 59-70.

[7] GE Energy, 2013, Media Center, http://www.ge-energy.com/about/photos_video_audio.jsp

[8] ACT Independent Turbo Services, 2013, Photo Gallery, http://www.act-texas.com/areas-of-excellence/combustion-repair/

[9] Southall L., and G. McQuiggan, G., 1995, "New 200 MW Class 501G Combustion Turbine", paper 95-GT-215, *International Gas Turbine Conference*, Houston, TX.

[10] Corman, J. C., 1996, "H Gas Turbine Combined Cycle Technology and Development Status", 96-GT-11, *International Gas Turbine Conference*, Birmingham, UK.

[11] Pallotta, A. A., 1993, "Trends in Combustion Materials and Coatings—Westinghouse's Perspective", *Proceedings: Workshop on Directions for Combustion Turbine Materials*, 10/92, EPRI Report TR-102954, S. T. Scheirer and R. Viswanathan.

[12] Hoeft, R., Janawitz, J., Keck, R., 2003, "Heavy-Duty Fas Turbine Operating and Maintenance Considerations," GE Energy Services, GE Power Systems, Atlanta, GA.

[13] Schwieger, S., 2012, "When Bad Things Happen to Good Turbines," *Combined Cycle Journal*, July, 10, 2012.

[14] Betten, J., 2002, *Creep Mechanics*, Springer-Verlag, Berlin, German.

[15] Kassner, M. E. , and Pérez-Prado M., 2004, *Fundamentals of creep in metals and alloys*, Elsevier, pp.47-49.

[16] Penny, R. K., and Marriott, D. L., 1995, *Design for Creep*, Springer, pp.11.

[17] Anderson, T. L., 1995, *Fracture mechanics: fundamentals and applications 2nd Edition*. CRC Press.

[18] Frost, H.J., and Ashby, M. F., 1982, Deformation-Mechanism Maps, The Plasticity and Creep of Metals and Ceramics, Pergamon Press, Oxford, UK.

[19] Larson, R. and Miller, J., 1952, "A Time-Temperature Relationship for Rupture and Creep Stress," *Transactions of the ASME*, **74**, pp. 765.

[20] Viswanathan, R., 1989, "Damage Mechanisms and Life Assessment of High-Temperature Components", *ASM International*, pp. 65-67.

[21] Dieter, G. E., 1961, *Mechanical Metallugry*, McGraw-Hill, New York.

[22] Nomoto, A., Yaguchi, M. and Ogata, T., 2000, "Study on Creep Properties and Microstructural Relation in Directionally Solidified Nickel Base Superalloy", *Key Engineering Materials*, Vols. 171-174, pp. 569-576.

[23] Ibanez, A. R., Srinivasan, V. S., and Saxena, A., 2006, "Creep Deformation and Rupture Behaviour of Directionally-solidified GTD 111 Superalloy," *Fatigue & Fracture of Engineering Materials & Structures*, **29**(12), pp. 1010 – 1020.

[24] Monkman, F. and Grant, N., 1956, "An Empirical Relationship Between Rupture Life and Minimum Creep Rate in Creep-Rupture Tests," *Proceedings of ASTM*, **56**, p. 593-596.

[25] Guo, J., Yuan, C., Yang, H., Lupinc, V and Maldini, M., 2001, "Creep-Rupture Behavior of a Directionally Solidified Nickel-Base Superalloy", Metallurgical and Materials Transactions A, **32**, pp. 1103-1110.

[26] Lakki, A, Herzog, R., Weller, M., Schubert, H., Reetz, C., Gorke, O., Kilo, M., and Borchardt, G., 2000, "Mechanical Loss, Creep, Diffusion, and Ionic Donductivity of ZrO2-8 mol% Y2O3 Polycrystals," *Journal of the European Ceramic Society*, **20**, pp. 286-296.

[27] Chokshi, A. H., 1996, "An Analysis of Creep Deformation in Nanocrystalline Materials," *Scripta Materialia*, **34**(12), pp. 1905-1910.

[28] Andrade, E. N., 1910, "The Viscous Flow in Metals and Allied Phenomena," *Proceedings of the Royal Society*, **A 84**, pp 1-12.

[29] Andrade, E. N., 1914, “Flow of Metals under Large Constant Stress,” *Proceedings of the Royal Society*, **A 90**, pp 329-342.

[30] Nabarro, F. R. N., 1997, “Thermal Activation and Andrade Creep,” *Philosophical Magazine Letters*, **74**(4), pp 227-233.

[31] Pantelakis, S., 1983, *Kriechverhalten metallischer Werkstoffe bei zeitveranderlicher Spannug*, PhD Thesis, RWTH-Aachen.

[32] Norton, F. H., 1929, *The creep of steel at high temperatures*, McGraw-Hill, London.

[33] Dorn, J.E., 1955, "Some Fundamental experiements on high temperature creep", *Journal of the Mechanics and Physics of Solids*, **3**, pp. 85-116.

[34] Garofalo, F., 1965, *Fundamentals of Creep and Creep-Rupture in Metals*, Macmillan, New York.

[35] Webster, G. A., and Ainsworth, R. A., 1994, *High Temperature Component Life Assessment*, Chapman & Hill, London, UK.

[36] Kachanov, L. M., 1967, *The Theory of Creep*, National Lending Library for Science and Technology, Boston Spa, England, Chaps. IX, X.

[37] Rabotnov, Y. N., 1969, *Creep Problems in Structural Members*, North Holland, Amsterdam.

[38] Evans, R., and Wilshire, B., 1985, *Creep of metal and alloys*, Institute of Metals, London.

[39] Prager, M., 1995, Development of the MPC Omega Method for Life Assessement in the Creep Range, *Journal of Pressure Vessel Technology*, **117**(2), pg. 95-103.

[40] Skrzypek, J. and Ganczarski, A., 1999, *Modeling of material damage and failure of structures: theory and applications*, Springer, New York, NY.

[41] Robinson, E. L., 1938, Effect of Temperature Variation on the Creep Strength of Steels, *Transactions of the ASME*, **160**, pp. 253-259.

[42] Lieberman, Y., 1962, “Relaxation, Tensile Strength and Failure of E1 512 and Kh1 F-L Steels,” *Metalloved Term Obrabodke Metal*, **4**, pp. 6-13.

[43] Voorhees, H. R., and Freeman, F. W., 1959, “Notch Sensitivity of Aircraft Structural and Engine Alloys,” *Wright Air Development Center Technical Report*, Part II.

[44] Abo-El-Ata, and Finnie, I., 1971, “A Study of Creep Damage Rules,” *ASME Paper No. 71-WA/Met-1*, American Society of Mechanical Engineers, p. 89.

[45] Chaboche, J. L., 1988, “Continuum Damage Mechanics: Part I – General Concepts,” *Journal of Applied Mechanics*, **55**(1), pp. 59-64.

[46] Chaboche, J. L., 1988, “Continuum Damage Mechanics: Part II – Damage Growth, Crack Initiation, and Crack Growth,” *Journal of Applied Mechanics*, **55**(1), pp. 65-72.

[47] Leckie, F. A., 1978, “The Constitutive Equations of Continuum Damage Mechanics,” *Philosophical Transactions of the Royal Society of London. Series A, Mathematical and Physical Sciences*, **288**, pp. 27-47.

[48] Kowalewski, Z. L., Hayhurst, D. R., and Dyson, B. F.,1994, “Mechanisms-based Creep Constitutive Equations for an Aluminum Alloy,” *The Journal of Strain Analysis for Engineering Design*, **29**(4), pp. 309-316.

[49] Murakami, S., 1987, “Progress of Continuum Damage Mechanics,” *JSME International Journal*, **30**(263), pp. 701-710.

[50] Zheng, Q. S., and Betten, J., 1996, “On Damage Effective Stress and Equivalence Hypothesis,” *International Journal of Damage Mechanics*, **5**(3), pp. 219-240.

[51] Stephens, R. I., and Fatemi, A., 2001, *Metal Fatigue in Engineering 2nd Edition*, Wiley-Interscience, New York. NY.

[52] Canale, L.C.F., Mesquita, R.A., and Tottent, G. E., 2008, *Failure Analysis of Heat Treated Steel Components*, ASM International, Materials Park, OH.

[53] Berling, J. T. and Slot, T., 1969, “Effect of Temperature and Strain Rate on Low-Cycle Fatigue Resistance of AISI 304, 316, and 348 Stainless Steels”, ASTM STP 459, American Society for Testing and Materials, pp. 3-30.

[54] Suresh, S., 1998, *Fatigue of Metals, 2nd Edition*, Cambridge University Press, Cambridge, UK.

[55] Saxena, A., 1998, *Nonlinear Fracture Mechanics for Engineers*, CRC Press, Boca Raton, FL.

[56] Norris, R. H., Grover, P. S., Hamilton, B. C., and Saxena, A., 1977, “Elevated-Temperature Crack Growth,” *Fatigue and Fracture, ASM Handbook*, **19**, ASM International, Materials Park, Waterloo, Cananda, pp. 263.

[57] Coffin, L. F., Jr., 1973, "Fatigue at High Temperature," Fatigue at Elevated Temperatures, ASTM STP 520, American Society for Testing and Materials, pp. 5-34.

[58] Osgerby, S., and Dyson, B. F., 1993, “Constant Strain-Rate Testing: Prediction of Stress-Strain Curves From Constant-Load Creep Data,” *Creep and Fracture of Enginering Materials and Structures*, Eds. Wilshore, B. and Evans, R. W., The Institute of Metals, London, 53-61.

[59] Hill, R., 1998, *The Mathematical Theory of Plasticity*, Oxford University Press, New York.

[60] Araújo, M. C., 2002, *Non-Linear Kinematic Hardening Model for Multiaxial Cyclic Plasticity*. Master's Thesis, Louisiana State University, Baton Rouge, LA.

[61] Levy, M., 1870, *Comptes Rendus de l'Académie des Sciences Paris*, **70**, 1323.

[62] Levy, M., 1871, *Journal de Mathématiques Pures et Appliquées*, **16**, 369.

[63] von Mises, R., 1913, *Gottinger Nachrichten, Mathematisch-Physikalische Klasse*, 582.

[64] Prandtl, L., 1924, *Proceedings of the 1st International Congress on Applied Mechanics*, Delft, **43**.

[65] Reuss, A., 1930, "Berucksichtigung der Elastichen Formanderungen in der Plastizitatststherie", *Zeitschrift für Angewandte Mathematik und Mechanik*, **10**, 266.

[66] Gilman, J. J., 1966, "Progress in the Microdynamical Theory of Plasticity," *Proceedings of the Fifth U.S. Congress of Applied Mechanics*, New York, NY, pp. 385-403.

[67] Rice, J. R., 1970, "On the Structure of Stress-Strain Relations for Time-Dependent Plastic Deformation in Metals," *Journal of Applied Mechanics*, **37**(92), pp.728-737.

[68] Chaboche, J.L., 2008, "A Review of Some Plasticity and Viscoplasticity Constitutive Theories," *International Journal of Plasticity*, **24**, pp. 1642-1693.

[69] Chen, W.-F., & Han, D.-J, 2007, *Plasticity for structural engineers*, J. Ross Publishing, New York, NY.

[70] Helling, D. E., and Miller, A. K., 1987, "The Incorporation of Yield Surface Distortion into a Unified Constitutive Model, Part 1: Equation Development," *Acta Mechanica*, **69**(1-4), pp. 9-23.

[71] Bodner, S. R., and Partom, Y., 1975, "Constitutive Equations for Elastic-Viscoplastic Strain-Hardening Materials," *Transactions of ASME - Journal of Applied Mechanics*, **42**(2), pp. 385-389.

[72] Krempl, E., McMahon, J. J., and Yao, D., 1986, "Viscoplasticity based on overstress with a differential growth law for the equilbrim stress," *Mechanics of Materials*, **5**(1), pp. 35-48.

[73] Fatemi, A., and Yang, L., 1998, "Cumulative Fatigue Damage and Life Prediction Theories: A Survey of the State of the Art for Homogenous Materials," *International Journal of Fatigue*, **20**(1), pp. 9-34.

[74] Albert, W. A. J., 1838, "Über Treibseile am Harz," *Archive für Mineralogie Geognosie Bergbau und Hüttenkunde*, **10**, pp. 215-34.

[75] Palmgren, A., 1924, “Die Lebensdauer von Kugellagern (The Life of Ball Bearings)” *Zeitschrift des Vereines Deutscher Ingenieure*, **68**, pp. 339-341.

[76] Miner, M. A., 1945, “How Cumulative Damage Affects Fatigue Life,” *Machine Design*, 17(12), pp. 111-115.

[77] Kaechele, L. 1963, “Review and Analysis of Cumulative-Fatigue-Damage Theories,” *Rand Corporation Research Memoranda*, AF 49(638)-700.

[78] Marco, S. M., and Starkey, W. L., 1954, *A Concept of Fatigue Damage*, Trans. ASME, **76**(4) , 627-632.

[79] Chaboche, J. L.,1974, “Une Loi Differentielle d'Endommagement de Fatigue avec Cumulation non Lineaire,” *Revue Francaise de Mecanique* 50-51, English translation in "Annales de l'IBTP," HS 39 .

[80] Manson, S. S.,1979, *Some Useful Concepts for the Designer in Treating*, I.CM, **3**(1), pp. 13-45.

[81] Manson, S. S., Halford, G. R., and Hirschberg, M. H, 1971, “Creep-Fatigue Analysis by Strainrange Partitioning,” *NASA-Lewis Research Center*: NASA TM X-67838.

[82] Lemaitre, J., and Desmorat, R., 2005, *Engineering Damage Mechanics:Ductile, Creep, Fatigue, and Brittle Failures*, Springer-Verlag, Berlin, German.

[83] Ostergren, W. J., 1976, “Damage Function and Associated Failure Equations for Predicting Hold Time and Frequency effects in Elevated Temperature, Low Cycle Fatigue,” *Journal of Testing and Evaluation*, **4**(5), pp. 327-339.

[84] Venkatesh, V., and Rack, H. J., 1999, “A Neural Network Approach to Elevated Temperature Creep-Fatigue Life Prediction,” *International Journal of Fatigue*, **21**(3), pp. 225-234.

[85] Plumbridge, W. J., Dean, M. S., and Miller, D. A., 1982, “The importance of failure mode in fatigue-creep interactions,” *Fatigue and Fracture of Engineering Materials and Structures*, **5**(1). pp.101-114.

[86] Grover, P.S. and Saxena, A., 1999, “Modeling the effect of creep-fatigue interaction on crack growth,” *Fatigue and Fracture of Engineering Materials and Structures*, **22**(2). pp.111-122.

[87] Evans, W. J., Jones, J. P., and Williams, S., 2005, “The Interactions Between Fatigue, Creep and Environmental Damage in Ti 6246 And Udimet 720Li,” *International Journal of Fatigue*, **27**(10-12), pp.1473-1484.

[88] Manson, S. S., and Halford, G. R., 2009, *Fatigue and Durability of Metals at High Temperatures*, ASM International, Materials Park, OH.

[89] Goswami, T., 1999, "Low Cycle Fatigue –Dwell Effects and Damage Mechanisms," *International Journal of Fatigue*, **21**(1), pp. 55-76.

[90] Srinivasa, K., Samit, G., and Thomas, W., 2011, "Intergranular Cracking of Oil Field Tubular Components Resulting from the Tempering Process," *Society of Petroleum Engineers - SPE/IADC Drilling Conference and Exhibition 2011*, pp. 163-175.

[91] Bendick, W., 1991, "Analysis of Material Exhaustion and Damage by Creep," *The International Journal of Pressure Vessels and Piping*, **47**(1), pp. 57-78.

[92] Betten, J., 1989, "Generalization of nonlinear material laws found in experiments to multiaxial states of stress," *European Journal of Mechanics - A/Solids*, **8**, pp. 325-339.

[93] Yang, X. J., Chow, C. L., and Lau, K. J., 2003, "A Unified Viscoplastic Fatigue Damage Model for 63Sn-37Pb Solder Alloy under Cyclic Stress Control," *International Journal of Damage Mechanics*, **12**(3), pp. 225-243.

[94] Gyllenskog, J. D., 2010, *Fatigue Life Analysis of T-38 Aileron Lever using a Continuum Damage Approach*, M.S. Thesis, Utah State University, Logan, Utah.

[95] Fortino, S., And Bilotta, A., 2004, "Evaluation of the Amount of Crack Growth in 2D LEFM problems," *Engineering Fracture Mechanics*, **71**(9-10), pp. 1403-1419.

[96] Nuismer, R. J., 1975, An Energy Release Rate Criterion for Mixed Mode Fracture, *International Journal of Fracture*, **11**, pp. 245-250.

[97] Erdogan, F., and Sih G., 1963, "On the Crack Extension in Plates under Plane Loading and Transverse Shear," *Journal of Basic Engineering*, **85**, pp.519-527.

[98] Sih, G., 1974, "Strain Energy Density Factor applied to Mixed Mode Crack Problems," *International Journal of Fracture*, **10**, pp. 305-321.

[99] Goldstein, R V and Salganik, R L, 1974, "Brittle Fracture of Solids with Arbitrary Cracks", *International Journal of Fracture*, **10**(4),pp. 507-523.

[100] McDowell, D., 1997, *Application of Continuum Damage Mechanics to Fatigue and Fracture*, American Society for Testing and Materials, West Conshohocken, PA.

[101] Lemaitre, J., 1986, "Local Approach of Fracture," *Engineering Fracture Mechanics*, **25**(5-6), pp. 523-537.

[102] Murakami, S., Kawai, M., and Rong, H., 1988, "Finite Element Analysis of Creep Crack Growth By a Local Approach," *International Journal of Mechanical Sciences*, **30**(7), pp. 491-502.

[103] Backuckas, J., LAU, A., Tan, T., & Awerbuch, J., 1995, "Computational Methodology to Predict Damage Growth in Unidirectional Composites - I. Theoretical Formulation and Numerical Implementation," *Engineering Fracture Mechanics*, 52(5), pp. 937-951.

[104] James, M. A., 1998, "A Plane Stress Finite Element Model for Elastic-Plastic Mode I/II Crack Growth," Manhattan Kansas: Kansas State University Department of Mechanical and Nuclear Engineering.

[105] Nourbakhshnia, N., and Liu, G. R., 2011, "A Quasi-Static Crack Growth Simulation Based on the Singular ES-FEM," *International Journal for Numerical Methods in Engineering*, **88**(5), pp. 473-492.

[106] Hayhurst, D. R., Brown, P. R., and Morrison, C. J., 1984, "The Role of Continuum Damage in Creep Crack Growth," *Philosophical Transactions of the Royal Society of London. Series A, Mathematical and Physical Sciences*, **311**(1516), pp. 131-158.

[107] Chung, S. W., Lee, C. S., and Kim, S. J., 2006, "Large-Scale Simulation of Crack Propagation Based on Continuum Damage Mechanics and Two-Step Mesh Partitioning," *Mechanics of Materials*, **38**, pp.76-87.

[108] JianPing, J., Guang, M., Yi, S., and Songbo, X., 2003, "An effective continuum damage mechanics model for creep-fatigue life assessment of a steam turbine rotor," *International Journal of Pressure Vessels and Piping*, **80**(6), pp. 389-396.

[109] Yatomi, M., Yokobori, A. J., and Nikbin, K., 2006, "Comparison of two creep crack growth parameters, C* and Q*, with FE Analysis," *Strength, Fracture and Complexity*, **4** , pp. 83-92.

[110] Götting, M., and Rösler, J., 2007, "A finite element creep crack growth model for Waspaloy. Computers & Structures," **85**(3-4), pp. 225-232.

[111] Bogard, F., Lestriez, P., and Guo, Y. Q., 2010, "Damage and Rupture Simulation for Mechanical Parts Under Cyclic Loadings," *Journal of Engineering Materials and Technology*, **132**(2), pp. 1-8.

[112] Martin Wicke, Daniel Ritchie, Bryan M. Klingner, Sebastian Burke, Jonathan R. Shewchuk, and James F. O'Brien, "Dynamic Local Remeshing for Elastoplastic Simulation," *In Proceedings of ACM SIGGRAPH 2010*, Los Angelos, CA, pp. 1–11.

[113] Vorsatz, J., Rossl, Ch., and Seidel, H.-P., 2003, "Dynamic Remeshing and Applications," *SM2003: Proceedings of the Eight ACM Symposium on Solid Modeling and Applications*, Seattle, Washington, pp. 167-175.

[114] Murakami, S., Liu, Y., and Mizuno, M., 2000, "Computational methods for creep fracture analysis by damage mechanics," *Computer Methods in Applied Mechanics and Engineering*, **183**, pp. 15-33.

[115] Liu, Y., and Murakami, S., 1998, "Damage Localization of Conventional Creep Damage Models and Preposition of a new Model for Creep Damage Analysis," *JSME International Journal Series A*, **41**(1), pp. 57-65.

[116] Liu, Y., Kageyama, Y., and Murakami, S., 1998, "Creep fracture modeling by use of continuum damage variable based on voroni simulation of grain boundary cavity," *International Journal of Mechanical Sciences*, **40**(2-3), pp. 147-158.

[117] Stewart, C. M., and Gordon, A. P., 2012, "Methods to Determine the Critical Damage Criterion of the Kachanov-Rabotnov Law," *ASME IMECE 2012, IMECE2012-88389*, Houston, Texas.

[118] Janson, J., and Hult, J., 1977, "Fracture Mechanics and damage mechanics: a combined approach," *Journal of Applied Mechanics*, **1**, pp. 69-84.

[119] ASTM Standard A276, 2013, "Standard Specification for Stainless Steel Bars and Shapes," *ASTM International*, West Conshohocken, PA.

[120] ASTM Standard A479/A479M, 2013, "Standard Specification for Stainless Steel Bars and Shapes for Use in Boilers and Other Pressure Vessels," *ASTM International*, West Conshohocken, PA.

[121] Antoun, B., Korellis, J., and Song, B., 2007, "Techniques for Testing 304L Stainless Steel over a Wide Range of Temperatures," 2007 SEM Annual Conference & Exposition on Experimental and Applied Mechanics, June 4-7, 2007, Springfield, Massachusetts, USA.

[122] Simmons, W. F., and Cross, H., 1952, "Elevated-Temperature Properties of Stainless Steels," ASTM Special Technical Publication No. 124, American Society for Testing and Materials, Philadelphia, PA.

[123] Simmons, W. F., and Van Echo, J. A., 1965, "Report on the Elevated-Temperature Properties of Stainless Steels," The ASTM-ASME Joint Committee on Effect of Temperature on the Properties of Metals, American Society for Testing and Materials, Philadelphia, PA.

[124] AK Steel, 304/304L Stainless Steel Specification Sheet. West Chester, OH.

[125] SandMeyer Steel Company. Alloy 304 Spec Sheet. Philadelphia, PA.

[126] Sikka, V. K., 1978, "Elevated Temperature Ductility of Types 304 and 316 Stainless Steel," Oak Ridge National Lab. Metals and Ceramics Div., ORNL/TM-6608, Oak Ridge, Tn.

[127] Kuang, H, W. , 1990, "Static and Cyclic Loading of Notched 304 Stainless Steel Bars at 650C," *Fatigue and Fracture of Engineering Materials and Structures*, **13(**2), pp. 155-169.

[128] ASM International, 1988, *Atlas of Creep and Stress-Rupture Curves*, Editor Boyer, H. E., Metals Park, Ohio.

[129] Kim, S. J., Kong, Y.S., Roh, Y. J., and Kim, W. G., 2008, "Statistical Propertise of Creep Rupture Data Distribution for STS304 stainless steels," *Materials Science and Engineering A*, **483-484**, pp. 529-532.

[130] Booker, M. K., 1978, "Use of Generalized Regression Models for the Analysis of Stress-Rupture Data," United States Department of Energy by Union Carbide Corporation, Contract W-7405-eng-26, CONF-780609-5, Oak Ridge, Tn.

[131] Kim, H.K., Mohamed, F. A., Earthman, J. C., 1991, "High-Temperature Rupture of Microstructurally Unstable 304 Stainless Steel Under Uniaxial and Triaxial Stress States," Metallurgical Transactions A, **22A**, pp.2629-2636.

[132] McCoy, H. E., and Waddel, R. D., 1975, "Mechanical Properties of Several Products from a Single Heat Of Type 304 Stainless Steel," *Journal of Engineering Materials and Technology*, **97**(4), pp 343-350.

[133] Wilson, D. J., 1971, "Extrapolation of Rupture Data for Type 304 (18Cr-10Ni), Grade 22 (2-1/4Cr-1Mo) and Grade 11(1-1/4Cr-1/2Mo-3/4Si) Steels," Progress Report to: The Metal Properties Council, Report 34006-2P, New York, NY.

[134] Bynum, J. E., Ellis, F. V., Roberts, B. W., and Canonico, D. A., 1992, "High Temperature Creep of Type 304 Stainless Steel," *Stress Classification, Robust Methods, and Elevated Temperature Design*; presented at the 1992 Pressure Vessels and Piping Conference, New Orleans, La, pp. 67-83.

[135] Sritharan, T., and Jones, H., 1980, "The Creep of Type 304 Stainless Steel at Low Stresses", *Acta Metallurgica*, **28**(12), pp. 1633-1639.

[136] Gold, M., Leyda, W. E., and Zeisloft, R. H., 1975, "The Effect of Varying Degrees of Cold Work on the Stress-Rupture Properties of Type 304 Stainless Steel," *Journal of Engineering Materials and Technology*, **97**(4), pp. 305-312.

[137] Coffin, L. F., 1973, "Fatigue at High Temperature," *Fatigue at Elevated Temperatures, ASTM STP 520*, American Society for Testing and Materials, pp. 5-34.

[138] Nahm, H., Michel, D. J., and Moteff, J., 1973, "On the Influence of Deformation Rate on Intergranular Crack Propagation in Type 304 Stainless Steel," *Journal of Material Science*, **8**, pp. 104-108.

[139] Merah, N., Bui-Quoc, T., and Bernard, M., 1999, "Creep-Fatigue Crack Growth in Notched SS-304 Plates at 600°C," *Engineering Fracture Mechanics*, **63**(1), pp. 39-55.

[140] Suh, C. M., Lee, J. J., and Kang, Y. G., 1990, "Fatigue Microcracks in Type 304 Stainless Steel at Elevated Temperature," *Fatigue and Fracture of Engineering Materials and Structures*, **13**(5), pp.487-496.

[141] Nishino, S., Sakane, M., and Ohnami, M., 1986, "Creep, Fatigue, and Creep-Fatigue Damage Evaluation and Estimation of Remaining Life of SUS 304 Austenitic Stainless Steel at High Temperature (Creep-Fatigue damage Evaluation by X-Ray Analysis)," *Journal of the Society of Materials Science*, **35**(390), pp. 292-298.

[142] Forrest, P. G., 1962, *Fatigue of Metals*, Pergamon Press, London.

[143] Sines, G., 1955, "Failure of Materials Under Combined Repeated Stresses with Superimposed Static Stresses," NACA TN 3495.

[144] Basaruddin, K. S., and Wooi, L. C., 2009, "Uniaxial Ratcheting of Mild Steel under Cyclic Tension," *Proceedings of International Conference on Applications and design in Mechanical Engineering (ICADME)*, October 11-13,Batu Ferringhi, Penang, Malaysia.

[145] Gao, Q., Kang, G. Z., and Yang, X. J., "Uniaxial Ratcheting of SS304 Stainless Steel at High Temperature; Visco-Plastic Constitutive Model," *Theoretical and Applied Fracture Mechanics*, **40**(1), pp. 105-111.

[146] Kang, G. Z., Zhang, J., Sun, Y. F., and Kan, Q. H., 2007, "Uniaxial Time-Dependent Ratcheting of SS304 Stainless Steel at High Temperature," *International Journal of Iron and Steel Research*, **14**(1), pp. 53-59.

[147] Berling, J. T., and Slot, T., 1969, "Effects of Temperature and Strain Rate on Low Cycle Fatigue Resistance of AISI 304,316, and 348 Stainless Steels," *Fatigue at High Temperature*, ASTM STP, ASTM, West Conshohocken, PA, p. 3.

[148] Coffin, L. F., "Fatigue at High Temperature," *Fatigue at Elevated Temperature*, ASTM STP 520, American Society for Testing Materials, pp. 5-34

[149] ASM International, 1986, *Atlas of Fatigue Curves*, Editor Boyer, H. E., Metals Park, Ohio.

[150] James, L. A., 1972, "The Effect of Frequency upon the Fatigue-Crack Growth of Type 304 Stainless Steel at 1000°F," *Stress Analysis and Growth of Cracks*, ASTM STP 513, ASTM, West Chonshohocken, PA, p. 218.

[151] Berling, J.T., and Conway, J. B., 1969, "Effects of Hold-Time on the Low-Cycle Fatigue Resistance of 304 Stainless Steel at 1200°F," *First International Conference of Pressure Vessel Technology, Part 2*, Delft, Netherlands, p. 1233.

[152] Koterazawa, R., and Nosho, T., 1992, "Acceleration of Crack growth Under Intermittent Overstressing in Different Environments," *Fatigue and Fracture of Engineering Materials and Structures*, **15**(1), pp. 103-113.

[153] Yablinsky, C. A., Flores, K. M., Mills, M. J., Willams, J. C., and Rigney, J., 2008, "Fatigue Behavior in Monocrystalline Ni-Based Superalloys for Blade Applications," *Superalloys 2008*, pp. 535-540.

[154] Cheng, C. Y, and Diercks, D. R., 1973, "Effects of Hold Time on Low-Cycle Fatigue Behavior of AISI Type 304 Stainless Steel at 593°C," *Metallurgical Transactions: A, Physical Metallurgy and Materials Science*, **4**(2), pp 615-617.

[155] Plumtree, A., Tang, N. Y., 1989, "Effect of Hold-Time Damage on High temperature Fatigue Behaviour," *Fatigue and Fracture of Engineering Materials and Structures*, **12**(5), pp. 377-386.

[156] Lee, S. R., Lee, H. J., Chung, J. O., Oh, S. W., Huh, C.W., and Yoon, D. P., 1990, "Waveform effect on the low cycle fatigue behavior of AISI 304 Stainless Steel at High Temperature" *Key Engineering Materials*, **51-52**, p. 1-6.

[157] James, L.A., 1972, "Hold-time effects on the elevated temperature fatigue-crack propagation of type 304 stainless steel," *Nuclear Technology*,**16**, pp. 521–530.

[158] Michel, D. J., and Smith, H. H., 1977, *Effect of Hold Time and Thermal Aging on Elevated Temperature Fatigue Crack Propagation in Austenitic Stainless Steels*, Ft. Belvoir Defense Technical Information Center, Naval Research Lab, Washington, DC.

[159] Nikitin, I., Scholtes, B., Maier, H. J., and Altenberger, I., 2004, "High Temperature Fatigue Behavior and Residual Stress Stability of Laser-Shock Peened and Deep Rolled Austenitic Steel AISI 304," *Sripta Materialia*, **50**(10), pp 1345-1350.

[160] McVetty, P. G., 1943, "Creep of Metals at Elevated Tempeartures – Hyperbolic-Sine Relation Between Stress and Creep Rate" *Transactions of the ASME*, **65**(7), pp. 761-767.

[161] Dyson, B.F., and McLean, M., 2001, "Micromechanism-quantification for Creep ConstitutiveEquations," In: Murakami, S. and Ohno, N. (eds), IUTAM *Symposium on Creep in Structures*, Dordrecht, Kluwer, pp. 3-16.

[162] Perrin, I.J., and Hayhurst, D.R., 1994, "Creep Constitutive Equations for a 0.5Cr-0.5Mo-0.25V Ferritic Steel in the Temperature Range 600-675C," *Journal of Strain Analysis*, **31**, pp. 299-314.

[163] Williams, J. A, and Carter, J. W., 1967, "Creep Annealed Type 304 Stainless Steel During Irradiation and Its Engineering Significance," STP41322S, *ASTM International*, pp. 149-160.

[164] Naumenko, K., Altenbach, H., and Kutschke, A., 2011, "A Combined Model for Hardening, Softening, and Damage Processes in Advanced Heat Resistant Steels at Elevated Temperature," *International Journal of Damage Mechanics*, **20**, pp. 578-597.

[165] Calì, C., Cricrì, G., and Perrella, M., 2008, "An Advanced Creep Model Allowing for Hardening and Damage Effects," *Strain*, **46**(4), pp. 347-357.

[166] Phaniraj, C., Nandagopal, M., Mannan, S. L., Rodriguez, P., 1991, "The Relationship between Transient and Steady State Creep in AISI 304 Stainless Steel," *Acta Metallurgica et Materialia*, **39**(7), pp. 1651-1656.

[167] Conway, J. B., and Mullikin, M. J., 1966, "A Graphical Solution of the Garofalo Equation [For Creep, 1960]," *Transactions of the Metallurgical Society of AIME*, **236**(6), pp. 946-947.

[168] Evans, W. J., and Wilshire, B., 1968, "Transient and Stead-State Creep Behavior of Nickel, Zinc, and Iron," *Transactions of the Metallurgical Society of AIME*, **242**(7), pp.1303-1307.

[169] Przystupa, M. A., and Ardell, A. J., 2002, "Predictive Capabilities of the Dislocation-Network Theory of Harper-Dorn Creep," *Metallurgical and Materials Transactions A: Physical Metallurgy and Materials Science*, **33**(2), pp. 231-239.

[170] Stewart, C.M., and Gordon, A. P., 2012, "Consitutive Modeling of Multistage Creep Damage in Isotropic and Transversely-Isotropic Alloys with Elastic Damage," *Journal of Pressure Vessel Technology*, Accepted For Publication.

[171] Stewart C. M., Gordon A. P., Hogan, E. A., and Saxena, A. 2011, "Characterization Of The Creep Deformation And Rupture Behavior Of DS GTD-111 Using The Kachanov-Rabotnov Constitutive Model," *Journal of Engineering Materials and Technology*, 1 3 3(2), pp.1-11.

[172] Stewart, C. M., and Gordon A. P., 2011, "Strain and Damage-Based Analytical Methods to Determine the Kachanov-Rabotnov Tertiary Creep Damage Constants," *International Journal of Damage Mechanics*, Dec 21st, 2011.

[173] Stewart C. M., Gordon A. P., Ma, Y. W., and Neu, R. W., 2011, "An Anisotropic Tertiary Creep-Damage Constitutive Model for Anisotropic Materials," *International Journal of Pressure Vessel and Piping*, **88**(8-9), pp. 356-364.

[174] Stewart C. M., Gordon A. P., Ma, Y. W., and Neu, R. W., 2011, "An Improved Anisotropic Tertiary Creep Damage Formulation," *Journal of Pressure Vessel Technology*, **133**(5), pp. 1-10.

[175] Murakami, S., Liu, Y., and Sugita, Y., 1992, "Interrelation between Damage Variables of Continuum Damage Mechanics and Metallographical Parameters in Creep Damage," *International Journal of Damage Mechanics*, **1**, pp. 172-190.

[176] Ankit, K., 2008, "Remaining Creep Life Assessment Techniques Based on Creep Cavitation Modeling," *The e-Journal of Nondestructive Testing*, October 2008.

[177] ECCC, 2005, ECCC Recommendations, Residual Life and Microstructure Volume 6, Concari, S., pp. 1-30.

[178] Shammas, M.S., 1988, "Metallographic Methods for Predicting the Remanent Life of Ferritic Coarse-Grained Weld Heat Affected Zones Subject to Creep Cavitation", International Conference on Life Assessment, EPRI, Palo Alto, pp. 238-244.

[179] Dyson, B. F., and McLean, D., 1977, "Creep of Nimonic 90A in Torsion and Tension, *Metal Science*, **11**(2), pp. 37-45.

[180] Hutchinson, J. W., 1983, "Constitutive Behavior and Creep Tip Fields for Materials Undergoing Creep-Constrained Grain Boundary Cavitation, *Acta Metallurgica*, **31**(7), pp. 1079-1088.

[181] Riedel, H., 1987, *Fracture at High Temperatures*, Springer-Verlag.

[182] Schmidt M., Lipson, H., 2009, "Distilling Free-Form Natural Laws from Experimental Data," *Science*, **324**(5923), pp. 81 – 85.

[183] Trampczynski, W. A., Hayhurst, D. R., and Leckie, F. A., 1981, "Creep Rupture of Copper and Aluminum Under Non-Proportional Loading**,"** *Journal of the Mechanics and Physics of Solids*, **29**(5-6), pp. 353-374.

[184] Yao, H. T., Xuan, F. Z., Wang, Z., and Tu, S. T., 2007, "A Review of Creep Analysis and Design Under Multi-Axial Stress States," *Nuclear Engineering and Design*, **237**(18), pp. 1969-1986.

[185] Yatomi, M., O'Dowd, N. P., and Nikbin, K. M., 2004, "Modelling of Damage Development and Failure in Notched bar Multiaxial Creep Tests," *Fatigue and Fracture of Engineering Materials and Structures*, **27**(4), pp 283-295.

[186] Rice J.R. and Tracey D.M., 1969, "On the Ductile Enlargement of Voids in Triaxial Stress Fields," *Journal of the Mechanics and Physics of Solids*, **17**(3), pp. 201-217.

[187] Cocks A.C.F. and Ashby M.F., 1980, "Intergranular Fracture in Power Law Creep under Multiaxial Stress," *Metal Science*, **14**(8-9), pp. 395-402.

[188] McClintock F.A., 1968, "A Criterion for Ductile Fracture by the Growth of Holes," *Journal of Applied Mechanics*, **35**(2), pp. 363–371.

[189] Budiansky B., Hutchinson J.W. and Slutsly S.,1982, "Void Growth and Collapse in Viscous Solids" *Mechanics of Solids*, H.G. Hokins and M.J. Sewell (eds.), Pergamon Press, Oxford.

[190] Spindler, M.W.,1994, "The Multiaxial Creep of Austenitic Stainless Steels" *Fatigue and Fracture of Engineering Materials and Structures*, **27**(4), pp.273-281.

[191] Sdobyrev, V.P, 1958, "Long Term Strength of Alloy E1-437B Under Complex Stress," Izv. An SSSr, OTN4.

[192] Hyde, T. H., Xia, L., and Becker, A. A., 1996, "Prediction of Creep Failure in Aeroengine Materials Under Multi-Axial Stress States," International Journal of Mechanical Sciences, **38**(4), pp. 385-403

[193] Hayhurst, D. R., Dimmer, P. R., and Morrison, C. J., 1984, "Development of Continuum Damage in Creep Rupture of Notched Bars," *Philosophical Transactions of the Royal Society of London. Series A, Mathematical and Physical Sciences*, **311**, pp. 103-129.

[194] Johnson, A. E., Henderson, J., and Kathu, B., 1960, "Complex Stress Creep Fracture of an Aluminum Alloy," *Aircraft Engineering*, **32**, pp. 161-170.

[195] Webster, G. A., Cane, B. J., Dyson, B. F., and Loveday, M. S., 1991, *A Code of Practice for Notched Bar Creep Rupture Testing: Procedures and Interpretation of Data for Design*, National Physics Laboratory, Teddington.

[196] Bridgman, P. W., 1952, *Studies in Large Plastic Flow and Fracture*. McGraw Hill, New York.

[197] Kachanov, L. M., 1986, "On Creep Stresses in a Bridgman Notched Bar," *Mechanics of Materials*, **5**(3), pp.229-234.

[198] Webster, G. A., Holdsworth, R., Loveday, M. S., Nikbin, K., Perrin, I. J., Purper, H., Skelton, R. P., and Spindler, M. W., 2004, "A Code of Practice for Conducting Notched Bar Creep Test and for Interpreting the Data," *Fatigue and Fracture of Engineering Materials and Structures*, **27**(4), pp. 319-342.

[199] Pandey, M. C., Mukherjee, A. K., and Taplin, D. M. R., 1985, "Effect of Triaxial Stress-State on Creep Fracture in Inconel Alloy X-750," *Journal of Materials Science*, **20**(4), pp. 1201-1206.

[200] Hayhurst, D. R., 1972, "Creep Rupture Under Multi-Axial States of Stress," *Journal of the Mechanics and Physics of Solids*, **20**(6), pp. 381-390.

[201] Voyiadjis, G. Z., and Kattan, P. I., 2013, "Introduction to the Mechanics and Design of Undamagable Materials," *International Journal of Damage Mechanics*, **22**(3), pp. 323-335.

[202] Murakami, S., and Ohno, N., 1981, *IUTAM Symposium on Creep in Structures*, Eds. Ponter, A. R. S., and Hayhurst, D. R.; Springer.

[203] Chen, X. F., and Chow, C. L., 1995, "On damage Strain Energy Release Rate Y," *International Journal of Damage Mechanics*, **4**(3), pp. 251-263.

[204] Barbero, E. J., and De Vivo, L., 2001, "A Constitutive Model for Elastic Damage in Fiber-Reinforced PMC Laminae," *International Journal of Damage Mechanics*, **10**(1), pp. 73-93.

[205] Chow, C. L., and Lu, T. J., 1992, "Damage Mechanics Approach to Ductile Failure Analysis in Notched Plates," *ASME Applied Mechanics Division - Recent Advances in Damage Mechanics and Plasticity*, **132**, pp. 21-35.

[206] Cordebois, J. P., Sidoroff, F., 1982, "Anisotropic Damage in Elasticity and Plasticity," *Journal de Mecanique Theorique et Appliquee*, pp. 45-60.

[207] Dufailly, J., and Lemaitre, J., 1995, "Modeling Very Low Cycle Fatigue," *International Journal of Damage Mechanics*, **4**(2), pp. 153-170.

[208] Rides, M., Cocks, A. C., and Hayhurst, D. R., 1989, "The Elastic Response of Damaged Materials," *Journal of Applied Mechanics*, **56**(9), pp. 493-498.

[209] Zhang, W., 2011, *Continuum Damage Mechanics and Numerical Applications*, Springer.

[210] Penny, R. K., 1996, "The Use of Damage Concepts in Component Life Assessment," *International Journal of Pressure Vessels and Piping*, **66**(1-3), pp. 263-280.

[211] Skelton R. P., Rees C. J., and Webster G. A., 1996, "Energy damage summation methods for crack initiation and growth during block loading in high-temperature low-cycle fatigue," *Fatigue & Fracture of Engineering Materials & Structures*, **19**(2-3), pp. 287-297.

[212] Yang, L. and Fatemi, A., 1998, "Cumulative Fatigue Damage Mechanisms and Quantifying Parameters: A Literature Review," *Journal of Testing and Evaluation*, **26**(2), pp.89-100.

[213] Cheng, Y. S., and Huang, Y., 1988, "Measurement of Continuous Damage Parameter," *Engineering Fracture Mechanics*, **31**(6), pp. 985-992.

[214] Fan, Z. C., Chen, X. D., Chen, L., and Jiang, J. L., 2009, "A CDM-Based Study of Fatigue-Creep Interaction Behavior," *International Journal of Pressure Vessels and Piping*, **86**(9), pp. 628-632

[215] Lemaitre, J., and Dufailly, J., 1987, "Damage Measurements," *Engineering Fracture Mechanics*, **28**(5/6), pp. 643-661.

[216] Kim, H. K., Mohamed, F. A., and Earthman, J. C., 1991, "High-Temperature Rupture of Microstructurally Unstable 304 Stainless Steel Under Uniaxial and Triaxial Stress States," *Metallurgical Transactions A*, 22(11), pp. 2629-2636.

[217] Lemaitre, J., and Dufailly, J., 1987, "Damage Measurements," *Engineering Fracture Mechanics*, **28**(5/6), pp. 643-661.

[218] Voyiadjis, G. Z., and Kattan, P. I., 2009, "A Comparative Study of Damage Variables in Continuum Damage Mechanics," International Journal of Damage Mechanics, 18(4), pp. 315-340.

[219] Bonora, N., Ruggiero, A., Gentile, D., and De Meo, S., 2011, "Practical Applicability and Limitations of the Elastic Modulus Degradation Technique for Damage Measurements in Ductile Metals," *Strain*, **47**(3), pp. 241–254.

[220] Lin, G, 1999, "ANSYS USER Material Subroutine USERMAT," ANSYS, Inc., Canonsburg, PA.

[221] Betten, J., 1982, "Material Constitutive Equations for Describing the Secondary and Tertiary Creep of Anisotropic Materials," *Rheologica Acta*, **21**(4-5), pp. 406-408.

[222] Findley, W. N., Lai, J. S., and Onaran, K., 2011, *Creep and Relaxation of Nonlinear Viscoelastic Materials*, Courier Dover Publications.

[223] Maitland, K., 2010, *Problems with Incompressibility in Finite Element Analysis*, MS. Thesis, McMaster University.

[224] Nanthikensan, S., and Sunder, S. S., 1995, "Tensile Cracks in Polycrystalline Ice Under Transient Creep: Part I – Numerical Modeling," *Mechanics of Materials*, **21**(4), pp. 265-279.

[225] Predeleanu, M., and Gilormini, P., 1997, *Advanced Method in Materials Processing Defects*, Elsevier Science, Amsterdam, The Netherlands.

[226] Krempl, E., 1987, "Models of Viscoplasticity Some Comment on Equilbrim (Back) Stress and Drag Stress," *Acta Mechanica*, **69**(1-4), pp. 25-42

[227] Chow, C. L., and Wei, Y., 1999, "Constitutive Modeling of Material Damage for Fatigue Failure Prediction," *International Journal of Damage Mechanics*, **8**(4), pp. 355-375.

[228] Abu Al-Rub, R. K., Darabi, M. K., Little, D. N., and Masad, E. A., 2010, "A Micro-Damage Healing Model that Improves Prediction of Fatigue Life in Asphalt Mixes," *International Journal of Engineering Sciences*, **48**(11), pp. 966-990.

[229] Naumenko, K., Altenbach, H., and Kutschke, A., 2011, “A Combined Model for Hardening, Softening, and Damage Processes in Advanced Heat Resistant Steels at Elevated Temperatures,” *International Journal of Damage Mechanics*, **20**(4), pp.578-597.

[230] James, G. H., Imbrie, P. K., Hill, P. S., Allen, D. H., and Haisler, W. E., 1987, "An Experimental Comparison of Several Current Viscoplastic Constitutive Models at Elevated Temperature," *ASME Journal of Engineering Materials and Technology*, **109**(2), pp. 130-139.

[231] Hartmann, G., and Kollmann, F. G., 1987, "A Computational Comparison of the Inelastic Constitutive Models of Hart and Miller," *Acta Mechanica*, **69**, pp. 139-165.

[232] Hartmann, G., 1990, "Comparison of the Uniaxial Behavior of the Inelastic Constitutive Models of Miller and Walker By Numerical Experiments," *International Journal of Plasticity*, **6**, pp. 189-206.

[233] Hart, E. W., 1976, "Constitutive Relations for the Non-Elastic Deformation of Metals", *Journal of Engineering Materials and Technology*, **98**, pp. 97-105.

[234] Miller, A. K., 1997, “From ODS to MATMOD: Predicting Deformation Under Complex Histories,” *Creep and Fracture of Engineering Materials and Structures: Proceedings of the Seventh International Conference*, August, 10-15th, pp. 159-170.

[235] Kagawa, H., and Asada, Y., 1983, “Extension of Miller’s Constitutive Model for Multiaxial Deformation,” *ASME International Conference on Advances in Life Prediction Methods*, Albany, NY, April 18-20, pp. 33-39.

[236] Miller, A., 1976, “An Inelastic Constitutive Model for Monotonic, Cyclic, and Creep Deformation: Part I – Equations Development and Analytical Procedures,” *Journal of Engineering Materials and Technology*, **98**(2), pp. 97-105.

[237] Miller, A., 1976, “An Inelastic Constitutive Model for Monotonic, Cyclic, and Creep Deformation: Part II – Application to Type 304 Stainless Steel,” *Journal of Engineering Materials and Technology*, **98**(2), pp. 106-113.

[238] Chaboche, J. L., 1977, "Viscoplastic Constitutive Equations for the Description of Cyclic and Anisotropic Behaviour of Metals," *Bull. de l'Acad. Polonaise des Sciences, Série Sc. et Tech.*, **25**, pp. 33–42.

[239] Robinson, D. N., 1978 "A Unified Creep-Plasticity Model for Structural Metals at High Temperatures," ORNL/TM-5969, Oak Ridge National Laboratory.

[240] Cernocky, E.P., and Krempl, E., 1980, "A Theory of Thermoviscoplasticity Based on Infinitesimal Total Strain," *International Journal of Solids and Structures*, **16**(8), pp. 723–741.

[241] Walker, K. P., 1981, "Research and Development Program for Nonlinear Structural Modeling with Advanced Time-Dependent Constitutive Relationships," Final Report, NASA CR-165533, NASA.

[242] Armstrong, P.J., Frederick, C.O., 1966, "A mathematical representation of the multiaxial Bauschinger effect," Report RD/B/N731, CEGB, Central Electricity Generating Board, Berkeley, UK.

[243] Krieg, R. D., 1977, "Numerical Integration of Some new Plasticity-Creep Formulations," *Proceedings of the 4th International Conference on Structural Mechanics in Reactor Technology,* San Francisco, CA, paper M6/b.

[244] Miller, A. K., 1980, " Modelling of Cyclic Plasticity with Unified Constitutive Equations: Improvements in Simulating Normal and Anomalous Bauschinger Effects," *Journal of Engineering Materials and Technology*, **102**, pp. 215-222.

[245] Krieg, R. D., Swearengen, J. C., and Rhode, R. W., 1978, "A Physically-Based Internal Variable Model for Rate-Dependent Plasticity," *Proc. ASME/CSME PVP Conference*, pp. 15-27.

[246] Hogan, E. A., 2009, "An efficient method for the optimization of Viscoplastic constitutive model constants," Honors in the Major Undergraduate Thesis, University of Central Florida, Orlando, FL.

[247] DeMarco, J. P., Hogan, E. A., Stewart, C. M., and Gordon, A. P., 2010, "An Efficient Method for the Optimization of Viscoplastic Constitutive Model Constants," *ASME TURBOEXPO 2010*, GT2010-23311, Glasglow, UK, June 14-18, 2010.

[248] Corana, A., Marchesi, M., Martini, C., and Ridella, S., 1987, "Minimizing Multimodal Functions of Continuous Variables with the 'Simulated Annealing" Algorithm," *ACM Transactions on Mathematical Software*, **13**(3), pp. 262-280.

[249] Goffe, W. L., Gary, D. F., and Rogers, J., 1993, "Global Optimization of Statistical Functions with Simulated Annealing," *Journal of Econometrics*, **60**(1/2), pp. 65-100.

[250] Gurson, A. L., 1977, "Continuum Theory of Ductile Rupture by Void Nucleation and Growth: Part I-Yield Criterion and Flow Rules for Porous Ductile Media," *Journal of Engineering Materials and Technology*, **99**(1), pp. 2-15.

[251] Iino, Y., 1978, "Plastic Zones around Creep and Fatigue Cracks at 650°C in Type 304 Stainless Steel," *Metal Science*, **12**(4), pp. 207-214.

[252] Iino, Y., 1975, "Cyclic Crack Tip Deformation and its Relation to Fatigue Crack Growth," *Engineering Fracture Mechanics*, **7**(2), pp. 205-206.

[253] Iino, Y., 1976, “Accumulated Plastic Zone around Fatigue Crack in Type 304 Stainless Steel,” *Metal Science*, **10**, pp. 159.

[254] Iino, Y. 1980, “The Recrystallization Technique for Local Plastic-Zone Observation in Type 304 Stainless Steel in the Temperature Range of -196° to 950° C,” *Experiemental Mechanics*, **20**(9), pp. 316-319.

[255] Chaboche, J. L., and Lesne, P. M., 1988, “A Non-Linear Continuous Fatigue Damage Model,” *Fatigue and Fracture of Engineering Materials and Structures*, **11**(1), pp. 1-17.

[256] Cheng, G., and Plumtree, A., 1998, "A Fatigue Damage Accumulation Model Based on Continuum Damage Mechanics and Ductility Exhaustion," *International Journal of Fatigue*, **20**(7) pp. 495-501.

[257] Wang, J., 1992, "Low Cycle Fatigue and Cycle Dependent Creep with Continuum Damage Mechanics," *International Journal of Damage Mechanics*, **1**(2), pp. 237-244.

[258] Shang, D. G., and Yao, W. X., 1999, "A Nonlinear Damage Cumulative Model for Uniaxial Fatigue," *International Journal of Fatigue*, **21**(2), pp. 187-194.

[259] Hyde, T. H., Xia, L., Becker, A. A., and Sun, W., 1997, "Fatigue, Creep and Creep/Fatigue Behaviour of a Nickel Base Superalloy at 700°C," *Fatigue & Fracture of Engineering Materials & Structures*, **20**(9), pp. 1295–1303.

[260] Kachanov, L.M., 1958, "Time to Creep Fracture," *lzv. Akad. Nauk SSSR, Otd. Tekh. Nauk*, (8), pp. 26-31.

[261] Johnson, G. R. , and Cook, W. H., 1985, “Fracture Characteristics of Three Metals Subjected to Various Strains, Strain Rates, Temperatures and Pressures,” *Engineering Fracture Mechanics*, **21**(1), pp. 31-48.

[262] Wilkins, M. L., 1964, “Calculation of elastic–plastic flow,” B. Adler (Ed.) et al., *Methods of Computational Physics*, **3**, Academic Press, New York, USA.

[263] Huang, J., and Griffith, D. V., 2008, “Observations on Return Mapping Algorithms for Piecewise Linear Yield Criteria,” *International Journal of Geomechanics*, **8**(4), pp. 253-265.

[264] Coffin, L. F., “Fatigue at High Temperature,” *Fracture 1977, The Fourth International Congress on Fracture*, ICF-4, **1**, University of Waterloo Press, Waterloo, Canada, 1977, p. 263.

[265] Jaske, C. E., Mindlin, H., and Perrin, J.S., 1973, “Cyclic Stress-Strain Behavior of Two Alloys at High Temperature,” *Cyclic Stress-Strain Behavior Analysis, Experimentation and Failure Prediction*, ASTM STP 519, American Society for Testing and Materials, pp. 13-27.

[266] Giannopoulos, I. P., and Burgoyne, C. J., 2011, "Prediction of the Long-Term Behaviour of High Modulus Fibres using the Stepped Isostress Method (SSM)," *Journal of Material Science*, **46**(24), pp. 7660-7671.

[267] Golub, V. P., 2000, "The Nonlinear Mechanics Of Continual Damage And Its Application To Problems Of Creep And Fatigue," *International Applied Mechanics*, **36**(3), pp. 303-342.

[268] Basaran, C., and Nie, S., 2004, "An Irreversible Thermodynamics Theory for Damage Mechanics of Solids," *International Journal of Damage Mechanics*, **13**(3), pp. 205-223.

[269] Biegler M.W. and Mehrabadi, M. M., 1995, "An Energy-Based Constitutive Model for Anisotropic Solids Subject to Damage," *Mechanics of Materials*, **19**(2-3), pp. 151-164.

[270] Paas, M. H. J. W., 1990, "Continuum Damage Mechanics with an Application to Fatigue," Ph.D. Thesis, Eindhoven University of Technology, Eindhoven, The Netherlands.

[271] Silberschmidt, V. V., and Chaboche, J. L, 1994, "Effect of Stochasticity on the Damage Accumulation in Solids," *International Journal of Damage Mechanics*, **3**(1), pp. 57-70.

[272] Bhattacharya, B., and Ellingwood, B., 1998, "Continuum Damage Mechanics-Based Model of Stochastic Damage Growth," *Journal of Engineering Mechanics*, **124**(9), pp. 1000-1009.

[273] Kraft, S. M. and Gordon, A. P., 2011, "Characterization of the Tensile Behavior of a Metallic Fiber Woven Structure," *Textile Research Journal*, **81**(12), pp. 1249-1272.